

Auroral Radio Absorption: Modelling and Prediction

A thesis presented for the degree of Doctor of Philosophy

in the

Department of Physics

Lancaster University

Lancaster, UK

By

Olugbenga Ayotunde Ogunmodimu (M.Sc)

October, 2016

Dedicated first to the glory of God almighty, and to my son Toluwanimi Zion Olumodimu and by faith to my daughter Temiloluwa glory Olumodimu.

Declaration

I declare that the work contained in this thesis is my own, except where stated otherwise, and has been completed in the Department of Physics at Lancaster University. No part of this thesis has been submitted elsewhere for the award of a higher degree.

Results of Chapter 4 have been presented at the International Ionospheric Effects Symposium, May 2011.

Acknowledgements

There are many people I will like to appreciate for various reasons. First, my profound gratitude goes to my supervisor Professor Farideh Honary for giving me the opportunity to study in the Space Plasma Environment and Radio Sciences group (SPEARS) and her uncommon understanding at points when I had difficulties. Many thanks to other members of the group especially Dr(s) Andrew Kavanagh, Matthew Beharrell, Neil Roger, Steve Marple and Professor Jim Wild for supports ranging from computing advice, to offering very useful information and their friendliness.

My appreciation goes to my wife Toyin Olumodimu for her extreme understanding and support while studying. Immense gratitude to Dr Bamidele Adebisi and his family for their outstanding contribution to my overall well-being and invaluable support. I appreciate Messrs Adekola and Kayode Ogunsua and their families for their financial support without which I would not have been able to complete this course. Dr Ife Akintunde for his faith and uncommon generosity towards me. My gratitude goes to members of the Overseas Fellowship of Nigerian Christians (OFNC) for their love and kindness, majorly, Dr(s) Abel Adegoke, Albert Okoye, the Nwegbus, the Sodipos and others too numerous to mention.

My appreciation goes to my siblings, Similoluwa Adeyanju, Morakinyo Ogunmodimu and Olawale Ogunmodimu for their prayers and love. To my parents, Chief Emmanuel Bayode and Mrs. Olukemi Ogunmodimu who are exemplary in every way. Thanks to the leadership of new covenant church Manchester, members of the teenage church and to my mentors: Dr Adekunle Salami and family, Late. Olaniyi Kolade, Rev Sunday Akingbelure and Rev Sunday Adelaja. I acknowledge my friends Ibrahim Ethem Bagci, Biodun Balogun, Tunde Kassim, Onome Asuilemen, Uche Okere, Dayo Akenroye, Bayo Ojo, Biola Oladipo, Hayk Sargsyan, Pastor Andrew

Eluwa and Steve Niafas for their help with proofreading the final thesis. It is a joy working with staff members of the Lancaster University International Office. Many thanks to the postgraduate coordinator of the Physics department, Lancaster University Ms Sandra Irving.

List of symbols and acronyms

χ	:	Solar-zenith angle
\AA	:	$10^{-10} m$
AA	:	Auroral Absorption
ACE	:	Advanced Composition Explorer (satellite)
AE	:	Auroral Electrojet
AGARD	:	Advisory Group for Aerospace Research and Development (NATO)
A_p	:	A planetary geomagnetic index
1AU	:	149,598,000 km
B	:	Magnetic field
B_y	:	Eastward component of the IMF (in GSM coordinates)
B_z	:	Northward component of the IMF (in GSM coordinates)
CCIR	:	Comité Consultatif International pour la Radio
CARISMA	:	Canadian Array for Realtime Investigation of Magnetic Activity
CME	:	Coronal Mass Ejections
CNA	:	Cosmic Noise Absorption
DMI	:	Danish Meteorological Institute
DRAP	:	D-Region Absorption Prediction
D_{st}	:	A geomagnetic index (Disturbance - Storm Time)
EM	:	Electromagnetic
EUV	:	Extreme Ultraviolet
FAC	:	Field-aligned current
GLORIA	:	Global Riometer Array
GOES	:	Geostationary Operational Environmental Satellite
GSM	:	Geocentric Solar Magnetospheric (coordinates)

eV	:	Electron-Volt. (keV = 10^3 eV, MeV = 10^6 eV, etc.)
$F_{10.7}$:	Solar flux at 10.7cm wavelength
FPGA	:	Field Programmable Gate Array
GGG	:	Global Geospace Science
GOF	:	Goodness of Fit
HAF	:	Highest Affected Frequency
HF	:	High-Frequency (3-30 MHz)
HSS	:	High Speed Solarwind stream
ICME	:	Interplanetary Coronal Mass Ejections
IGRF	:	International Geomagnetic Reference Field
IMAGE	:	International Monitor for Auroral Geomagnetic Effects
IMF	:	Interplanetary Magnetic Field
IRIS	:	Imaging Riometer for Ionospheric Studies
ITU	:	International Telecommunications Union
K_p	:	A planetary geomagnetic index
L1	:	First Lagrangian point
MAG	:	Magnetic Feld Monitor
MLT	:	Magnetic Local Time
NASA	:	National Aeronautics and Space Administration (USA)
NATO	:	North Atlantic Treaty Organization
N_e	:	Free-electron density
NOAA	:	National Oceanic and Atmospheric Administration (USA)
OLE	:	Ordinary Least Estimation
OLS	:	Ordinary Least Square
PCA	:	Polar Cap Absorption
Q(1)	:	Probability of 1dB absorption on a riometer at 30MHz
QDC	:	Quiet Day Curve
R_E	:	Earth radius, ($1R_E=6371$ km)
R_\odot	:	Solar radii, ($1R_\odot = 6.957 \times 10^5$ km)
SAMNET	:	Sub-Auroral Magnetometer Network

SCA	:	Sudden Commencement Absorption
SD	:	Standard Deviation
SEP	:	Solar Energetic Particles
SOA	:	Sharp-Onset Absorption
SPE	:	Solar Proton Event / Solar Particle Event
SRE	:	Solar Radio Emission
SSC	:	Storm Sudden Commencement
SVA	:	Slowly-Varying Absorption
SWF	:	Shortwave Fadeout
SWE	:	Solar Wind Experiment
SWEPAM	:	Solar Wind Electron Proton and Alpha Monitor
SWPC	:	Space Weather Prediction Center (NOAA)

Abstract

Energetic particle precipitation with ($>keV$) energetic electrons from closed field lines and ($>MeV$) protons from the solar wind are responsible for enhanced high frequency radiowave absorption in the high latitude ionosphere. Measuring the propagation of radio waves through the ionosphere has been utilised for investigating particle precipitation into the upper atmosphere. Although various methods and models previously proposed for auroral and polar cap absorptions have significantly contributed to our knowledge, there are progressive efforts to improve these models as a result of improved understanding of already made assumptions, development of more efficient equipment and availability of real-time data. This study seeks to contribute to this field. The method utilised combines data from ground-based imaging riometer during solar cycle 23 (1996-2009) and solar wind parameters measured at the L1 point between the Earth and Sun to provide empirical relationship as the basis for a statistical model of auroral absorption. The variation of cosmic noise absorption (CNA) has been modelled using the Akasofu epsilon parameter which characterises the energy transfer between the solar wind and the magnetosphere. The result shows that the absorption model based on the epsilon parameter is reliable for periods with low to moderate solar activity but breaks down during periods of high solar activity such as solar flare and interplanetary coronal mass ejections (ICMEs). Hence, separate models for ICME and flare induced absorptions are produced. The modelled results have been compared with IRIS data. On ICME absorption, key observation shows that absorption associated with ICMEs exhibits different character depending on ICME start times. ICMEs were categorised into day time events (solar zenith of riometer station $\chi \leq 80^\circ$) and as night time events ($\chi \geq 100^\circ$). Differing absorption signatures were observed for day and night ICME events. This work ranked various

solar wind parameters to obtain the best coupling parameter for day and night time absorption. For example, day time ICME model is based on solar wind dynamic pressure and VB_z , while night time ICME model is based on B_z and nV^3 . In the case of modelling of solar flare induced absorption, the magnitude and duration of absorption is seen to be dependent on different classes of solar flares. Properties of solar flare such as the rise time, the maximum intensity and decay time were used as the building block of the flare model. Comparing ICME induced absorption with absorption induced by solar flares, it was observed that ICME induced absorption is seen to have longer duration (\sim of hours) and stronger magnitude than those associated with solar flares (\sim of minutes).

Table of Contents

Dedication	i
Declaration	ii
Acknowledgements	iii
List of symbols and acronyms	vi
Abstract	ix
List of Figures	xiv
1 The Solar Terrestrial Environment	1
1.1 Introduction	1
1.2 The Sun	2
1.2.1 Solar activity	3
1.2.2 Solar flares	4
1.2.3 Coronal mass ejections (CMEs)	5
1.2.4 The solar wind	6
1.2.5 Interplanetary magnetic field	8
1.3 The Earth's magnetosphere	9
1.3.1 Structure of the Earth's magnetosphere	9
1.3.2 Particles in the magnetosphere	11
1.3.3 Van Allen belts	12
1.3.4 Motion of charged particles	12
1.3.5 Magnetospheric currents	19

1.4	Ionosphere	21
1.4.1	Production processes	22
1.4.2	Loss processes	25
1.4.3	High latitude ionosphere	25
1.4.4	Particle precipitation	27
1.5	Observations of the ionosphere	27
2	Radio wave absorption in the ionosphere	29
2.0	Introduction	29
2.1	Appleton-Hartree formula	30
2.1.1	Deviative absorption	32
2.1.2	Non-deviative absorption	32
2.1.3	Collision frequency in the ionosphere	33
2.2	The auroral oval	35
2.2.1	Statistics of the aurora oval	36
2.2.2	The polar cap	37
2.3	Geomagnetic and ionospheric storms	38
2.4	Types of radio absorption	39
2.4.1	Cosmic noise absorption	39
2.4.2	Auroral absorption (AA)	40
2.4.3	Sharp-onset absorption (SOA)	40
2.4.4	Slowly varying absorption (SVA)	40
2.4.5	Sudden commencement absorption (SCA)	41
2.5	Polar cap absorption (PCA)	42
2.6	E and F region absorption	42
2.7	Chapter summary	43
3	Instrumentation and geomagnetic indices	44
3.1	Introduction	44
3.2	Imaging riometer for ionospheric studies	45
3.2.1	Riometry	45

3.2.2	Limitations of the riometer	47
3.2.3	Imaging riometer for ionospheric studies (IRIS) Kilpisjärvi	48
3.3	Magnetometers	48
3.4	Satellites	49
3.4.1	Solar wind measurements (ACE and WIND)	50
3.4.2	WIND satellite	50
3.4.3	GOES (Geosynchronous operational environmental satellites)	51
3.5	Geomagnetic activity and indices	52
4	Prediction modelling of radio auroral absorption: an empirical relationship with the epsilon parameter	54
4.1	Introduction	54
4.2	Auroral absorption prediction models	57
4.2.1	The effect of solar wind on absorption	59
4.3	Energy coupling between the solar wind and the magnetosphere	61
4.4	Methodology	64
4.4.1	Modelling of absorption	65
4.5	Observations	74
4.6	Results and Analysis	75
4.7	Conclusion	78
5	Cosmic noise absorption induced by interplanetary coronal mass ejections	80
5.1	Introduction	80
5.2	Interplanetary coronal mass ejections (ICMEs)	81
5.3	Signatures of ICMEs	83
5.4	Classification of ICMEs based on magnetic and non-magnetic cloud events	85
5.5	ICME data	85
5.5.1	Solar cycle dependence of ICMEs	87
5.5.2	Geoeffectiveness of ICMEs	89

5.5.3	Energetic particle associated with ICMEs	90
5.5.4	The DRAP model	91
5.6	Methodology	94
5.6.1	Event selection criteria	94
5.6.2	Epoch analysis	95
5.7	Observations	97
5.8	Model and parameterisation	99
5.9	Discussion	122
5.10	Conclusion	124
6	Cosmic noise absorption induced by solar flares	126
6.0	Introduction	126
6.1	Emission and classification of solar flare	128
6.2	Flare models	130
6.3	Data and methodology	132
6.3.1	Flare data	132
6.3.2	Flare catalogue	132
6.3.3	Cosmic noise absorption (CNA) data	133
6.4	Procedure and methodology	139
6.5	Results	140
6.5.1	Annual flare count	140
6.5.2	Flare duration	142
6.6	Relationships between flare parameters and absorption parameters . .	143
6.7	Methodology for flare model	144
6.8	Analysis and discussion	149
7		160
7.1	Conclusions	160
7.2	Further work	163
	References	165

List of Figures

1.1	Structure of the solar regions showing distinct temperature and densities for each region [Kivelson and Russell, 1995]	2
1.2	Sunspot number from 1880-2012 (Source: Solar Influences Data Analysis Centre website).	4
1.3	The “Bastille Day” event. A large solar flare event on 14th July, 2000 [Jansen and Hippler, 2003]	5
1.4	A large coronal mass ejection (CME) erupting from the Sun on 2nd April 2001. The CME is seen as a bright cloud expanding towards the right hand side of the image taken using the LASCO coronagraph onboard SOHO. In this case an EUV image of the Sun has been superimposed onto the LASCO image to show the size and location of active regions on that day (http://sohowww.estec.esa.nl).	6
1.5	Parker’s original solution for solar wind flow speed as a function of heliocentric distances (r (10^6 km)) for different coronal temperature [From Gosling, 2012]	7
1.6	Parker spiral configuration of the solar wind and IMF [Kivelson and Russell, 1995]	8
1.7	A schematic of the Earth’s magnetosphere [Russell, 1993].	9
1.8	Distribution of trapped protons and electrons for a range of energies [From: Hess, 1968].	13
1.9	Typical charged particle motion in the magnetosphere [From: Yuting <i>et al.</i> , 2013]	14

1.10	Schematic of typical motions of particles trapped on closed field lines including the equatorial loss cone and the mirror points of bouncing particles [From Kavanagh, 2000]	15
1.11	Longitude drift caused by a gradient in the geomagnetic field intensity. Here, magnetic field is perpendicular to the effective direction of drift motion [From: Hess, 1968]	17
1.12	Curvature drift caused by combination of centrifugal force with the gyromotion [From: Shirley and Fainbridge, 1997]	18
1.13	Plasma population and current system in the magnetosphere [Shirley and Fainbridge, 1997]	19
1.14	Schematic representation of the major magnetospheric current systems. (a): magnetopause currents, (b): ring current, (c): tail currents [From: Olsen, 1982]	20
1.15	A schematic showing plasma density of the Earth's ionosphere at different altitude.	21
1.16	Production rates of monoenergetic electrons of various initial energies. Energies given in MeV (From Rees, 1963).	24
1.17	A schematic of ionisation altitude [From A.D. Richmond, in solar terrestrial physics, Reidel, 1983].	26
2.1	Schematic of height variation of the electron collision frequency, electron density and the product (Nv) that is a measure of radio absorption [From: Davies, 1989].	34
2.2	Occurrence of auroral absorption in latitude and time measured at several longitudes. [From a] Holt <i>et al.</i> , 1961; b] Hartz <i>et al.</i> , 1963; c] Driatsky, 1966; d] Hargreaves and Cowley, 1967. [a] Shows the percentage of time that absorption exceeds 0.5 dB; [b] and [c] show the percentage of time that absorption equals or exceeds 1.0 dB and [d] gives the median intensity in dB. [Schematic from Hargreaves, 2009]	36

2.3	An example of absorption measurement from IRIS Kilpisjärvi due to sudden commencement on 3rd April, 2004. [From Ritchie and Honary, 2009].	41
3.1	A typical quiet day. Blue line: Received power, red line: length of 14 day period during which the quiet day occurs	46
3.2	IRIS phased array during summer (top panel). Bottom panel: IRIS winter scene when snow increases the height of the ground plane [Browne, 1994]	49
3.3	Beam projection of IRIS at 90 km altitude. The contours define the -3 dB points and the black square shows the calculated field of view used in the IRIS images.	50
4.1	10-min averaged absorption binned by IMF B_z . A northward IMF does not affect the absorption, whereas increasingly negative B_z increases the level of absorption during the night and morning sectors. [From: Kavanagh <i>et al.</i> , 2004].	59
4.2	Magnetic local time variation of absorption in the zenithal beam for the five ranges of solar wind speed [From: Kavanagh, 2000].	60
4.3	Variation of zenithal beam absorption in universal time based on epsilon ranges.	61
4.4	CNA (dB) hourly bins Spring season 1995-2006.	64
4.5	Plot of median CNA (dB) v Epsilon (W) Winter (1995–2006).	67
4.6	Plot of median CNA (dB) v Epsilon (W) Spring (1995–2006)	69
4.7	Plot of median CNA (dB) v Epsilon (W) Summer (1995–2006).	71
4.8	Plot of median CNA (dB) v Epsilon (W) Autumn (1995–2006).	73

4.9	Plot of measured absorption v modelled absorption for 7 days in a Spring season (4 th to 8 th April, 2006). Measured absorption shows differing signatures over days. 1 st -4 th April characterise with low absorption signature (between -0.2 and 0.15 dB, 5 th is an active day with absorption reaching 1.7 dB, 7 th April has maximum absorption of 0.5 dB. Modelled absorption could predict up to 0.3 dB. Modelled prediction shows good correlation with measured absorption but shows significant deviation from measured absorption during active periods with absorption spikes.	75
4.10	Plot of measured absorption v modelled absorption 4 days in a Winter season in 1998 (25 th to 29 th February, 1998). Absorption spikes are noticed between 6-11 UT. Measured absorption varies considerably from -0.2 dB to 1.8 dB, modelled absorption could predict up to 0.35 dB. Modelled prediction shows good correlation with measured absorption for low absorption periods but shows significant deviation from measured absorption during periods with absorption spikes. . . .	76
4.11	Plot of measured absorption v modelled absorption 1 day in a Summer season in 2001 (19 th June, 2001). Measured absorption varies with modelled absorption.	76
4.12	Plot of measured absorption v modelled absorption 2 days in a Summer season in 1996 (17 th to 19 th July, 1996). Post-midnight absorption spikes are noticed on the first day and pre-midnight spikes for the second day. Measured absorption varies considerably from -0.2 dB to 1.2 dB, modelled absorption could predict up to 0.2 dB.	77
4.13	Plot of measured absorption v modelled absorption 2 days in a Summer season in 1996 (17 th to 19 th July, 1996). Post-midnight absorption spikes are noticed on the first day and pre-midnight spikes for the second day. Measured absorption varies considerably from -0.2 dB to 1.2 dB, modelled absorption could predict up to 0.2 dB.	77

4.14	Panel <i>A</i> showing comparison of modelled and measured absorption. Panel <i>B</i> shows measurement of magnetometer components of <i>H</i> , <i>D</i> and <i>Z</i> . During periods of absorption spiked, there is corresponding depression in <i>H</i> component of magnetometer signifying the occurrence of substorm.	78
5.1	A schematic of solar related effects on the ionosphere	81
5.2	Occurrence statistics of storms driven by solar wind structures v magnetosheath plasma- β [From Borovsky and Denton, 2006]	84
5.3	Yearly distribution of ICME events for solar cycle 23 (1996-2009).	88
5.4	Distribution of ICME with SSN and mean 10.7 cm radio flux. (1996-2009)	88
5.5	Proton cutoff energy versus invariant latitude as a function of geomagnetic activity K_p [From Saucer and Wilkinson, 2008]	94
5.6	An epoch analysis of the CNA response at IRIS to HSSs presented as a time series in MLT. The black line is the median value from the central beam; the dotted red lines show the interquartile range [Kavanagh <i>et al.</i> , 2012].	95
5.7	An epoch analysis of the superposed epoch time series of 33 ICME-driven storms [Red line] and 38 CIR storms [Blue]. Mean CNA from the Abisko riometer. The zero epoch is the time of the first clear minimum in D_{st} for each event [Longden <i>et al.</i> , 2008]. There are 2 peaks observed observed, the first at ~ 3 hours before zero epoch and the second ~ 5 hours after zero epoch.	96
5.8	Epoch analysis [-1 day to 2 days] of IRIS CNA absorption (dB). Top panel is absorption during day time commencing ICME events, bottom panel is absorption during night time commencing ICME events during [1996-2009]. The black line is the median (Q2) value while Q3 and Q1 are the upper and lower quartiles respectively.	97

5.9	Epoch analysis [−1 to 2 days] of the z -component of IMF (B_z -nT). Top panel is for day time commencing ICME events, bottom panel is for night time commencing ICME events during [1996-2009]. The black line is the median (Q2) value while Q3 and Q1 are the upper and lower quartiles respectively.	98
5.10	Epoch analysis [−1 to 2 days] of the dynamic pressure (nPa). Top panel is pressure variation during day time commencing ICME events. Bottom panel is for night time commencing ICME events during [1996-2009]. The black line is the median (Q2) value while Q3 and Q1 are the upper and lower quartiles respectively.	99
5.11	Epoch analysis [−1 to 2 days] of $[\sin(\theta/2)]$ where θ is the clock angle. Top Panel is for day time commencing ICME event. Bottom Panel is for night time commencing ICME events during [1996-2009]. The black line is the median (Q2) value while Q3 and Q1 are the upper and lower quartiles respectively.	100
5.12	Epoch analysis of solar wind dynamic pressure on the top panel, with the epoch analysis of day time absorption on the bottom panel. The maximum point of the top and bottom panel haws a delay of 60 minutes (~ 2 hours before start time) showing that dynamic pressure bears corresponding effect on day time absorption. The events analysed are ICME events during [1996-2009].	101
5.13	Plot of pressure (nPa) against absorption (dB) for day and night time commencing absorption. Top Panel is for day time commencing ICME events.	102
5.14	Epoch analysis of night time absorption on the top panel, with the epoch analysis of z -component of the magnetic field (B_z) (nT) i.e the unit of B_z on the bottom panel. The maximum point of the top and bottom panel differ with a delay of 25 minutes (~ 5 hours after start time) showing that B_z bears corresponding effect on night time absorption. The events analysed are ICME events during [1996-2009].	102

5.15	Plot of z -component of the IMF($(B_z)(nT)$) against absorption (dB) for day and night time commencing absorption. Top panel is for day time commencing ICME events with a correlation coefficient $R = -0.027$, bottom panel is for night time commencing ICME events with a correlation coefficient $R = -0.44$. Dataset are for solar cycle 23 [1996-2009].	103
5.16	Epoch analysis [-1 to 2 days] of solar wind speed during ICME events. Top panel is for day time commencing ICME event, bottom panel is for night time commencing ICME events during [1996-2009]. The black line is the median (Q2) value while Q3 and Q1 are the upper and lower quartiles respectively. A steady rise in solar wind speed form (~ 6 hours before start time) up to start time (0), in both day and night time ICME events is observed.	103
5.17	Epoch analysis [-1 to 2 days] of day time absorption signature and K_p index. Top Panel is for day time absorption signature, bottom panel shows K_p variation for day time ICME events [1996-2009]. The black line is the median (Q2) value while Q3 and Q1 are the upper and lower quartiles respectively. A gradual increase in K_p is seen from (~ 4 hours) before start time up to ~ 4 hours after start time (maximum point).	104
5.18	Epoch analysis [-1 to 2 days] of night time absorption signature and K_p index. Top panel is for night time absorption signature, bottom panel shows K_p variation for night time ICME events [1996-2009]. The black line is the median (Q2) value while Q3 and Q1 are the upper and lower quartiles respectively. A gradual increase in K_p is seen from (~ 6 hours) before start time up to ~ 1.5 hours after start time (maximum point).	104

5.19	Plot of K_p index against median (dB) for day and night time commencing absorption. Top panel is for day time commencing ICME events with a correlation $R = 0.0022$. Bottom panel is for night time commencing ICME events $R = 0.189$. Dataset are for solar cycle 23 [1996-2009].	105
5.20	Epoch analysis [-1 to 2 days] of day time absorption signature and auroral electrojet (AE) index. Top Panel is for day time absorption signature, bottom panel shows AE variation for day time ICME events [1996-2009]. The black line is the median (Q2) value while Q3 and Q1 are the upper and lower quartiles respectively. A gradual increase in K_p is seen from (~ 6 hours) before start time up to ~ 2 hours after start time (maximum point).	106
5.21	Epoch analysis [-1 to 2 days] of night time absorption signature and auroral electrojet (AE) index. Top panel is for day time absorption signature, bottom panel shows AE variation for night time ICME events [1996-2009]. The black line is the median (Q2) value while Q3 and Q1 are the upper and lower quartiles respectively. A gradual increase in K_p is seen from (~ 8 hours) before start time up to ~ 5 hours after start time (maximum point).	106
5.22	Plot of AE index against absorption (dB) for day and night time commencing absorption. Top panel is for day time commencing ICME events with a correlation $R = 0.016$. Bottom panel is for night time commencing ICME events $R = 0.3696$. The day plot(top panel) has negative correlation while the night plot(bottom panel) shows positive correlation. Dataset are for solar cycle 23 [1996-2009].	107
5.23	IRIS v modelled absorption for ICME event of 27 th September, 2011. This event is classified as day time event. The modelling utilised the dynamic pressure as the coupling parameter for absorption.	109

5.24	IRIS v modelled absorption for ICME event of 28 th May, 2011. This event is classified as day time event. The modelling utilised the dynamic pressure as the coupling parameter for absorption.	110
5.25	IRIS v modelled absorption for ICME event of 4 th August, 2010. This event is classified as day time event. The modelling utilised the dynamic pressure as the coupling parameter for absorption.	110
5.26	IRIS v modelled absorption for ICME event of 13 th September, 2014. This event is classified as night time event. The modelling utilised the z -component of the magnetic field (B_z) as the coupling parameter for absorption.	111
5.27	IRIS v modelled absorption for ICME event of 26 th September, 2011. This event is classified as night time event. The modelling utilised the z -component of the magnetic field (B_z) as the coupling parameter for absorption.	111
5.28	Measured absorption v modelled result for day time absorption during ICME events of 1996-2009.	115
5.29	Example plots of measured v modelled results for ICME absorption. The plots are event dates within the time frame utilised for the model (1996-2009).	116
5.30	Example plots of measured v modelled results for ICME absorption. The plots are event dates within the time frame utilised for the model (1996-2009)	117
5.31	Example plots of measured v modelled results for day time ICME absorption. The plots is event dates outside the time frame utilised for the model	118
5.32	Measured absorption v modelled result for night time absorption during ICME events of 1996-2009	120

5.33	Example plots of measured v modelled results for ICME absorption. The plots are event dates within the time frame utilised for modelling (1996-2009). The missing gaps in the model result are times with no upstream data.	121
5.34	A plot of IRIS absorption v modelled absorption for an ICME event of 27th September, 2011, a date outside the dates used in the model.	122
6.1	Cosmic noise absorption event following X-class solar flare of 14 th July, 2000. The X-class flare began \sim 10:24 UT; gradual increase in riometer absorption began just after 10:24 UT from less than 1 dB up to over 10 dB at 17:00 hours.	127
6.2	Showing solar flare events of 12 th July, 2000 and a powerful X5 class flare on 14 th July, 2000 as measured by the geostationary operational environmental (GOES) satellite	128
6.3	A schematic evolution of flare intensities at different wavelengths. The phases indicated at the top vary greatly in duration. In large events, the pre-flare phase lasts 10 min, the impulsive phase 1 min, the flash phase 5 min and the decay phase 1 hour [From encyclopaedia of astronomy and astrophysics, 2001].	129
6.5	Plot of flare mean duration v log of flare intensity. The flares are binned by class and the mean duration is calculated for each. The error bar represents the standard error of the mean. The mean duration shows positive trend with the log of flare intensity. More variation is evident in the higher intensity flares due to the smaller sample size.	139
6.6	Annual flare count for C, M and X-class flare covering solar cycle 23 (1996-2009). Counts for all classes show a clear variation with solar cycle.	140
6.7	Variation of flare based on monthly occurrence during solar cycle 23 (1996-2009).	141

6.8	Variation of flare based on seasonal occurrence during solar cycle 23 (1996-2009). Winter (December-February), Spring (March-May), Summer (June-August), Autumn (September-November).	142
6.9	Showing mean duration for X, M and C-class flares between (1996-2009) as measured by the GOES satellites in 1.8E X-ray flux spectral band. The error bar represents the standard error of the mean. Increase in mean duration for higher peak intensity is apparent.	143
6.10	Plot of flare mean duration v log of flare intensity. The flares are binned by class and the mean duration is calculated for each. The error bar represents the standard error of the mean. The mean duration shows positive trend with the log of flare intensity. More variation is evident in the higher intensity flares due to the smaller sample size.	144
6.11	Superposed epoch analysis of median absorption signature for X, M and C-class flare between 1996-2009. The start times are as recorded by GOES. Absorption data is from beam 25 of IRIS Kilpisjärvi.	145
6.12	Median signature of absorption during solar flare events for M class flares (top panel) and X-class flares (bottom panel). Y-axis is absorption axis (dB); X-axis is time (minutes). Median absorption signature is seen from 20 minutes before start time to 90 minutes after start time. From the start time (0) there is a depression of 0.02 dB in median absorption signature in both M and X-class plots. Maximum is noticed about 18-19 minutes after start times in both plots.	146
6.13	Plots of absorption (dB) and solar flare intensity for 4 different X-class flares. The rise time and decay time are somewhat symmetrical and delays are seen in the peak of intensity and peak of absorption.	148
6.14	Showing delay between peak intensity of flare and peak absorption for X-class solar flare events of 1996-2009. Delay range from 4 minutes before to 5 minutes after flare intensity. Majority of the events do not show any delay (0) delay between peak intensity of flares and peak absorption.	149

6.15	Plot of rise time of flare v rise time of absorption. Top panel show M-class relation, bottom panel shows X-class relation.	150
6.16	Plot of decay time of flare v decay time of absorption. Top panel show M-class relation, bottom panel shows X-class relation.	151
6.17	Plot of maximum absorption (dB) v square root of maximum flare intensity (Wm^{-2}). Top panel show M-class relation, bottom panel shows X-class relation.	152
6.18	Plots of measured absorption (IRIS) in blue compared with model result in red for 4 M-class events. The events are within the dates utilised in obtaining the model (1996-2009). Measured absorption is shown as Kil (Kilpisjärvi riometer) riometer measurement, the model result is shown as prediction model in the legend of the plots.	154
6.19	Plots of measured absorption (IRIS) in blue compared with model result in red for two X-class events. The events are within the dates utilised in obtaining the model (1996-2009). Measured absorption is shown as Kil (Kilpisjärvi riometer) riometer measurement, the model result is shown as prediction model in the legend of the plots.	155
6.20	Plots of measured absorption (IRIS) in blue compared with model result in red for two X-class events. The events are X-class events that occurred outside the time frame utilised in the model. Measured absorption is shown as Kil (Kilpisjärvi riometer) riometer measurement, the model result is shown as prediction model in the legend of the plots.	156

Chapter 1

The Solar Terrestrial Environment

1.1 Introduction

A key reason for studying the Sun in great detail is to improve our understanding of the various ways in which it affects our terrestrial environment. For more than a century, scholars studying the Sun and Sun-Earth connection have identified different regions within the Sun, the solar wind and its mechanism through interplanetary space to the Earth's magnetosphere and regions of the Earth's atmosphere [e.g. William Gilbert in 1602, Samuel Heinrich Schwabe in 1843, Arthur Carrington in 1859 etc.]. Workers also established the effect of solar activities and magnetic disturbances in the development of electromagnetic laws [e.g. Durham, 2006]. In recent times, there has been growing interest in solar-terrestrial studies as a result of the availability of satellite observations of space, particularly in the near-Earth environment.

The solar-terrestrial environment comprises fully ionised plasmas, partially ionised plasma (the ionosphere) and Earth's neutral atmosphere. The Sun-Earth interaction depends on chains of coupling processes involving the solar interior, the solar atmosphere, and solar wind-magnetosphere, magnetosphere-ionosphere, and ionosphere-atmosphere interactions. These interactions occur through radiative, dynamic and electromagnetic processes. Within the chain of relations, the Sun is the primary driver of change as it continuously emits charged particles and radiation in the solar-terrestrial environment. In this chapter, a synopsis of the solar-terrestrial environment from the Sun through to the Earth's ionosphere will be given.

1.2 The Sun

The Sun is the closest star to the Earth, at a distance varying from 147,100,000 to 149,157,000 km [Zolesi and Cander, 2014] and it is the most important source of ionisation for the terrestrial upper atmosphere. The Sun emits magnetic energy across the entire electromagnetic spectrum. X-rays and ultraviolet (UV) radiation are of particular interest in the interaction of the Sun with the terrestrial atmosphere. The Sun comprises of distinct layers, each with its distinct feature. These layers are: The core, the radiative zone, the interface layer and the convective zone (Figure 1.1).

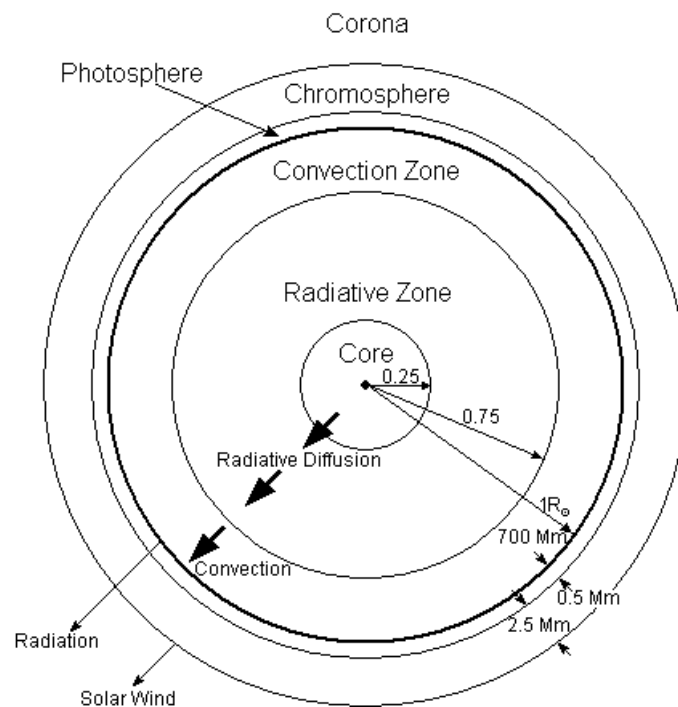


Figure 1.1: Structure of the solar regions showing distinct temperature and densities for each region [Kivelson and Russell, 1995]

The core of the Sun extends from its centre to 0.25 solar radii (R_{\odot}) with a temperature of about 15 million degrees Celsius. At this layer, energy is generated by nuclear fusion by transmuting hydrogen to helium. Next to this region is the radiative zone that extends from the outer edge of the core to the base of the convection zone. Here, energy is transported by radiation to the convective zone. Between the

radiative interior and the convection zone is an interface layer called the tachocline. Here, the fluid motion found in the convective zone slowly disappear from the top of this layer to its bottom. It is believed that there are sudden changes in the chemical composition of this layer. At the convection zone, there is a severe temperature gradient cool enough for heavier ions to hold on to some of their electrons. Hence, it is harder for radiation to penetrate. In the process, heat is trapped and fluid becomes unstable [Christensen-Dalsgaard *et al.*, 1996].

At the solar atmosphere, there are three distinct layers: the photosphere, the chromosphere, and the corona. The photosphere is the surface of the Sun above the convection zone where most of the visible light from the Sun originates. The photosphere has a temperature of about 5700 °K. The chromosphere is located further on outside the photosphere. The corona is characterised by a temperature increase as it moves away from the Sun. The corona extends beyond the chromosphere into the interplanetary space and beyond the planets. Table 1.1 gives a summary of the main characteristics of the Sun.

Table 1.1: Main characteristics of the Sun [After Zelosi and Cander, 2014]

Solar radius	695,990 km
Solar mass	1.989×10^{30} kg
Solar luminosity (energy output of the Sun)	3.846×10^{33} ergs s^{-1}
Surface temperature	5770 K
Surface density	2.07×10^{-16} kg m^{-3}
Surface composition	70% H, 28% He, 2% (C,N,O etc).
Central temperature	15,600,000 K
Central density	1.622×10^5 kg m^{-2}
Solar age	4.57×10^9 years

1.2.1 Solar activity

As a result of the high temperature of the Sun, there is constant movement of solar materials leading to distinct variability in the magnetic fields of the Sun. The

pattern follows a 22-year cycle, which coincides with a reversal of the polarity of the Sun's magnetic poles [Schunk and Nagy, 2000]. A primary signature of solar activity is sunspots. Sunspots appear on the photosphere, visible as dark spots and characterised with lower temperature than the surrounding photosphere. The earliest reference to a sunspot could be traced to the middle of the fourth century [Bray and Loughhead, 1957]. Scientists track solar cycles by counting sunspots. During solar maximum hundreds of sunspots are observed whereas during solar minimum there are only a few (~ 10) sunspots. The most widely used formula for computing sunspot was proposed by Rudolph Wolf in 1848:

$$R = k(10g + s)$$

R is the sunspot number; g is the number of sunspot groups on the solar disk; s is the total number of individual spots in all the groups and k is a variable scaling factor (usually < 1) Figure 1.2 shows average sunspot numbers from 1880–2012 with the solar cycle clearly visible.

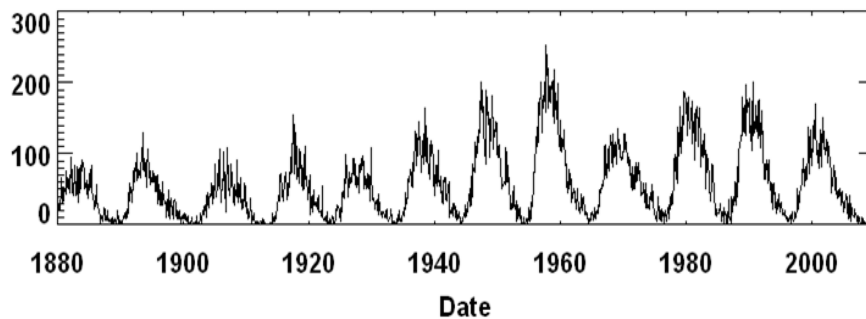


Figure 1.2: Sunspot number from 1880-2012 (Source: Solar Influences Data Analysis Centre website).

1.2.2 Solar flares

Solar flares are sudden explosive releases of stored magnetic energy in the atmosphere of the Sun causing sudden brightening of the photosphere which can last from few minutes to several hours [Keith, 1991]. During solar flare events, particles and electromagnetic emissions can affect the Earth's upper atmosphere. Three phases of the flare have been identified, the pre-flare phase, the rise phase, and the main

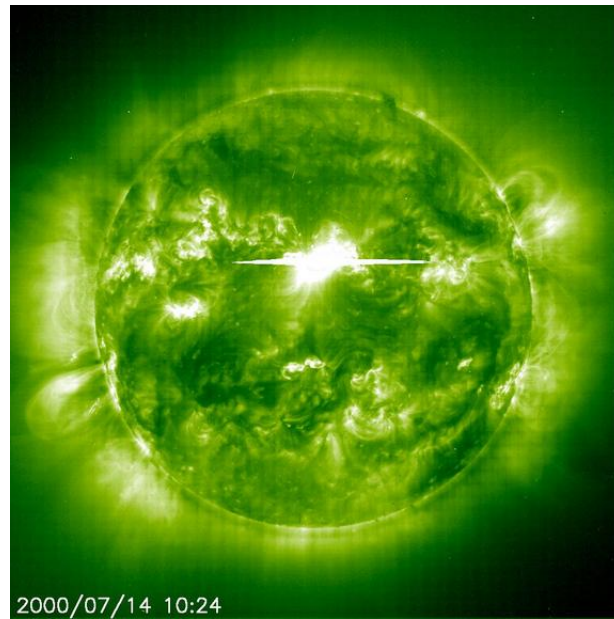


Figure 1.3: The “Bastille Day” event. A large solar flare event on 14th July, 2000
[Jansen and Hippler, 2003]

phase. The pre-flare phase is characterised by slowly rising prominence on the solar surface due to some weak eruptive instability. Normally, this phase lasts for half an hour and is accompanied by X -ray brightening. During the rise phase, the stretched magnetic field lines start to break and reconnect. In the process, prominences erupt more quickly with a steep rise in H_α and soft X -ray emissions. The main phase can last up to several hours with declining intensity. Here, the reconnection point rises, hot X -ray loops and H_α ribbons are created [Hudson, 2000]. Solar flares sometimes occur together with other signatures of solar activity such as CMEs and interplanetary shock waves (although, the exact relationship between these events is not yet completely understood). Figure 1.3 shows an unusually large flare, which took place on 14/7/2000 [Jansen and Hippler, 2003]. This event is known as the “Bastille Day” event. The effect of solar flare on radio absorption is discussed in Chapter 6 of this thesis.

1.2.3 Coronal mass ejections (CMEs)

Coronal mass ejections are very important solar events from the Earth’s perspective. A CME is characterised by the eruption of a huge bubble of plasma from the

Sun's outer atmosphere. It can occur with or without solar flares, and can impinge on the Earth's atmosphere. Once it escapes the Sun's gravity, the velocity of a CME can be from 400 km s^{-1} to 2000 km s^{-1} [e.g. Yohsuke and Abraham, 2007]. A typical CME can carry more than 10 billion tonnes of plasma into the solar system [e.g. Zang and Low, 2005].

As it interacts with the solar wind, a CME can create a shock wave that accelerates particles to very high energies. Behind the shock wave, the CME cloud travels through the solar system bombarding planets, asteroids, and other objects with radiation and plasma. If a CME erupts on the side of the Sun facing Earth, and if the Earth's orbit encounters the path of the cloud, the results can be spectacular and sometimes hazardous. Figure 1.4 shows a large coronal mass ejection (CME) erupting from the Sun on 2nd April 2001.

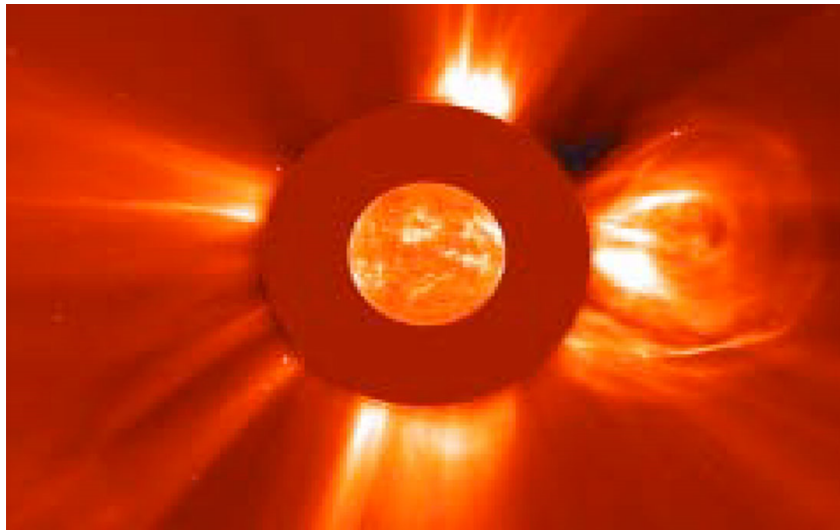


Figure 1.4: A large coronal mass ejection (CME) erupting from the Sun on 2nd April 2001. The CME is seen as a bright cloud expanding towards the right hand side of the image taken using the LASCO coronagraph onboard SOHO. In this case an EUV image of the Sun has been superimposed onto the LASCO image to show the size and location of active regions on that day (<http://sohowww.estec.esa.nl>).

1.2.4 The solar wind

The solar wind was theoretically modelled by Parker [1958] and experimentally verified in 1962 (Figure 1.5). It has since then been observed throughout the he-

liosphere. The solar wind results from the expansion of the solar atmosphere, with continuous outflowing of ionised plasma and magnetic field filling the interplanetary

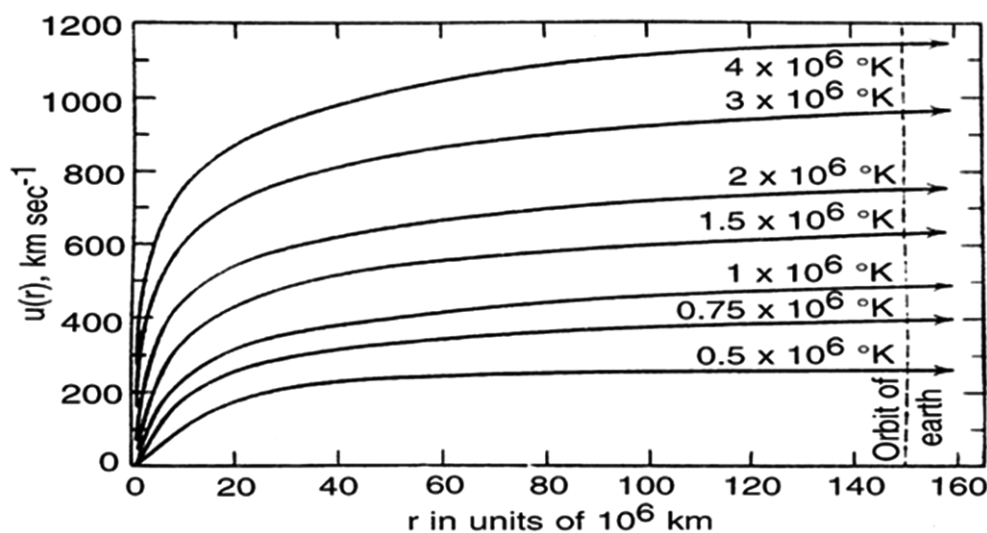


Figure 1.5: Parker's original solution for solar wind flow speed as a function of heliocentric distances (r (10^6 km)) for different coronal temperature [From Gosling, 2012]

medium. This results from the pressure difference between the solar corona and interplanetary space. This plasma is dominated by protons and electrons, but it also comprises other ions that have enough energy to escape solar gravity. Factors such as adiabatic cooling, heating due to stream interactions and shocks, dissipation of waves and transfer of energy determines the temperature of the solar wind that decreases away from the Sun [e.g. Richardson and Smith, 2003]. Near the Earth's orbit (at 1AU), the solar wind velocity typically ranges between 300 km s^{-1} and 2000 km s^{-1} [e.g. Wolfgang and Rudolf, 1996].

Streams with velocities less than 400 km s^{-1} are classified as low-speed while streams with velocities over 600 km s^{-1} are classified as high speed solar winds. The fast solar wind originates from coronal holes where magnetic field is open, while slow solar wind originates from regions close to the heliospheric current sheet at the heliomagnetic equator during solar minimum. At solar maximum, slow solar wind originates above the coronal helmet streamers in active regions where magnetic field lines are closed [Kamide and Chian, 2007]. The solar wind forms a vital connection

between the Sun and the Earth and plays an essential role in shaping and formation of the Earth's magnetosphere. It is the prime source of space weather.

1.2.5 Interplanetary magnetic field

The interplanetary magnetic field [IMF] is a part of the Sun's magnetic field that is carried into interplanetary space by the solar wind. IMF lines are said to be “frozen in” to the solar wind plasma (Figure 1.6). When the electrical conductivity of the plasma is large, relative motion between the plasma and magnetic field is impossible [Alfvén and Falthammar, 1963]. In the solar wind, the energy of the plasma is larger than that of the magnetic field; for this reason, it is the plasma that determines the overall motion. The IMF is embedded in the solar wind plasma; the field line is dragged by a parcel of plasma radially from the Sun.

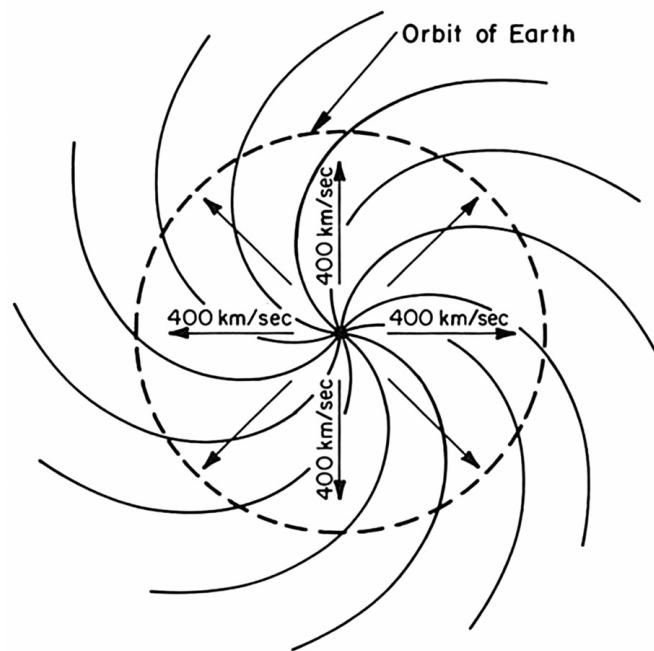


Figure 1.6: Parker spiral configuration of the solar wind and IMF [Kivelson and Russell, 1995]

The IMF consists of three directional components, two of which (B_x and B_y) are oriented parallel to the ecliptic in GSM co-ordinate system. The third component (B_z) is perpendicular to the ecliptic and is affected by waves and other disturbances in the solar wind. When the IMF and geomagnetic field lines are oriented opposite or “anti-parallel” to each other, they can “merge” or “reconnect”, resulting in the

transfer of energy, mass and momentum from the solar wind flow to magnetosphere. The strongest coupling is known to (with the most dramatic magnetospheric effects) occur when the B_z component is oriented southward.

The IMF is a weak field, varying in strength near the Earth from 1 to 37 nT, with an average value of ~ 6 nT [Kamide and Chian, 2007].

1.3 The Earth's magnetosphere

The Earth's magnetic field is a magnetic dipole believed to be generated by a dynamo process resulting from the Earth's rotation and the motion of a fluid core [Cowan, 1980]. At the magnetosphere, interactions are between the Earth's magnetic field, IMF, and the solar wind. The solar wind impinges on the Earth's dipolar magnetic field, is slowed and deflected around it forming the magnetosphere [Kamide and Chian, 2007, and references within]. The Earth's magnetosphere provides protection to the Earth and forms a barrier to the solar wind resulting in the formation of a magnetic cavity.

1.3.1 Structure of the Earth's magnetosphere

Figure 1.7 is a schematic of the configuration of the Earth's magnetosphere showing the major components.

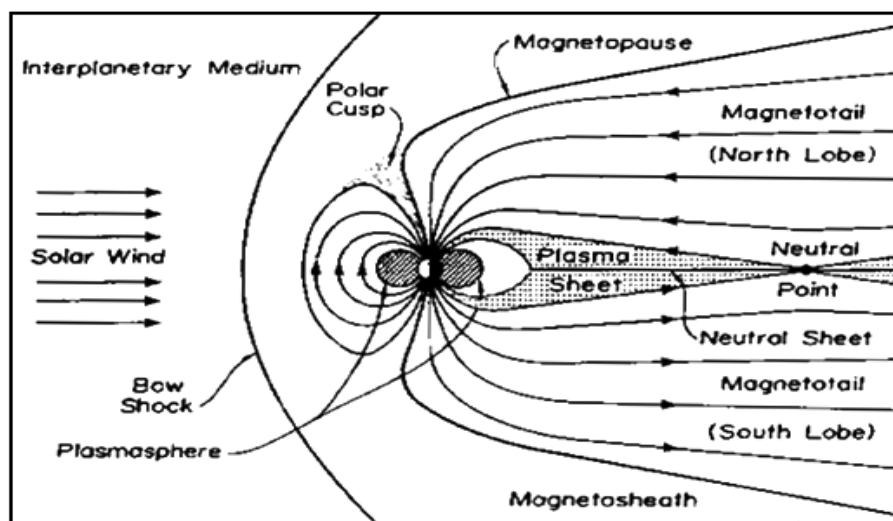


Figure 1.7: A schematic of the Earth's magnetosphere [Russell, 1993].

Bow shock: A bow shock is formed at the front of the magnetosphere as the solar wind travelling at supersonic speed and collisionless encounters the magnetic field of the Earth. At the bow shock, solar wind plasma is decelerated and a substantial fraction of its kinetic energy is converted to thermal energy.

Magnetosheath: This region consists of shocked solar wind plasma that has gone through the bow shock.

Magnetopause: This is the boundary separating the shocked solar wind plasma from the plasma of the magnetosphere. The separation between the solar wind and the magnetosphere occurs at $\sim 10.5R_E$, due to the compression of the incident solar wind and to the flanks abreast of the Earth about $15R_E$, while the radius of the distant tail is $25\text{-}30R_E$.

Polar cusps: The polar cusps are key regions for the transfer of mass, momentum and energy from the solar wind to the magnetosphere. They are funnel-shaped areas between the sunward magnetic field and the tailward magnetic field where the solar wind enters and follows the magnetic field lines toward Earth. The cusps provide an excellent site for monitoring the coupling between the solar wind and the magnetosphere.

Magnetotail: In the dayside magnetosphere, the Earth's magnetic field is compressed by the incident solar wind while on the night side, the field is stretched forming the magnetotail.

Plasma sheet: The magnetosphere is filled with magnetospheric plasma composed mostly of electrons and protons. The sources of these particles are both the solar wind and the ionosphere. Most of the magnetotail plasma is concentrated in the plasma sheet around the tail-midplane. Near the Earth, the plasma sheet reaches the high-latitude ionosphere. Due to differences associated with plasma in this region, the plasma sheet is further subdivided into the outer and inner plasma sheets. The plasma in this region is hotter and denser than in the surrounding region [Kivelson and Russell, 1995].

Tail lobes: The outer region of the magnetotail is the magnetotail lobe. Here, the magnetic field lines are not closed. There are two lobes of oppositely directed

fields extending from the polar caps into space. The upper lobe is known as the north lobe and the lower lobe the south lobe. This region contains high temperature plasma.

Neutral Sheet: Magnetic field lines in the northern lobe are directed toward the Earth while those in the southern lobe are directed away from the Earth. Such a configuration can persist only if plasma concentration exists between the lobes in the region of field direction reversal. This plasma concentration, which stretches down the magnetotail from about $30 R_E$, is called the neutral sheet. Protons and electrons from the solar wind diffuse across the magnetopause in the magnetotail, drift toward the plasma sheet, and accelerate earthward. Electric current flows from dawn to dusk in the neutral sheet in order to keep the magnetic lobes separated. This is called the cross-tail current. The energy of electrons in the neutral sheet ranges from 200 eV to more than 12 keV. Proton energy ranges from 1 to 20 keV.

Plasmasphere: The plasmasphere is located within the magnetosphere just outside the upper ionosphere. It is a region of high density ($\sim 10^3 \text{ cm}^{-3}$, cold ($\sim 1\text{eV}$) plasma that surrounds the Earth. Although plasma is found throughout the magnetosphere, the plasmasphere usually contains the coldest plasma. This is because it is free from the influence of the solar wind and the IMF. At the plasmopause, the cold dense plasma suddenly terminates. The population of the plasmasphere results from the steady flow of plasma upwards from the planet proceeding from the high latitude ionosphere.

1.3.2 Particles in the magnetosphere

The polar caps and the cusps are significant in that they are the main particle entry regions from the solar wind into the magnetosphere. The magnetosphere is populated with charged particles whose sources are both external and local to the magnetosphere. Charged particles in the magnetosphere are usually classified as cold plasma ($\leq 10 \text{ eV}$), as belonging to the radiation belt ($> 200 \text{ keV}$), and intermediate energetic particles in the range (1-200 keV) belonging to the ring current and nightside plasmashet. [Kamide and Chains, 2007 and references therein]. Cold

plasma consists of ions and electrons that drift at $(\mathbf{E} \times \mathbf{B})$ velocity across the ambient magnetic field, radiation belt particles drift across \mathbf{B} at energy dependent rates. Energetic particles have various origins such as cosmic rays emission, particles from the Sun corona emitted during a solar flare and particles trapped in the Van Allen radiation belts. The configuration of the inner magnetosphere of the Earth is such that charged particles are trapped in a form of magnetic bottle. The nature and the energy of these particles depend on their origin. Particles are accelerated in the cusps resulting at energies of 10s of KeV. The tail lobe of the magnetosphere connects to the polar caps and contains low-density plasma ($< 0.1 \text{ cm}^{-3}$) of low energy. The open field lines in the tail are dominated by plasma of solar wind origin.

1.3.3 Van Allen belts

Van Allen [1958] identified two distinct zones (inner and outer belts) where high-energy particles are trapped in the inner magnetosphere. The inner belt is located between $1.1R_E$ – $3R_E$ in the equatorial plane. This zone comprises mainly of protons with energies exceeding 10 MeV. Population within the inner belt is fairly constant and their variations result from the 11 year solar cycle and large geomagnetic storms [Hargreaves, 1992]. The outer belt comprises mainly electrons with energies up to 1 MeV, located between 3 – $9 R_E$ in the equatorial plane and is unstable. The instability is consequent on the disturbances arising from the injection and acceleration of particles from geomagnetic storms resulting at variation of particle population within a time frame of hours. Figure 1.8 shows the distribution of trapped protons and electrons in the magnetosphere for a range of energies.

From Figure 1.8a, it can be observed that particles with higher energy are trapped closer to the Earth and vice-versa.

1.3.4 Motion of charged particles

Particle population within the magnetosphere has been discussed in Sections 1.4.2-1.4.3. In this section, the motion of these particles and the process by which they are deposited into the ionosphere will be highlighted. To start with, the inner

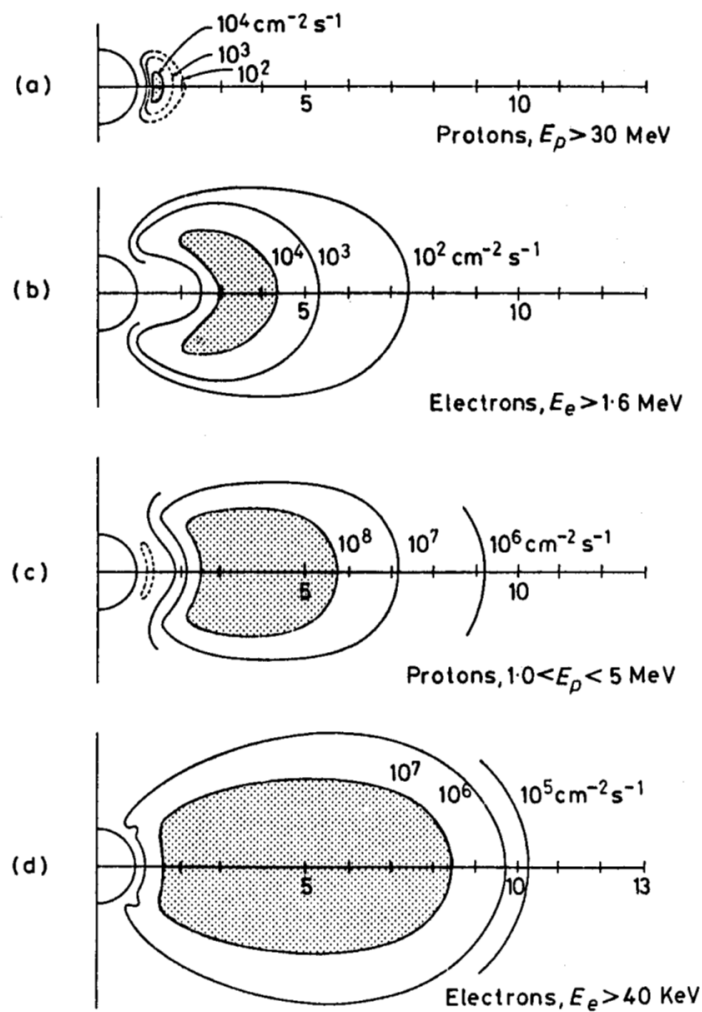


Figure 1.8: Distribution of trapped protons and electrons for a range of energies [From: Hess, 1968].

magnetosphere is described as being fairly dipolar and consists of two important regions: the plasmasphere and the radiation belts. The plasmasphere consists of cold plasma whereas the radiation belts are composed of most energetic particles found in the magnetosphere.

Particles whose motion are bounded within the magnetosphere are denoted as trapped whereas those that escape into the ionosphere are said to have precipitated in there. Particles trapped in the magnetosphere of the Earth perform three basic motions: they gyrate about the field line, bounce between mirror points, and azimuthally drift [Figure 1.9]. Generally, the motion of charged particles depends on

the magnetic field \mathbf{B} , the electric field \mathbf{E} , and a non-electromagnetic force \mathbf{F} . These

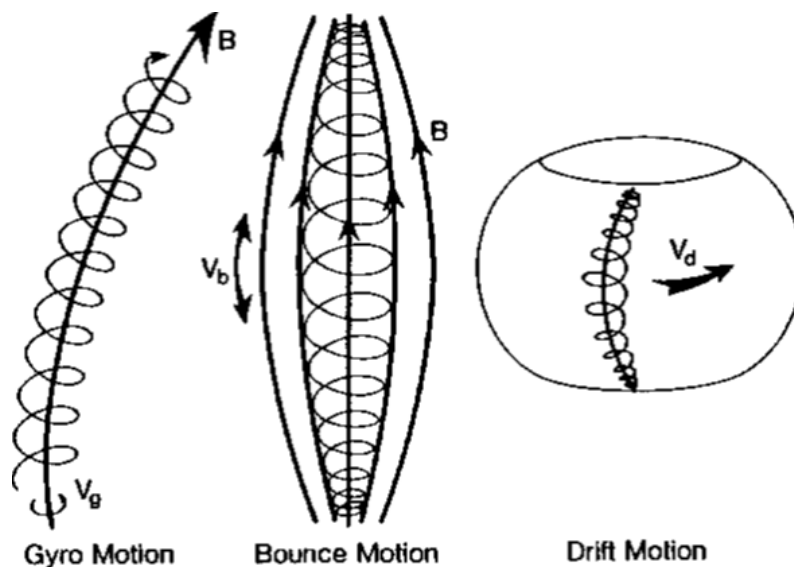


Figure 1.9: Typical charged particle motion in the magnetosphere [From: Yuting *et al.*, 2013]

parameters are related as in the Lorentz equation in equation 1.1 below.

$$\mathbf{F} = q[\mathbf{E} + (\mathbf{v} \times \mathbf{B} + \mathbf{E})] \quad (1.1)$$

p is the particle momentum, v , the velocity and q the particle charge. The different types of particle motions mentioned above will be discussed below.

- **Gyration motion**

Particles in the magnetosphere rotate around field lines with opposite charges rotating in opposite directions. Around a field line that points upwards, ions circle clockwise while electrons circle anti-clockwise. The rate of gyration is known as the gyration frequency as shown in equation 1.2 below.

$$f_B = \frac{Bq}{2\pi m} \quad (1.2)$$

f_B is the gyro frequency of particle, B is the magnetic field, q , the charge on the particle while m is the particle mass [Davies, 1989].

- **Bounce motion and the loss cone**

Particles can be trapped on a magnetic field line. If a particle (electron or

proton) in the magnetosphere has a velocity v_{\perp} normal to the magnetic field and v_{\parallel} along it, the trajectory would be a spiral (Figure 1.10). With no work done on the particle, no electric field can be present, hence magnetic flux through the orbit is constant. This is as in Equation (1.3)

$$\phi = B \cdot r_G^2 \pi = \frac{2mE_{\perp} \pi}{e^2 B} = \text{constant} \quad (1.3)$$

Where m is the particle mass, r_G is the gyroradius, e is the charge of an electron, B the magnetic field strength and E_{\perp} the kinetic energy associated

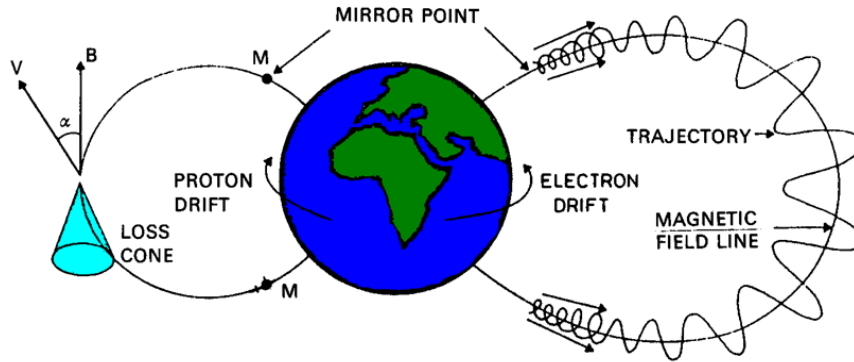


Figure 1.10: Schematic of typical motions of particles trapped on closed field lines including the equatorial loss cone and the mirror points of bouncing particles [From Kavanagh, 2000]

with the field-normal velocity component. $\frac{E_{\perp}}{B}$ is constant and represents the magnetic moment of the current loop represented by the gyrating particle. The condition holds so long as the magnetic field does not change significantly during one gyration period. The perpendicular velocity of the particle can be expressed as a function of the angle between the velocity vector and the magnetic field direction. This angle is denoted by the pitch angle.

$$V_{\perp} = V \sin \alpha \quad (1.4)$$

Equation 1.4 can be expressed in terms of energy as:

$$\frac{mv_{\perp}^2}{2B} = \frac{E_{\perp}}{B} = \frac{E \sin^2 \alpha}{B} = \text{constant} \quad (1.5)$$

$\sin^2 \alpha$ is proportional to the magnetic field (B).

For a charged particle that moves from the equator to higher latitudes in a dipole field, it will encounter an increasing magnetic field (B) and consequently increased pitch angle. At the point at which $\alpha = 90^\circ$ all forward motion ends and the particle will be reflected back along the field line towards the equator. The point at which this reflection takes place is denoted the *mirror point*. The parallel energy at the mirror point is zero while the parallel velocity is given by:

$$V_{\parallel}^2 = v^2 - v_{\perp}^2 = v^2 \cos^2 \alpha \quad (1.6)$$

At mirror point $\alpha = 90^\circ$, hence $v_{\parallel} = 0$.

The relationship between the pitch angle and the mirror point is such that pitch angle determines the position of the mirror point as a particle crosses the equator at the point where the field is weakest (i.e. B_{eq}). This is as represented in Equation 1.7 below:

$$\frac{B_{eq}}{B_M} = \sin^2 \alpha_{eq} \quad (1.7)$$

Particles of a particular equatorial pitch angle will mirror at the same latitude in a dipole regardless of their L shell. In the case of the Earth's dipole, there is an upper limit for the mirror latitude for a given field line, this is because the mirror point must always lie above the surface of the Earth and literally above the denser atmosphere ($< 100 \text{ km}$). At this point, a particle is prone to colliding and consequently getting lost to the upper atmosphere. The fraction of particles that are no longer trapped on closed field lines are construed to be within a '*loss cone*' as represented in Figure 1.10.

McIlwain [1961] described the L -shell parameter for measuring latitude of points where magnetic field lines cross the Earth's surface. To a good approximation, L parameter is equal to the greatest distance of magnetic dipole from the Earth centre in the equatorial plane. The relationship between the latitude and the L number is given as:

$$\cos^2 \lambda = \frac{1}{L} \quad (1.8)$$

Hence,

$$\lambda = \cos^{-1} \left[\frac{1}{L} \right]^{\frac{1}{2}} \quad (1.9)$$

Where λ is the invariant magnetic latitude and L (measured in R_E) varies between 1 and infinity according to latitudes between 0 and 90° .

For a particle to properly mirror, the equatorial pitch angle must satisfy the relationship given below.

$$\sin^2 \alpha_{eq} > \sin^2 \alpha_L \quad (1.10)$$

When a particle approaches the mirror point, the pitch angle increases and the loss cone widens.

- **Gradient curvature drift**

If there exists an electric field that is perpendicular to the magnetic field (\mathbf{B}), the particle will drift in an orthogonal direction ($\mathbf{E} \times \mathbf{B}$ drift). In the particle frame of reference $\mathbf{E} = 0$, hence, the motion of the particle is circular. A gradient in the magnetic field strength changes the gyroradius of a particle. The gyroradius is inversely proportional with the magnetic field, resulting in a drift (Figure 1.11). The velocity of this drift can be derived from the continuous

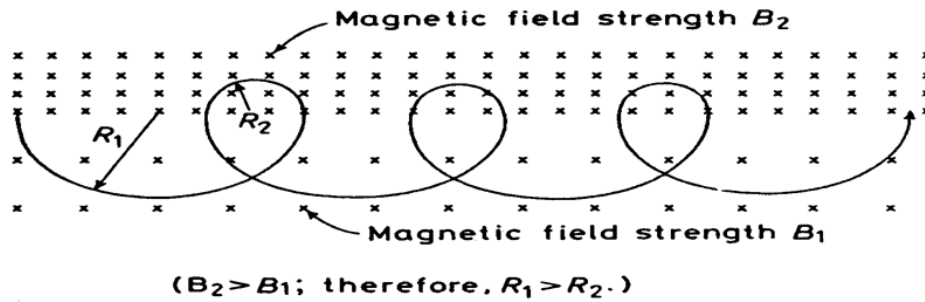


Figure 1.11: Longitude drift caused by a gradient in the geomagnetic field intensity. Here, magnetic field is perpendicular to the effective direction of drift motion [From: Hess, 1968]

gyro motion in two differing field strengths and using the limit case of small variation in B . The gradient drift velocity is expressed as:

$$\mathbf{V}_{\nabla B} = \frac{mv_{\perp}}{2qB^3} \cdot \mathbf{B} \times \nabla \mathbf{B} \quad (1.11)$$

Also, the curvature of the geomagnetic field lines produce a second drift of particles as in Figure 1.12. A bouncing particle experiences a centrifugal force that combines with the motion of gyration to produce a lateral movement. The motion is in a similar direction with the gradient drift but depends on the parallel velocity of the particle instead of the velocity perpendicular to the magnetic field as in equation 1.12

$$\mathbf{V}_c = \frac{mv_{\parallel}}{qB^3} \cdot \mathbf{B} \times \left[\left(\frac{\mathbf{B}}{B} \cdot \nabla \right) \mathbf{B} \right] \quad (1.12)$$

Combining 1.11 and 1.12 to obtain a singular expression for gradient of curvature drift by simplifying and considering a local field line radius (r_c) yields:

$$\mathbf{V}_{GC} = \frac{mv^2}{eB^2} \cdot \frac{\delta \mathbf{B}}{\delta \mathbf{R}} \cdot \left(\frac{1}{2} \mathbf{V}_{\perp}^2 + \mathbf{V}_{\parallel}^2 \right) \quad (1.13)$$

$$\mathbf{V}_{GC} = \frac{mv^2}{2eBr_C} \cdot (1 + \cos^2 \alpha) = \frac{\mathbf{E}}{2eBr_C} \cdot (1 + \cos^2 \alpha) \quad (1.14)$$

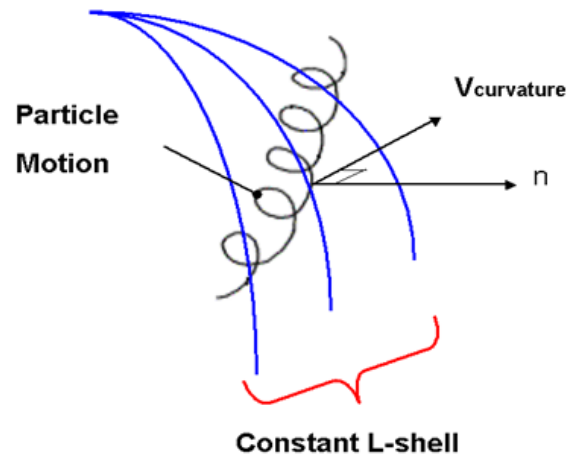


Figure 1.12: Curvature drift caused by combination of centrifugal force with the gyromotion

[From: Shirley and Fainbridge, 1997]

This drift motion is charge-dependent, electrons drift eastward while proton and ions drifts westward as a result of opposing gyro-motions, producing a net current called a ring current. A considerable amount of energy is contained in the ring current during geomagnetic storms [Berko *et al.*, 1975].

1.3.5 Magnetospheric currents

As a result of plasma population and electric fields, several current systems are created in the magnetosphere. Variation of magnetospheric current system results at the perturbation of global magnetic field. Figure 1.13 shows the various current systems which are discussed below.

Ring current

The ring current is an electric current carried by particles. It is produced as a result of longitudinal drift of these particles [10–200 KeV] in the Van Allen belts. The most numerous ions with these energies are H^+ , O^+ , He^+ , and He^{++} [e.g. Daglis *et al.*, 1999]. Changes in this current are responsible for global decreases in the Earth's surface magnetic field, otherwise termed geomagnetic storms. The configuration is as shown in Figure 1.13.

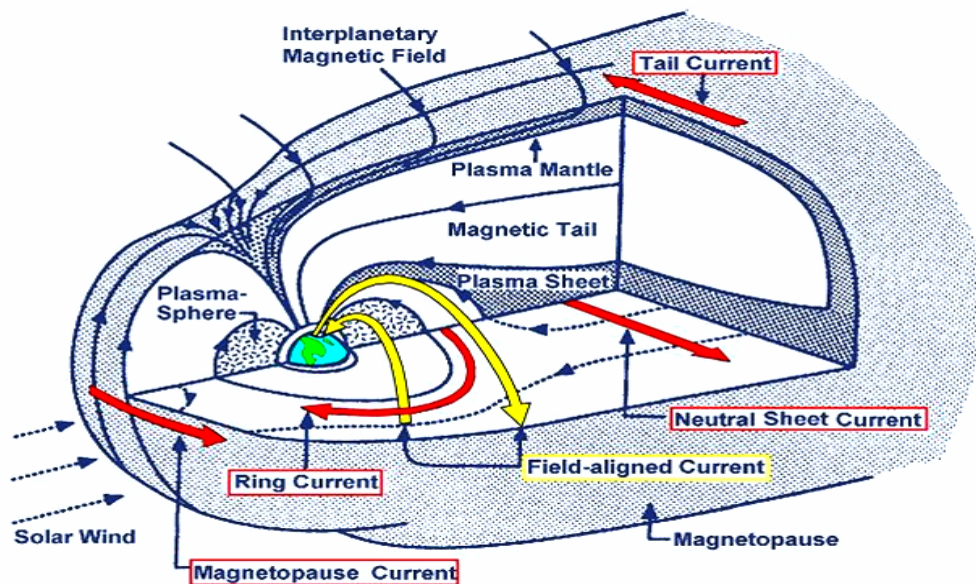


Figure 1.13: Plasma population and current system in the magnetosphere [Shirley and Fainbridge, 1997]

Magnetopause current

Otherwise known as the Chapman and Ferraro current, the magnetopause current is formed at the boundary between the magnetosphere and the solar wind and flows in a single sheet. It balances the geomagnetic field inside the magnetosphere and confines the geomagnetic cavity (Figure 1.14a). The field of this current decreases the Earth's field outside the boundary and increases it inside.

Field-aligned currents (FAC)

Otherwise known as Birkeland currents, they form part of the coupling between the magnetosphere and the ionised region of the upper atmosphere. These currents extend from the magnetosphere into the high latitude ionosphere following the orientation of magnetic field lines [e.g. Gombosi, 2004, Longden, 2007]. In the magnetosphere, the currents are driven by the solar wind, the IMF and by bulk motions of plasma through the magnetosphere whereas in the high latitude ionosphere (or auroral zones), field-aligned currents close through the region of the auroral electrojet which flows perpendicular to the local magnetic field in the ionosphere. The field-aligned currents occur in two pairs of field-aligned current sheets. A pair extends from noon through the dusk sector to the midnight sector, while the other pair extends from noon through the dawn sector to the midnight sector.

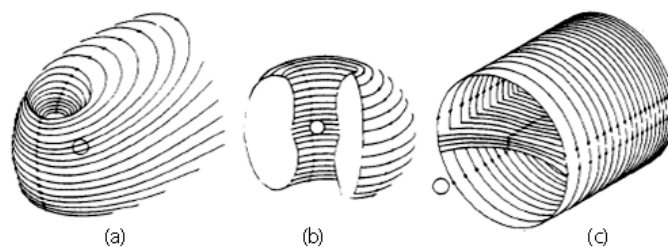


Figure 1.14: Schematic representation of the major magnetospheric current systems. (a): magnetopause currents, (b): ring current, (c): tail currents [From: Olsen, 1982]

Tail currents

This current flows over the bounding surface of the magnetotail, closing westward through the centre of the tail across the plasmashet [e.g. Kivelson and Russell, 1995]. This current system approximates a double solenoid configuration, one for each of the oppositely polarised tail lobes as shown in Figure 1.14c.

1.4 Ionosphere

The ionosphere is a region that represents the lower boundary of the magnetosphere, the ionised part of the atmosphere and more importantly, one of the main sinks of energy which is transmitted from the solar wind to the magnetosphere. The ionosphere stretches from about 60 km to 1000 km altitude in the atmosphere, held in place by the Earth's gravity. It consists of weakly ionised plasma that co-exists with the neutral atmosphere. Ionisation in this region is primarily caused by photoionisation from incident solar radiation and impact ionisation from magnetospheric particles.

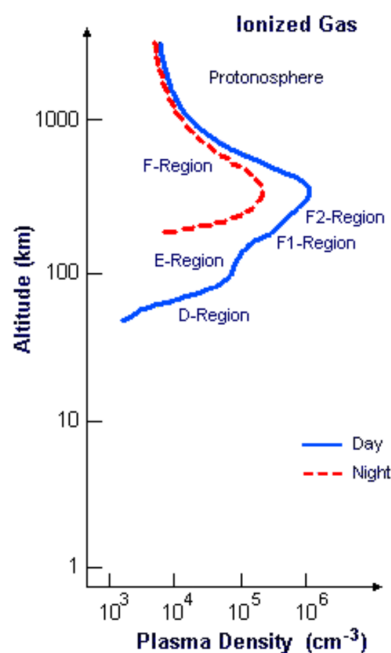


Figure 1.15: A schematic showing plasma density of the Earth's ionosphere at different altitude.

The characteristic energy of the ionospheric plasma is well below 1 eV. However, the different couplings with the atmosphere or the magnetosphere contribute to energising this plasma. Depending on the mechanism, the energy gained may result at heating (thermal energy gain), or acceleration (kinetic energy gain). Due to the changing composition with heights in the atmosphere, ion production also changes. Balancing the ionisation rate with the recombination rate leads to the formation of layers in the ionosphere. These layers are denoted D, E and F in ascending altitude. The F-layer is sub divided into the F1 and F2 regions in the day time. The D and E regions, being the farthest from the Sun, are weakly ionised (Figure 1.15). They exist only in daylight hours, during which they tend to absorb radio signals in the medium frequency range from 300 kHz to 3 MHz. The height profile of the main regions of the dayside ionosphere after Hargreaves [1992] is as illustrated in Figure 1.15:

- D region: 60–90km
- E region: 105–160km
- F1 region: 160–180km
- F2 region: peak electron density at ~ 300 km

The variation of electron density in a given ionospheric layer is governed by the balance of production, loss and transport processes which satisfies the continuity Equation 1.15:

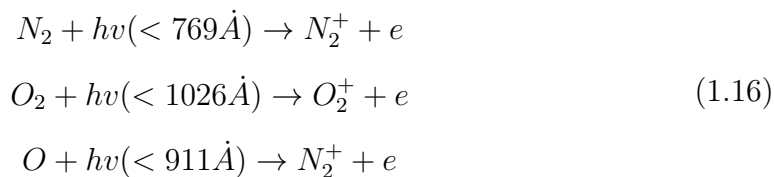
$$\frac{\delta n_e}{\delta t} = Q - L - \nabla \cdot (n_e V) \quad (1.15)$$

n_e is the electron density, Q is the production rate, L is the loss rate due to recombination or attachment and v is a plasma velocity.

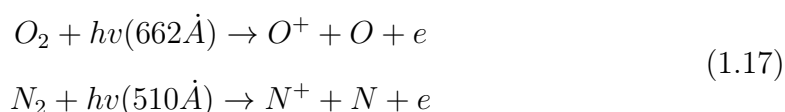
1.4.1 Production processes

As mentioned above, the two main production processes are:

- Ionisation of solar radiation in the EUV and X-ray spectrum.
- Ionisation by precipitating particles. Nonetheless, photoionisation is the primary process for ionisation by radiation. Production processes with respect to the major species [i.e. N_2 , O_2 and O], is as in equation 1.16



h , is Planck's constant, while v is the frequency of photon. The wavelengths are as reported in Rees [1989] and are the ionisation thresholds for the production of ions in their ground electronic state. Apart from photoionisation, an additional source of atomic ions and electrons is dissociative ionisation



The production rate from photoionisation processes can be obtained from the Chapman production formula as in equation 1.18

$$q = \eta\sigma nl \tag{1.18}$$

The formula gives the relation between the radiation intensity at a given height, (I) and the rate of production of ion-electron pairs (q), the ionisation efficiency (η), σ is the cross-section of photon absorption, n is the number density of neutrals.

The Chapman derivation in equation 1.18 above is based on the following assumptions [e.g. Hargreaves, 1992]:

- The atmosphere is composed of a single species exponentially distributed
- There are no variations in the horizontal planes
- Solar radiation is absorbed in proportion to the concentration of gas particles
- The absorption coefficient is a constant or there is monochromatic radiation

Since the ionosphere is more complicated than the assumed state as above, the Chapman formula may not describe a true ionosphere. Primarily, the source of production for E and F regions are extreme ultra violet radiation (EUV) and soft X-rays. Nonetheless, the D region has more complicated chemical composition with a number of ionisation sources. Hargreaves [1992] enumerates the ionisation sources for D region ionosphere as below:

- A. Lyman - α line at 1215\AA nitric oxide
- B. EUV ionisation of O_2 and N_2
- C. EUV spectrum between $1027 - 1118\text{\AA}$ ionises an excited oxygen state.
- D. Hard X-rays, $2 - 8\text{\AA}$ ionising all constituents
- E. Galactic cosmic rays

The input of each effect varies depending on latitude, time of the day and level of solar activity. At low latitudes, production in the ionosphere is controlled by radiation processes, whereas at higher latitudes (i.e. in and above the auroral oval), particle precipitation play an important role in the production process. Section 1.5.3 further discusses particle precipitation into the ionosphere. Figure 1.16 shows the production rate for a model atmosphere for a range of monoenergetic electrons of various energies.

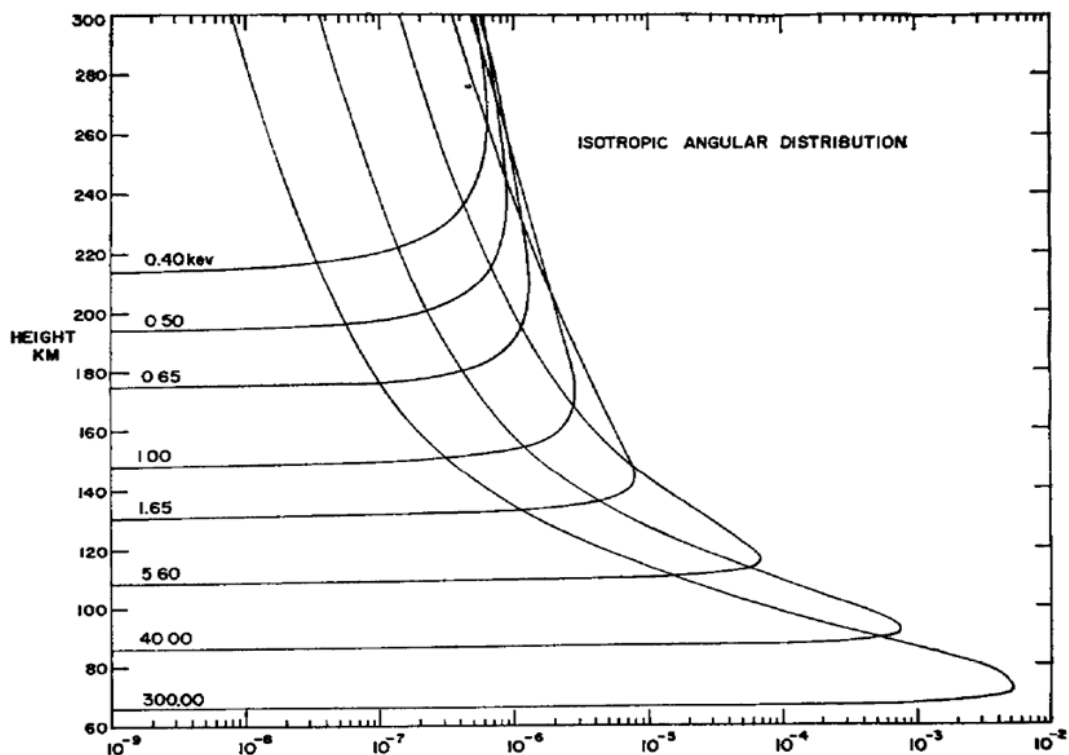


Figure 1.16: Production rates of monoenergetic electrons of various initial energies. Energies given in MeV (From Rees, 1963).

1.4.2 Loss processes

Loss processes in the ionosphere are relative to altitude. The three mechanisms proposed for electron loss in the ionosphere are:

- **Radiative recombination:** An electron recombines with an ion to produce a neutral particle and photon



- **Dissociative recombination:** An electron recombines with an ionised molecule to produce neutral particles



- **Attachment:** An electron recombines with a neutral particle to produce a negative ion



The rate of production and combination depends on the ion composition and height profile. Therefore, these processes will be different at the different layers of the ionosphere.

Observations and theory behind the dynamics of the Earth's ionosphere are presented in detail [e.g. Franco Verniani, 1974, Hargreaves, 1992, Schunk and Nagy, 2009]. The geomagnetic orientation at low and high latitudes is responsible for deviations from normal ionospheric behaviour. At equatorial latitudes, the geomagnetic field lines are virtually horizontal leading to depletion in electron density. West to east electric fields generated in the E region result in a vertical drift of the F region plasma [electrodynamic lifting].

1.4.3 High latitude ionosphere

As a result of the interaction of the solar wind with the geomagnetic cavity, magnetic field lines at high latitudes extend deep into the magnetosphere or are open into interplanetary space in the polar cap. Therefore, magnetospheric processes have

effect on the high latitude ionosphere. At high latitude the magnetic field lines open into interplanetary space in the polar cap making direct entry of solar wind particle possible. This produces a drizzle of low energy particles, a process called polar rain. On the other hand, light ions of ionospheric origin (mostly H^+ and H_e^+) are also lost from the high altitude polar cap. The energies of these ions are sufficient to escape the gravitational potential well, hence, they travel along the open flux tubes in the polar cap. High energy particles precipitate from the magnetospheric plasma sheet at high latitudes. When they arrive at the atmosphere they emit photons and produce optical aurora. Aurora can either be discrete or diffuse. Discrete aurora are structured and intense while diffused aurora appears as a glow in the sky. Auroral events are associated with auroral radio absorption. This occurs when more energetic particles penetrate into the lower layer of the ionosphere. On the contribution of protons and electrons to auroral absorption, Eather and Burrows [1966] used H_β emission observations from the ground to indicate the contribution of ionisation from protons as negligible, while Hargreaves and Sharp [1965] also show that proton usually contribute less than 10% of the total precipitating energy (Figure 1.17). The morphology and coupling between the high latitude ionosphere and magnetosphere will be discussed in Chapter 2.

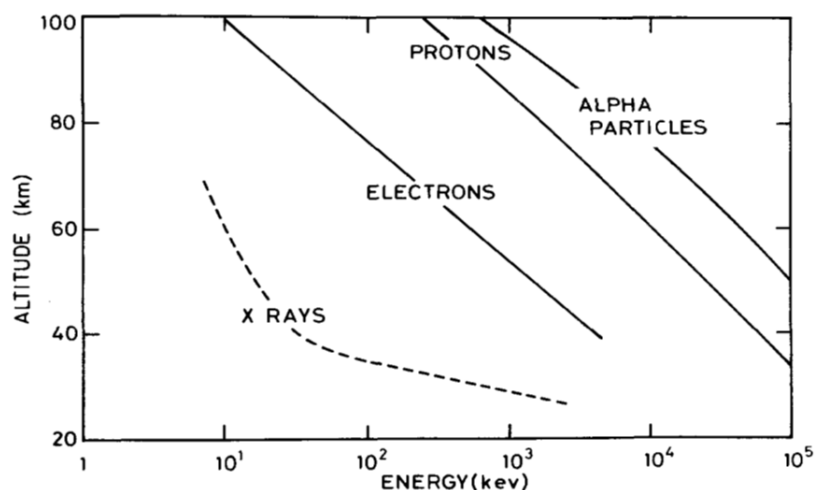


Figure 1.17: A schematic of ionisation altitude [From A.D. Richmond, in solar terrestrial physics, Reidel, 1983].

1.4.4 Particle precipitation

Particle precipitation describes the process whereby particles trapped to magnetic field lines in the magnetosphere propagate into the high latitude ionosphere. These particles are accelerated by field-aligned currents and propel impact ionisation. Particle precipitation plays an important role in the ionosphere-magnetosphere coupling and contributes immensely to the energy input of the ionosphere. Precipitating particles are the primary source of ionisation at altitudes below ~ 190 km on the nightside.

Radio absorption in the ionosphere is dependent on the variation of electron density and the effective collision frequency, these factors enhance their variation consequently affect the rate of change of radio absorption. It is important to study the roles played by these changing parameters during active periods. In the *D* and *E* layers electron-neutral collision frequency is high and contributes to radio absorption. As the altitude increases, the electron-ion collision frequency also increases. In the *F*-layer an increase in temperature will produce a decrease in absorption as the atmosphere gets thinner with height. The processes of radio absorption in the ionosphere and geomagnetic activity will be discussed in Chapter 2.

1.5 Observations of the ionosphere

Ionospheric probing has two major techniques. One is the remote sensing of the ionosphere mostly with ground based instrumentation e.g. radars and optical equipment. These instruments have the capacity to produce large scale images of the auroral region that complement the observation of ground based radars. The second method makes use of in-situ observations such as satellites and rockets. When studying the ionosphere on small scale, ground based auroral imagers are important. Instruments such as imaging radio ionospheric opacity meters (Riometers) measure the extent and variation of energetic particle precipitation in the auroral regions. The large coverage combined with high spatial resolution allows detailed observation of the structure of high frequency (HF) radio absorption which acts as a proxy for

detecting particle precipitation. The main instrument used in this investigation is the imaging riometer for ionospheric studies (IRIS) based at Kilpisjärvi in northern Finland [Brown *et al.*, 1995]. This facility has a 240×240 km field of view in the D region (90 km altitude) and provides maps of energetic particle precipitation well within the auroral zone. The procedure of operation of IRIS is discussed in Chapter 3.

Chapter 2

Radio wave absorption in the ionosphere

2.0 Introduction

The electron density of the ionosphere varies with height (see Figure 1.15) as a result of the stratification of atmospheric constituents by gravity and the variation in ionisation cross-section between these constituents (see Section 1.5), therefore the ionosphere exhibits several distinct regions (i.e. D, E and F regions). Radio waves on the shortwave bands are refracted or reflected back to Earth as they pass through the ionosphere. In addition, signals passing through this region are also known to be attenuated [e.g. Appleton *et al.*, 1933; Hargreaves, 1966; Davies, 1969; Milan *et al.*, 1996; Stauning, 1996a, and b]. Ionospheric absorption is one of the primary contributors to the reduction in signal strength [Stauning, 1998]. The absorption of radio waves in the ionosphere reveals information on the physics of this region.

Scholarly investigation of radio wave absorption has progressed for over a century. In 1901, Marconi succeeded in transmitting a radio signal from Cornwall, England, to Newfoundland, Canada and by this evinced that radio waves could travel around the curvature of the Earth. Subsequently, Kennelly [1902] and Heaviside [1902] observed that signals were reflecting from a conducting layer of atmospheric ions at an altitude of approximately 80 km. Thenceforth, other workers [e.g. Appleton and Barnett, 1925; Breit and Tuve 1925] indicated that there are reflecting layers in the ionosphere and they determined the approximate heights of these layers. Subsequent discoveries [e.g. Appleton, 1925; Nichols and Schelleng, 1925] demonstrated

that the magnetic field of the Earth affects the return of radio waves. Appleton and Builder [1932] then developed the magneto-ionic theory based on the postulation of wave interaction in ionospheric plasma. The electron density, gyrofrequency, and electron collision with neutral atoms and molecules are important factors that affect the passage of radio waves through the ionosphere. Schunk and Nagy [2009], Hargreaves [1992], and Davies [1968] identified the electron density, the gyrofrequency as the most important factors that affect the passage of radio waves through the ionosphere. These sequence of findings are foundational to other equally important studies on radio wave propagation in the ionosphere. This chapter discusses the propagation of high frequency (HF) radio waves and their reflection by the ionosphere and the processes of radio waves absorption in the lower ionosphere. The discussion is imperative to ionospheric modelling which is the objective of this thesis.

2.1 Appleton-Hartree formula

The Appleton-Hartree formula gives the refractive index of an electromagnetic wave propagating through an isotropic ionised medium in the presence of a magnetic field. The dispersion relations are more commonly expressed in terms of the angular frequency (ω) and the wave number (k).

$$\omega = 2\pi f \quad (2.1)$$

$$f = \frac{c}{v} \quad (2.2)$$

For electromagnetic waves in vacuum, the angular frequency is proportional to the wave number (k)

$$\omega = ck \quad (2.3)$$

A dispersion relation relates the wave number to the frequency of the wave. The relationship between wave propagation number and the refractive index for an exponentially decaying plane wave of the form $e^{i(\omega t - kx)}$ is defined as:

$$n = (\mu - ix) = \frac{ck}{\omega} \quad (2.4)$$

The Appleton-Hartree equation defines the refractive index of a magnetoplasma as being complex in nature. Davies [1969], gives the full derivation of the Appleton-Hartree dispersion relation equation as in equation (2.5):

$$n^2 = (\mu - ix)^2 = 1 - \frac{X}{1 - iZ - \frac{Y^2 \sin^2 \theta}{2(1 - X - iZ)} \pm \left[\frac{Y^4 \sin^4 \theta}{4(1 - X - iZ)^2} + Y^2 \cos^2 \theta \right]^{1/2}} \quad (2.5)$$

Where n is the complex refractive index. The expression is complicated because it used dimensionless quantities (X , Y and Z) each being defined as a ratio between the wave frequency and a frequency characteristic of the medium [Hunsucker and Hargreaves, 1992].

$$X = \frac{\omega_p^2}{\omega^2} = \frac{N_e e^2}{\varepsilon_0 m_e \omega^2} \quad (2.6)$$

$$Y = \frac{\omega_H}{\omega} = \frac{eB}{m_e \omega} \quad (2.7)$$

$$Z = \frac{\nu}{\omega} \quad (2.8)$$

Where ω_H is the electron angular gyrofrequency, ω_p is the plasma angular frequency, ω is the wave angular frequency, N_e is the plasma electron density, e is the electric charge on an electron, m_e is the electron mass, ε_0 is the permittivity of free space, ν is the collision frequency between electrons and neutrals that is dependent on the atmospheric density, and B is the external magnetic field magnitude. θ is the angle between the direction of wave phase propagation and the external magnetic.

The dispersion relation is complex but can be simplified by making a number of assumptions. Neglecting magnetic field and collision frequency, the equation simplifies to:

$$n^2 = 1 - X = 1 - \frac{\omega_p^2}{\omega^2} \quad (2.9)$$

In this case, the imaginary part of the refractive index is zero. A wave with an angular frequency that equals the plasma frequency will reflect. Hence a wave with a frequency that exceeds the plasma frequency will pass straight through the ionosphere. There are two distinct cases of ionospheric absorption of HF radio waves and they will be discussed in Sections 2.2.1 and 2.22. These are known as deviative and non-deviative absorption.

2.1.1 Deviative absorption

Deviative absorption applies in the F -region ionosphere where the collision frequency is small. In this case, (2.4) becomes:

$$k = \frac{v}{2c} \left(\mu - \frac{1}{\mu} \right) \quad (2.10)$$

where c is the speed of light in a vacuum and v is the effective collision frequency. This equation shows that absorption will be enhanced as the ray approaches the reflection level where ($\mu \rightarrow 0$) and the wave group velocity approached zero. However, non-deviative absorption (2.2.2) is more important to this study as we consider absorption in the D region ionosphere.

2.1.2 Non-deviative absorption

Radio waves passing through an ionised medium cause the electrons to vibrate. If the electrons collide with heavy particles, energy is transferred from the wave to the medium in the form of plasma thermal energy. The rate of wave attenuation is dependent on the number of collisions per oscillation. In the case of ionospheric absorption, it is important to include the effects of collisions. If a radio wave propagates close to the direction of the magnetic field, the dispersion relation becomes further simplified as $\theta \rightarrow 0$, hence $\cos \theta \rightarrow 1$ while $\sin \theta \rightarrow 0$. The Appleton-Hartree equation as shown in (2.5) becomes:

$$n^2 = 1 - \frac{X}{1 - iZ \pm Y \cos \theta} = 1 - \frac{\frac{\omega_p^2}{\omega^2}}{1 - \frac{iv}{\omega} \pm \frac{\omega_H \cos \theta}{\omega}} = (\mu - iX)^2 \quad (2.11)$$

The wave can be defined in terms of the refractive index ($\mu - iX$), recalling the wave solution $e^{i(\omega t - kx)}$ and considering that the wave number is complex,

$$k = \frac{n\omega}{c} = (\mu - iX) \frac{\omega}{c} \quad (2.12)$$

Substituting yields

$$k = \exp \left[- \left(\frac{\omega x}{c} \cdot x \right) \right] \exp \left[i \left(\omega t - \frac{\omega \mu}{c} \cdot x \right) \right] \quad (2.13)$$

The first term of (2.13) is the attenuation rate k of $\frac{\omega}{c} \cdot x$ nepers per metre. If (2.13) is separated into its real and imaginary parts, it is possible to define the value of X .

$$\mu^2 - x^2 = 1 - \frac{X \cdot (1 \pm Y \cdot \cos \theta)}{(1 \pm Y \cdot \cos \theta)^2 + Z^2} \quad (2.14a)$$

$$2 \cdot \mu \cdot x = \frac{Z \cdot x}{(1 \pm Y \cdot \cos \theta)^2 + Z^2} \quad (2.14b)$$

Substituting the values of X , Y and Z in (2.6-2.8), a value for the coefficient of attenuation (K) can be deduced as:

$$k = \frac{\omega x}{c} = \frac{w}{c} \cdot \frac{1}{2\mu} \cdot \frac{\omega_p^2}{\omega} \cdot \frac{v}{[v^2 + (\omega \pm \omega_H \cos \theta)^2]} \quad (2.15a)$$

$$k = \frac{e^2}{2m_e c \varepsilon_0} \cdot \frac{1}{\mu} \cdot \frac{N_e v}{v^2 + (\omega \pm \omega_H \cos \theta)^2} \quad (2.15b)$$

The total absorption over a path can be described as:

$$A = 4.6 \times 10^{-5} \int \frac{N_e v \cdot dl}{v^2 + (\omega \pm \omega_H \cos \theta)^2} \text{ (dB)} \quad (2.16)$$

In the D and E regions, HF radio waves undergo very little refraction and $\mu \approx 1$. the velocity of the wave is unaltered hence there is no bending. This is termed non-deviative absorption. With a small collision frequency (v) relative to the angular wave frequency (ω), the absorption coefficient is proportional to the product of the electron density and the collision frequency and is inversely related to the square of the wave frequency.

2.1.3 Collision frequency in the ionosphere

Aggarwal *et al.*, [1979] established the relationship between ionospheric electron density and ionospheric radio absorption. However, radio absorption also depends on the effective collision frequency between electrons and other species. The velocity dependent monoenergetic collision frequency of an electron is given as:

$$V_m = nvQ_m(V) \quad (2.17)$$

n is gas number density, v is relative speed of the colliding momentum, and $Q_m(V)$ is the velocity dependent momentum transfer cross-section.

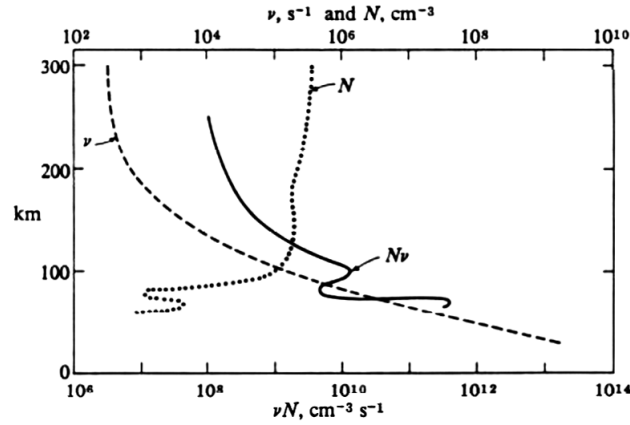


Figure 2.1: Schematic of height variation of the electron collision frequency, electron density and the product (Nv) that is a measure of radio absorption [From: Davies, 1989].

Hence, an average V_m is taken over the entire distribution to obtain the effective collision frequency such that the total effective electron collision frequency is given by the sum of the electron-ion and electron neutral collision rate.

$$\langle V_e f f \rangle = \langle V_e n \rangle + \langle V_e i \rangle \quad (2.18)$$

In the case of elastic scattering of electrons in a pure field of ions, the electron-ion collision frequency is given by:

$$\langle V_e i \rangle = \frac{8\pi}{3} \cdot \frac{Z^2 e^4 N_i}{(2m_{e\pi})^{\frac{1}{2}} (KT_e)^{\frac{3}{2}}} I n \left[\frac{K^{\frac{3}{2}}}{1.78 Z e^3} \cdot \left(\frac{T_e^3}{N_{e\pi}} \right)^{\frac{1}{2}} \cdot \left(\frac{T_i}{Z T_{e+T_i}} \right)^{\frac{1}{2}} \right] \quad (2.19)$$

M , N_e and T_e are the mass, number density and temperature of the electron respectively. K is the Boltzmann constant. The electron-neutral collision frequency is derived from the sum of the collision rates between electrons and the neutral constituents of the upper atmosphere. Schunk and Nagy [1987] derived the Maxwellian average electron-neutral collision frequencies from laboratory data as (2.20–2.24) below:

$$\langle V_{eN_2} \rangle = 2.33 \times 10^{11} \cdot N(N_2) \cdot \left[1 + 1.21 \times 10^{-4} T_e \right] T_e \quad (2.20)$$

$$\langle V_{eO_2} \rangle = 1.82 \times 10^{-10} N(O_2) \left[1 + 3.6 \times 10^{-2} T_e^{\frac{1}{2}} \right] T_e^{\frac{1}{2}} \quad (2.21)$$

$$\langle V_{eO} \rangle = 8.9 \times 10^{-11} N(O) [1 + 5.7 \times 10^{-4} T_e] T_e^{\frac{1}{2}} \quad (2.22)$$

$$\langle V_{eH_e} \rangle = 4.6 \times 10^{-10} N(H_e) \cdot T_e^{\frac{1}{2}} \quad (2.23)$$

$$\langle V_{eH} \rangle = 4.5 \times 10^{-9} N(H) [1 - 1.35 \times 10^{-4} T_e] T_e^{\frac{1}{2}} \quad (2.24)$$

Non-deviative absorption occurs as a result of the enhancement of the D region electron density, by solar illumination or electron precipitation. In the case of auroral absorption the D region enhancement is produced by the precipitation of > 30 keV electrons in the splash and drizzle precipitation regions. The location and level of auroral absorption have been determined from riometer observations [Hartz *et al.*, 1963] and empirically modelled [Foppiano and Bradley, 1983]. The flux of auroral precipitation, and consequently the level of auroral absorption, is dependent on geomagnetic activity, and models require suitable parameterisation of this behaviour. Previous works have utilised solar activity factors as a model input, but some inadequacies were identified in such models. For example, Foppiano and Bradley [1985] used sunspot number as a model input but this does not adequately reflect the much more rapidly varying level of magnetic disturbance at the Earth. On the use of other indices, Hargreaves *et al.*, [1987] employed a_p while and Foppiano and Bradley, [1983] used K_p . However, auroral absorption varies with the occurrence of substorms [Jelly and Brice, 1967] on a timescale of ~ 10 minutes [Reid, 1967]. Consequently, the 3-hourly indices (i.e. a_p and K_p) are poor indicators of absorption level. In this work, parameterisation based on the availability of real-time solar wind parameters are utilised.

2.2 The auroral oval

The auroral oval describes an annular region at about 67° geomagnetic latitude eccentric to the geomagnetic pole where visible and radio aurorae occur as a result of particle precipitation into the upper atmosphere from magnetospheric sources. This precipitation causes ionisation of the atmosphere, in addition to the ionisation produced by solar radiation leading to the excitation of atmospheric constituents to produce the luminous aurora. The region with the greatest statistical likelihood of observation of luminous auroral features is defined by the poleward and equatorward

boundaries of the auroral oval. To determine this region, Feldstein and Starkov [1967] used photographic data for different levels of geomagnetic activity. The position of the oval is fixed relative to the Sun. The dimension of the oval broadens and moves to lower latitudes with increasing geomagnetic activity.

2.2.1 Statistics of the aurora oval

Several workers [e.g. Holt *et al.*, 1961; Hartz *et al.*, 1963; Driatsky, 1966; Hargreaves and Cowley, 1967; Foppiano and Bradley, 1985 and references therein] have investigated the statistics of auroral absorption from many latitudes and longitudes (Figure 2.2).

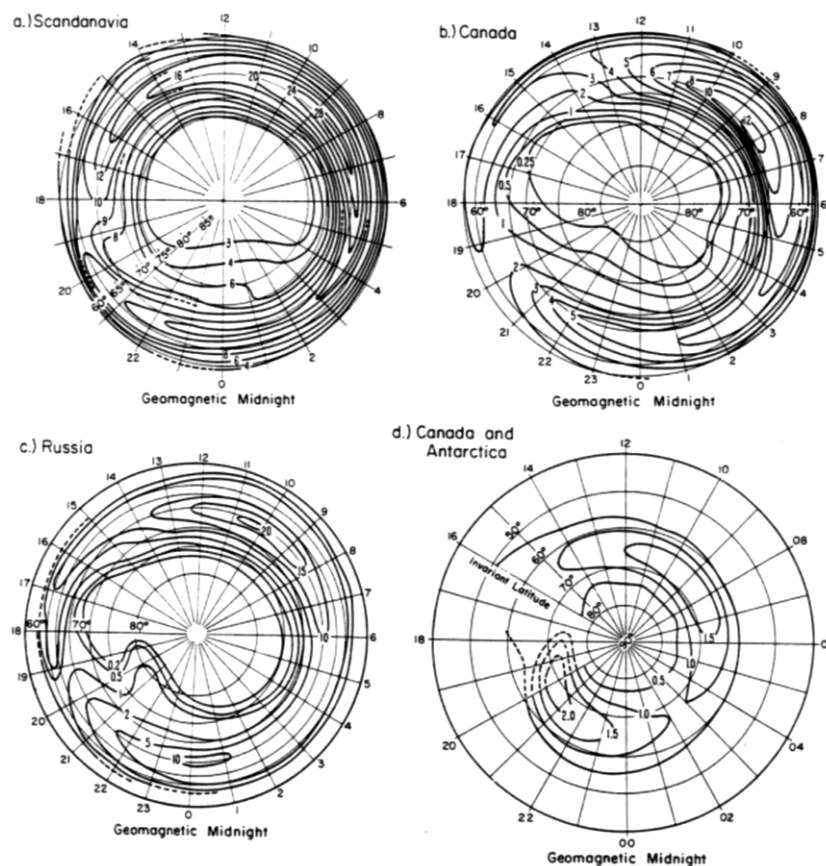


Figure 2.2: Occurrence of auroral absorption in latitude and time measured at several longitudes.

[From a] Holt *et al.*, 1961; b] Hartz *et al.*, 1963; c] Driatsky, 1966; d] Hargreaves and Cowley, 1967. [a] Shows the percentage of time that absorption exceeds 0.5 dB; [b] and [c] show the percentage of time that absorption equals or exceeds 1.0 dB and [d] gives the median intensity in dB. [Schematic from Hargreaves, 2009]

Usually, the diurnal occurrence shows two peaks, one close to magnetic midnight and the other before noon. Hargreaves, [1969] noted that differences arise due to the differing methods of compiling the statistics. The absorption oval covers several degrees of latitude centred between 64° and 68° magnetic latitude, a few degrees equatorward of the auroral oval [Hartz *et al.*, 1963; Basler, 1963; Driatsky, 1966; Hook, 1968]. A notable effect is the deep minimum in the afternoon [Hargreaves and Cowley, 1967]. Studies that employ direct particle precipitation measurements also demonstrate this pattern of dislocated ovals and local time variations [e.g. Hartz, 1971]. Enhanced geophysical activity shifts the absorption zone to lower latitudes, affecting the night sector more than the day [Basler, 1963; Driatsky, 1966; Hargreaves, 1966; Hook, 1968]. The diurnal pattern seen by a riometer is usually interpreted in terms of precipitation patterns fixed with respect to the Sun; however there is possibly a longitudinal effect due to the displacement of the Earth's dipole from the spin axis. This effect has been looked for in the statistics [Hartz *et al.*, 1963 and Driatsky, 1966] but the results are inconclusive.

2.2.2 The polar cap

The polar cap describes the region of the ionosphere that is enclosed within the auroral oval. This region plays a very substantial role in solar-terrestrial physics. One of the key observations of this region is that it exhibits different behaviour during Summer and Winter seasons. During Summer, the polar cap is under constant solar illumination whereas, during the winter the polar cap is in constant darkness. Consequently, in winter the ionospheric electron density of the polar cap is maintained by sources aside from solar photo-ionisation. The structure of the polar cap is dependent on the northward or southward orientation of the interplanetary magnetic field. After the mid-latitude region, the polar cap is regarded as the most benign for HF radio communications as propagation is usually undisturbed except for polar cap absorption (PCA) events [e.g. Milan 1996]. PCAs causes severe black-out over the whole HF spectrum across large regions of the polar cap and have durations from hours to days, but are less frequent events than auroral absorption, occurring

approximately once per month at solar maximum, and less often at solar minimum [Collins *et al.*, 1961]. PCA absorption is caused by intense enhancement of the D region electron density by solar proton events (SPEs), protons with energies greater than 1 MeV ejected from the Sun. These particles are confined to the polar cap, geomagnetic latitudes greater than $\sim 65^\circ$, by the terrestrial magnetic field [Holt, 1968; Davies, 1990]. PCA is further discussed in Section 2.8.

2.3 Geomagnetic and ionospheric storms

Geomagnetic storms are a consequence of shockwaves in the solar wind, produced by solar flares or coronal mass ejections (CMEs), or prolonged periods of coupling between the IMF and the magnetosphere. Geomagnetic storms can be identified by the characteristic variation they produce in disturbance storm time (D_{st}) [Matsushita, 1967]. The D_{st} index is an index of magnetic activity derived from a network of near-equatorial geomagnetic observatories that measures the intensity of the globally symmetrical equatorial electrojet. The typical variation includes the main phase, in which D_{st} falls rapidly below the pre-storm value, and the recovery phase, a slow return to quiet-time levels. The main phase is often preceded by a small, short-lived increase in D_{st} , the initial phase, produced by compression of the geomagnetic field by a shockwave in the solar wind. An abrupt change in magnetometer records at the start of a storm is known as a storm sudden commencement or SSC [e.g. Ritchie and Honary, 2006]. During geomagnetic storms, enhanced energy deposition in the auroral ionosphere, by precipitation and Joule heating, causes heating of the atmosphere and global modification of the neutral wind pattern. These changes have a direct influence on the ionospheric electron density, especially in the F region, which becomes perturbed from quiet-time values for hours or days during the so called “ionospheric storm”. In the F region, the effects are seen in the positive storm effect (increase of critical frequency) or the negative storm effect (decrease of critical frequency). Shock waves in the solar wind can be accompanied by energetic (MeV) solar protons ejected from the Sun during solar flares and CMEs. These protons, which produce polar cap absorption (PCA) events can stream ahead of the solar wind shock front

and so be incident on the Earth hours or days before the geomagnetic storm effects are felt.

2.4 Types of radio absorption

2.4.1 Cosmic noise absorption

Fundamentally, precipitating trapped particles can change the characteristics of the Earth's ionosphere by providing source for ionisation impact that can increase the electron number density in the ionosphere and consequently cause the absorption of radio waves. For cosmic noise absorption (CNA), radio waves of cosmic origin propagate through the ionosphere transmitting energy to the free electrons in the area, if the electrons collide with neutral particles, molecules or ions, this energy is absorbed in the collision instead of being re-radiated [Stauning, 1996]. Although CNA can be observed at higher layers of the ionosphere, it is to a large extent confined to the D region, this is because collision frequency is greatest at the D region as electrons are most likely to collide with neutrals there. This collision frequency is directly proportional to the electron temperature. Hence, heating in this region can affect absorption. Absorption due to precipitating particles is conveniently divided into two phenomena. Namely, auroral absorption and polar cap absorption (PCA). These are described in Sections 2.4.2 and 2.5. The two phenomena are fundamentally different in their characteristic time variations and geographic distribution. Auroral absorption is short lived, irregular and confined to an oval near to the auroral region, whereas PCA tend to last for several days and varies smoothly across the sunlit polar cap [Hargreaves, 1992].

Auroral absorption is an important indicator of the presence of fluxes of energetic electrons that deposit energy into the atmosphere while polar cap absorption demonstrates the massive effects that space weather can have on the ionosphere. Beside auroral and PCA, there are other types of absorption peculiar to the E and F region ionosphere [e.g. Stauning,1996] described in Section 2.6.

2.4.2 Auroral absorption (AA)

The phenomenon known as auroral absorption describes radio absorption occurring within a band of geomagnetic latitudes of about 60° to 75° . During the onset of a substorm (substorms are brief magnetospheric disturbances that occur when the interplanetary magnetic field turns southward, permitting interplanetary and terrestrial magnetic field lines to merge at the dayside magnetopause and energy to be transferred from the solar wind to the magnetosphere), there is associated absorption in the nightside auroral oval as a result of energetic electrons with energies of 10 to 100 keV. The most distinguishing character of auroral absorption is its temporal and spatial variability. Absorption is not random from minute to minute but occurs in events whose time of beginning, maximum absorption and end may be identified. While there is no general classification of AA that covers all events, some recognised types based on the different precipitation mechanism are sharp-onset absorption, slowly varying absorption and sudden commencement absorption [e.g. Hunsucker and Hargreaves, 1992; Richie and Honary, 2009]. The occurrence and magnitude of absorption is known to vary with local time, it is maximum in the late morning and before midnight.

2.4.3 Sharp-onset absorption (SOA)

SOA occurs near the magnetic midnight as a result of short burst of high energy precipitation, the so called splash precipitation. The events rise within a few minutes and lasts between tens of minutes to an hour. They often coincide with the beginning of substorm. The regions of absorption are often elliptical in shape, with an east-west-aligned major axis of typically 190 km and north-south extent of approximately 80 km [Hunsucker and Hargreaves, 2007].

2.4.4 Slowly varying absorption (SVA)

Slowly varying absorption occurs in the morning sector at about 0600-1200 magnetic local time (MLT). The duration is between 1 and 2 hours, injection of electron during the main phase of a substorm are trapped on field lines and begin to drift

due to combined effects of the gradients in the geomagnetic field and magnetospheric electric fields. Precipitation of these electrons into the morning sector occur due to small pulses in solar wind pressure, driving particle interaction [Kavanagh *et al.*, 2002]. Particles are of energies of 30-300 keV and are generally hardened during the drift to the dayside. This type of AA event is more spatially widespread than the SOA.

2.4.5 Sudden commencement absorption (SCA)

An enhancement in the solar wind dynamic pressure that compresses the dayside magnetosphere leads to an increase in the H-component of the Earth's geomagnetic field. Precipitation of normally trapped electrons in the range of 30-300 keV can accompany sudden commencement. This enhanced ionisation results at increase in radiowave absorption. An example of sudden commencement event is shown in Figure 2.3 for cosmic noise absorption at Kilpisjärvi. The sudden commencement started

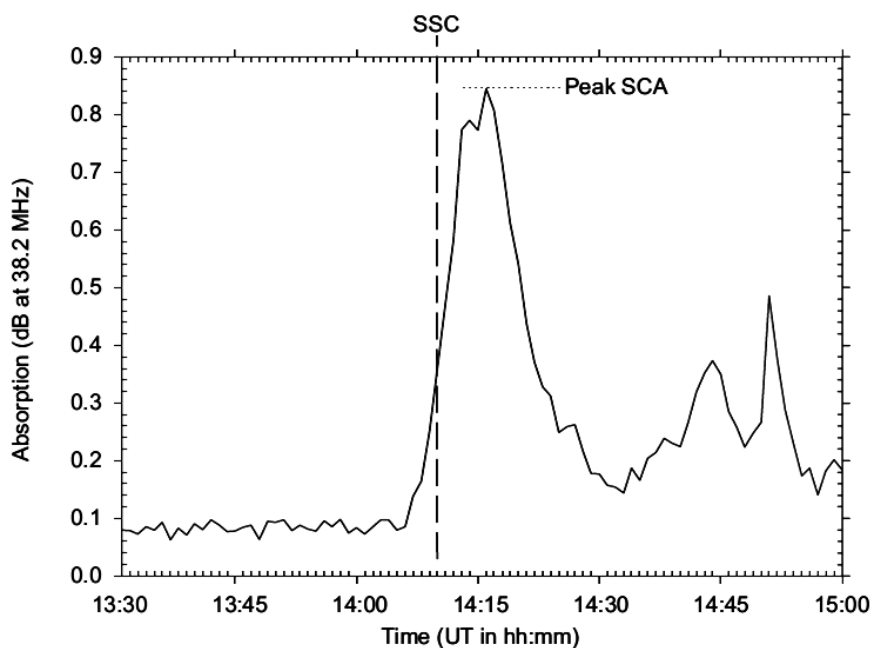


Figure 2.3: An example of absorption measurement from IRIS Kilpisjärvi due to sudden commencement on 3rd April, 2004. [From Ritchie and Honary, 2009].

at 14:10UT with a fast rise in absorption maximising at 0.8 dB few minutes later. SCA was first observed by Brown *et al.*, [1961] while Ortner *et al.*, [1962] observed

that absorption maximized near the central line of the auroral zone. Sudden commencement can occur both during night and day times [Ritchie and Honary, 2009], however, for SCA to occur during geomagnetically quiet times, the change in the Earth's geomagnetic field due to the solar wind shock must reach a certain threshold. [Wild, 2011; Osepian and Kirkwood, 2004].

2.5 Polar cap absorption (PCA)

PCA occur as a result of the eruption of solar X -ray flares that emit energetic (MeV) protons that reach the Earth. Although PCA occurrence are less frequent compared with auroral absorption event, when they occur the effect is more drastic and the intensity of absorption is higher (typically between 1 and 5 dB at 30 MHz). The duration is usually for several days (averagely more than 2 days). The occurrence of PCA has been identified to follow solar cycle variation. In a solar maximum year, there could be more than ten events and about one to three events during solar minimum [Hunsucker and Hargreaves, 1992]. Their occurrence could lead to high frequency (HF) communications “blackout” during which HF propagation is not supported by the ionosphere.

2.6 E and F region absorption

Stauning [1996] reviewed a number of types of absorption event including mechanisms for non-precipitation related absorption; e.g. F-region absorption due to low temperatures [Rosenberg *et al.*, 1993; Wang *et al.*, 1994; Nishino *et al.*, 1997], and electron heating absorption [EHA] from the E region during periods of high ionospheric convection [Stauning, 1984; Stauning and Olesen, 1989]. Both of the aforementioned event types result in much weaker absorption changes than a typical precipitation event [of the order of 0.5 dB for F region absorption]. Principally, there are two sources of precipitation that lead to enhanced cosmic radio noise absorption at high latitudes: the solar wind [and ultimately the Sun] and the magnetosphere.

2.7 Chapter summary

This chapter provides background to radio waves absorption in the ionosphere. The Appleton-Hatree equation of refractive index is presented and discussed as it is used to describe the absorption of charged particles through an ionised medium. This describes the dispersion relationship of radio waves in plasma and in this case the ionosphere. From the Appleton-Hatree equation, it has been shown that changes in ionospheric parameters (majorly electron density but also temperature) can result at the increase in the non-deviative absorption of radio waves. The majority of this absorption occurs in the lower portion of the ionosphere (i.e. D layer). Also, radio wave absorption and the various mechanism of each type of absorption event is discussed. This thesis is primarily concerned with the prediction of radio waves absorption, Chapter 4 represent statistical model based on the epsilon parameter [i.e. energy coupling function] and a review of existing absorption prediction models. The drivers of the geomagnetic storms [i.e. coronal mass ejections and solar flares] and their effect on radio absorption models is given in Chapters 5 and 6.

Chapter 3

Instrumentation and geomagnetic indices

3.1 Introduction

The theoretical foundation for the use of radio waves absorption observations as diagnostics of the ionospheric plasma condition and examination of the precipitation of high-energy charged particles into the upper atmosphere are well established [e.g. Little and Leinbach 1958; 1959; Rawer, 1976; Detrick, 1990; Stauning; 1996]. Techniques that rely on the operation of transmitters to generate the probing signals [e.g. attenuation of reflected continuous radiowave signals, attenuation of reflected pulsed radiowave signal and attenuation of transmitted signal] have been utilised for detecting radiowave absorption. These methods are influenced by effects such as focusing, scintillation and scattering other than absorption processes along the signal path and by effects from variable match of polarisation, phase and frequency between the transmitter and receiving system [Stauning,1998]. Utilising cosmic noise absorption measured by relative ionospheric opacity meters [riometers] yields an improvement on the previous methods as it is fairly reliable and simple.

The riometer was developed as a means to regularly measure the ionospheric absorption [e.g. Little and Leinbach,1959]. This is based upon the principle of monitoring cosmic radio noise absorption as developed by previous workers [e.g. Shain and Higgins, 1954 ; Mitra and Shain, 1953; and Blum *et al.*, 1954]. Although the riometry technique has some limitations [discussed in Section 3.2.2]. For riometry purposes, the average height of the absorbing layer is usually considered to be 90 km.

Riometers can be further classified as wide beam or imaging riometers. Wide beam riometers consist of a simple antenna system with an azimuthally symmetric radiation pattern that enables a wide field of view. They however do not have imaging capabilities. Hence, they do not provide information on both the spatial structure and dynamics within their field of view. Nevertheless, they are useful for a general overview of the current state of the ionosphere and are relatively inexpensive to build and operate. Imaging riometers offer improvements on wide beam counterpart in that they allow higher spatial resolution and observation of the viewing area [e.g. Honary *et al.*, 2011]. Imaging riometers operate based on the noise balancing technique. This is further discussed in Section 3.2.

3.2 Imaging riometer for ionospheric studies

3.2.1 Riometry

Riometers operate passively by constantly monitoring the background cosmic noise from the sky. Because this method entails radio wave propagation through the ionosphere, the frequency must be greater than the critical frequency (f_oF2). Measurement of the received power is accomplished by rapid switching between receiver input and a local noise source. The current passing through the noise diode is constantly altered to keep the power of the two noise sources equal. The power of the local noise source is proportional to the current passing through it. Hence, recording of the current is only required for the measurement of the antenna power [Little and Leinbach, 1958]. The procedure is such that the receiver works in a way that measurements are not affected by variations in the received gain.

Absorption measured in dB is defined as the log ratio of the received power with reference to a day where no absorption has occurred. This is expressed as:

$$A = -10 \log \left(\frac{P}{P_0} \right) \quad (3.1)$$

P and P_0 are the received power and power in the absence of absorption respectively. Due to the non-uniform nature of cosmic noise power across the sky, it is necessary to create quiet day curves (QDC) which represent the variation of cosmic noise power

in the absence of absorption over the course of a sidereal day. Due to solar radiation in the D -region, QDC are required to be regularly created. Browne *et al.*, [1995] describe how to create QDC; data are arranged into 14 sidereal days, the median is then taken for 10 minutes periods for each day. After this, the mean of the second and third highest values is calculated. Interpolation between the 10 minute values allows calculation of 1 second resolution of the quiet day values. Figure 3.1 shows a typical quiet day curve.

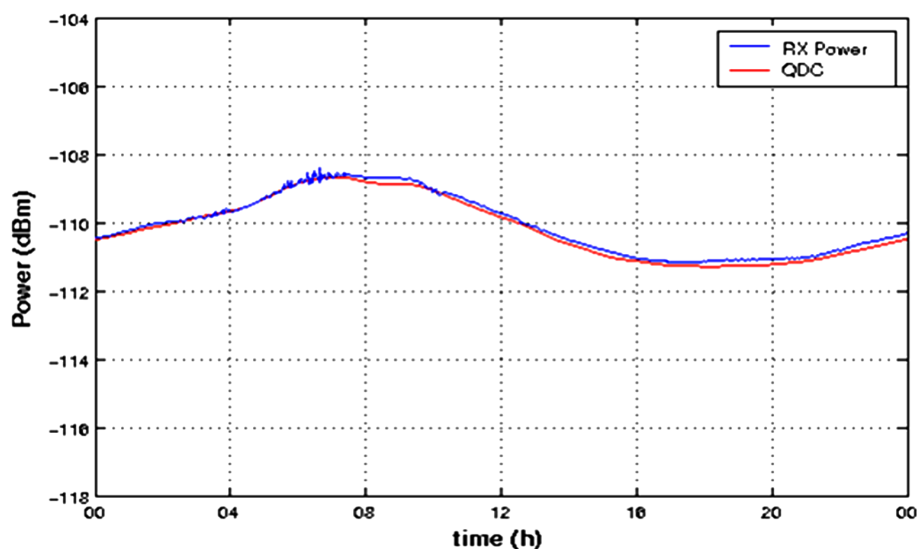


Figure 3.1: A typical quiet day. Blue line: Received power, red line: length of 14 day period during which the quiet day occurs

Riometers usually operate within a frequency range of 30-50 MHz. As previously mentioned, the most common form of riometer uses a broad or wide beam antenna with beamwidths of the order of 60 degrees. This means that small spatial scale details of the absorption variation are lost since this method integrates over a large portion of the sky ($\sim 8500 \text{ km}^2$ at 90 km altitude). Narrow beams (10 to 20 degrees) can probe these small-scale features, but the area of the ionosphere that is monitored is much reduced. In the 1990s, the development of an imaging riometer [Detrick and Rosenberg, 1990] provided the ability to observe small-scale features with narrow beam width as well as imaging a portion of the sky. First imaging riometer was deployed at the south pole by the University of Maryland, USA. This system operates as a fast-scan multiple beam instrument to examine the

entire ionospheric sky to 45 degrees from the zenith. Several of these systems have now been deployed including one operated by Lancaster University as part of the global riometer array (GLORIA) network. Recently [e.g. Honary *et al.*, 2011] a new generation digital imaging riometer systems was developed by Lancaster University. This new type of beamforming utilises field-programmable gate arrays [FPGAs] to produce tools for remote system testing. This class of riometers can obtain improved spatial resolution. The FPGA method is essentially useful in remote locations such as the Arctic and Antarctic. Also, advances in riometry have led to the implementation of the first Fourier-based interferometric riometry technique for measuring electron density induced ionospheric opacity at VHF radio frequencies [Mckay *et al.*, 2015]. Unlike multibeam riometers, which form discrete beams on the sky, the interferometric technique permits all-sky sampling of incoming cosmic radio noise emissions resulting in a spatially-continuous radiogram of the entire sky. The map of the received power at each time may then be compared to the equivalent map from a “quiet day”, allowing the morphology of ionospheric absorption of cosmic radio noise to be ascertained. In this thesis, IRIS data from the central beam was utilised.

3.2.2 Limitations of the riometer

Riometers provide measurements of absorption that would be impracticable on HF systems such as ionosondes. However, there are various limitations in the riometer technique:

- (i) The definition of the QDC is not uniquely defined and its calculation may vary widely between institutions [e.g. Foppiano and Bradley, 1985; Krishnaswamy, 1985].
- (ii) Riometers can only measure absorption along a trans-ionospheric path and cannot measure the height profile of specific absorption.
- (iii) In the majority of cases, the riometer beam is relatively wide – typically 50-60° between -3 dB points, which projects to approximately 100 km at 90 km altitude (which is approximately the height of maximum specific absorption).

The absorption measured by wide-beam riometers is an average across the beam and a correction is required to account for non-vertical propagation at the edges of the beam (i.e. where the obliquity factor is greater than unity). This correction requires an estimate of the beam gain pattern, which may vary with conditions local to the antenna (e.g. changes to ground plane conductivity after rain, or changes in the dielectric constant due to snow layers).

3.2.3 Imaging riometer for ionospheric studies (IRIS) Kilpisjärvi

Investigation into energetic particle precipitation has been achieved through the use of wide beam and imaging riometers [e.g. IRIS] which monitor the absorption of cosmic radio noise, a parameter that is directly related to the electron density in the D layer. The imaging riometer for ionospheric studies (IRIS) [Browne *et al.*, 1995] is located at Kilpisjärvi in northern Finland (69.05° N, 20.79° E). It began operations in September 1994 and is operated by the space plasma environment and radio sciences group of Lancaster University in collaboration with the Sodankylä Geophysical Observatory (SGO), Finland. IRIS samples the cosmic radio noise at 38.2 MHz (a protected frequency for astronomy) and consists of an imaging array and a single, wide beam riometer. The system uses 64 circularly polarized cross dipole antennas grouped in a square array and separated by half a wavelength (Figure 3.2).

The signals from each row of eight antennas are phased by Butler matrices and produce 49 narrow beams of width between 13° and 16° (Figure 3.2). The outputs are fed into 7 riometers through the use of time division switching. The whole array is sampled every second and switching is arranged so that each second is divided into 8 time slots. The eighth time slot is used to record the output from the co-located wide beam antenna.

3.3 Magnetometers

In order to provide a more complete picture of geomagnetic conditions and track any changes, ground based magnetometers can be used to complement in-situ measurements made by satellites. Chains of magnetometers situated around the globe



Figure 3.2: IRIS phased array during summer (top panel). Bottom panel: IRIS winter scene when snow increases the height of the ground plane [Browne, 1994]

can be used to identify the signature of geomagnetic activity. Magnetometers at high latitudes are also used to identify magnetic activity driven by reconnection between the magnetosphere and the IMF. A high latitude magnetometer chain including the danish meteorological institute (DMI), international monitor for auroral geomagnetic effects (IMAGE) and canadian array for realtime investigation of magnetic activity (CARISMA) covers the area from western Canada to eastern Europe. Low and mid latitude magnetometers are able to investigate global scale geomagnetic field effects. They are somewhat isolated from the variability present at high latitudes [Tsunomura, 1998; Longden, 2007]. The sub-auroral magnetometer network (SAMNET) chain provides coverage of the mid latitude geomagnetic field across Europe. Data from these magnetometer stations can be used to identify the timing and location of substorm onset and signatures of particle precipitation (Takahashi *et al.*, 1995).

3.4 Satellites

Direct measurements of key solar wind parameters (solar wind velocity, the strength and orientation of the interplanetary magnetic field (IMF), ion and electron number densities) are possible through satellites. Measurements from geosyn-

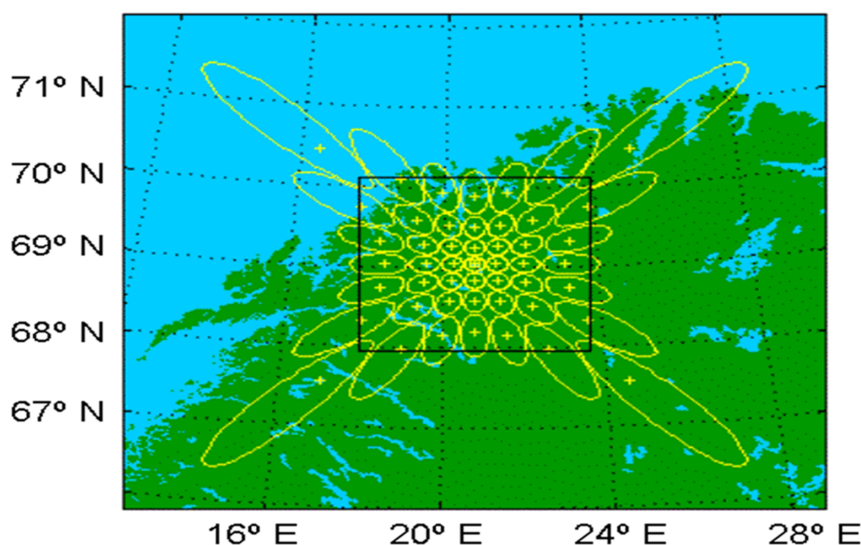


Figure 3.3: Beam projection of IRIS at 90 km altitude. The contours define the -3 dB points and the black square shows the calculated field of view used in the IRIS images.

chronous operational environmental satellite (GOES), the advanced composite explorer (ACE) and the comprehensive solar wind laboratory for long-term solar wind measurements (WIND) have been used in this work.

3.4.1 Solar wind measurements (ACE and WIND)

The ACE [Advanced composition explorer] spacecraft was launched in August 1997, it is located at the first Lagrangian point (L1) approximately 1.5 million km from the Earth in the Sun-Earth plane. ACE includes the solar wind electron proton and alpha monitor (SWEPAM) instrument, [McComos *et al.*, 1998] used to sample low energy solar particles, and the magnetic field monitor (MAG) instrument [Smith *et al.*, 1998]. The fixed position of ACE provides a consistent data set for monitoring the solar wind conditions during periods of geomagnetic activity.

3.4.2 WIND satellite

WIND, [Comprehensive solar wind laboratory for long term solar wind measurements] is a global geospace science (GGS) satellite of NASA, launched on November 1, 1994. It has since provided measurements of solar wind and IMF parameters. The original orbit of WIND was designed as a sunward, multiple lunar swing-by with the

spacecraft occasionally travelling up to $250 R_E$ into the solar wind at apogee whilst at other times reaching less than $100 R_E$. This allowed measurements to be taken in a large portion of the upstream solar wind. In 1998, WIND spent several months at the L1 point calibrating its instruments with ACE, before undertaking a series of petal orbits with dimensions of $10 \times 80 R_E$, outside of the ecliptic plane. WIND carries a solar wind experiment (SWE) to provide bulk velocity and density data, as well as a magnetometer experiment (MFI).

3.4.3 GOES (Geosynchronous operational environmental satellites)

NOAA (national oceanic and atmospheric administration) operates a series of satellites known as geosynchronous operational environmental satellites (GOES). These carry a package of instruments designed to monitor space weather variations. There are three main components measured by the space environment monitor (SEM) system: X -rays, energetic particles and magnetic fields. The majority of observations presented in this thesis are from the GOES-8 satellite that was launched in 1995. This is the first of the GOES satellites that is “3-axis stabilised” rather than spin stabilised. This Section concentrates on brief descriptions of the X -ray and energetic particle sensors carried on board GOES-8.

The X -ray sensor (XRS) measures the solar X -ray flux for the 0.5–4.0 and 1.0–8.0 Angstroms wavelength bands. The two bands allow the hardness of the spectrum to be estimated. Observations from XRS provide a means for detecting the start of solar X -ray flares, though occasionally there is a low channel response to either energetic particles or X -ray production from precipitation of energetic particles. The EPS instrument measures energetic particles, a series of solid-state detectors with pulse-height discrimination that measures proton, alpha particle and electron fluxes. There are seven proton channels, the lowest energy (P1) responds to primarily trapped outer-zone particles; the energies are given in Table 3.1. P2 occasionally responds to trapped particles during magnetically disturbed periods. However the higher channels are sensitive only to fluxes originating outside the magnetosphere. The proton data provided by NOAA is in two forms: integral and differential fluxes.

Table 3.1: Lists of the GOES data energy channels supplied by NOAA/SEC

Channel	Differential (P)	Integral (I)
1	0.6-4.2 MeV	> 1 MeV
2	4.2-8.7 MeV	> 5 MeV
3	8.7-14.5 MeV	> 10 MeV
4	15-44 MeV	> 30 MeV
5	39-82 MeV	> 50 MeV
6	84-200 MeV	> 60 MeV
7	110-500 MeV	> 100 MeV

3.5 Geomagnetic activity and indices

A geomagnetic storm (see Section 2.4) describes the prolonged period of geomagnetic disturbance. By definition, geomagnetic storms refer to the temporary disturbance of the Earth's magnetosphere caused by a solar wind shock wave or cloud of the magnetic field which interacts with the Earth's magnetic field. The level of energy transfer from the magnetosphere to the ionosphere does not remain constant but is dependent on the efficiency of coupling between the IMF and the magnetosphere. During periods of enhanced loading and unloading of the magnetosphere, currents flowing in the magnetosphere and auroral ionosphere produce magnetic disturbances measured by ground magnetometers. The level of disturbance or geomagnetic activity is quantified by several indices. Each index highlights different aspects of the disturbance. For example, the three-hour resolution planetary indices K_p and A_p give an indication of the global level of geomagnetic activity, determined from mid-latitude magnetometer stations. AE, AU and AL, the one-minute resolution auroral indices, measure the level of disturbance produced by currents flowing in the auroral ionosphere and are determined by a chain of magnetometers located at auroral latitudes. The storm disturbance index (D_{st}) is measured with one-hour resolution and gives the change produced in the equatorial magnetic field by the enhancement of the ring current. This is because the ring current is enhanced dur-

ing geomagnetic storm periods. For detailed description of geomagnetic indices see Kivelson and Russell [1995, page 451].

Conclusively, solar wind based satellites provide measurements of the IMF and changing particle speeds that interact with the magnetosphere. Thus the history of events can be traced from the solar wind down to the ionosphere. Analysis of some of the measurements will be given in successive chapters.

Chapter 4

Prediction modelling of radio auroral absorption: an empirical relationship with the epsilon parameter

4.1 Introduction

The discovery of the phenomenon known as auroral absorption (Section 2.7) by Appleton *et al.*, [1933] prompted the development of auroral absorption prediction models. Ever since the prediction quest started, there has been gradual progress on improving these models as a result of improved understanding on previously made assumptions, development of more efficient equipment and availability of data. On previous assumptions, incipient auroral absorption prediction models [e.g. national bureau of standards (NBS) Circular, 1948; Vladimirov, 1969; Jelly, 1970] assumed that the geographical expanse of auroral absorption is coincident with the visual auroral zone. However, it was soon realised that such a relationship was difficult to establish. Afterwards, the international radio consultative committee [CCIR, 1975] proposed a technique of comparing measured field strength data for auroral and non-auroral paths. However, auroral absorption estimates given in this way are dependent on the prediction procedure adopted to specify all other system loss factors. Though this procedure was relatively easy in its application, it does not account for the dependence of auroral absorption on solar cycle, radio-frequency or geomagnetic longitude [Foppiano and Bradley, 1983]. The proposition of magneto-ionic theory by Ratcliffe [1959], made it possible to compute absorption based on the height distribution of electron concentration and the neutral atmosphere, but the limitation

is that the magneto-ionic theory may not be able to quantify the electron concentration in the D and lower E regions. The methods discussed above were useful in assimilating absorption estimation. However they did not explain the morphology of absorption.

On instrument and data, the invention of radio ionospheric opacity meters (riometers) by Little and Leinbach [1959] provided the possibility of continuous measurement of absorption and besides serves as an aid in studying the spatial features of auroral absorption. With the availability of riometer data, prediction models such as those proposed by Hartz *et al.* [1963], Hargreaves [1966], Herman and Vargas-Vila [1972], and Foppiano [1975] all used the monthly median values of hourly absorption to determine the percentage of times that absorption exceed some thresholds (usually termed Q . e.g. $Q1$ for a threshold of 1 dB, $Q0.5$ for a threshold of 0.5 dB absorption etc.). As part of their coupling parameters, they mostly utilised geophysical indices such as (K_p, A_p) and sunspot number. However, advances in this study area have identified a degree of inconsistency in models that use geophysical indices and sunspot number as inputs [Foppiano 1985; Hargreaves, 2009].

Some studies [e.g. Foppiano and Bradley, 1985, Kavanagh *et al.*, 2004, Senior *et al.*, 2002, and Hargreaves 2009] established statistical relations between solar wind parameters (e.g. flow speed, IMF orientation, solar wind density, z -component of the IMF and the electrical conductance in the auroral zone) and auroral radio absorption. While relating their studies and observations to the prediction of radio absorption, they posited that utilising a combination of solar-wind parameters as coupling coefficient for auroral absorption may lead to an improved predictive outcome, particularly because solarwind parameters are now available in online repositories and could be found in real time. Following their suggestion, this study identified energy coupling functions (see Table 4.1) as a coupling coefficient for absorption. Energy coupling functions are functions that represent the rate of the solar-wind energy input into the Earth's magnetosphere. Although various coupling functions have been proposed, the Akasofu epsilon parameter has been widely used [Aoki, 2005] perhaps

because the epsilon parameter is first proposed. The variable composition of other coupling functions are very similar to the epsilon parameter.

The Akasofu solar wind-magnetosphere coupling function (otherwise termed epsilon parameter) is derived from the combination of solar wind parameters such as solar-wind velocity, total IMF (B) and clock-angle [e.g. Perreault and Akasofu, 1978]. The epsilon parameter estimates energy transfer via the solar wind into the magnetosphere and the unloading processes of the magnetosphere. The expression relates solar wind energy transfer to the magnetosphere based on the input energy flux [$V \times B^2$] and magnitude of the orientation of the IMF. This study has through statistical analytics presents an hourly empirical relationship of auroral absorption and the epsilon parameter and based on this relationship examines epsilon as a predictor for absorption.

Empirical modelling is commonly used to determine structures by observed relationship among experimental data. Usually, this method is used to develop relationships for forecasting and describing trends. Over the years, a number of empirical and physics-based models studying various parts of the solar-terrestrial environment have evolved. Examples include the Wang-Sheeley-Argge (WSA) model that predicts two important parameters required for predicting geomagnetic activity, i.e. the background solar wind speed and the interplanetary magnetic field (IMF) polarity at Earth, the adaptive linear prediction of radiation belt electrons model [Rigler *et al.*, 2010], the magnetosphere and space weather prediction model [Li *et al.*, 2002], the linear prediction filter analysis of relativistic electron properties model [Baker *et al.*, 1990]. In recent times, there has been remarkable progress towards coupling these empirical models from the Sun to the Earth together [e.g. Baker *et al.*, 2004]. Previously, empirical models were used to observe the Sun, specify the solar boundary conditions, follow the subsequent solar wind propagation to 1 astronomical unit (1AU), and thereby forecast solar wind parameters such as mass density (ρ), speed (V), and magnetic field strength (B). With such parameters forecasted in the vicinity of Earth's dayside magnetopause, it is further possible to predict quantities such as geomagnetic indices (e.g. A_p , K_p , or D_{st}), magnetic field fluctuations at mid and

high-latitudes, global magnetospheric field configurations, and the relativistic electron fluxes in Earth's radiation belts. However, there are still significant challenges in the Sun–Earth connections modelling. There remains the need to improve the basic building blocks of models, to develop suitable code-coupling strategies that can ingest and assimilate appropriate data sets, and ultimately provide accessible specification and space weather forecast products that meet users needs [Baker *et al.*, 2007]. This study will utilise the predicted model at 1AU to provide values of auroral absorption in the lower region of the ionosphere.

4.2 Auroral absorption prediction models

Auroral absorption and its sub-categories have been discussed in Section 2.7. Radio absorption observations have been used as diagnostics of the ionospheric plasma conditions and for the examination of the precipitation of high-energy charged particles into the upper atmosphere. The study of auroral radio absorption commenced over eight decades ago when discovered by Appleton, Naismith and Builder [1933]. Since discovery, more studies have identified its characteristics such as the location of the auroral zone, auroral motion, the spatial and temporal distribution of auroral absorption, general pattern of auroral particle precipitation and their variation with geomagnetic activities. Stauning [1994] highlighted qualities such as precursor to the occurrence of auroral absorption, causes, estimated duration and intensity were highlighted. However, predicting the magnitude of auroral absorption is a challenge, because of its high variability. Previous works, [e.g. Agy, 1972; Foppiano and Bradley, 1983; Hargreaves 2009] have all resolved that while precision prediction of auroral absorption may be difficult, predicting the likelihood of occurrence and magnitude at some location based on magnetic latitude and local time should be possible. This deduction has been valuable to the methodologies subsequently utilised in the prediction quest. Previous workers [Agy, 1972; Herman and Vargas-Villa, 1972; Foppiano, 1975; Vodka *et al.*, 1978, Foppiano and Bradley 1984, 1985] have all proposed prediction models using different choices of input parameters. These works have in general utilised statistical approaches due to the high variability of auroral absorp-

tion; they have mostly used riometry technique (see Section 3.1) and suggest the use of parameters such as the geographical longitude and latitude of the riometer station, time history and geomagnetic activity factors as the building blocks of a prediction model. Using solar activity factor (e.g. sunspot number) as input in a prediction model has been discovered to be somewhat unreliable. For example, Foppiano and Bradley [1983] model showed some relationship between sunspot activity and geomagnetic activity within some years but the relationship was inconsistent for other years. Some of the previous models were based on geomagnetic indices [e.g. Vodka *et al.*, 1978, Foppiano and Bradley 1984, Greenberg and Labelle, 2000], however, Kavanagh *et al.*, [2004] in highlighting the statistical dependence of auroral absorption on geomagnetic and solar wind parameters observed the possibility of low absorption at periods when geophysical activity is high. Hence, the global models of absorption based on only K_p values are also somewhat unreliable, whereas most of the previous prediction models used K_p values as input parameter. Hargreaves [2009] suggested that since one of the obvious characteristics of auroral absorption is that it occurs in bursts, which has a clear relation to the occurrence of substorms, knowledge of event properties and their connection to substorms could have some predictive value. It may be possible to predict the incidence of events from other indicators, or the duration of the activity once begun. While Agy [1970] proposed that the occurrence of auroral absorption is frequent enough for median absorption to be useful, Kavanagh *et al.*, [2004] observed that median absorption varies strongly with the solar wind speed and demonstrated strong variation with the z -component of the IMF, this in a way informed on the possibility of making predictions based on the combination of more than one solar wind parameters as adopted in this work. The effect of the solar wind velocity and IMF on absorption is given in Section 4.2.1.

A recent work towards the prediction of absorption is the web based D region absorption prediction release 2 (DRAP2). The first version of the DRAP model addressed HF absorption due to solar X-ray flares which primarily affect low and middle latitudes on the sunlit side of the Earth. The DRAP model is based on precipitation due to protons and not electrons. However, Bailey [1955] showed that for

similar energies, it is the electrons that dominate the absorption in the D region. Eather and Burrows, [1966] used H-emission observations from the ground to indicate that the contribution of ionisation from protons to auroral absorption was negligible. Satellite observations [e.g. Hargreaves and Sharp, 1965] have found that protons usually carry less than 10 % of the total precipitating energy. Riometer absorption as reported in this work is primarily due to electron precipitation. Since absorption is highly dependent on the population of energetic particles in the magnetosphere, in this study, we perform a post-event correlation analysis of riometer absorption using Akasofu epsilon parameter for the coupling coefficient. The epsilon parameter as proposed by Akasofu and Perrault [1978] consists of a combination of solar wind parameters (e.g. velocity, IMF and clock angle) and is discussed in Section 4.3. Solar-wind parameters are from the OMNI dataset repository.

4.2.1 The effect of solar wind on absorption

The solar wind and the interplanetary magnetic field (IMF) are the main drivers of geomagnetic activity. Therefore, variations in their condition can have a notable effect on absorption. Kavanagh *et al.*, [2004] in their statistical study looked at

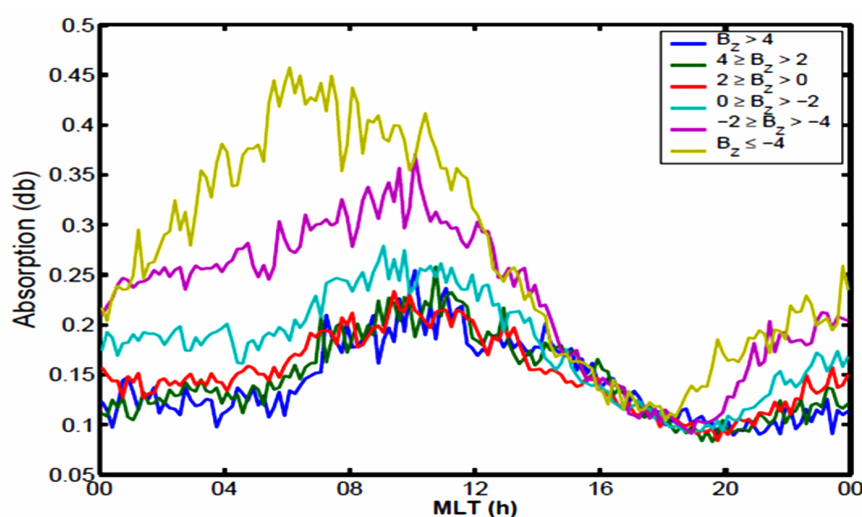


Figure 4.1: 10-min averaged absorption binned by IMF B_z . A northward IMF does not affect the absorption, whereas increasingly negative B_z increases the level of absorption during the night and morning sectors. [From: Kavanagh *et al.*, 2004].

the average absorption as a function of magnetic local time (MLT) during differing

levels of solar wind velocity and z -component of the IMF. Figure 4.1 shows 10-minute averaged absorption from the zenithal beam of IRIS at Kilpisjärvi from 1995 to 2001 under varying north-south IMF conditions. Under northward IMF ($+ve B_z$), the average absorption profile does not vary significantly based on the strength of the magnetic field whereas for $-ve B_z$, in general, the absorption increases as the IMF becomes stronger in the southward direction. However, the minimum in the local evening sector [$\sim 1500 - 1800$ MLT] is not affected by the strength of the IMF. In addition to the peak in the average absorption in the local morning increasing with increasingly southward IMF, the peak is also shifted to an earlier local time.

Also, Figure 4.2 shows 10-minute averaged absorption from the zenithal beam of IRIS Kilpisjärvi from 1995 to 2001 at times with different solar wind velocity. Averaged absorption appears to be directly proportional to the solar wind velocity except at the time of minimum in local time evening sector.

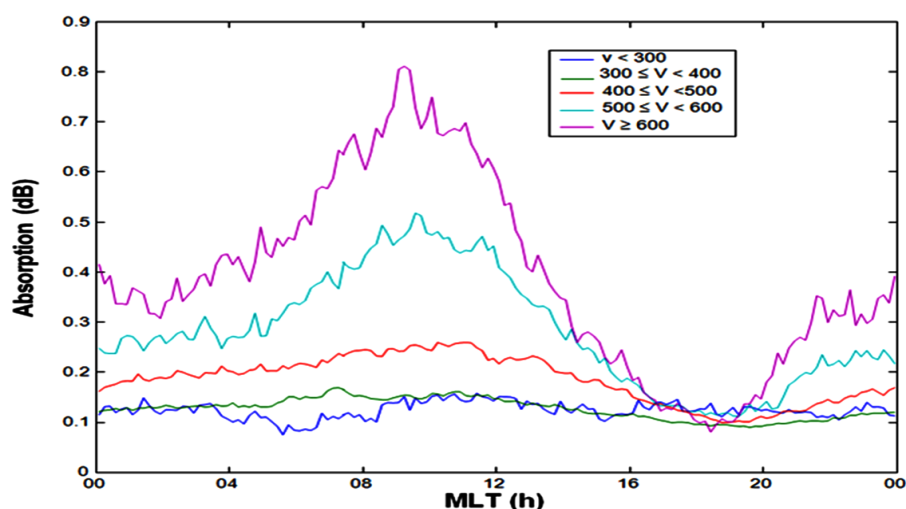


Figure 4.2: Magnetic local time variation of absorption in the zenithal beam for the five ranges of solar wind speed [From: Kavanagh, 2000].

Figure 4.3 below shows the variation of CNA with epsilon parameter in UTC.

Epsilon variation with CNA is clearly seen as from the threshold of 6×10^{12} W and above. This epsilon threshold corresponds to the range of value that causes substorms as reported by Hargreaves [1992].

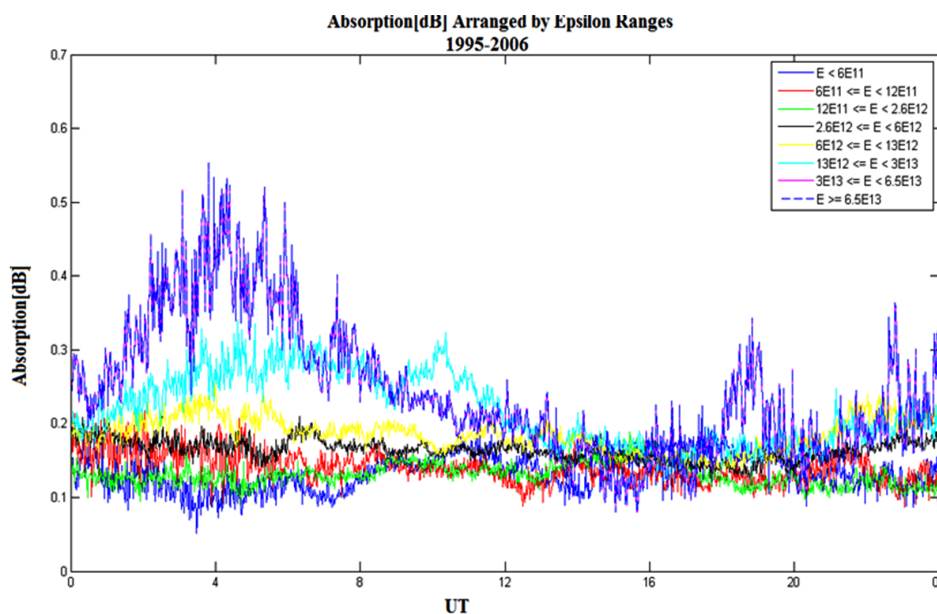


Figure 4.3: Variation of zenithal beam absorption in universal time based on epsilon ranges.

4.3 Energy coupling between the solar wind and the magnetosphere

The relationship between the solar wind and the magnetosphere is such that the solar wind interacts with the magnetosphere and the magnetosphere reacts to this interaction. The solar wind impinging on the magnetosphere creates stress on it and enhances the transport of energy into the magnetosphere. This process controls the major energisation events within the magnetosphere from smaller-scale disturbances ‘substorms’, to large scale ‘storms’. The coupling between the solar wind and the magnetosphere is strongest when their magnetic fields reconnect in regions of nearly opposite directions. Russell [2010] explains this reconnection as occurring on the sub-gyroscale where the ions and eventually the electrons encounter magnetic structure that demagnetises the charged particles in such a way that they no longer are tied to the magnetic field rather they drift across it. This process allows field lines from different plasma regimes to connect.

In studying the solar wind dynamo, Perreault and Akasofu [1978] and Akasofu [1979] found an interplanetary quantity that both correlates well with magnetic storms, and also with individual magnetospheric substorms. The quantity is referred

to as the energy coupling function between the solar wind and the magnetosphere (epsilon parameter). Although, after this derivation, other coupling functions have been proposed (Table 4.1).

Table 4.1: Some proposed coupling functions and references

No.	Name	Coupling Function	Reference
1	I_B	VB_s	Burton <i>et al.</i> , [1975]
2	ε	$VB^2 \sin^4\left(\frac{\theta}{2}\right) l_0^2$	Perreault and Akasofu[1978]
3	E	$VB_T \sin^2\left(\frac{\theta}{2}\right)$	Lee [1979]
4	I_V	$n^{\frac{1}{6}} V^{\frac{4}{3}} B_T \sin^4\left(\frac{\theta}{2}\right)$	Vasyliunas <i>et al.</i> , [1982]
5	I_N	$V^{\frac{4}{3}} B_T^{\frac{2}{3}} \sin^{\frac{8}{3}}\left(\frac{\theta}{2}\right)$	Newell <i>et al.</i> , [1982]
6	I_W	$VB_T \sin^4\left(\frac{\theta}{2}\right)$	Wygant <i>et al.</i> , [1983]
7	I_{SR}	$P^{\frac{1}{2}} VB_T \sin^4\left(\frac{\theta}{2}\right)$	Scurry and Russell [1991]
8	I_{TL}	$P^{\frac{1}{2}} VB_T \sin^6\left(\frac{\theta}{2}\right)$	Temerin and Li [2006]
9	P	$V^{\frac{4}{3}} B_T^{\frac{2}{3}} \sin^{\frac{8}{3}}\left(\frac{\theta}{2}\right)$	Newell <i>et al.</i> , [2007]

The Akasofu epsilon parameter is based on the admittance of Poynting flux into the magnetosphere. Epsilon parameter correlates best with absorption among the coupling functions hitherto proposed.

The Poynting flux (S) is given by:

$$\mathbf{S} = \frac{\mathbf{E} \times \mathbf{B}}{\mu_0} \quad (4.1)$$

Where E is the interplanetary electric field, B the interplanetary magnetic field and μ_0 the permeability of free space.

The effective cross-section in which Poynting flux enters the magnetosphere is:

$$4\pi \sin^4\left(\frac{\theta}{2}\right) l_0^2 \quad (4.2)$$

θ is the IMF clock angle, calculated from

$$\tan \theta = \left(\frac{B_Y}{B_Z} \right) \quad (4.3)$$

is the projection of the polar angle of the IMF onto the $Y - Z$ plane in the solar-magnetospheric (GSM) coordinates and l_0 is the effective length of the reconnection area (an empirical parameter approximated to 7 Earth radii).

Alfven [1950] showed that in idealised plasma, ions and electrons move along magnetic field lines under magnetohydrodynamic [MHD] conditions

$$E = -\underline{V} \times \underline{B} \quad (4.4)$$

V is the steady bulk flow plasma and B is the magnetic field. Multiplying (4.1) and (4.2) and substituting the electric field E from (4.4) gives the epsilon parameter in the SI unit as

$$\varepsilon = \frac{4\pi}{\mu_0} \sin^4 \left(\frac{\theta}{2} \right) l_0^2 V B^2 \text{ (Watts)} \quad (4.5)$$

V is the upstream solar wind velocity; ε is the epsilon parameter, which transfers the power. The CGS-Gaussian unit representation of the epsilon gives

$$\varepsilon = V B^2 \sin^4 \left(\frac{\theta}{2} \right) l_0^2 \text{ erg/s} \quad (4.6)$$

$V B^2 l_0^2$ in (4.6) is mostly referred to as the driving term while $\sin^4 \frac{\theta}{2}$ is the merging term. Magnetic energy reaching the magnetosphere per unit time is proportional to the driving term and the merging term represents the fraction of the power coupled into the magnetosphere. It gives a gradual transition between full coupling when IMF is fully southwards ($\sin^4 \left(\frac{\theta}{2} \right) = 1$) and zero coupling when the IMF is fully northward ($\sin^4 \left(\frac{\theta}{2} \right) = 0$). Substorms occur most frequently when B_z is southward, also the beginning of substorms often coincide with a southward turning of the IMF [Tsurutani and Gonzalez, 1997]. Epsilon exceeding 10^{11} Watt is likely to cause a substorm and during big storms epsilon may exceed 10^{13} .

From Table 4.1, it would be observed that most of the proposed coupling functions comprise of quite similar solar wind components (i.e. solar wind velocity (V), the magnetic field (B, BT) clock angle θ). Some others contain proton number density (n) and solar wind dynamic pressure (P).

4.4 Methodology

This study examines the correlation of the epsilon parameter measured at the Earth's L1 Lagrangian point with absorption measured on the IRIS riometer at Kilpisjärvi (69.04°N, 20.79°E). Solar-wind parameters (velocity and IMF) are as recorded in the OMNI dataset repository. The code computation yields the clock angle as the tangent of the y and z components of the IMF.

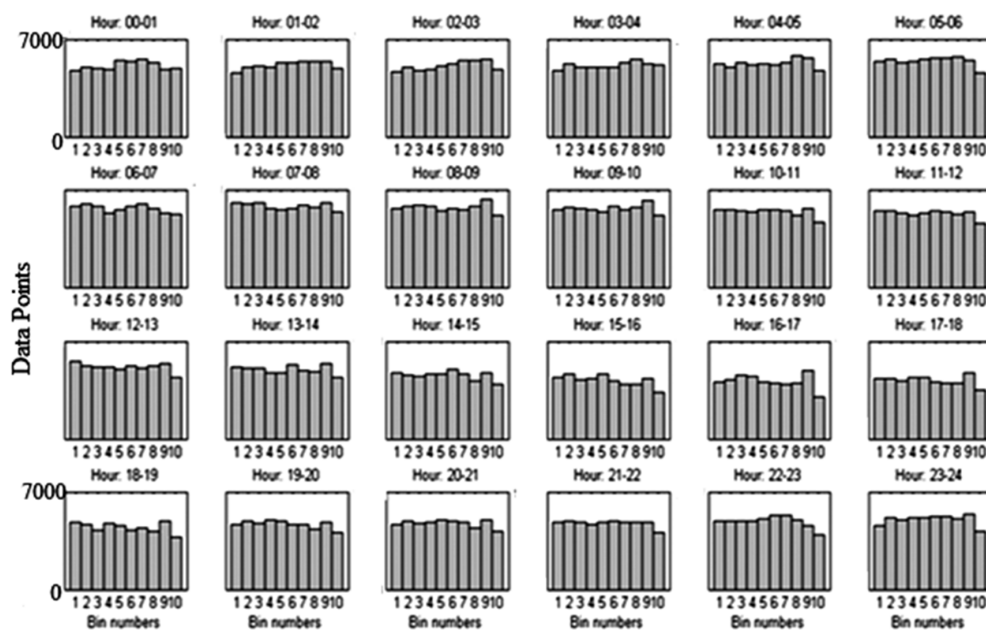


Figure 4.4: CNA (dB) hourly bins Spring season 1995-2006.

Cosmic noise absorption data covers 1995–2006 with one minute resolution from the zenithal beam of IRIS. During this period, polar cap absorption (PCA) events previously identified by Kavanagh and Marple (private communication) were filtered out of the dataset. CNA with negative absorption signature was also excluded. Negative absorption is known to be due to solar radio emission (SRE) and is not useful within the prediction model. For the 12 year period, CNA dataset is sub-divided into seasons: Winter, Summer, Autumn and Spring. Seasons are described as: Winter: December-February, Summer: June-August, Autumn: September-November and Spring: March-May. Each seasonal dataset is further subdivided to hourly dataset (i.e. 00-23 UTC). For each hour, ten equal bins of absorption are created based on set

epsilon ranges, computation to calculate the bin edges of epsilon was implemented and the result of the bin edges is as shown in Table 4.2. A counter is set to confirm the number of elements in the absorption bins. This is to ensure that each bin has

Absorption bin number	Epsilon Range [W]
One	$0 - 2.2 \times 10^{11}$
Two	$2.2 \times 10^{11} - 4.3 \times 10^{11}$
Three	$4.3 \times 10^{11} - 1.1 \times 10^{12}$
Four	$1.1 \times 10^{12} - 2.4 \times 10^{12}$
Five	$2.4 \times 10^{12} - 5.8 \times 10^{12}$
Six	$5.8 \times 10^{12} - 1.1 \times 10^{13}$
Seven	$1.1 \times 10^{13} - 2.9 \times 10^{13}$
Eight	$2.9 \times 10^{13} - 6.0 \times 10^{13}$
Nine	$6.0 \times 10^{13} - 1.4 \times 10^{14}$
Ten	1.4×10^{14} and above

Table 4.2: Absorption bin number based on epsilon ranges

enough elements that are similar in quantity such that taking averages (mean or median) of each bin is statistically viable. Figure 4.3 shows the number of elements in each of the hourly bins for the spring season, similar plots are made for every hour within all seasons to confirm the number of elements in each bin (typically between 5000–6400 data points). The number of elements allow for satisfactory statistical analysis as there are enough data represented. From Figure 4.3, it would be observed that for most hours, there is not exactly the same number of elements in all bins, this is because negative absorption and polar cap absorption were neglected in this study.

4.4.1 Modelling of absorption

Following the binning procedure as explained above, mean and median values of absorption within each bin are computed. A plot of the mean and median values within each bin is made for each hour within each season. The plots show a linear relationship of the form $Y = MX + C$. Where M is the gradient and C the intercept. For each hour, a unique fit equation is derived. The equations describe the variation

between absorption and epsilon for particular hours of each season. The fit equations for median absorption (dB) are as shown in Tables 4.3–4.6 below, the corresponding plots are as in Figures 4.5–4.8.

Table 4.3: Fit equation of hourly absorption and epsilon parameter Winter (1995–2006)

Hour (UT)	Gradient value (M)	Intercept value (C)	Standard deviation (SD)
00-01	6.705×10^{-15}	0.0736	0.013×10^{-15}
01-02	7.6125×10^{-15}	0.0764	0.013×10^{-15}
02-03	8.0684×10^{-15}	0.0904	0.014×10^{-15}
03-04	9.1083×10^{-15}	0.0851	0.016×10^{-15}
04-05	1.0218×10^{-14}	0.1032	0.014×10^{-15}
05-06	1.0043×10^{-14}	0.1402	0.013×10^{-15}
06-07	9.5495×10^{-15}	0.1632	0.016×10^{-15}
07-08	7.4003×10^{-15}	0.1374	0.015×10^{-15}
08-09	6.2796×10^{-15}	0.1043	0.023×10^{-15}
09-10	6.0276×10^{-15}	0.4257	0.023×10^{-15}
10-11	3.2615×10^{-15}	0.1409	0.017×10^{-15}
11-12	2.0353×10^{-15}	0.0308	0.114×10^{-15}
12-13	9.4204×10^{-16}	0.1572	0.142×10^{-15}
13-14	1.0717×10^{-16}	0.2388	0.153×10^{-15}
14-15	2.6385×10^{-16}	0.0531	0.164×10^{-15}
15-16	7.0325×10^{-16}	0.0422	0.168×10^{-15}
16-17	1.2152×10^{-15}	0.0336	0.173×10^{-15}
17-18	2.2205×10^{-15}	0.0153	0.113×10^{-15}
18-19	4.3508×10^{-15}	0.0176	0.033×10^{-15}
19-20	3.6473×10^{-15}	0.0328	0.023×10^{-15}
20-21	3.5601×10^{-15}	0.0647	0.016×10^{-15}
21-22	3.9541×10^{-15}	0.0691	0.012×10^{-15}
22-23	5.1436×10^{-15}	0.0818	0.014×10^{-15}
23-00	6.5471×10^{-15}	0.0682	0.013×10^{-15}

The linear relations shown in Tables (4.3–4.6) are unique for each hour within each season and define every hour within seasons in the proposed model. In all, there

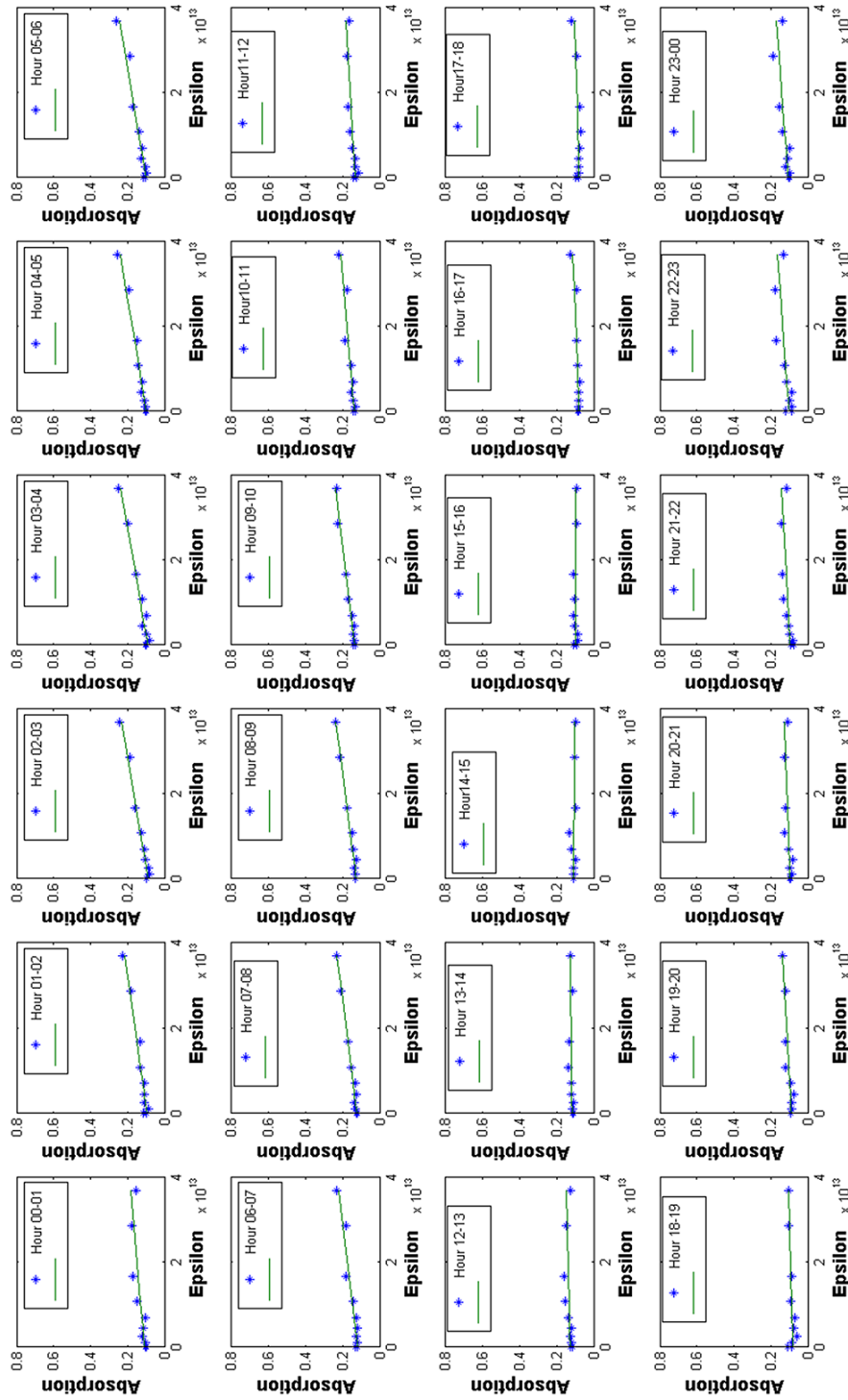


Figure 4.5: Plot of median CNA (dB) v Epsilon (W) Winter (1995–2006).

Table 4.4: Fit equation of hourly absorption and epsilon parameter Spring (1995–2006).

Hour (UT)	Gradient value (M)	Intercept value (C)	Standard deviation (SD)
00-01	6.715×10^{-15}	0.0756	0.011×10^{-15}
01-02	7.7125×10^{-15}	0.0764	0.015×10^{-15}
02-03	8.3684×10^{-15}	0.0924	0.018×10^{-15}
03-04	9.7083×10^{-15}	0.0991	0.011×10^{-15}
04-05	1.0318×10^{-14}	0.1356	0.012×10^{-15}
05-06	1.0249×10^{-14}	0.1512	0.017×10^{-15}
06-07	9.3495×10^{-15}	0.1831	0.016×10^{-15}
07-08	7.7903×10^{-15}	0.1970	0.015×10^{-15}
08-09	6.4793×10^{-15}	0.2043	0.023×10^{-15}
09-10	6.1476×10^{-15}	0.1757	0.023×10^{-15}
10-11	3.1616×10^{-15}	0.1536	0.017×10^{-15}
11-12	2.1153×10^{-15}	0.1508	0.114×10^{-15}
12-13	9.4809×10^{-16}	0.1472	0.156×10^{-16}
13-14	1.0919×10^{-16}	0.1388	0.153×10^{-15}
14-15	2.8285×10^{-16}	0.1031	0.174×10^{-15}
15-16	7.0625×10^{-16}	0.0612	0.168×10^{-16}
16-17	1.2152×10^{-15}	0.0336	0.173×10^{-15}
17-18	2.4405×10^{-15}	0.0273	0.113×10^{-15}
18-19	4.1408×10^{-15}	0.0206	0.033×10^{-15}
19-20	3.8873×10^{-15}	0.0448	0.023×10^{-15}
20-21	3.8001×10^{-15}	0.0647	0.016×10^{-15}
21-22	3.9571×10^{-15}	0.0721	0.012×10^{-15}
22-23	5.1537×10^{-15}	0.0828	0.034×10^{-15}
23-00	6.5771×10^{-15}	0.0782	0.033×10^{-15}

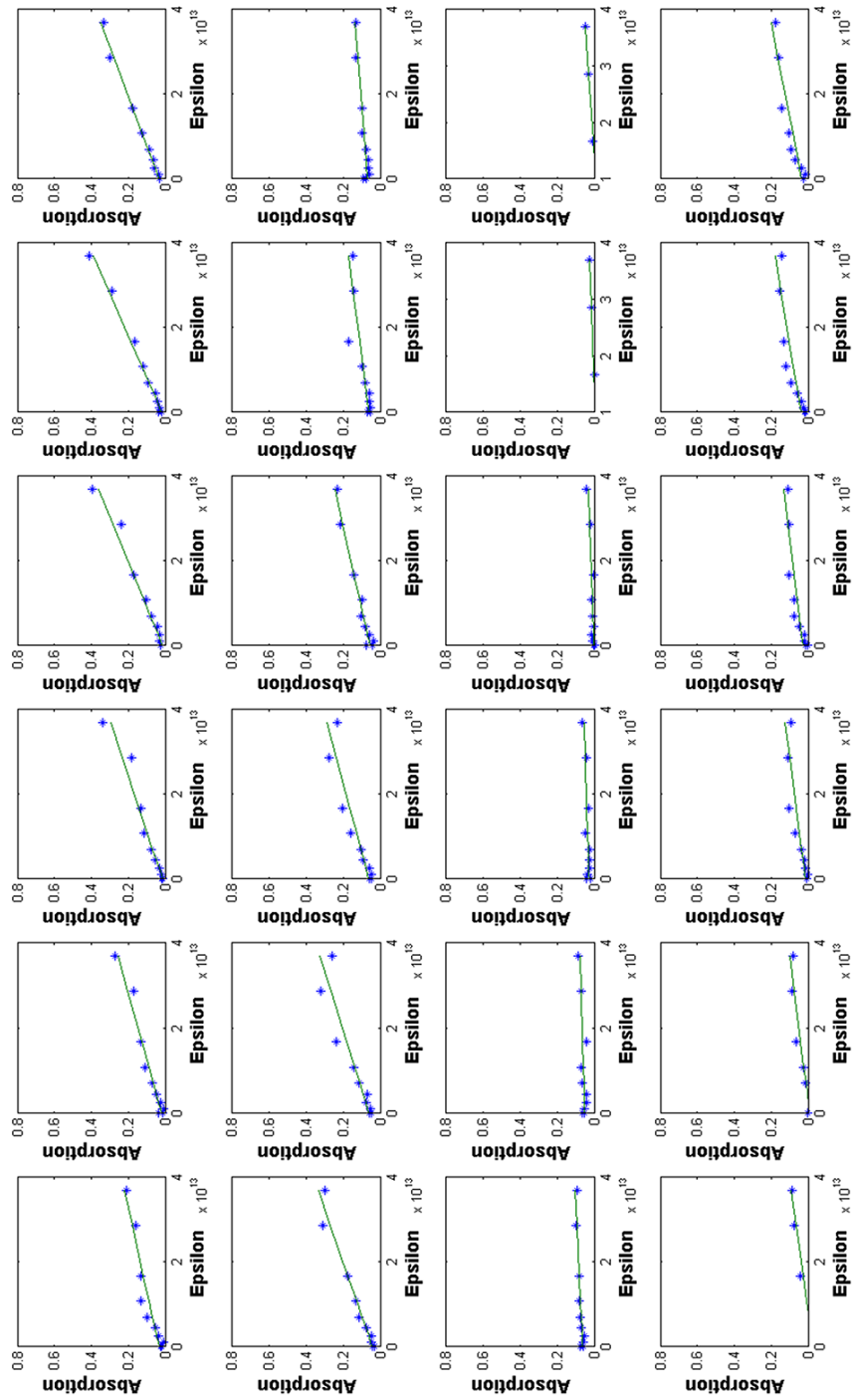


Figure 4.6: Plot of median CNA (dB) v Epsilon (W) Spring (1995–2006)

Table 4.5: Fit equation of hourly absorption and epsilon parameter Summer (1995-2006)

Hour (UT)	Gradient value (M)	Intercept value (C)	Standard deviation (SD)
00-01	4.4181×10^{-15}	0.1407	0.013×10^{-15}
01-02	3.5417×10^{-15}	0.1628	0.013×10^{-15}
02-03	3.9156×10^{-15}	0.1668	0.016×10^{-15}
03-04	4.4295×10^{-15}	0.1753	0.015×10^{-15}
04-05	4.3816×10^{-14}	0.1855	0.013×10^{-15}
05-06	5.2557×10^{-14}	0.1866	0.013×10^{-15}
06-07	7.2706×10^{-15}	0.1842	0.013×10^{-15}
07-08	7.0404×10^{-15}	0.1594	0.015×10^{-15}
08-09	3.8086×10^{-15}	0.1749	0.043×10^{-15}
09-10	64.0251×10^{-15}	0.1735	0.066×10^{-15}
10-11	5.0181×10^{-15}	0.1236	0.036×10^{-15}
11-12	5.1567×10^{-15}	0.1226	0.174×10^{-15}
12-13	3.5828×10^{-16}	0.11207	0.172×10^{-15}
13-14	2.5413×10^{-16}	0.1314	0.193×10^{-16}
14-15	3.4415×10^{-16}	0.0897	0.154×10^{-16}
15-16	3.2329×10^{-16}	0.0659	0.158×10^{-16}
16-17	3.3926×10^{-15}	0.0438	0.173×10^{-15}
17-18	2.001×10^{-15}	0.0737	0.183×10^{-15}
18-19	1.0343×10^{-15}	0.1124	0.025×10^{-15}
19-20	2.2156×10^{-15}	0.1174	0.023×10^{-15}
20-21	1.6690×10^{-15}	0.1341	0.019×10^{-15}
21-22	1.4532×10^{-15}	0.1624	0.022×10^{-15}
22-23	2.8090×10^{-15}	0.1463	0.043×10^{-15}
23-00	3.6180×10^{-15}	0.1465	0.017×10^{-15}

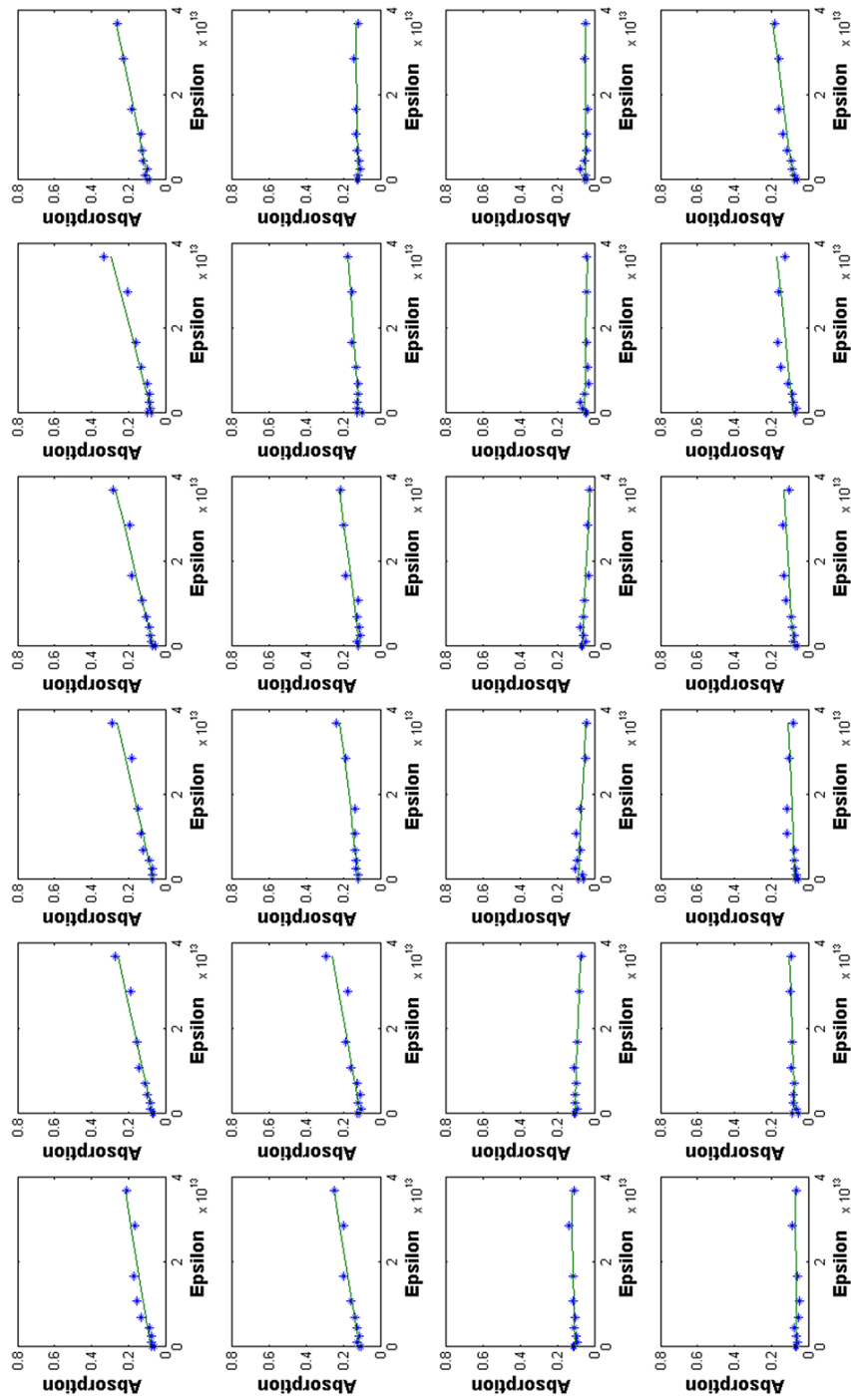


Figure 4.7: Plot of median CNA (dB) v Epsilon (W) Summer (1995–2006).

Table 4.6: Fit equation of hourly absorption and epsilon parameter Autumn (1995–2006)

Hour (UT)	Gradient value (M)	Intercept value (C)	Standard deviation (SD)
00-01	6.715×10^{-15}	0.0756	0.013×10^{-15}
01-02	7.7125×10^{-15}	0.0764	0.013×10^{-15}
02-03	8.3684×10^{-15}	0.0924	0.016×10^{-15}
03-04	9.7083×10^{-15}	0.0991	0.015×10^{-15}
04-05	1.0318×10^{-14}	0.1356	0.013×10^{-15}
05-06	1.0249×10^{-14}	0.1512	0.013×10^{-15}
06-07	9.3495×10^{-15}	0.1831	0.013×10^{-15}
07-08	7.7903×10^{-15}	0.1970	0.015×10^{-15}
08-09	6.4793×10^{-15}	0.2043	0.043×10^{-15}
09-10	6.1476×10^{-15}	0.1757	0.066×10^{-15}
10-11	3.1616×10^{-15}	0.1536	0.036×10^{-15}
11-12	2.1153×10^{-15}	0.1508	0.174×10^{-15}
12-13	9.4809×10^{-16}	0.1472	0.172×10^{-15}
13-14	1.0919×10^{-16}	0.1388	0.193×10^{-16}
14-15	2.8285×10^{-16}	0.1031	0.154×10^{-16}
15-16	7.0625×10^{-16}	0.0612	0.158×10^{-16}
16-17	1.2152×10^{-15}	0.0336	0.173×10^{-15}
17-18	2.4405×10^{-15}	0.0273	0.183×10^{-15}
18-19	4.1408×10^{-15}	0.0206	0.025×10^{-15}
19-20	3.8873×10^{-15}	0.0448	0.023×10^{-15}
20-21	3.8001×10^{-15}	0.0647	0.019×10^{-15}
21-22	3.9571×10^{-15}	0.0721	0.022×10^{-15}
22-23	5.1537×10^{-15}	0.0828	0.043×10^{-15}
23-00	6.5771×10^{-15}	0.0782	0.017×10^{-15}

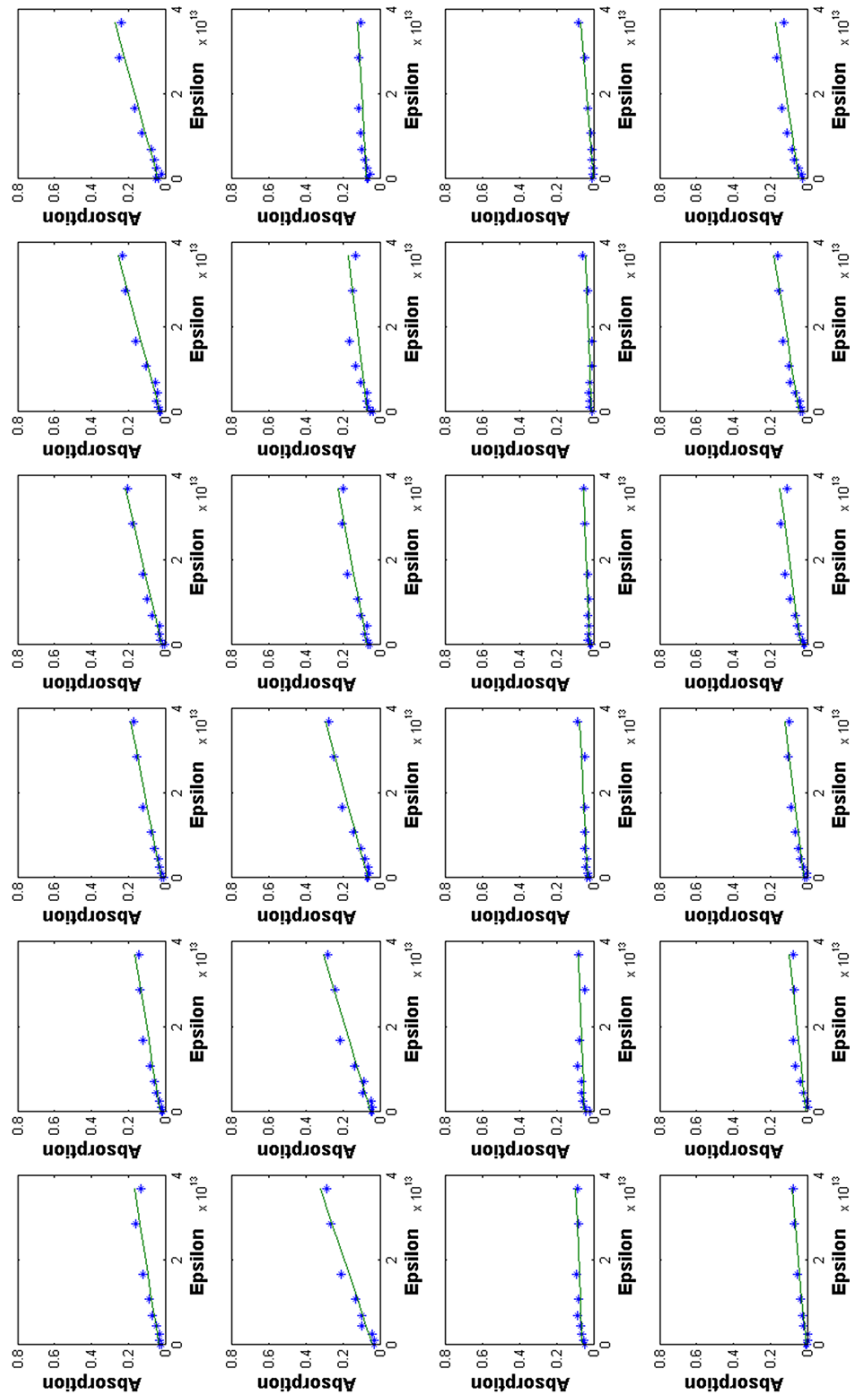


Figure 4.8: Plot of median CNA (dB) v Epsilon (W) Autumn (1995–2006).

are 96 fit equations (24 for each season) that are combined for modelling purposes. The algorithm recognizes each season and identifies each hour of a particular season. When a particular time history is given, the algorithm first determines the period based on the month and subsequently utilises the day and time component of the time history to locate the hour. Once the particular time is identified, the algorithm uses the appropriate fit equation to model expected absorption. Other inputs of the model are the geographic location of riometer (i.e. longitude and latitude), season, time of the day and solar wind parameters. Solar wind parameters can be obtained in real time from the OMNI repository. The results are subsequently verified by comparison with measured riometer absorption.

4.5 Observations

A key observation from Figures 4.5–4.8 is that the result of averaging CNA over a period shows less than 1dB absorption in all hours and during all seasons. While median fits are statistically better, it is the mean fits that show higher values. Although the local time dependence of absorption has been well established [e.g. Hartz *et al.*, 1963, Foppiano 1983, Hargreaves 1967, Kavanagh *et al.*, 2004], and previous studies have found that strongest absorption occur in the morning sector extending back towards midnight and slightly beyond, the observation is similar in this study. It is observed that absorption is higher during the post-midnight (01:00-04:00 UT) and pre-midnight (21:00-23:00 UT) periods while there is only a weak relationship between absorption and epsilon from 13:00-18:00 UT (Figures 4.5–4.8), at this period absorption is at its minimum and does not correspond to changes in epsilon parameter. This result of the statistical study of IRIS measurement given by [Kavanagh *et al.*, 2004] as in Figure 4.2 shows that solar wind velocity do not vary strongly with absorption from 16:00 to ~20:00 MLT. Particle precipitation at high latitude is known to maximize at night due to substorm activity [e.g. Piggot, 1964, Hargreaves, 1992]. Foppiano and Bradley [1983] have shown the diurnal variation of absorption to exhibit post-midnight (absorption caused by drizzle precipitation) and pre-midnight (absorption caused by splash precipitation) peaks. Other studies [e.g.

Ansari, 1964; Ranta *et al.*, 1981] characterise pre-midnight absorption to precipitation of electron associated with substorm activity, while Kavanagh *et al.*, [2002] and references therein link precipitation in the morning sector to eastward drift of electrons following substorm injection. Both morning and pre-midnight absorption are important to HF communication circuits.

4.6 Results and Analysis

The model presented in this study provides graphical representation for all times and season. In this Section some of the results of the comparison of model with measured absorption are given. For each season, three periods that coincide with periods of low absorption, moderate and high absorption events are shown.

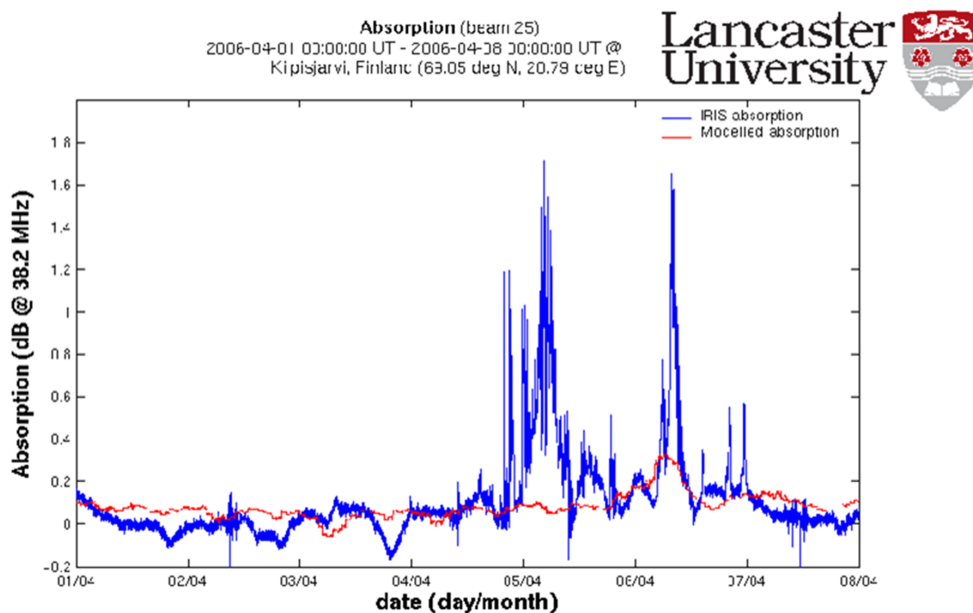


Figure 4.9: Plot of measured absorption v modelled absorption for 7 days in a Spring season (4th to 8th April, 2006). Measured absorption shows differing signatures over days. 1st-4th April characterise with low absorption signature (between -0.2 and 0.15 dB, 5th is an active day with absorption reaching 1.7 dB, 7th April has maximum absorption of 0.5 dB. Modelled absorption could predict up to 0.3 dB. Modelled prediction shows good correlation with measured absorption but shows significant deviation from measured absorption during active periods with absorption spikes.

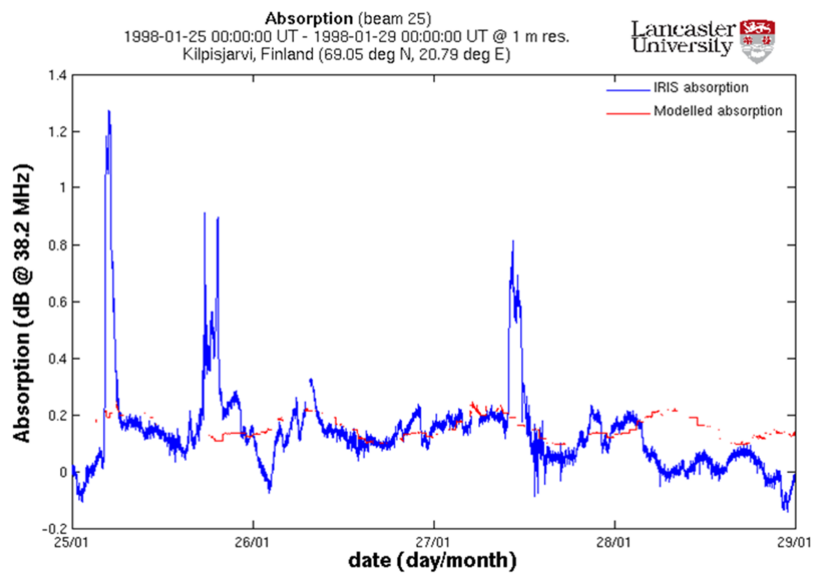


Figure 4.10: Plot of measured absorption v modelled absorption 4 days in a Winter season in 1998 (25th to 29th February, 1998). Absorption spikes are noticed between 6-11 UT. Measured absorption varies considerably from -0.2 dB to 1.8 dB, modelled absorption could predict up to 0.35 dB. Modelled prediction shows good correlation with measured absorption for low absorption periods but shows significant deviation from measured absorption during periods with absorption spikes.

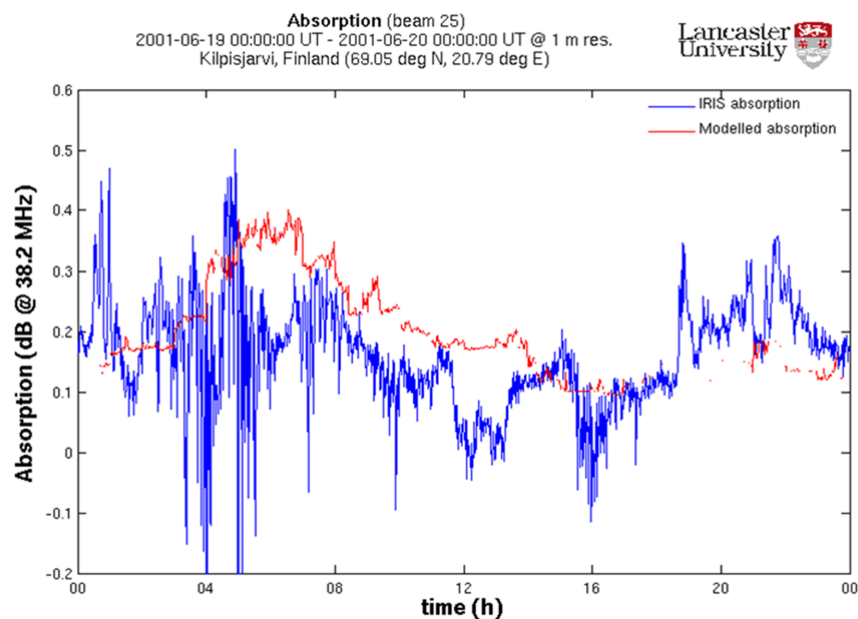


Figure 4.11: Plot of measured absorption v modelled absorption 1 day in a Summer season in 2001 (19th June, 2001). Measured absorption varies with modelled absorption.

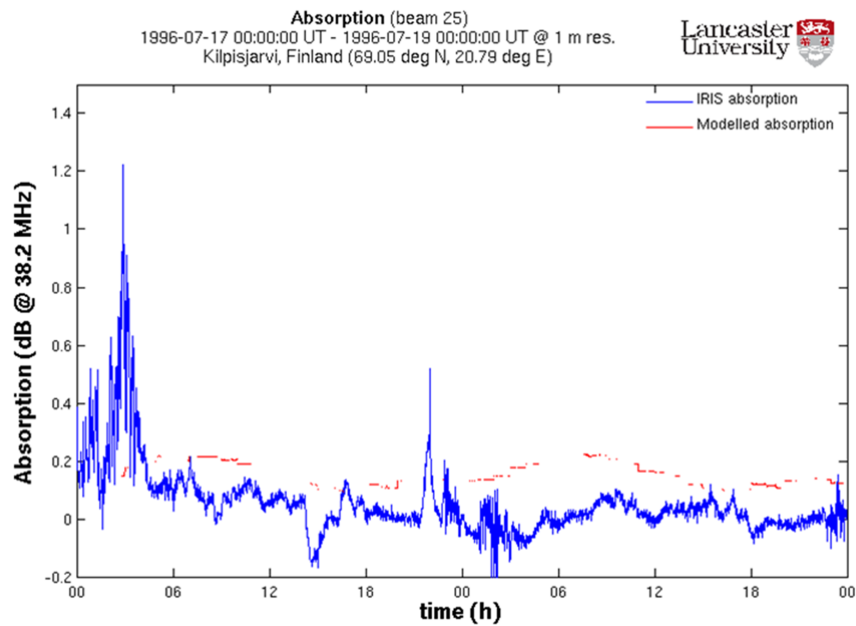


Figure 4.12: Plot of measured absorption v modelled absorption 2 days in a Summer season in 1996 (17th to 19th July, 1996). Post-midnight absorption spikes are noticed on the first day and pre-midnight spikes for the second day. Measured absorption varies considerably from -0.2 dB to 1.2 dB, modelled absorption could predict up to 0.2 dB.

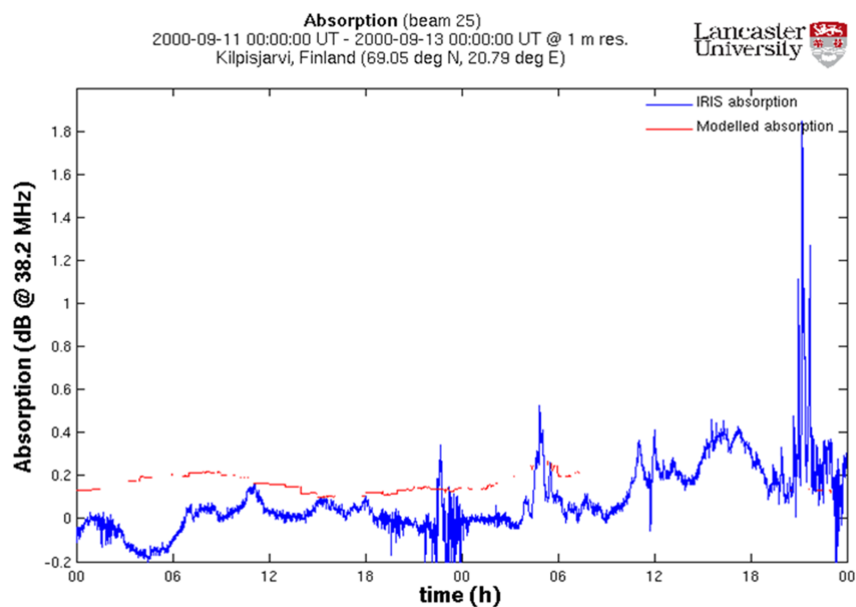


Figure 4.13: Plot of measured absorption v modelled absorption 2 days in a Summer season in 2000 (11th to 13th September, 2000). Post-midnight absorption spikes are noticed on the first day and pre-midnight spikes for the second day. Measured absorption varies considerably from -0.2 dB to 1.2 dB, modelled absorption could predict up to 0.2 dB.

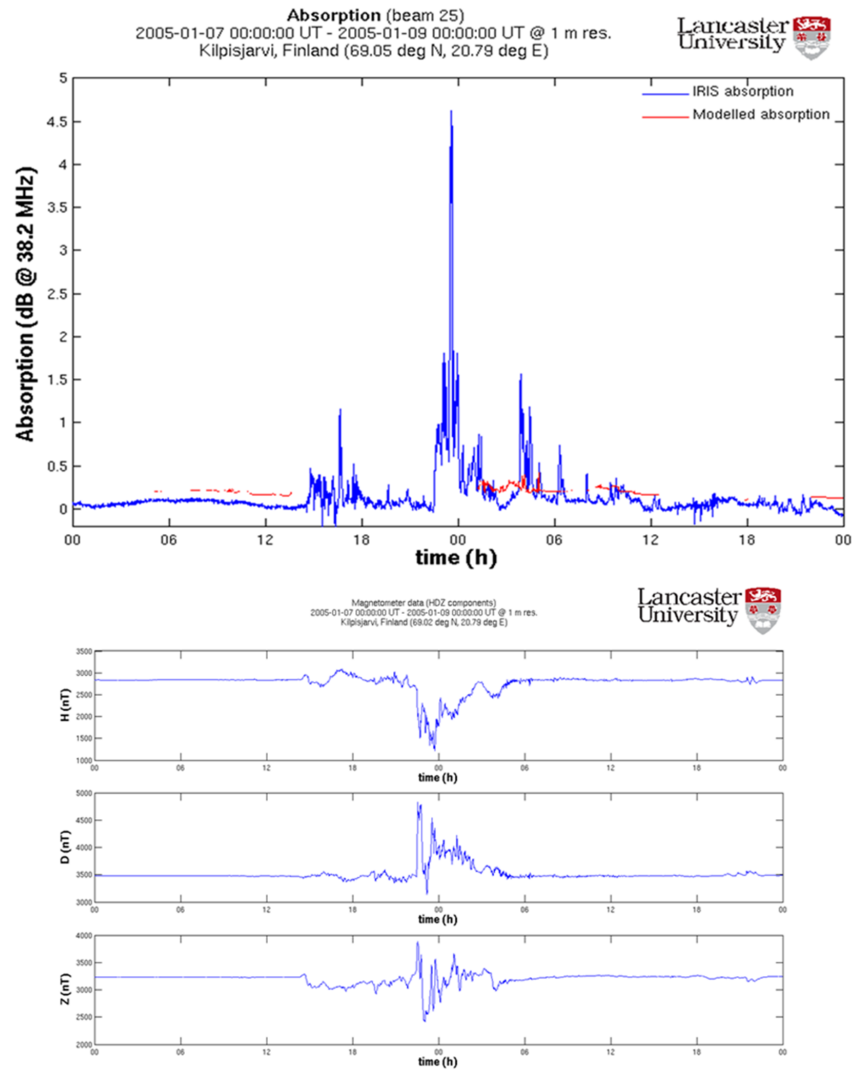


Figure 4.14: Panel A showing comparison of modelled and measured absorption. Panel B shows measurement of magnetometer components of H , D and Z . During periods of absorption spiked, there is corresponding depression in H component of magnetometer signifying the occurrence of substorm.

The data gaps noticed in the model (red lines) in Figures 4.10–4.13 are due to data gaps in upstream solar-wind data recorded in the OMNI repository.

4.7 Conclusion

Radio wave absorption processes in the upper, partly ionised atmosphere, the ionosphere, has served as diagnostic for the behavior of this region, therefore, predicting absorption will further help to understand certain intrinsic characteristics

of the ionosphere. This study has utilised statistical means to estimate absorption at high latitude (e.g. Kilpisjarvi 69.05°N, 20.79°E) considering all conditions (i.e. ranging from quiet conditions to very disturbed conditions) for a solar cycle (1996–2009). The model was set not to include negative absorption. It is observed clearly that median absorption hardly exceeds 0.1-0.2 dB at riometer frequency (Stauning, 1998, as in other models), although this model predicts median absorption up to about 0.4 dB. On the seasonal variation, a considerable higher absorption is observed during Winter season (figure 4.10) as absorption is known to be high during Winter than at other seasons. This is observable especially within the morning hours of 03:00-06:00 hours. Absorption diurnally is justified as epsilon predicts higher at post-midnight periods (e.g. 03:00-06:00 UT) and pre-midnight (e.g. 22:00-23:00 UT). Absorption varies as a function of epsilon for values of $\epsilon \geq 6 \times 10^{12}$ Watt (Figure 4.3), below this value of epsilon there is no correlation between epsilon and absorption. Although the use of a combination of solar wind parameter as represented in the Akasofu coupling function showed a degree of correlation with riometer absorption. For prediction purposes, to estimate absorption intensity will require more than improved ionospheric modelling, details such as the knowledge of atmospheric motion and composition, electrodynamics conditions and energetic particle precipitation would be required. From the result, it is seen that in days with moderate absorption (Figure 4.11), this model can predict near accurately. However during periods with high absorption, (Figures 4.9 and 4.10) the prediction does not represent the measured value. Absorption spikes coincide with substorm activities. Aminael *et al.*, [2006] classified night time absorption spikes into individual spikes, spikes followed by injection absorption, spikes preceded by injection absorption and spikes embedded in injection absorption. These spikes appear as sudden increase in absorption which falls off rapidly after reaching their peak level. Since present knowledge already could identify severe solar events such as coronal mass ejections and solar flare events, it will be necessary to model absorption based on the occurrence of these classes of event (e.g. solar flares and ICMEs). Chapters 5 and 6 of this study will focus on modelling solar flare and ICME induced absorption respectively.

Chapter 5

Cosmic noise absorption induced by interplanetary coronal mass ejections

5.1 Introduction

Solar and solar wind disturbances are the fundamental reasons for most of the main changes in the ionosphere. Solar events such as interplanetary coronal mass ejections (ICMEs) (ICME is discussed in 5.2) and solar flares could be detrimental to ionospheric radio propagation resulting in propagation disruptions which could last from few minutes to hours and sometimes days. Presently some work has been done to archive details such as the start times, end times and magnitude of these solar events. Knowing how the ionosphere has responded to radio absorption during the archived events is key to understanding the character of the ionosphere during such events and provides insight to predicting radio absorption for future events. Figure 5.1 gives a summary of solar related effects on the ionosphere.

This chapter details the analysis and results of the study of cosmic noise absorption (CNA) during periods of interplanetary coronal mass ejections (ICMEs). CNA is from imaging riometer for ionospheric studies (IRIS) discussed in Section 3.2 and ICME events utilised were from the Richardson and Cane ICME catalogue (see Section 5.3) covering solar cycle 23. In this catalogue, a total of about 315 ICME events were recorded for 1996-2009. Certain event selection criteria were employed to choose ICME events that were considered appropriate for this study. The selection criterion is as discussed in Section 5.5.1. Based on the selected events, a total of 201 events were identified, the events were further categorised into day time and

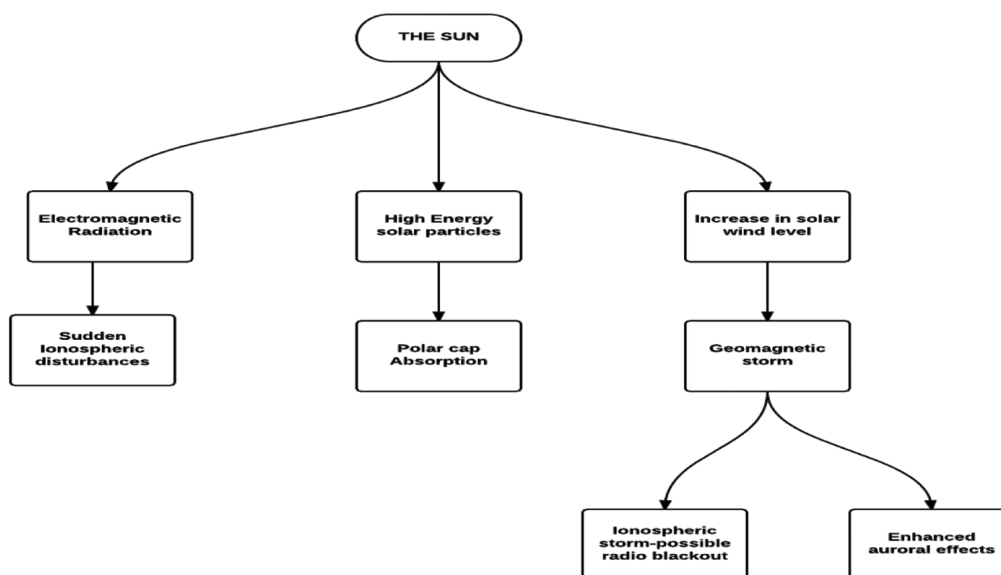


Figure 5.1: A schematic of solar related effects on the ionosphere

night time onset events based on the zenith angle of riometer location. Out of the 201 events, 89 are categorised as day onset events and 112 as night onset events. Superposed epoch analysis is performed on both day and night events to study precipitation effect following ICME events. Prediction models for night and day time events are then presented. This chapter is organised as follows: Section 5.1 gives an overview of ICMEs, Section 5.2 highlights the identifying signatures of ICMEs from literatures, and Section 5.3 discusses Richardson and Cane ICME catalogue used in this study. Section 5.4 describes the methodology utilised in this study and the analytical procedure is shown in Section 5.6, Section 5.7 shows the results and Section 5.8 has the concluding remarks.

5.2 Interplanetary coronal mass ejections (ICMEs)

Coronal mass ejections (CMEs) are energetic solar events involving the ejection of solar material into the heliosphere [e.g. Hundhausen 1996 and 1997]. The ejected plasma consists of as much as 1×10^{24} J of energy and up to 1×10^{13} kg of solar matter [Gonzalez-Esparza *et al.*, 2004]. The occurrence of a CME is associated with enormous changes in the coronal magnetic field, and magnetic reconnection is

usually assumed to be the responsible mechanism. Interplanetary coronal mass ejections (ICMEs) are solar wind structures that are believed to be the counterparts of coronal mass ejections at the Sun [Hirshberg, J *et al.*, 1970; Sheeley, N. R. Jr. *et al.*, 1985; Webb, D. F *et al.*, 2000; Liu *et al.*, 2013 and references therein]. It has been established that solar wind structures such as ICMEs and co-rotating interaction regions (CIRs) drive particle precipitation [e.g. Denton *et al.*, 2006; Longden, 2007 and references therein]. CIRs occur from the interaction between fast solar-wind streams emanating from coronal holes with slow streams producing co-rotating interaction regions in interplanetary space [e.g., Belcher, J. W., and Davis L, 1971; Jian, L.; Russell, C. T.; Luhmann, J. G.; Skoug, R. M., 2006]. These solar wind structures (i.e. ICMEs and CIRs) are important to ionospheric modelling because they may trigger geomagnetic storms [e.g. Tsurutani, B. T., and W. D. Gonzalez 1997, Gosling *et al.*, 1991, Zhang *et al.*, 2007; Echer *et al.*, 2008; Guarnieri *et al.*, 2006, Richardson 2013, Richardson and Cane, 2011; Richardson *et al.*, 2001; Zhang and Burlaga, 1988; Wu and Lepping, 2007; Gosling *et al.*, 1991; Huttunen *et al.*, 2008; Longden *et al.*, 2008].

When a CME erupts from the Sun, magnetised plasma is hurled into space interrupting the steady solar wind. The ejected coronal material (the ICME) moves through the solar wind and may drive a shock wave that moves ahead of the CME, accelerating some solar wind particles to high energies [Cane and Lario, 2006 and references therein]. ICMEs can also influence the propagation of cosmic rays and solar energetic particles in the heliosphere [e.g. Forbush, S.E., 1937; Simpson, J.A., 1954; Barnden, L.R., 1973a; Barnden, L.R., 1973b; Cane, H.V., 2000; Richardson and Cane, 1996; Gopalswamy, 2010, Cane and Lario, 2006]. While Chapter 4 of this thesis had utilised statistical method of data analysis with no consideration for periods of specific solar events such as ICME and solar flares, the current chapter and the chapter that follows (Chapters 5 and 6) will focus on modelling cosmic noise absorption during ICMEs and solar flares. ICME catalogue produced by Richardson and Cane [2010] is discussed in Section 5.4. In the catalogue, they utilised solar wind composition and charge state observations as identifying signatures of ICMEs.

5.3 Signatures of ICMEs

Previous reviews of interplanetary coronal mass ejections [e.g. Zwickl *et al.*, 1983, Neugebauer and Goldstein 1997, Gosling, 1973, Zurbuchen and Richardson 2006 and references therein] have summarised the identification of the physical drivers for ICME material and their key signatures. ICMEs can drive shocks that accelerate energetic particles; they are the predominant drivers of intense geomagnetic storms and provide diagnostic information on conditions during these eruptions [Cane and Richardson 2010, Rakowski, Laming and Lepri; 2007]. ICMEs can modulate the intensity of the galactic cosmic rays [Cane, 2000 and references therein]. One of the characteristic signatures is a flux-rope-like helical magnetic field configuration [e.g. Klein and Burlaga, 1982] that forms part of the ICME such a structure is termed a magnetic cloud and is found in about one-third of ICME cases. Magnetic cloud are characterised by enhanced magnetic field strength, a large-scale smoothly rotating component of the magnetic field, also low plasma beta due to the strong fields, but beta is currently discussed below and a depressed proton temperature. Such depressed proton temperatures result from the expansion of ICME plasma in the solar wind [Gosling, J.T., Pizzo, V., Bame, S.J., J. 2001] and are a common signature of ICMEs [Richardson, I.G., Cane, H.V., 1995]. Another signature of some ICMEs is the detection of bi-directional or counter-streaming solar wind superthermal flows (BDEs) indicating the presence of looped magnetic structures connected to the Sun at both ends [e.g., Gosling, J.T., Baker, D.N., Bame, S.J., Feldman, W.C., Zwickl, R.D., Smith, E.J., 1987; Shodhan, S., Crooker, N.U., Kahler, S.W., Fitzenreiter, R.J., Larson, D.E., Lepping, R.P., Siscoe, G.L., Gosling, J.T., 2000]. An additional signature considered is plasma beta. The beta of plasma [β] is the ratio of the plasma pressure (5.1) to the magnetic pressure (5.2)

$$p = [nK_B T] \quad (5.1)$$

$$p_{mag} = \frac{B^2}{2\mu_0}. \quad (5.2)$$

where n is the number of molecules, K_B is Boltzmann's constant, T is temperature B is the magnetic field and μ_0 is the magnetic permeability.

Borovsky and Denton [2006] found that the β for ICME-driven storms was low whereas for CIR driven storms it was high [Figure 5.2].

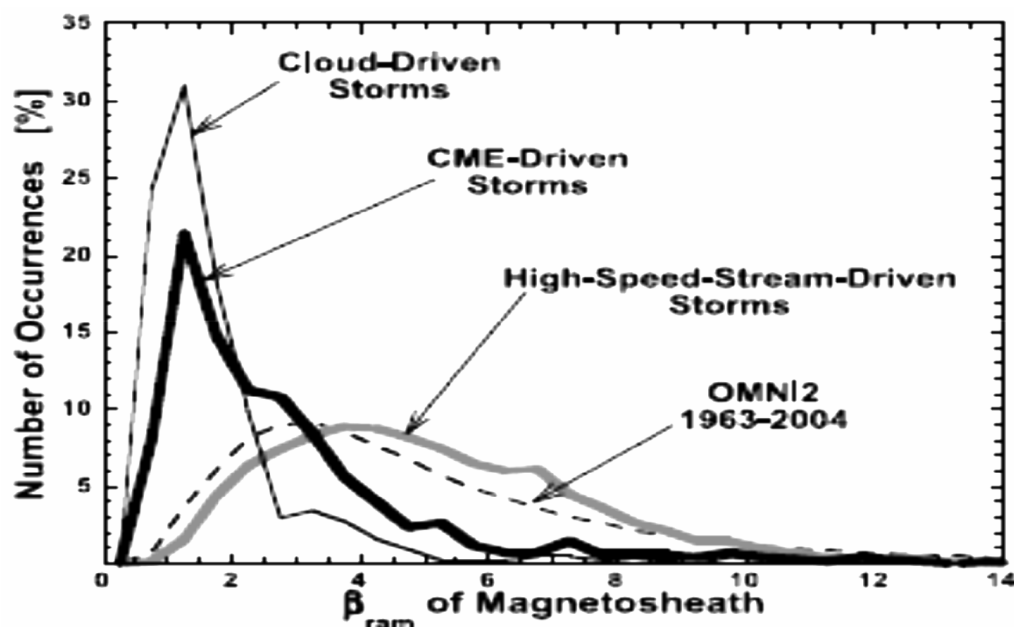


Figure 5.2: Occurrence statistics of storms driven by solar wind structures v magnetosheath plasma- β [From Borovsky and Denton, 2006]

Table 5.1 below highlights some of the established signatures highlighted by Zurbuchen and Richardson [2006].

Table 5.1: Identifying Signatures of ICME Events [Details extracted from Zurbuchen & Richardson 2006]

No	Signatures	Remarks	References
1	Enhanced IMF	> 10 nT	Hirshberg & Colburn 1969. Klein & Burlaga, 1982.
2	Low Variance of IMF	IMF Variance Decrease	Putovkin <i>et al.</i> , 1979. Klein & Burlaga, 1982.
3	Smooth Rotation of IMF	$\gg 300^\circ$ smooth	Putovkin <i>et al.</i> , 1979. Klein & Burlaga, 1982.
4	Low Beta [$\beta < 1$]		Klein & Burlaga, 1982.
5	Proton Temperature decrease.	$T_p < 0.5T_{exp}$	Richardson & Cane, 1996
6	Bi-Directional electron streaming		Gosling <i>et al.</i> , 1990

5.4 Classification of ICMEs based on magnetic and non-magnetic cloud events

The identifying signatures for ICMEs have been mentioned in Table 5.1 above. In particular, ICMEs are divided into those which include the signatures of magnetic cloud (enhanced IMF, smooth rotation of IMF and low plasma beta) and those that lack such signatures.

Statistics of magnetic and non-magnetic cloud events is shown in Tables 5.2-5.4. Table 5.2 shows the statistics of parameters such as CNA(dB), solar wind velocity, total IMF(nT), D_{st} (nT) and K_p , while table 5.3 shows the same statistics for non-magnetic cloud events. In table 5.5 a comparison between the mean values of magnetic and non-magnetic cloud categories is shown.

5.5 ICME data

The list¹ of near-Earth [ICMEs] used here was compiled by Richardson and Cane [2010]. About 315 ICMEs that passed the Earth during solar cycle 23 (i.e. 1996-2009) were identified. Their original motivation was driven by the need to study the effects of ICMEs on energetic particles. They combined a number of available datasets and try to assess when ICMEs were probably present in the near-Earth solar wind, using the criteria characteristics of ICMEs in Table 5.1 and visual inspection of the data. The dataset are those available from the advance composition explorer (ACE), and other near-Earth spacecraft (e.g. WIND). Before the launch of ACE [August, 1997], and during occasional ACE data gaps, the catalogue referred to observations from other spacecraft (such as IMP 8) and the OMNI near-Earth database at resolutions of ≈ 1 minute to 1 hour. Other repositories used are ACE/SWEPAM solar wind electron pitch-angle database, solar wind ion composition and charge state observations [1- or 2-hour averages] made by the solar wind ion composition spectrometer (SWICS) instrument and the solar and heliospheric observatory [SOHO] spacecraft. The philosophy was premised on the fact that ideally as many different signatures as

¹www.srl.catech.ace/src/data/level3/icmetablw2.htm

possible should be examined when identifying ICMEs. The hypothesis is that these data can help to link shocks and ICMEs with specific solar events/CMEs through the intensity-time profiles and can also indicate the arrival of ICMEs through the abrupt decrease in intensity that may occur at these time(s) over a wide range of particle energies (keV to GeV galactic cosmic rays).

Also, they observed that some of the problems when identifying ICMEs using different datasets is that the boundaries may not agree exactly or some signatures may be completely absent. Reasons such as event to event variations in the conditions at the Sun during CME ejection, the different physical processes that give rise to the various signatures and which may occur at the Sun [e.g. composition/charge states, formation of magnetic clouds], during ICME expansion in the solar wind (e.g. abnormally low proton temperatures), or depend on the magnetic field line topology and connection to the Sun (e.g. energetic particle decreases and bidirectional flows) that may be influenced by reconnection between field lines in the ICME and ambient solar wind were stated. ICME start and end times based predominantly on solar wind plasma and magnetic field observations are recorded in the catalogue produced by Richardson and Cane [2010] and are useful for modelling ICME.

The first approach towards analysis in this chapter is to investigate if there are considerable differences in the statistics of data utilised (i.e the flow speed (V_x), D_{st} and K_p) as they compare with CNA based on the magnetic cloud and non-magnetic cloud signatures for the period captured in the catalogue. Tables 5.2 and 5.3 show the related statistics with both categories.

Table 5.2: Statistics for magnetic cloud events based on Richardson and Cane catalogue

	CNA(dB)	V_x ($km\ s^{-1}$)	B (nT)	D_{st} (nT)	K_p
Minimum	-5.25	289	0.816	-422	0
Maximum	6.84	993	31.50	72	9
Mean	0.251	473	12.4	-41.3	2.88
Median	0.143	445	7.24	-31.0	2.70
Standard Deviation	0.508	6.74	1.91	45.4	1.90

Table 5.3: Statistics for non-magnetic cloud events based on Richardson and Cane catalogue

	CNA(dB)	V_x ($km\ s^{-1}$)	B (nT)	D_{st} (nT)	K_p
Minimum	-6.27	278	0.041	-358	0
Maximum	16.5	997	31.70	77.9	9
Mean	0.220	445	8.82	-33.5	2.70
Median	00.146	454	4.92	-24.0	2.30
STD	0.810	6.51	1.44	1.75	1.75

Comparing the statistics in Tables 5.2 and 5.3, the mean values of the magnetic cloud (MC) category (i.e Table 5.2) are higher than their non-magnetic cloud counterparts (i.e Table 5.3), see Table 5.4.

Table 5.4: Mean differences in magnetic cloud and non-magnetic cloud parameters

	Magnetic clouds	Non magnetic clouds	Mean value differences
CNA (dB)	0.251	0.22	0.031
V_x ($km\ s^{-1}$)	473	445	28
B (nT)	12.4	8.82	3.58
D_{st} (nT)	-41.3	-33.5	7.8
K_p	2.88	2.7	0.18

Although there seem not to be significant variation in CNA mean values in both categories, (the MC category is ~ 0.03 higher than non-MC, the value appears negligible), the significant mean variation is in the IMF. The mean IMF for the MC category is 12.4 (nT) while for non-MC, the mean value is 8.82 (nT) as variations in IMF are the only difference between magnetic and non-magnetic categories.

5.5.1 Solar cycle dependence of ICMEs

The occurrence rate of CMEs peaks strongly during solar maximum [Borovsky and Denton 2006; Webb, 1999] therefore, storms during solar maximum seem to be CME driven [Richardson *et al.*, 2001]. Figure 5.3 shows the distribution of recorded

ICME events within the 14 year period covered in the Richardson and Cane catalogue.

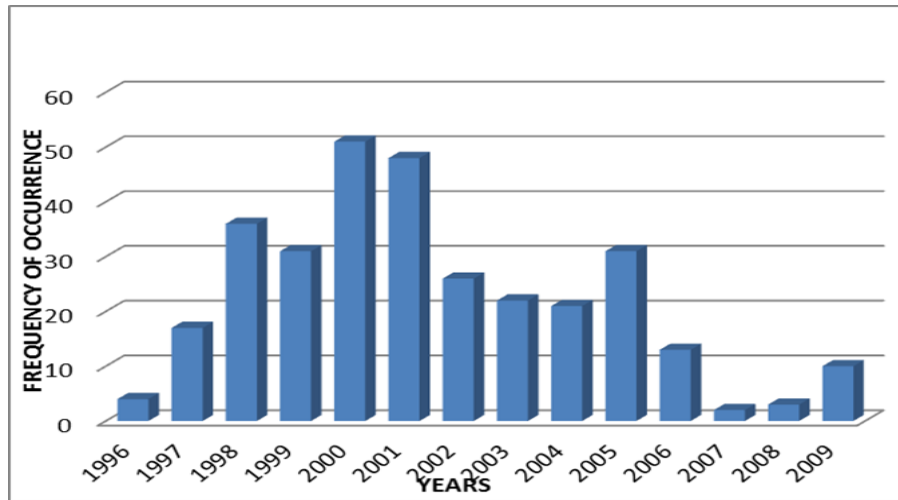


Figure 5.3: Yearly distribution of ICME events for solar cycle 23 (1996-2009).

As would be expected, the peaks coincide with solar maximum peak period (2000-2001)] while very few events were noticed during the very quiet periods of (1996, 2007-2009). In Figure 5.4, it is observed that the frequency of ICME occurrence is symmetric with the 12 months smoothed Sun spot number [SSN] and the mean 10.7 cm radio flux which are generally a proxy for solar activity. Hence, ICME occurrence correlates with solar activity factor.

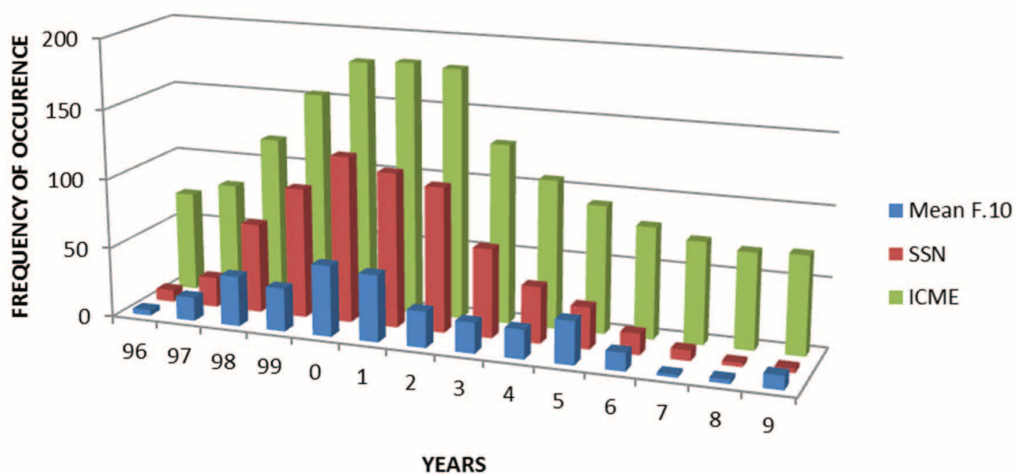


Figure 5.4: Distribution of ICME with SSN and mean 10.7 cm radio flux. (1996-2009)

5.5.2 Geoeffectiveness of ICMEs

The D_{st} index is widely used to define the occurrence, duration and magnitude of a geomagnetic storm [e.g. Burton, McPherron and Russell, 1975; Loewe and Pröls, 1997]. The minimum D_{st} value is often used to classify the strength of a magnetic storm. A common classification [after Kamide *et al.*, 1998] is as in Table 5.5 below. The relationship between solar wind structures and storms has been studied by various authors [e.g. Echer *et al.*, 2008; Guarnieri *et al.*, 2006, Zhang *et al.*, 2007, Richardson 2013; Richardson *et al.*, 2001]. They indicate that ICMEs and co-rotating interaction regions [CIRs] are the primary phenomena responsible for the main phase of geomagnetic storms.

Table 5.5: Classification of Magnetic Storm Strength

Storm Intensity	D_{st} Range
Weak storm	Minimum D_{st} below -30 nT
Moderate storm	Minimum D_{st} below -50 nT
Strong storm	Minimum D_{st} below -100 nT
Severe storm	Minimum D_{st} below -200 nT
Great storm	Minimum D_{st} below -350 nT

Table 5.6: Frequency of occurrence of storm Intensity During ICME [Cane and Richardson , 2010 Catalogue]

Storm Intensity	% Of ICME Occurrence [1996-2009]
Weak storm	33%
Moderate storm	31%
Strong storm	26%
Severe storm	8.5%
Great storm	1.5%

Table 5.6 shows the geo-effectiveness of ICME events. About 26% of ICME events have $D_{st} \leq -100$ nT, and are associated with strong storm, whereas about 9% are

associated with severe storms [$D_{st} \leq -200$ nT] and as few as 1.5% are associated with great storms. [$D_{st} \leq -350$ nT]. ICME events within this period of study demonstrated a wide range of geo-effectiveness.

5.5.3 Energetic particle associated with ICMEs

Previous works have identified precipitation effects following solar wind drivers [e.g. Longden, 2007 and Longden *et al.*, 2008]. Also, Kavanagh *et al.*, [2012] identified some features of electron precipitation on high speed solar wind stream [HSS] events. These studies performed superposed epoch analysis on cosmic noise absorption (CNA) based on time history of solar wind drivers. In the study of Longden *et al.*, [2008] the superposed epoch analysis compared the statistical properties of mean CNA during 38 CIR- and 33 ICME-driven geomagnetic storms and concluded that the effects of ICMEs on CNA are most pronounced during the early phase of storm development. Furthermore, the study showed that ICMEs provide a greater variety of driving mechanisms that can stimulate particle precipitation compared to CIRs. When they considered storms of all intensities, ICMEs were observed to drive the most intense CNA. The result of Kavanagh *et al.*, [2012], who undertook an epoch analysis of energetic (> 30 keV) electron precipitation during 173 high speed solar wind streams (HSS) using riometer observations of cosmic noise absorption as a proxy for the precipitation show that following the arrival of the HSS there is an enhancement in the CNA levels across all local times, including the statistical ‘deep’ minimum in the afternoon-dusk sector. CNA levels remain elevated above pre-HSS arrival times for about four days. The magnetic local time (MLT) variations of precipitation observed in the study were broadly explained in terms of substorm injections and gradient curvature drift. The location of the peak precipitation (in terms of CNA) in L-shell and local time is consistent with the results obtained by Meredith *et al.*, [2011] although the later used polar orbiting satellite data. Some other studies [e.g. Jianpeng *et al.*, 2011; Denton, 2006] have shown enhancement of energetic particle precipitation during solar events such as ICMEs and solar flares. In this study superposed epoch analysis is extended to 176 ICME events. Based on

the observed precipitation effects, the events are further subdivided to the day and night categories and a model for predicting cosmic noise absorption during ICME events is presented.

5.5.4 The DRAP model

Radio wave absorption has been discussed in Chapter 2. Radio waves absorption has been identified as a veritable tool for the diagnostic of the ionosphere and this makes its prediction important. A detailed review of existing prediction radio absorption models have been shown in Chapter 4. One of the recent prediction model is the *D*-Region absorption prediction model (DRAP).

(DRAP) is an online predictor of global D-region absorption provided² by the space weather prediction center (SWPC) of the US national oceanic and atmospheric administration (NOAA). Updated at 1-minute intervals, DRAP predicts the effects of both solar *X*-ray flux and SEPs in the form of a global map of the highest frequency affected by absorption of at least 1 dB on a vertical-incidence ionosonde [i.e. after two-way propagation through the ionosphere]. At polar latitudes, the highest affected frequency [HAF] is defined relative to 10 dB absorption. The 1-dB HAF due to *X*-ray flares in DRAP is determined for the dayside ionosphere using the empirical formula

$$HAF = \left(10 \log[\text{flux } \text{Wm}^{-2}] + 65 \text{ MHz} \right) (\cos \chi)^{0.75} \quad (5.3)$$

Where the *X*-ray flux is measured in the 1-8 Å band from the GOES satellites, and χ is the solar-zenith angle.

The absorption of 30 MHz riometer due to SEP events is determined from the theory of Sauer and Wilkinson [2008]. The model incorporates GOES geostationary satellite measurements of integral proton flux above energy thresholds of 5.2 MeV for the day side ($\chi < 80^\circ$) or 2.2 MeV for the night side ($\chi > 100^\circ$). Specifically,

²<http://www.swpc.noaa.gov/>

based on OV5-6 satellite and riometer observations by [Sellers, 1977], these are

$$A_d = 0.115 [J(E > 5.2 \text{ MeV})]^{1/2} \quad \text{for } \chi < 80^\circ \quad (5.4)$$

$$A_n = 0.020 [J(E > 2.2 \text{ MeV})]^{1/2} \quad \text{for } \chi > 80^\circ \quad (5.5)$$

Where A_d and A_n are the daytime and night-time absorption (dB) respectively and J is the proton flux ($\text{cm}^{-2}\text{s}^{-1}\text{sr}^{-1}$). A simple linear interpolation is used in the region of the solar terminator ($80^\circ < \chi < 100^\circ$). The DRAP model assumes a $f^{-1.5}$ frequency dependence of absorption [Sauer and Wilkinson, 2008] rather than the f^{-2} dependence suggested by Foppiano and Bradley, [1985].

The extent of the polar region is determined from a numerical model of the proton cut-off energy as a function of the invariant latitude and K_p index [Sauer and Wilkinson, 2008]. The cutoff energy then replaces the energy thresholds in the above expressions for A_d and A_n in order to include only protons able to reach the altitude of 50 km.

DRAP gives an estimate of the minimum duration of a PCA event based on analysis of the integral proton flux J ($E > 10 \text{ MeV}$) v time remaining to the end of an SEP event, based on the 30 largest events recorded by GOES in the period 1997-2003. The event duration, D , (in hours) is given as:

$$D = 24.235 \log (J(E > 10 \text{ MeV})/15) \quad (5.6)$$

where J is in ($\text{cm}^{-2}\text{s}^{-1}\text{sr}^{-1}$).

However, Rogers [2014] identified some limitations on the DRAP model and made some recommendations as in [1-3] below:

1. DRAP uses only integrated proton flux measurements from GOES and does not consider the spectral hardness of the energy spectrum, although including this information may provide only marginal improvement [Sellers *et al.*, 1977; Kavanagh, 2004].

2. It is assumed in the model that the proton flux at the GOES satellite geostationary orbit location is equivalent to that at higher latitudes, although it is noted by [Sauer and Wilkinson, 2008] that a component of proton flux at the GOES satellite is from lower-energy particles trapped in the closed geomagnetic field which may

not immediately precipitate into the ionosphere. The model could be improved using flux measurements from a satellite outside the magnetosphere in the solar wind [such as ACE].

3. The model may be improved near the solar terminator [$80^\circ < \chi < 100^\circ$], since the present linear interpolation to day and night-side absorption models is only a practical measure with no physical basis.

The DRAP model is distinct in that it considers proton precipitation, usually associated with polar cap absorption. PCA events cause strong radio absorption (typically 1-5 dB at 30 MHz) and persist across the whole polar cap region [$\gtrsim 65^\circ$ geomagnetic latitude] in both hemispheres, lasting for several days [with longest duration at the highest latitudes]. It is likely to cause an HF communications “blackout” in the region, during which HF propagation is not supported by the ionosphere. PCA is caused by the precipitation of highly energetic [1-200 MeV] protons which originate in solar flares and may be accelerated by shocks in the solar wind driven by coronal mass ejections [Shea and Smart, 1995]. The proton storm may be detected by satellites and designated a solar proton event (SPE). The geomagnetic latitude to which PCA’s extend is dependent on the ‘rigidity’ of the precipitating particles, defined as [Hunsucker and Hargreaves, 2007].

$$R = \frac{Pc}{z|e|} \quad (5.7)$$

Where P is the momentum, c is the speed of light, z is the atomic number and e is the charge on the electron. Analysis of particle trajectories in a dipole magnetosphere by Størmer, [1955] found that particles precipitating [vertically] to a minimum ‘cut-off’ magnetic latitude of λ_c required a minimum rigidity of [Hunsucker and Hargreaves, 2007 ; Davies, 1990]

$$R_c = 14.9 \cos^4 \lambda_c \quad (5.8)$$

Where R_c is in gigavolts (GV). A more precise calculation of the cut-off latitude requires a computer program, an example of which was developed for NASA by Smart and Shea [2001] and available online³. In this program the trajectory of the

³<http://ccmc.gsfc.nasa.gov/modelweb/sun/cutoff.html>

particle is traced vertically up from a ground location through the International Geomagnetic Reference Field [IGRF].

In Figure 5.5 it is clear that at higher invariant latitudes, the cut off energy is low and vice-versa.

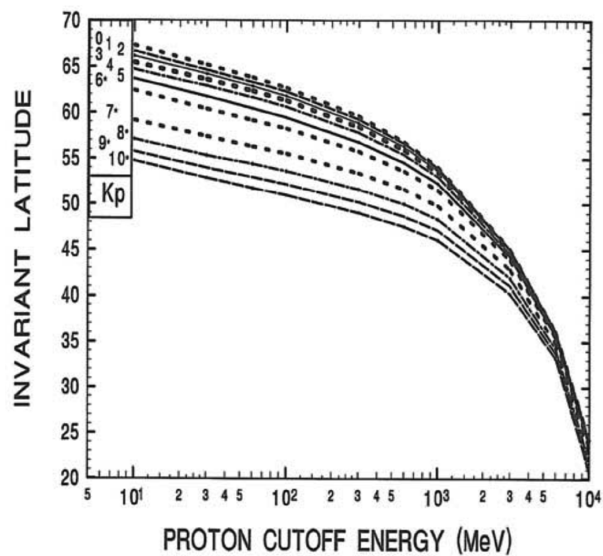


Figure 5.5: Proton cutoff energy versus invariant latitude as a function of geomagnetic activity K_p [From Saucer and Wilkinson, 2008]

5.6 Methodology

5.6.1 Event selection criteria

This study aims to analyse cosmic noise absorption using the superposed epoch analysis method. Events used in the epoch analysis study were the 314 events of the ICME catalogue compiled by Cane and Richardson [2010]. The list comprises ICME events occurring within 1996-2009. For the same period identified in the ICME catalogue CNA data are available from IRIS, Kilpisjärvi. All the 315 events could not be accommodated for this analysis, some events were omitted following the below criteria:

1. Events with incomplete data coverage
2. Over-lapping events (i.e. subsequent ICME events occurred within 48 hours of the start of an earlier event)

3. When no clear minimum in the D_{st} index could be observed, indicating that there is no geomagnetic storm driven by solar wind structure

Based on these criteria, 176 events were available. The available events were further classified into day and night events based on solar zenith angle. Data in the range of solar zenith angles $< 80^\circ$ are classified as day events while zenith angles $> 100^\circ$ are classified as night events. After [Sellers *et al.*, 1977] as in equations (5.4) and (5.5) above. Base on the classification, 112 events are night events while 89 are day events. Superposed epoch analysis is performed for day and night events. The result is discussed in Section 5.7.

5.6.2 Epoch analysis

Previous studies such as Longden, 2007 and 2008; Kavanagh *et al.*, 2012; Denton *et al.*, 2006 utilised epoch analysis for cosmic noise absorption during ICME events. For example, Kavanagh *et al.*, [2012] observed CNA variation during high solar wind stream events. The results are as shown in Figure 5.6.

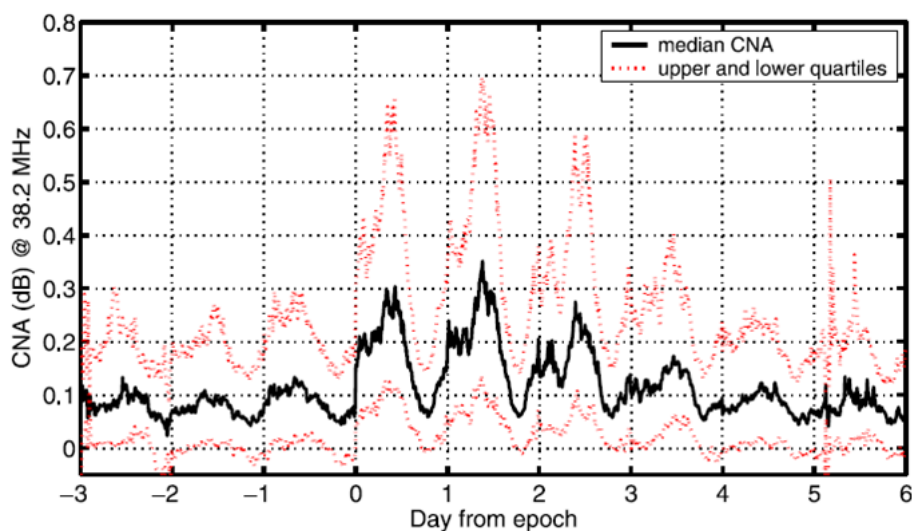


Figure 5.6: An epoch analysis of the CNA response at IRIS to HSSs presented as a time series in MLT. The black line is the median value from the central beam; the dotted red lines show the interquartile range [Kavanagh *et al.*, 2012].

From Figure 5.6, median absorption shows an increasing trend just before zero epoch, peaks after ~ 6 hours and gradually decreases. This trend is seen clearly for

about 2 days from zero epoch. In Longden *et al.*, [2008] (Figure 5.7), mean values of CNA were utilised. In this instance, the increasing trend is seen for zero epoch and a peak after ~ 5 hours. Although there are 2 peaks seen in Figure 5.7, one is seen ~ 3 hours before zero epoch and the other ~ 5 hours after zero epoch. This is because the CNA utilised was not categorised into day and night time events. There maybe different peaks for day time events different from night time events (see equations 5.4 and 5.5). The data utilised in this chapter was categorised as day and night time events to underscore the different peak periods of day and night time ICME events.

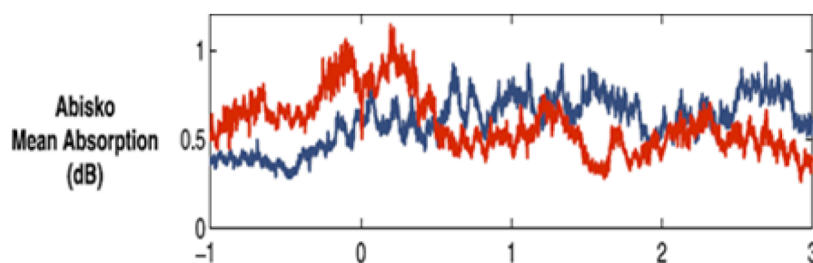


Figure 5.7: An epoch analysis of the superposed epoch time series of 33 ICME-driven storms [Red line] and 38 CIR storms [Blue]. Mean CNA from the Abisko riometer. The zero epoch is the time of the first clear minimum in D_{st} for each event [Longden *et al.*, 2008]. There are 2 peaks observed observed, the first at ~ 3 hours before zero epoch and the second ~ 5 hours after zero epoch.

In Denton *et al.*, [2006], the zero epoch of the analysis was taken as the first clear minimum observed in the D_{st} index following the arrival of the solar wind structure at the magnetosphere. For each event, data was taken a day before the zero epoch and 3 days after zero epoch. This is to account for the three phases of storm, namely: onset, main phase and recovery phase.

In this study, epoch analysis of median absorption is performed for CNA for the central beam of IRIS (beam 25) with data resolution of 5 minutes. The epoch analysis is implemented for selected events following the criteria in Section 5.5.1 for day and night time events. The result of the epoch analysis is shown in Figure 5.8.

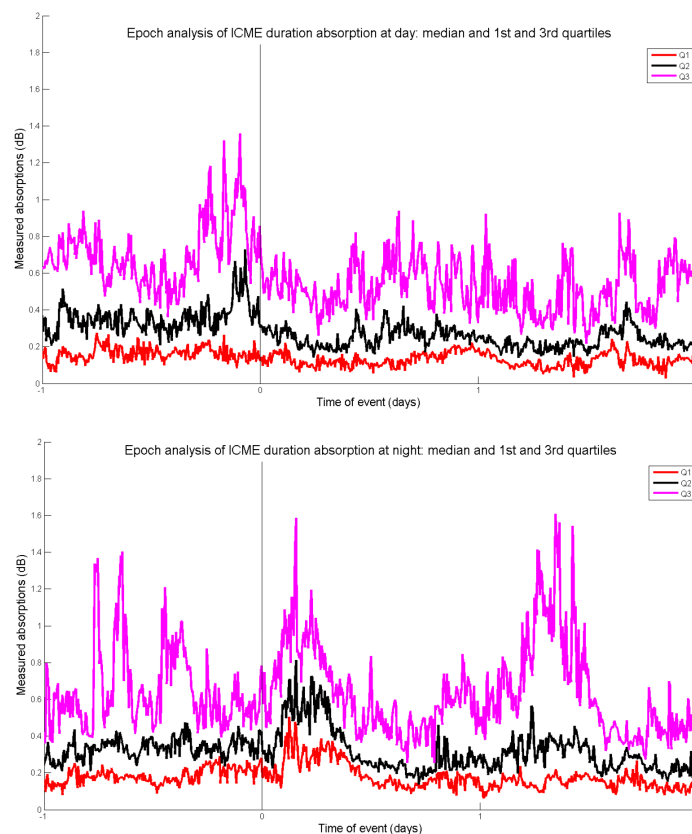


Figure 5.8: Epoch analysis [−1 day to 2 days] of IRIS CNA absorption (dB). Top panel is absorption during day time commencing ICME events, bottom panel is absorption during night time commencing ICME events during [1996-2009]. The black line is the median (Q2) value while Q3 and Q1 are the upper and lower quartiles respectively.

CNA for day time and night time ICME events [1996-2009].

5.7 Observations

The key features observed from top and bottom panels of Figure 5.8 can be explained from the differing response of the ionosphere to radio absorption based on time of the day. Previous works [e.g. Agy 1972, Foppiano and Bradley, 1984, Hartz and Brice, 1967, Hargreaves, 1966, 2009, Greenberg and LaBelle, 2002] explained the effect of drizzling and splash precipitation pattern. The splash term corresponds to discrete phenomena (i.e the substorm aurora) synonymous with night events, this most times show abrupt auroral absorption events on riometer record, while the drizzle term corresponds with diffuse phenomena that maximize in the late morning

hours, it also corresponds with slowly varying riometer absorption. Figure 5.8 shows that for night events, absorption gradually increases after zero epoch, peaks after about 4 hours followed by a decreasing trend. For day-time commencing events, the increase is noticed few hours before zero epoch with peak observed ~ 2 hours before the zero epoch. The point at which the peak absorption is noticed with reference to zero epoch underscores a clear difference in the distribution of CNA for the two category of times. While maximum absorption signature precedes zero epoch for day commencing events, for night time commencing events, maximum absorption is observed post zero epoch. This illustrates that the absorption due to particle precipitation precedes the minimum in D_{st} [zero epoch]. A stronger absorption response would be observed in the daytime ionosphere. When the minimum D_{st} occurs at night there will be a delay before absorption increases at sunrise. It is also observed that the magnitude of absorption is higher for night time events than the day time events.

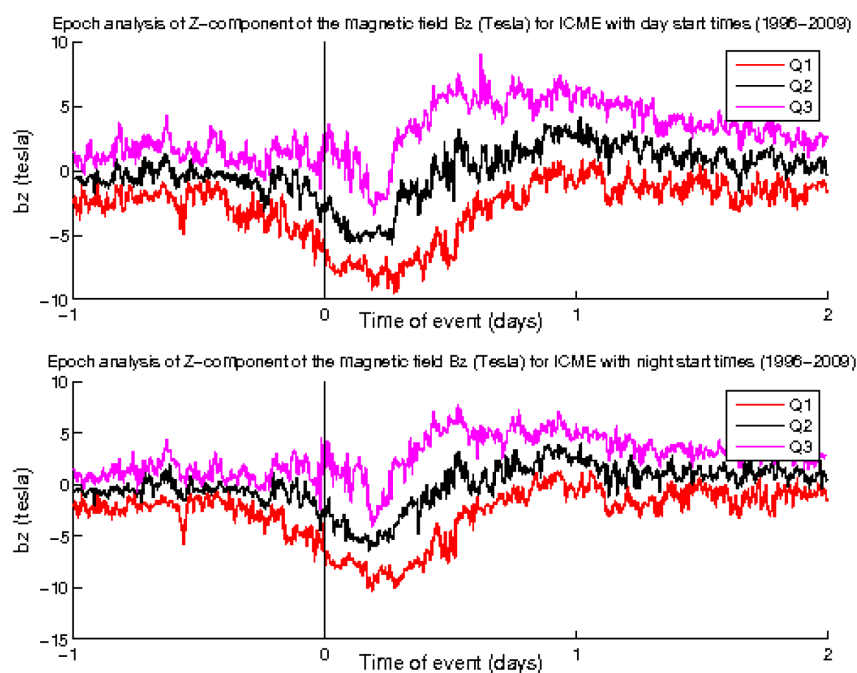


Figure 5.9: Epoch analysis $[-1$ to 2 days] of the z -component of IMF (B_z -(nT)). Top panel is for day time commencing ICME events, bottom panel is for night time commencing ICME events during $[1996-2009]$. The black line is the median (Q2) value while Q3 and Q1 are the upper and lower quartiles respectively.

5.8 Model and parameterisation

Kavanagh *et al.*, [2004] have shown that there are statistical relationship between absorption, geomagnetic and solar wind parameters. In order to identify coupling parameters for day and night time absorption, this work first explores statistical relations between day and night absorption and some geophysical and solar wind parameters such as the dynamic pressure, the z -component of the IMF, and IMF clock angle. Figures 5.9-5.11 shows epoch analysis of geophysical and solar wind parameters during day time and night time ICME events.

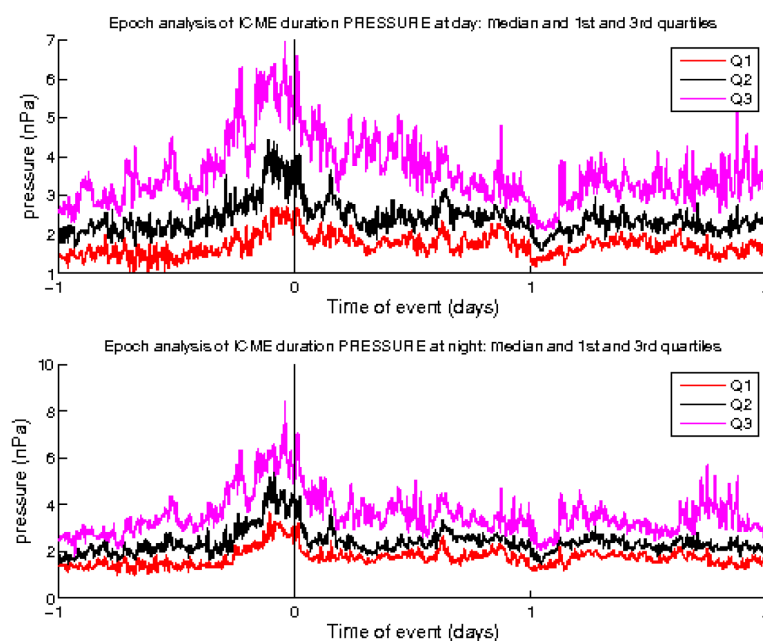


Figure 5.10: Epoch analysis [−1 to 2 days] of the dynamic pressure (nPa). Top panel is pressure variation during day time commencing ICME events. Bottom panel is for night time commencing ICME events during [1996-2009]. The black line is the median (Q2) value while Q3 and Q1 are the upper and lower quartiles respectively.

Comparing Figures 5.8-5.11, further observations are seen in the ICME leading edge typical ICME features represented in many of the plots. For example, (B_z) is negative in the leading edge of the ICME in the night events and there is enhanced energy deposition rate during ICME passage, while there is enhanced dynamic pressure in the magnetosheath ahead of the ICME in the day events.

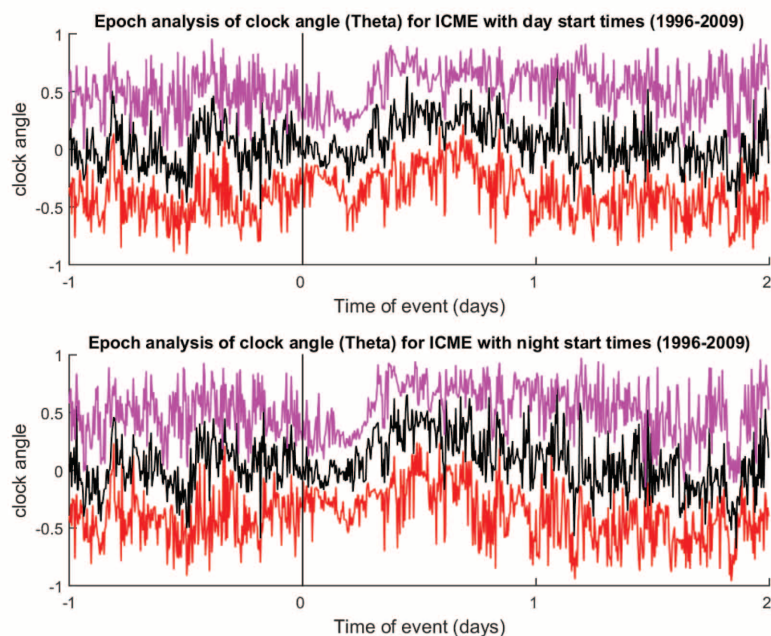


Figure 5.11: Epoch analysis $[-1$ to 2 days] of $[\sin(\theta/2)]$ where θ is the clock angle. Top Panel is for day time commencing ICME event. Bottom Panel is for night time commencing ICME events during [1996-2009]. The black line is the median (Q2) value while Q3 and Q1 are the upper and lower quartiles respectively.

The ICME results seem generally similar for night and day events (the only difference is seen is that the point of maximum signature for day event is different from the point of maximum signature for night time events) as might be expected since the ICME parameters are not dependent on time of day. Except in the absorption plot. In relating these parameters, the dayside absorption events are related to the arrival of the shock at the sheath and the increased dynamic pressure, which might have most impact on the day side, whereas the night absorption events are more associated with energy deposition related to reconnection, possibly into the tail, which might account for the effects on the night side and substorms.

For the day time absorption, the dynamic pressure appears better correlated, however, the correlation coefficients from the scattered plots are somewhat poor for dynamic pressure and day absorption ($r \sim 0.14$) for (B_z) against night time absorption the correlation coefficient ($r \sim 0.44$). In Figure 5.12, the maximum of day time absorption and dynamic pressure occur almost at the same time.

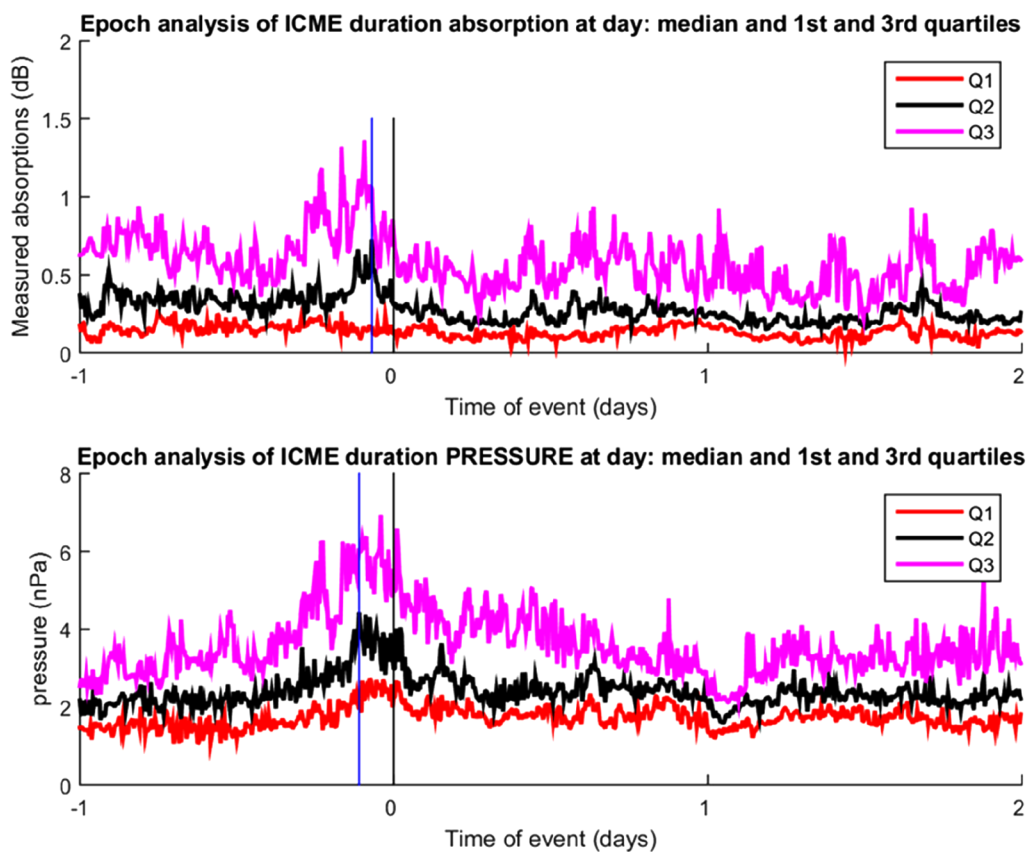


Figure 5.12: Epoch analysis of solar wind dynamic pressure on the top panel, with the epoch analysis of day time absorption on the bottom panel. The maximum point of the top and bottom panel shows a delay of 60 minutes (~ 2 hours before start time) showing that dynamic pressure bears corresponding effect on day time absorption. The events analysed are ICME events during [1996-2009].

For night time absorption, the maximum point corresponds with the point of strongest depression in B_z with 25 minutes delay (Figure 5.14). In the search for possible coupling parameter for absorption, apart from studying relationship with geophysical parameters, this work also consider geophysical indices. The results of relations between day and night time absorption signature compared with geophysical indices of K_p and auroral electrojet (AE) are shown in Figures 5.17-5.22.

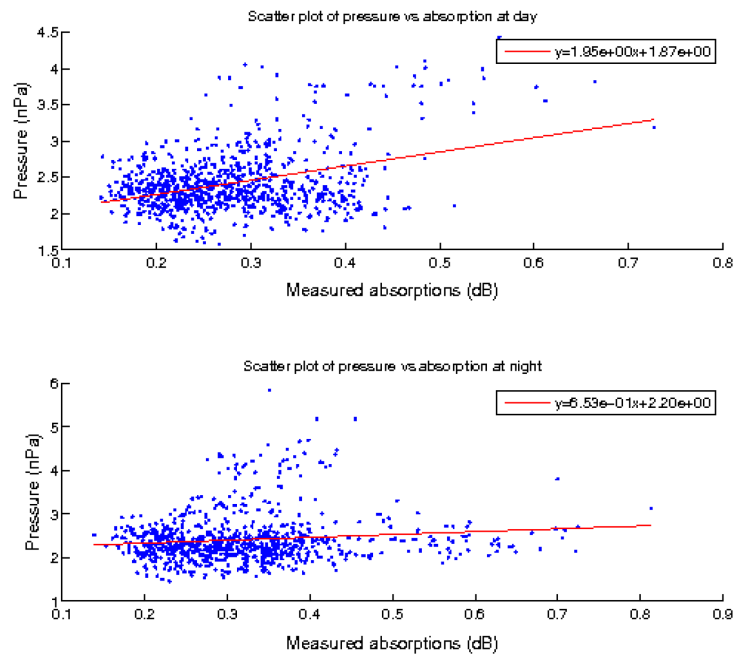


Figure 5.13: Plot of pressure (nPa) against absorption (dB) for day and night time commencing absorption. Top Panel is for day time commencing ICME events.

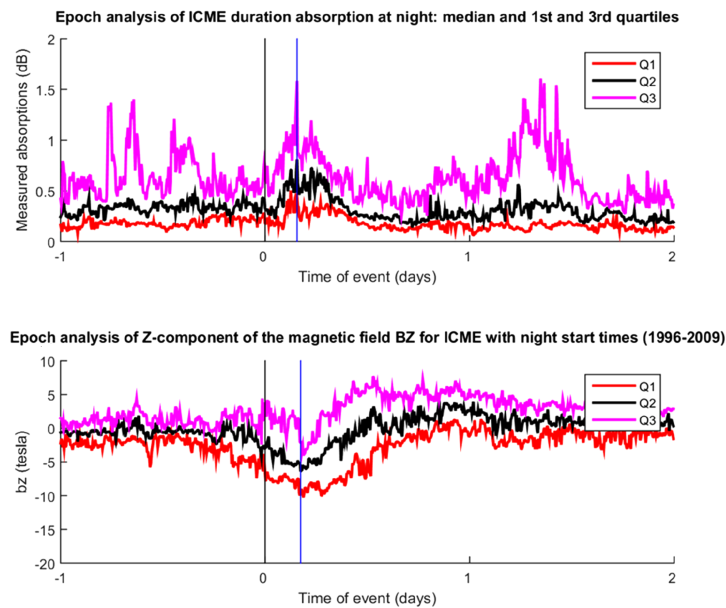


Figure 5.14: Epoch analysis of night time absorption on the top panel, with the epoch analysis of z-component of the magnetic field (B_z) (nT) i.e the unit of B_z on the bottom panel. The maximum point of the top and bottom panel differ with a delay of 25 minutes (~ 5 hours after start time) showing that B_z bears corresponding effect on night time absorption. The events analysed are ICME events during [1996-2009].

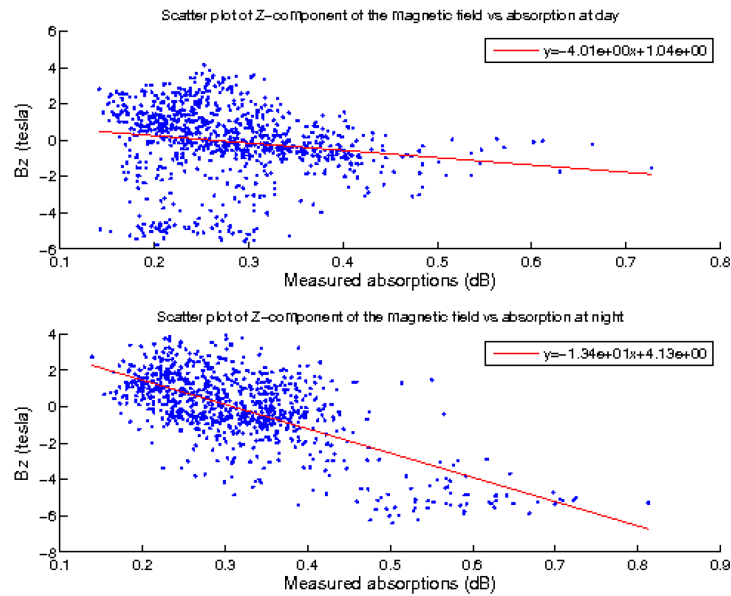


Figure 5.15: Plot of z -component of the IMF ($(B_z)(nT)$) against absorption (dB) for day and night time commencing absorption. Top panel is for day time commencing ICME events with a correlation coefficient $R = -0.027$, bottom panel is for night time commencing ICME events with a correlation coefficient $R = -0.44$. Dataset are for solar cycle 23 [1996-2009].

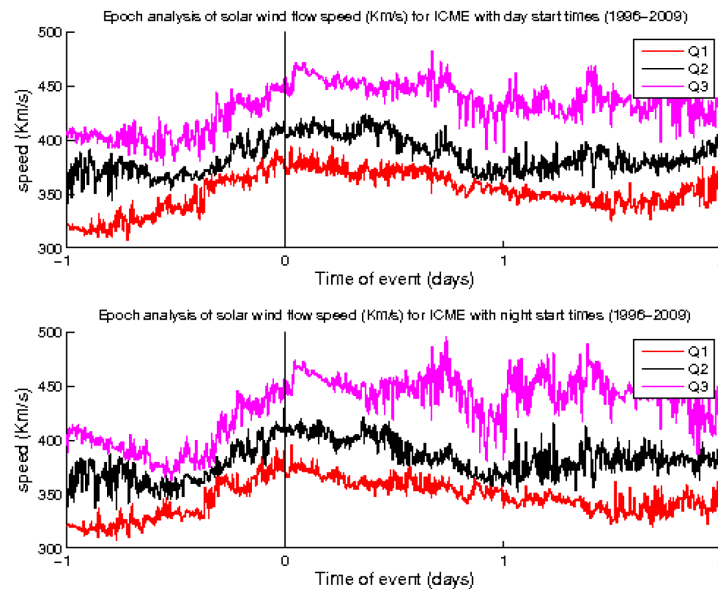


Figure 5.16: Epoch analysis $[-1$ to 2 days] of solar wind speed during ICME events. Top panel is for day time commencing ICME event, bottom panel is for night time commencing ICME events during [1996-2009]. The black line is the median (Q2) value while Q3 and Q1 are the upper and lower quartiles respectively. A steady rise in solar wind speed form (~ 6 hours before start time) up to start time (0), in both day and night time ICME events is observed.

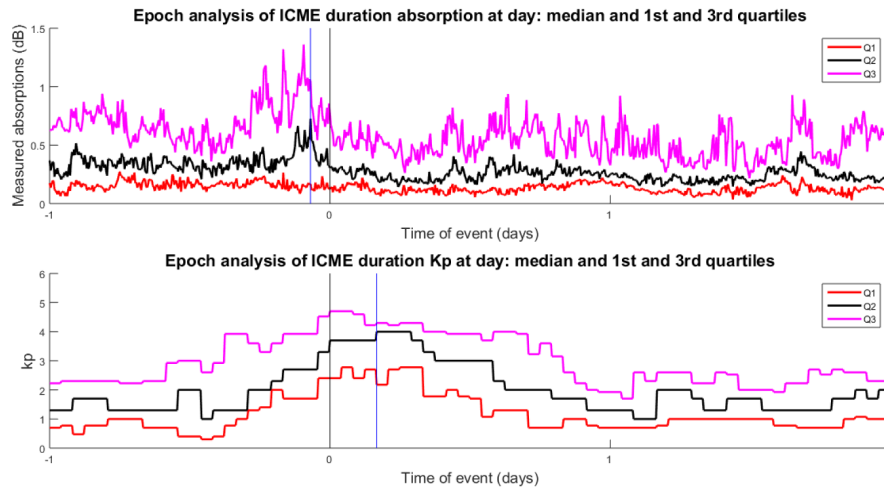


Figure 5.17: Epoch analysis $[-1$ to 2 days] of day time absorption signature and K_p index. Top Panel is for day time absorption signature, bottom panel shows K_p variation for day time ICME events [1996-2009]. The black line is the median (Q2) value while Q3 and Q1 are the upper and lower quartiles respectively. A gradual increase in K_p is seen from (~ 4 hours) before start time up to ~ 4 hours after start time (maximum point).

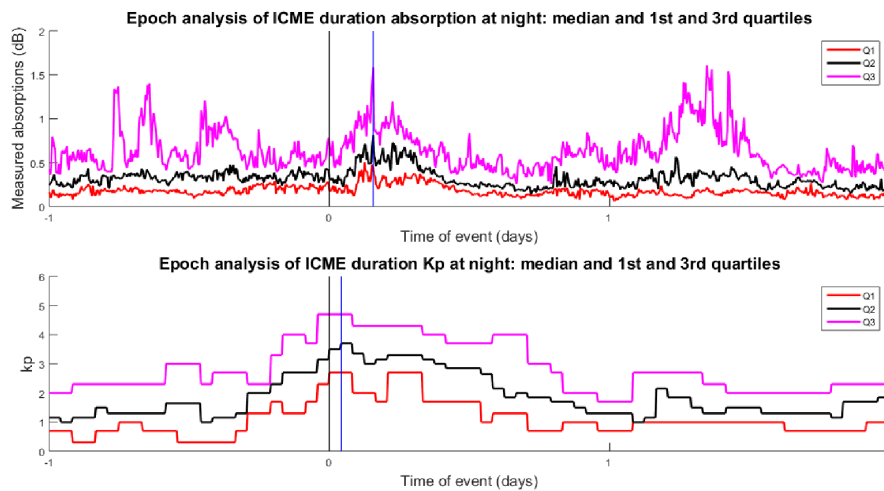


Figure 5.18: Epoch analysis $[-1$ to 2 days] of night time absorption signature and K_p index. Top panel is for night time absorption signature, bottom panel shows K_p variation for night time ICME events [1996-2009]. The black line is the median (Q2) value while Q3 and Q1 are the upper and lower quartiles respectively. A gradual increase in K_p is seen from (~ 6 hours) before start time up to ~ 1.5 hours after start time (maximum point).

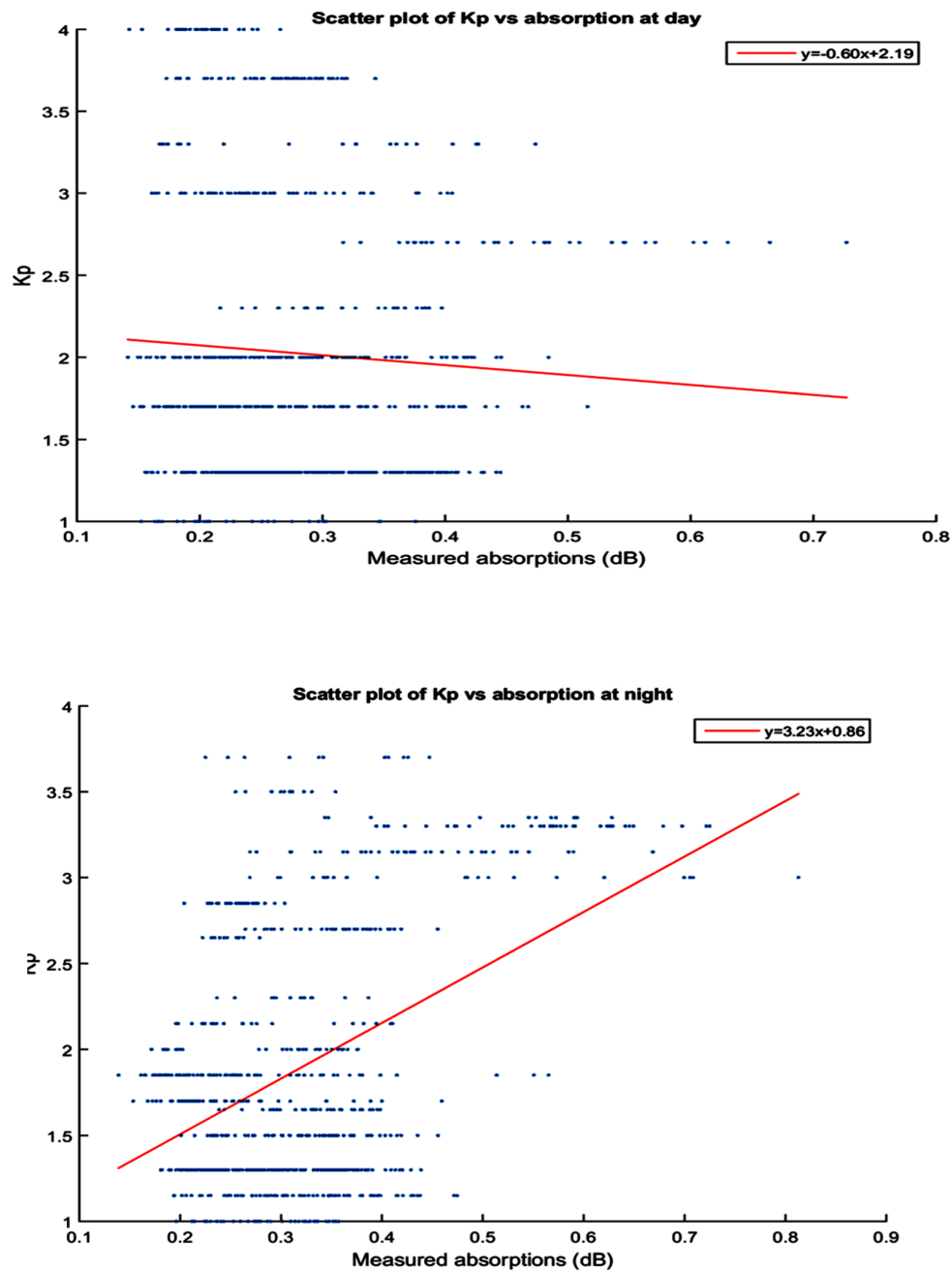


Figure 5.19: Plot of K_p index against median (dB) for day and night time commencing absorption. Top panel is for day time commencing ICME events with a correlation $R = 0.0022$. Bottom panel is for night time commencing ICME events $R = 0.189$. Dataset are for solar cycle 23 [1996-2009].

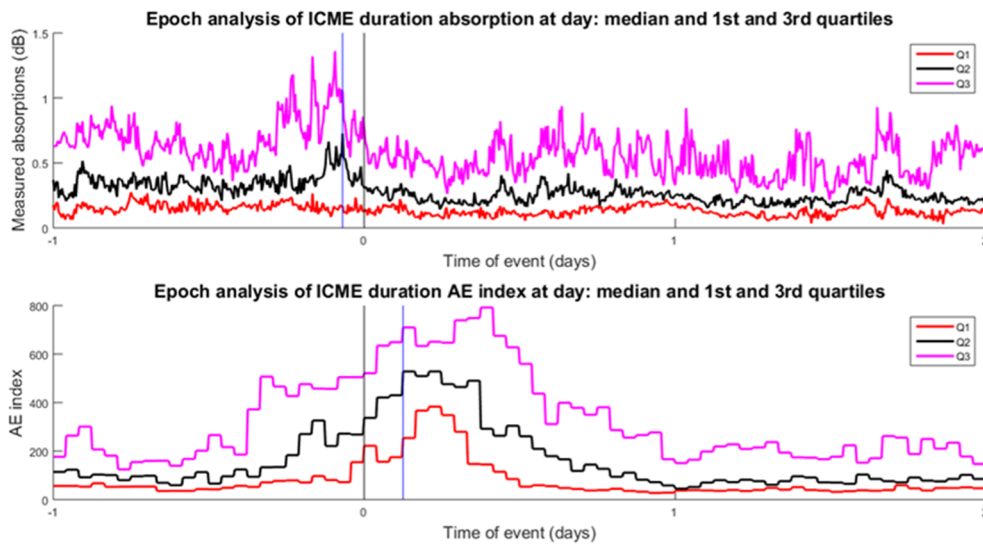


Figure 5.20: Epoch analysis [−1 to 2 days] of day time absorption signature and auroral electroject (AE) index. Top Panel is for day time absorption signature, bottom panel shows AE variation for day time ICME events [1996-2009]. The black line is the median (Q2) value while Q3 and Q1 are the upper and lower quartiles respectively. A gradual increase in K_p is seen from (~ 6 hours) before start time up to ~ 2 hours after start time (maximum point).

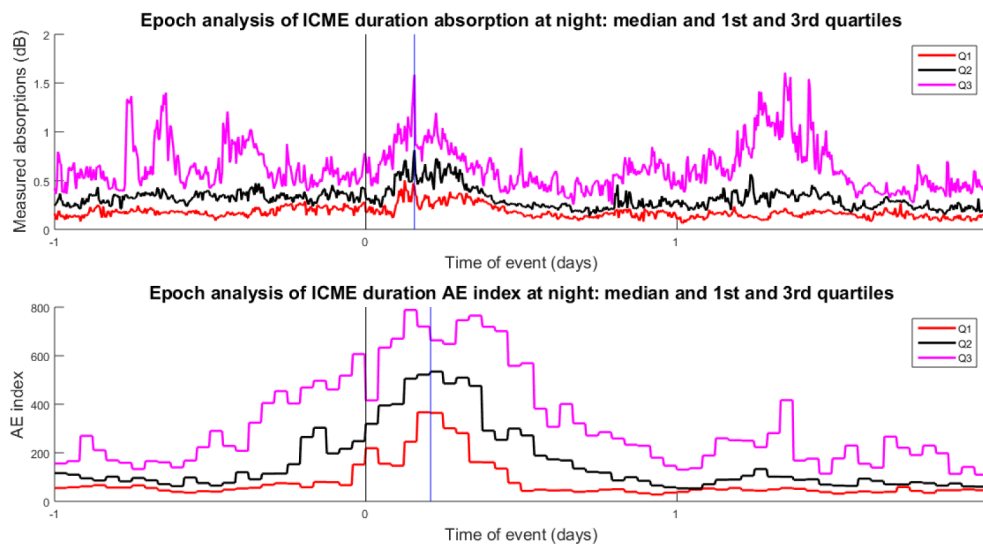


Figure 5.21: Epoch analysis [−1 to 2 days] of night time absorption signature and auroral electroject (AE) index. Top panel is for day time absorption signature, bottom panel shows AE variation for night time ICME events [1996-2009]. The black line is the median (Q2) value while Q3 and Q1 are the upper and lower quartiles respectively. A gradual increase in K_p is seen from (~ 8 hours) before start time up to ~ 5 hours after start time (maximum point).

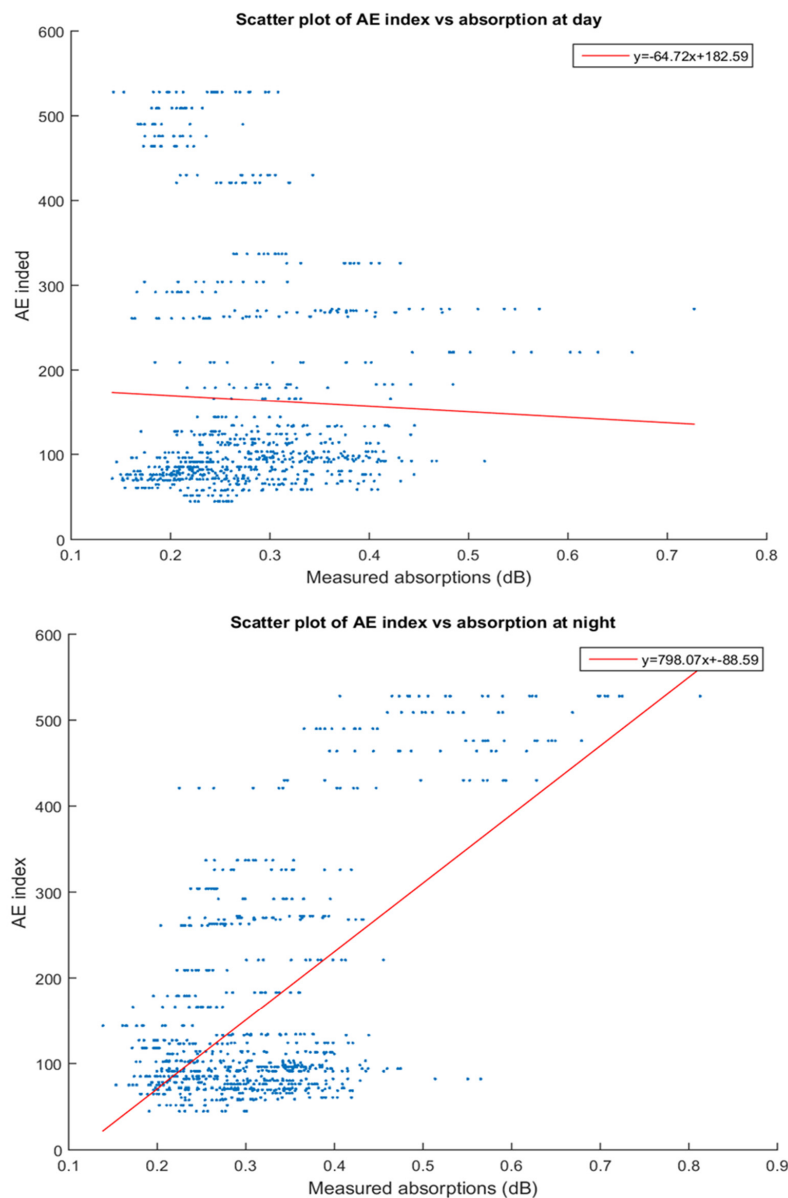


Figure 5.22: Plot of AE index against absorption (dB) for day and night time commencing absorption. Top panel is for day time commencing ICME events with a correlation $R = 0.016$. Bottom panel is for night time commencing ICME events $R = 0.3696$. The day plot(top panel) has negative correlation while the night plot(bottom panel) shows positive correlation. Dataset are for solar cycle 23 [1996-2009].

Tables 5.7 and 5.8 have a summary of the correlation coefficient of geophysical indices and parameters as they fair in predicting absorption.

Table 5.7: Showing parameters of goodness of fit (GOF) for day time ICME Absorption

Parameters	SSE	RSQUARE	DFE	ADJRSQUARE	RMSE
AE	1.5234×10^7	0.0016	862	4.2325×10^{-4}	132.9384
B_z	3.3180×10^3	0.0272	862	0.0261	1.9619
Clock angle	32.3885	1.1182×10^{-4}	862	-0.0010	0.1938
Dynamic Pressure	134.0819	0.2208	862	0.2198	0.3944
K_p	620.4112	0.0034	862	0.0022	0.8484
Solar wind velocity	1.0567×10^9	0.0159	862	0.0148	1.1072×10^3

Table 5.8: Showing parameters of goodness of fit (GOF) for night time ICME Absorption

Parameters	SSE	RSQUARE	DFE	ADJRSQUARE	RMSE
AE	9.6187×10^6	0.3696	862	0.3689	105.6340
B_z	1.9913×10^3	0.4428	862	0.4421	1.5199
Clock angle	44.0171	0.0029	862	0.0017	0.2260
Dynamic pressure	258.8395	0.0144	862	0.0132	0.5480
K_p	394.6821	0.1897	862	0.1888	0.6767
Solar wind velocity	1.4923×10^9	0.0633	862	0.0622	1.3157×10^3

From the above table, B_z ranks best for night time absorption based on the correlation coefficient (Rsquare) values and dynamic pressure for day time absorption. Parameterisation for day time absorption based on the best ranking parameter (i.e. dynamic pressure) and for the highest night time ranking parameter (B_z) are investigated using the equation of relation as in equations (5.9) and (5.10) below. Y give the absorption (dB) while X gives the value of the dynamic pressure (nPa) in (5.9) and $X = B_z$ in (5.10).

$$Y = 0.07209X + 0.1046 \quad (5.9)$$

$$Y = -0.03312X + 0.3136 \quad (5.10)$$

Using the derived relation to generate modelled result that could be compared with IRIS measurements for recent ICME events; the result is as shown in Figure 5.23-5.27.

From Figure 5.23-5.27 above it is seen that the model based on single parameters (i.e. B_z for night and dynamic pressure for day) does not adequately represent measured absorption. This will be expected considering the goodness of fit (GOF) parameters in Table 5.7 and 5.8. In a quest to improve these models, this work will explore the use of combined parameters such that predicting absorption will be consequent on more than one solar wind parameter. In a previous work, Newell *et al.*, [2008] investigated different characterisations of the magnetosphere using geomagnetic indices. They conclude that the use of pressure related parameters and merging related parameters yield an improvement in predicting the characterisation of the magnetosphere.

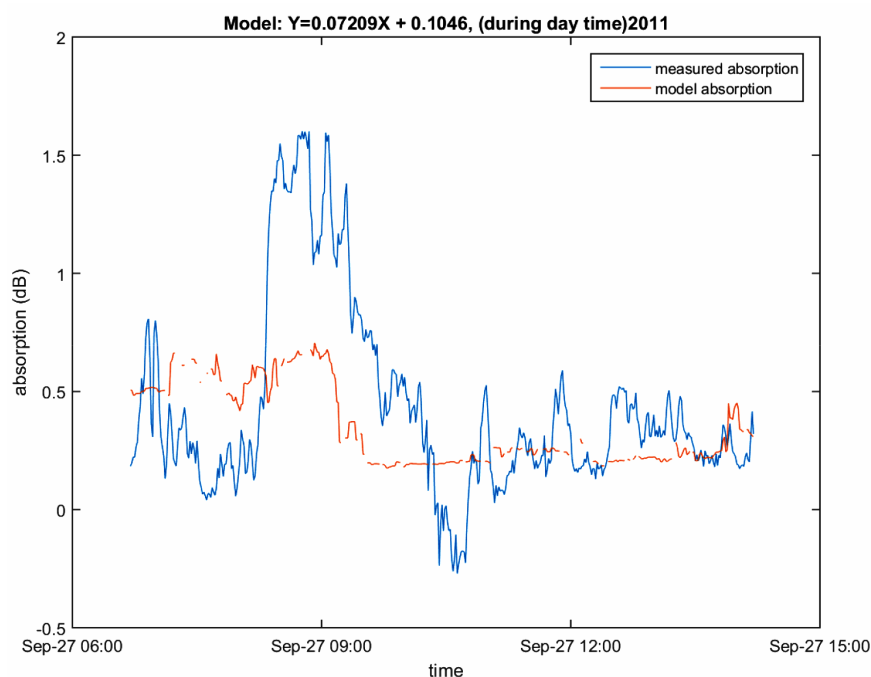


Figure 5.23: IRIS v modelled absorption for ICME event of 27th September, 2011. This event is classified as day time event. The modelling utilised the dynamic pressure as the coupling parameter for absorption.

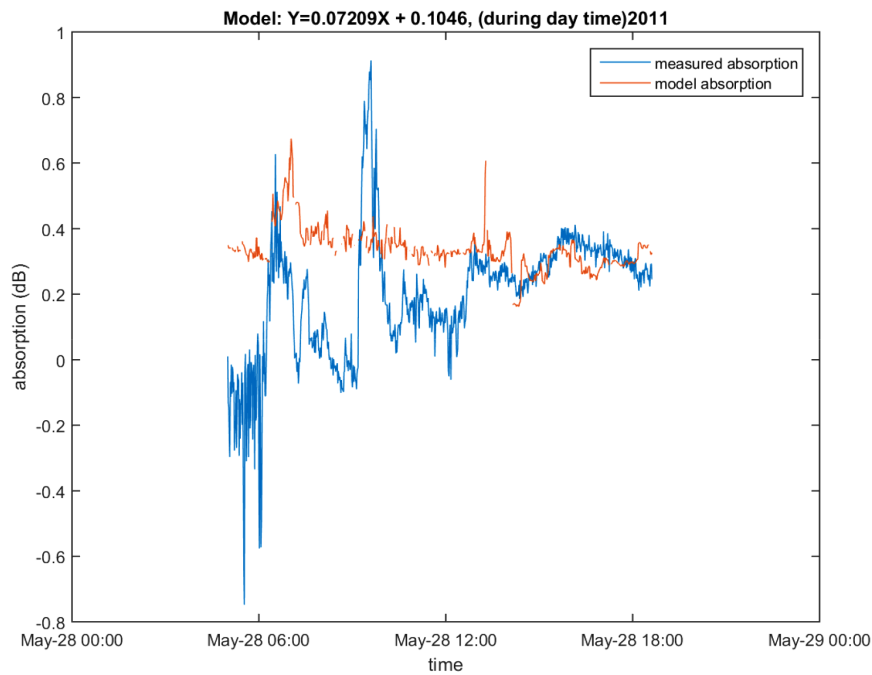


Figure 5.24: IRIS v modelled absorption for ICME event of 28th May, 2011. This event is classified as day time event. The modelling utilised the dynamic pressure as the coupling parameter for absorption.

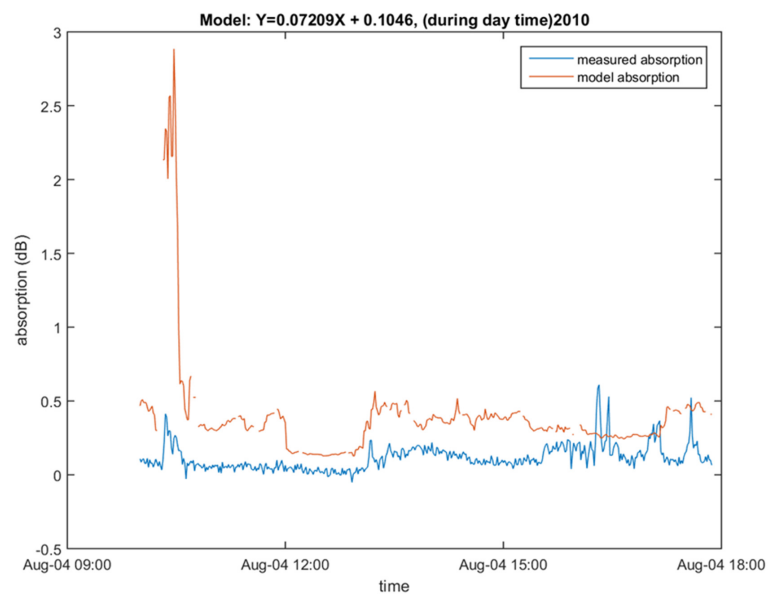


Figure 5.25: IRIS v modelled absorption for ICME event of 4th August, 2010. This event is classified as day time event. The modelling utilised the dynamic pressure as the coupling parameter for absorption.

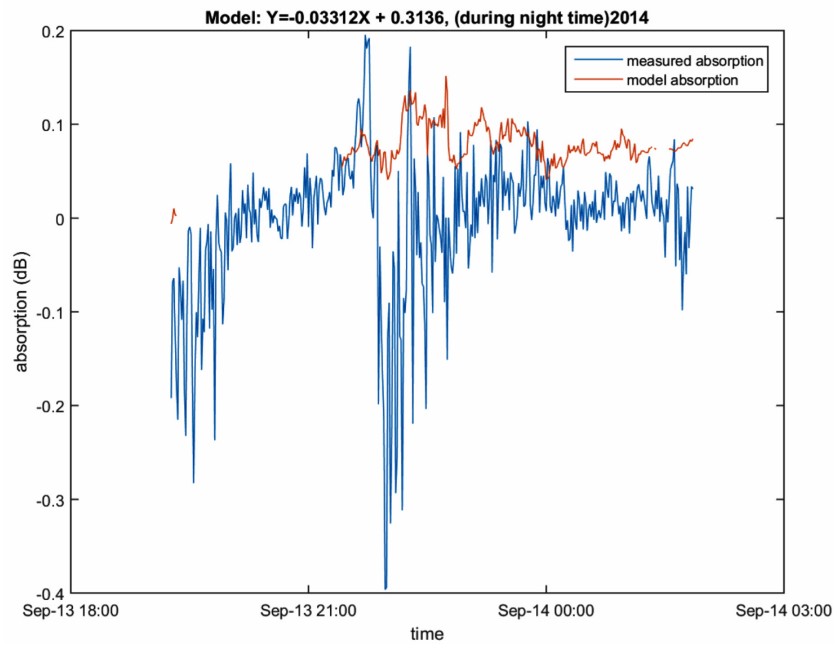


Figure 5.26: IRIS v modelled absorption for ICME event of 13th September, 2014. This event is classified as night time event. The modelling utilised the z -component of the magnetic field (B_z) as the coupling parameter for absorption.

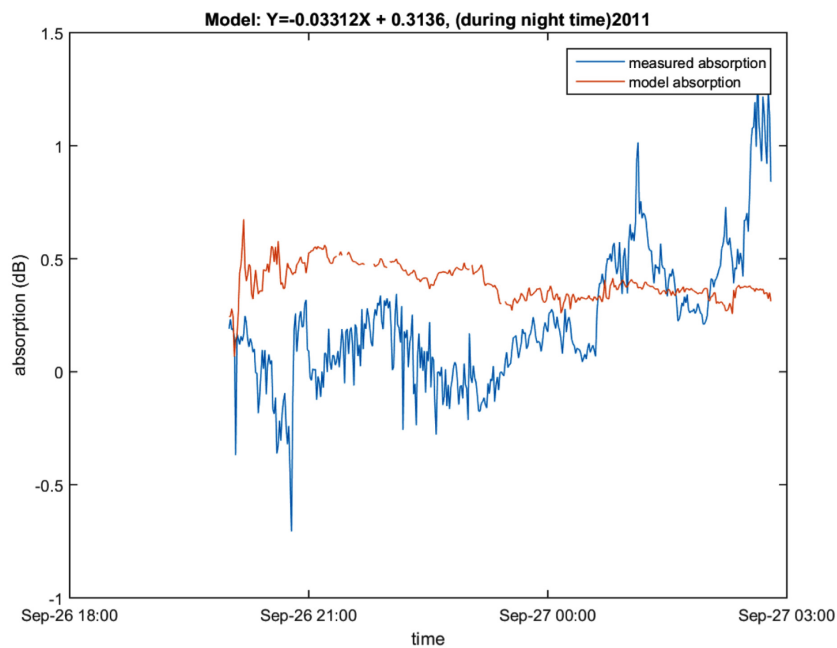


Figure 5.27: IRIS v modelled absorption for ICME event of 26th September, 2011. This event is classified as night time event. The modelling utilised the z -component of the magnetic field (B_z) as the coupling parameter for absorption.

The use of solar wind parameters over geomagnetic indices as coupling parameter for absorption is thought to be better because geomagnetic indices are synthesised from data and are not available in real time like upstream data, hence it will be better to utilise only upstream data as coupling parameters. This work then considers 6 viscous terms (pressure related parameters) and 3 IMF related terms (merging terms) that could be combined as a coupling parameters for day and night time absorption. In other to combine terms, the different combination possibilities were considered, a total of 18 combinations are possible if each IMF related terms are to be combined with each pressure related term to form a simple 2 parameter combination.

The pressure terms are mostly derivatives of the product of number density (n) index and velocity. V is measured in $km\ s^{-1}$, n in cm^{-3} , pressure is measured in nanopascal (nPa), B_{Total} and B_z are measured in nanotesla (nT).

These combinations are then ranked based on their correlation coefficient (each formulae is correlated with day and night time absorption), the best combination is then utilised as coupling parameter for day and night time absorption. The combined terms yielded less correlation when utilised as a linear equation, but when utilised as a second order polynomial they yielded better correlation.

Table 5.9: Showing pressure terms (mainly derivatives of number density and velocity) and IMF related (From Newel *et al.*, 2008).

Pressure terms	Magnetic field related terms
$n^{\frac{1}{2}}v^2$	B_z
$n^{\frac{1}{3}}v^2$	B_{Total}
$n^{\frac{1}{2}}v^3$	vB_z
$n^{\frac{1}{6}}v^2$	
nv^3	
p	

The method of combining two parameters has utilised linear regression using the (OLE) ordinary least square estimation. Utilising linear regression with only a first-order model did not result in a good correlation coefficient (R^2). So, to improve the performance, we assumed the model as second-order and polynomial regression was utilised. Polynomial regression is a form of linear regression in which the relationship between the independent variable and the dependent variable is modelled as an n^{th} ($n > 1$) degree polynomial. Polynomial regression is considered to be a special case of multiple linear regressions.

In the case of the combination utilised in this chapter, the independent variable is absorption while the dependent variables are the combined parameters. The first step was to construct a designed matrix (X) which has 6 columns. All of the elements of the 1st column are unitary (1). The second column contains the elements of the first parameter (i.e. pressure for day time absorption, B_z in the case of night time events). The third column consists of the second parameter (i.e. VB_z for day time events and nV^3 for night time events). The fourth column consists of the square of the first parameter (i.e. square of pressure for day time events and square of B_z for night time events). The fifth column consists of the product of the two combined parameters (i.e. product of pressure and VB_z for day time events, product of B_z and nV^3 for night time events). The sixth column has the square of the second parameter $(VB_z)^2$ for day time and $(nV^3)^2$ for night time events). In order to be able to compute the coefficients of the 6 defined variable, ordinary least square (OLS) method was applied.

$$Y = X \times \text{beta} + \text{epsilon}$$

According to OLS,

$$\text{beta} = (X^T X)^{-1} X^T y$$

So, Beta has 6 elements, beta(1) is the coefficient for constant, beta(2) is the coefficient for the first term (i.e. pressure for day, B_z for night), beta (2) are also computed. Hence parameters of the equations (5.10) and (5.11) are determined.

Table 5.10: Combination of terms as coupling coefficient for day time absorption and their correlation coefficients

Ranking number	Pressure term	IMF term	Correlation Coefficient
1	p	vB_z	0.615
2	$\frac{1}{n^2}v^2$	B_z	0.561
3	$\frac{1}{n^2}v^2$	B_{Total}	0.524
4	$\frac{1}{n^2}v^3$	B_{Total}	0.513
5	nv^3	vB_z	0.505
6	p	B_{Total}	0.483
7	$\frac{1}{n^3}v^2$	vB_z	0.354
8	nv^3	B_{Total}	0.267
9	nv^3	B_z	0.186
10	$\frac{1}{n^3}v^2$	B_{Total}	0.144
11	$\frac{1}{n^3}v^2$	B_z	0.123
12	$\frac{1}{n^2}v^2$	vB_z	0.121
13	$\frac{1}{n^6}v^2$	B_z	0.094
14	nv^3	vB_z	0.052
15	$\frac{1}{n^2}v^3$	B_z	0.041
16	$\frac{1}{n^6}v^2$	vB_z	0.038
17	$\frac{1}{n^6}v^2$	B_{Total}	0.029
18	p	B_z	0.016

For day time absorption, the first ranking pair (pressure and vB_z) are utilised as coupling parameters, they are related by equation (5.11)

$$\begin{aligned} \text{DAY ABSORPTION} &= \\ &= 0.628 - 0.313X - 0.9 \times 10^{-4}Y + 0.071X^2 + 0.000025XY - Y^2 \end{aligned} \quad (5.11)$$

Where X is pressure (nPa) and Y is vB_z .

Figure 5.28 shows IRIS absorption and the model result for day time ICME events. Example plots for individual events are as in Figures 5.29-5.31 below.

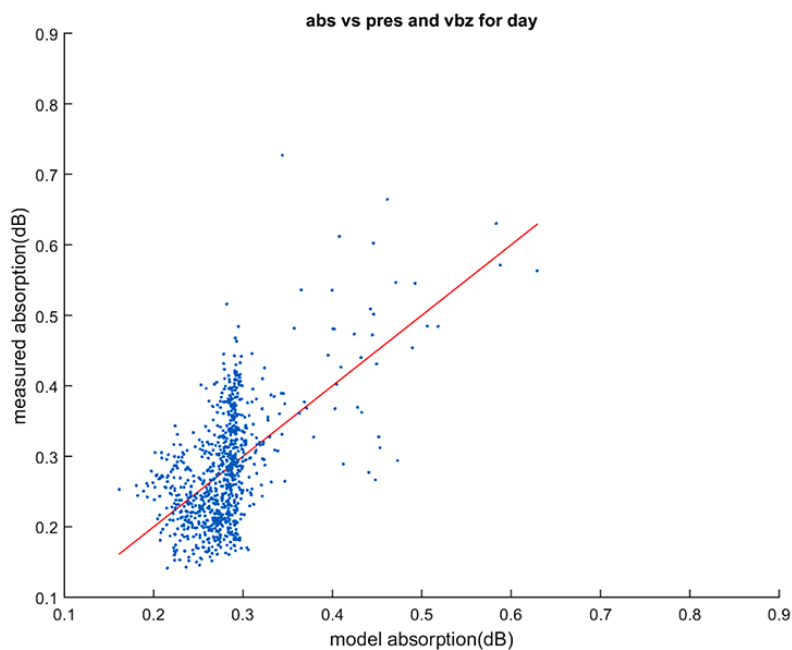


Figure 5.28: Measured absorption v modelled result for day time absorption during ICME events of 1996-2009.

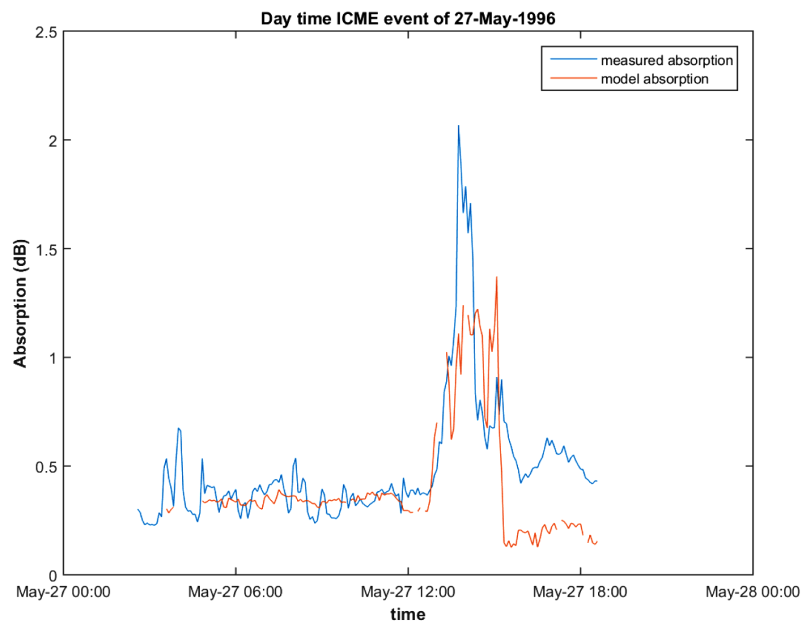
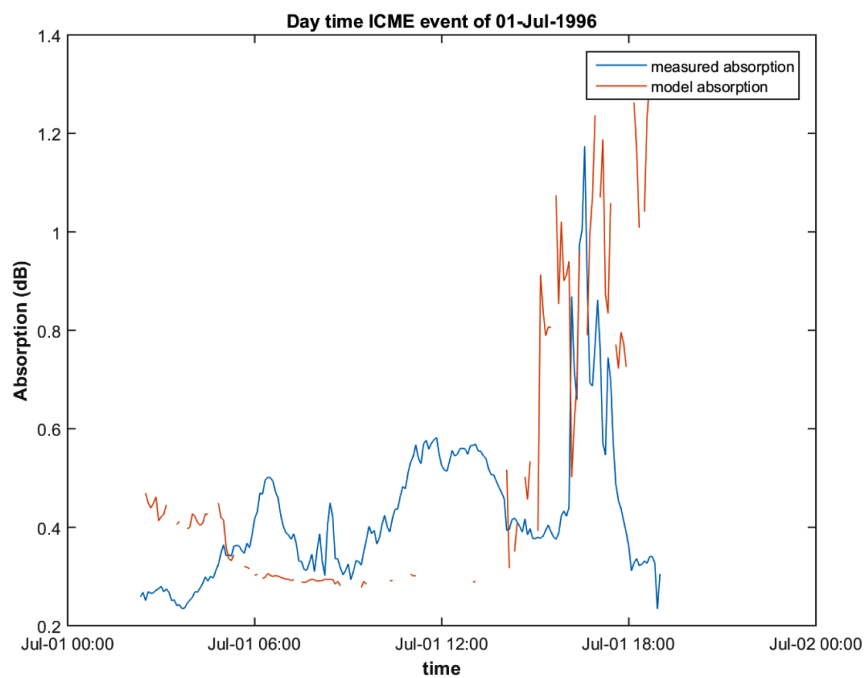


Figure 5.29: Example plots of measured v modelled results for ICME absorption. The plots are event dates within the time frame utilised for the model (1996-2009).



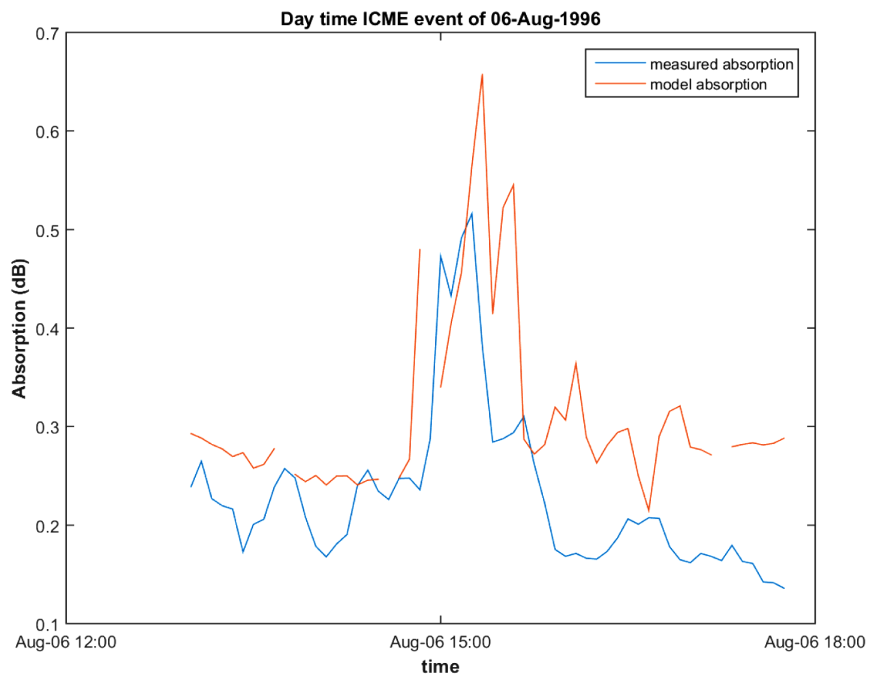
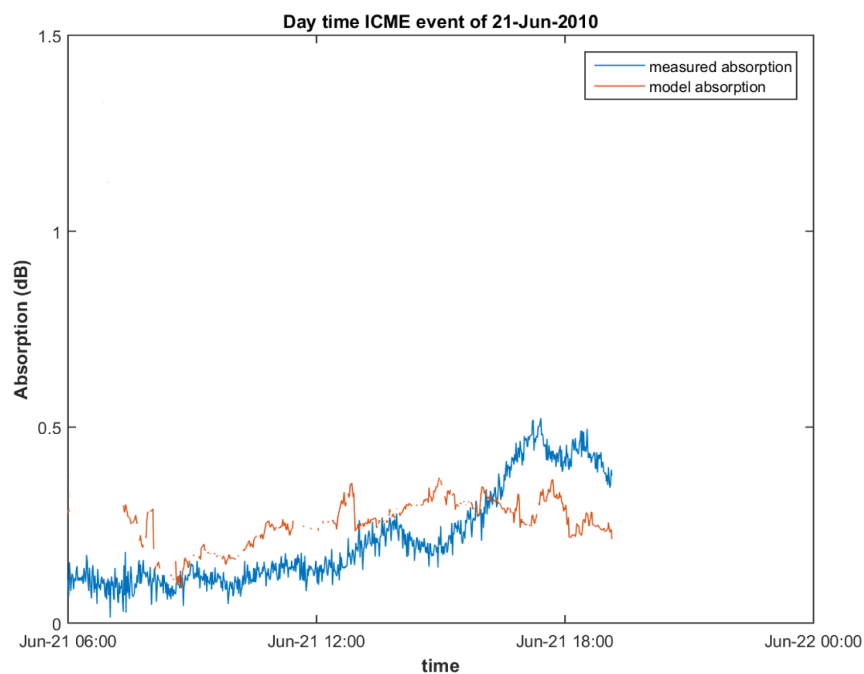


Figure 5.30: Example plots of measured v modelled results for ICME absorption. The plots are event dates within the time frame utilised for the model (1996-2009)



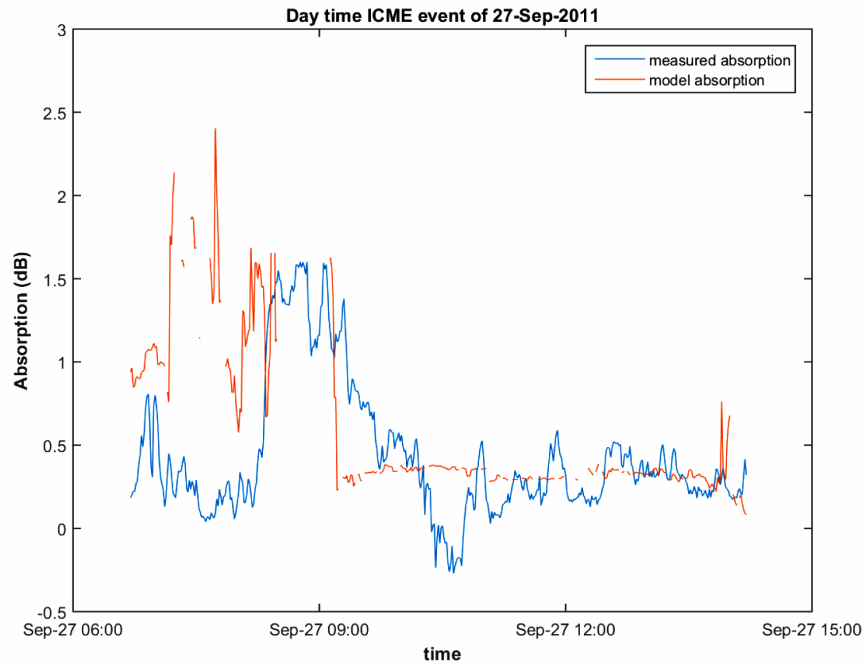


Figure 5.31: Example plots of measured v modelled results for day time ICME absorption. The plots is event dates outside the time frame utilised for the model

For night time absorption, the first ranking pair (nv^3 and B_z) are utilised as coupling parameters, they are related by equation (5.12)

$$\begin{aligned} \text{NIGHT ABSORPTION} &= \\ &= 0.387 - 0.38 \times 10^{-9}X - 0.062Y + X^2 + 0.8 \times 10^{-10}XY + 0.005Y^2 \end{aligned} \quad (5.12)$$

Where X is nv^3 and Y is B_z

The ranking of pair of parameters (pressure term and merging term) for night time absorption is as in Table 5.11 below:

Table 5.11: Combination of terms as coupling coefficient for night time absorption and their correlation coefficients

Ranking number	Pressure term	IMF term	Correlation Coefficient
1	nv^3	B_z	0.694
2	$n^{\frac{1}{2}}v^2$	B_z	0.591
3	$n^{\frac{1}{3}}v^2$	B_z	0.552
4	$n^{\frac{1}{2}}v^3$	B_z	0.513
5	$n^{\frac{1}{6}}v^2$	B_z	0.511
6	$n^{\frac{1}{2}}v^2$	B_{Total}	0.483
7	$n^{\frac{1}{2}}v^3$	B_{Total}	0.464
8	$n^{\frac{1}{3}}v^2$	vB_z	0.456
9	$n^{\frac{1}{3}}v^2$	B_{Total}	0.454
10	$n^{\frac{1}{2}}v^2$	vB_z	0.452
11	nv^3	B_{Total}	0.451
12	$n^{\frac{1}{6}}v^2$	vB_z	0.449
13	$n^{\frac{1}{6}}v^2$	B_{Total}	0.446
14	nv^3	vB_z	0.443
15	p	B_{Total}	0.433
16	nv^3	vB_z	0.382
17	p	vB_z	0.363
18	p	B_z	0.231

Figure 5.32 IRIS absorption and the model result for day time ICME events.

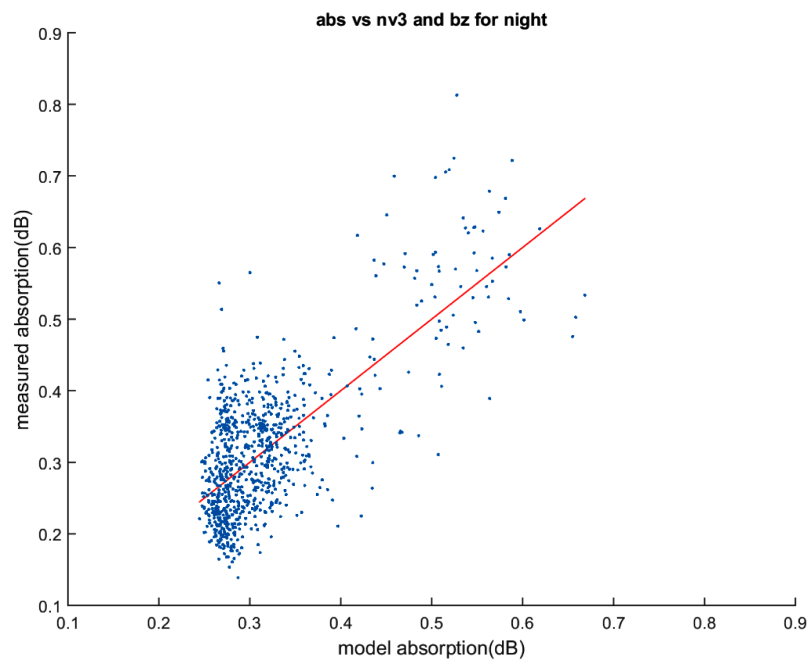
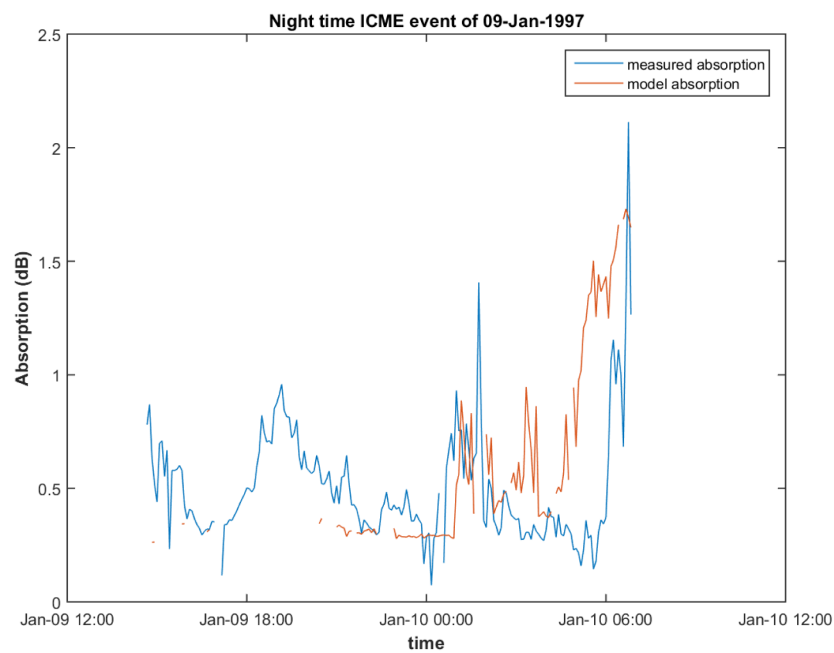


Figure 5.32: Measured absorption v modelled result for night time absorption during ICME events of 1996-2009

Example plots for individual events are as in Figures 5.33-5.34 below.



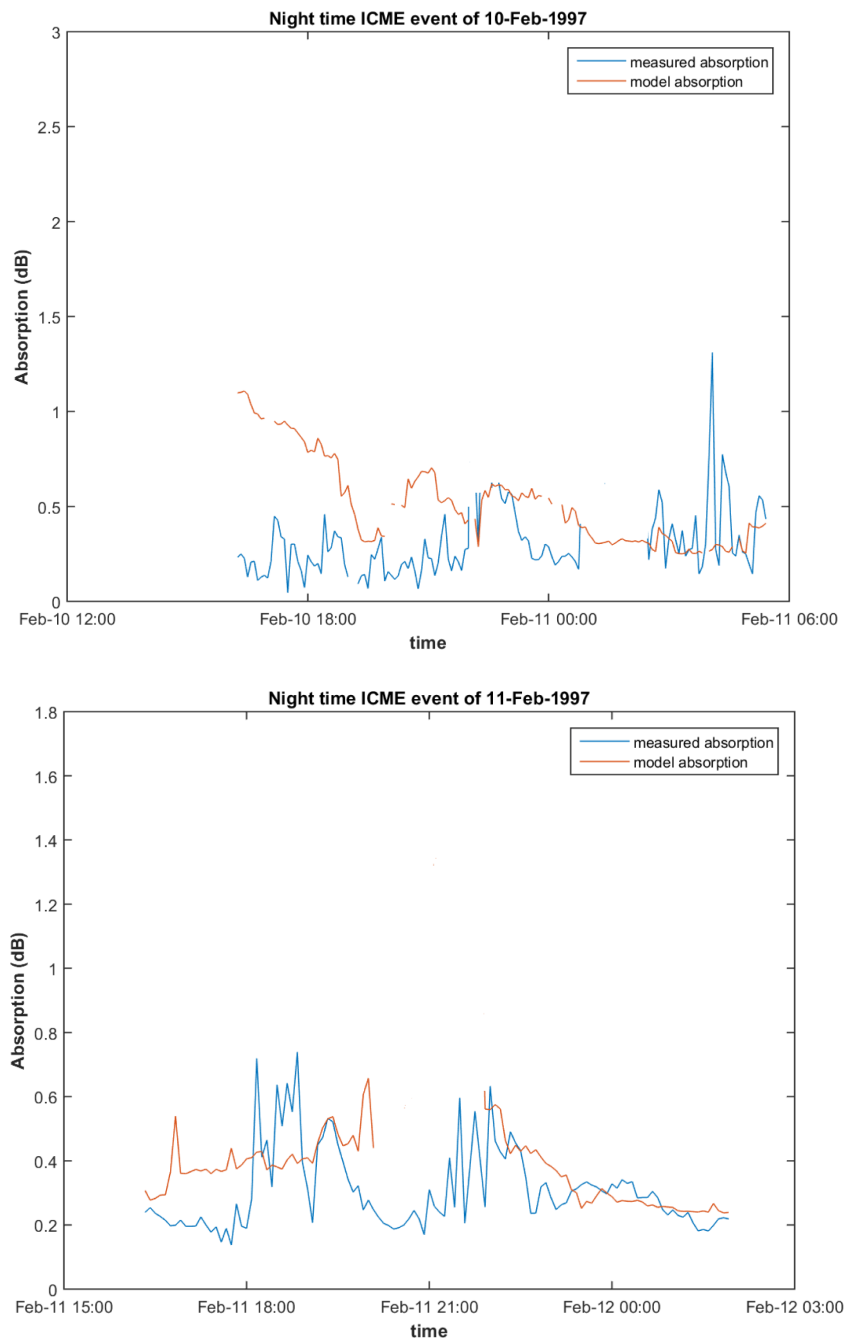


Figure 5.33: Example plots of measured v modelled results for ICME absorption. The plots are event dates within the time frame utilised for modelling (1996-2009). The missing gaps in the model result are times with no upstream data.

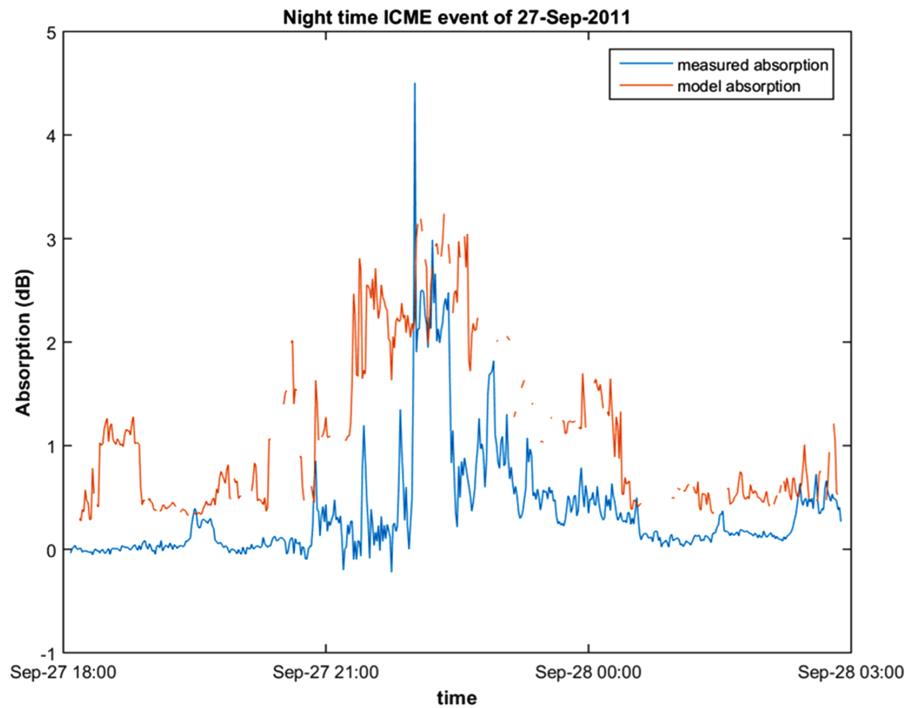


Figure 5.34: A plot of IRIS absorption v modelled absorption for an ICME event of 27th September, 2011, a date outside the dates used in the model.

5.9 Discussion

The epoch analysis for median absorption signature during ICME events did not show observable trend. To further probe absorption signature during ICMEs, the dataset was subdivided to day time and night start events based on the zenith angle relative to equations (5.4) and (5.5) after Sellers *et al.*, [1977]. In the analysis, the epoch plots was taken 1 day before event and up to 2 days after event (-1 day to 2 days) with the start time identified as 0. In the subdivisions, trends were noticed in absorption signature. For example, the epoch analysis of day time events showed maximum absorption signature at ~ 2 hours before the event start time, when compared with trend in the epoch analysis of some other solar wind parameters corresponds to the peak point observed in solar wind dynamic pressure with a delay of 60 minutes (Figure 5.12). Epoch analysis of absorption signature during night time events peaks at ~ 4 hours after start time, that aligns with the point of

strongest depression in B_z (Figure 5.15) with 25 minutes delay, whereas night time absorption signature did not show any useful relationship with some other geophysical parameters. Following suggestion [e.g. Foppiano and Bradley, 1984, Kavanagh *et al.*, 2004] that a prediction model may be better with a parameter that consists of more than one variable, this study experimented with a coupling function recently proposed by Newell *et al.*, as $d\Phi_{MP}/dt = v^{4/3}BT^{2/3} \sin^{8/3}(\theta_c/2)$, however, the correlation does not show any useful relationship. This work thenceforth first used single parameters (i.e. dynamic pressure) as the coupling coefficient for day time absorption and B_z (z -component of the magnetic field) as the coupling parameter for night time absorption. Using linear regression, the best fit equations were used to generate models for day and night time absorption. The model was then tested with ICME events that occurred outside solar cycle 23 as the data utilised in generating the model was from solar cycle 23. The results of measured absorption as compared with modelled absorption do not show good comparison with riometer observation (See Figures 5.23-5.27). In seeking for a more reliable model, this work observed relationships between geomagnetic indices such as AE and K_p . Combining some of these indices with other geophysical parameters resulted in an improved correlation but indices are predicted, hence, it will be somewhat difficult to use a predicted parameter as a coupling coefficient in a prediction model as upstream parameters that are available real time are deemed better for a prediction model. This work thence identified certain solar wind parameters that are viscous terms (pressure related terms) and some merging terms (IMF related terms). By ranking useful pairs of pressure terms and merging terms, dynamic pressure (p) and VB_z (VB_z is the product of solar wind velocity and the z -component of the IMF) ranked first as possible coupling function for day time absorption while B_z and nv^3 (nv^3 is the product of the number density and an index of the solar wind velocity) ranked best for night time absorption. These parameters were related to day and night time absorption through polynomial relations (Equations (5.11)-(5.12)). The result showed a considerable improvement on the measured v modelled plots although there are room for improvements.

5.10 Conclusion

Interplanetary coronal mass ejections (ICME) are a major driver of geomagnetic storms. A number of recent studies have identified the geomagnetic activity resulting from interaction between these solar wind structures and the Earth's magnetosphere. This study has observed energetic particle precipitation in the auroral region of the ionosphere during the passage of 89 ICMEs that arrived during the day time and 112 ICMEs that arrived at night time, the day and night time definition was based on zenith angle relative to the location of IRIS at Kilpisjärvi.

This study illustrates the effect of energetic particle precipitation during ICME events by modelling enhanced cosmic noise absorption (CNA) recorded by ground-based riometers. The results show differences in the intensity and duration of particle precipitation enhancement during day and night time commencing ICMEs. Night time commencing ICME events show higher CNA signature with the maximum ~ 4 hours after start times while day time commencing ICME events showed less absorption than night time events and maximum ~ 2 hours before start times. Epoch analysis of various solar wind parameters and geophysical indices were compared with the epoch in CNA, it is seen that for day time absorption, dynamic pressure is the best correlated parameter. The maximum in day time absorption and maximum in dynamic pressure have 25 minutes delay. Whereas for night time start events, the z -component of the IMF best correlates with absorption. The maximum in B_z and absorption has 60 minutes lag. The dayside absorption events are related to the arrival of the shock at the sheath and the increased dynamic pressure, which might have most impact on the day side, whereas the night absorption events are more associated with energy deposition related to reconnection, possibly into the tail, which might account for the effects on the night side and substorms.

Using single parameters as coupling coefficient in order to predict absorption did not yield good results (i.e. dynamic pressure was used as coupling parameter for day time absorption and B_z as coupling parameter for night time absorption). To get an improved result, a combination of solar wind parameters was utilised. Solar wind parameters were then categorised as pressure terms (otherwise called

viscous terms) and merging terms (IMF related terms), a combination of pressure terms and merging terms improved the correlation coefficients for day and night time start ICME absorption. Equations (5.11) and (5.12) were used to estimate absorption for day and night respectively. This work proposes equations (5.11) and (5.12) as possible relation for predicting day time and night time absorption during ICME events. In order to still improve the model, it should be possible to explore combination of more than two parameters, such combinations could yield higher correlation and give an improvement over the present result. Some suggestions are given in Section 7.2.

Chapter 6

Cosmic noise absorption induced by solar flares

6.0 Introduction

Currently, the main observing emphasis for space weather is focused on coronal mass ejections (CMEs) which directly impact the Earth's geomagnetic field (see Chapter 5) and solar flares which impact the Earth's upper atmosphere and can eject high energy particles that can adversely affect Earth's technologies. During solar flare phenomenon, the Sun throws out increased electromagnetic radiation in the X-ray and ultraviolet (UV) spectrums and also in a stream of particles of a wide spectrum of energies. Solar flare causes radio and magnetic disturbances on the Earth and is associated with sunspots. As discussed in Section 1.2.2, enormous quantities of energy (typically of the magnitude of 10^{27} Joules) are released into the interplanetary environment; such explosive release can drive energetic precipitation resulting at the emission of ultraviolet (UV) and X-ray radiation. At the time of the flare, the ionisation of the D-region of the dayside ionosphere can increase [e.g. Stauning, 1996]. When they are observed, the enhancement in ionisation is the so-called sudden ionospheric disturbances (SIDs) and the associated absorption are known as sudden cosmic noise absorption (SCNA).

Sudden cosmic noise absorption is riometer-detected sudden daytime absorption increases. The duration of the absorption is usually of the order of the flare [Stauning, 1996; Longden, 2007]. Figure 6.1 shows the incident power and absorption plots from the central beam of IRIS riometer at Kilpisjärvi during solar flare of 14th July, 2000.

SCNA is observed following apparent increase in the received noise power. This increase of received power is attributable to an increase in the solar radio emission at the time of the flare. During intense SIDs there can be considerable disruption and even blackouts to radio communications, particularly at the higher latitudes as a result of absorption in the D and lower E-regions.

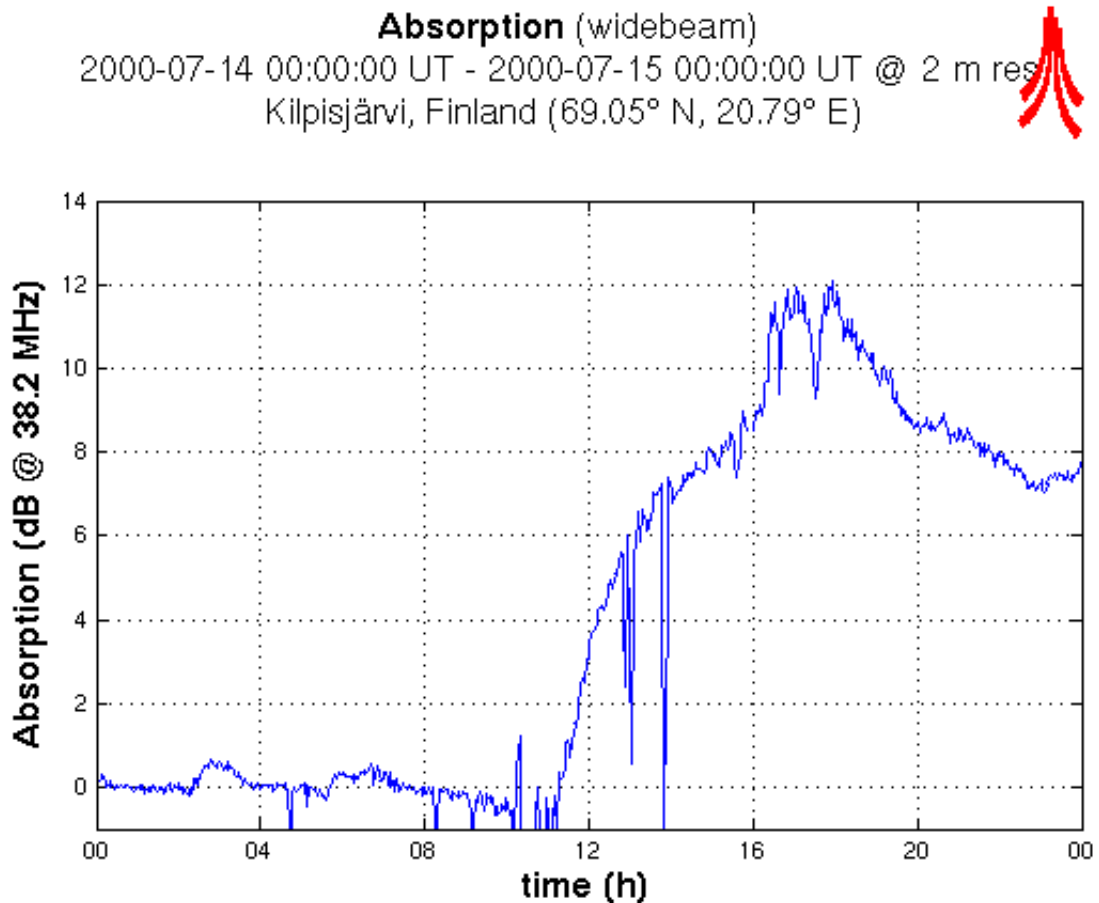


Figure 6.1: Cosmic noise absorption event following X-class solar flare of 14th July, 2000. The X-class flare began \sim 10:24 UT; gradual increase in riometer absorption began just after 10:24 UT from less than 1 dB up to over 10 dB at 17:00 hours.

Previous studies [e.g. Hultqvist *et al.*, 1999 and Contreira, 2004] associated the flare process to magnetic reconnection within the solar corona in which process magnetic energy is converted to thermal energy and particles are accelerated. The frequency and intensity of flares are known to depend on the solar cycle with more events occurring during solar maximum (Figure 6.5).

Changes in the electromagnetic spectrum have been monitored in the X-ray with satellites; an archive of hard and soft X-ray measurement is detailed in the national oceanic and atmospheric administration (NOAA) database. In the archive, flare events are classified based on intensity as in Figure 6.2 and Table 6.1. Solar Flares are classified by their X-ray flux in the 1.0-8.0 Angstrom band as measured by the NOAA GOES-8 satellite.

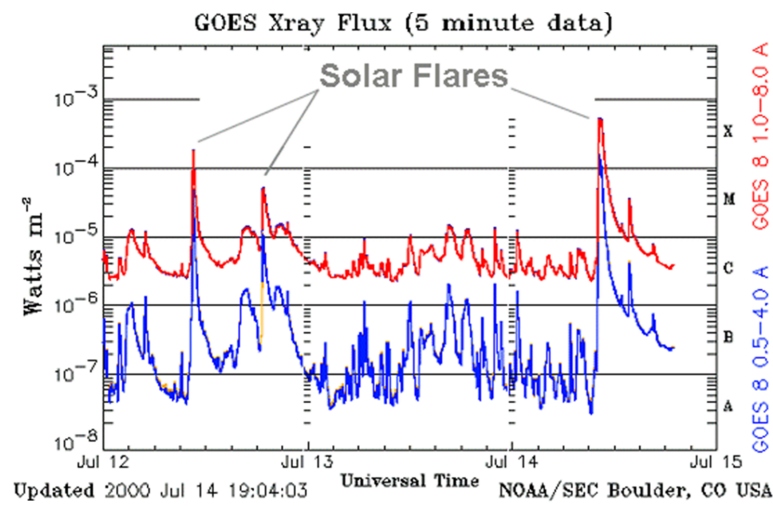


Figure 6.2: Showing solar flare events of 12th July, 2000 and a powerful X5 class flare on 14th July, 2000 as measured by the geostationary operational environmental (GOES) satellite

This chapter aims to investigate the effects of solar flares on cosmic noise absorption, the magnitude of absorption that would be expected following the occurrence of the different classes of solar flare events and the time scale of associated radio absorption. X-ray solar flux data¹ used in this work is from the geostationary operational environmental (GOES) satellite, the duration chosen in this analysis is solar cycle 23 (1996-2009), cosmic noise absorption (CNA) from IRIS at Kilpisjärvi is analysed for the same duration.

6.1 Emission and classification of solar flare

Flares vary significantly in their spatial shapes and relative intensities at different wavelengths (Figure 6.2). Following this observed variation, there have been

¹<http://www.ngdc.noaa.gov/stp/space-weather/solar-data/solar-features/solar-flares/>

many attempts to classify flares. The classification has been based on their emission in the optical wavelength. Solar flares are mostly classified according to their X-ray brightness in the wavelength range 1 to 8 Angstroms. There are 3 major categories: X-class flares, M-class flares, and C-class flares. X-class flares are big; they are major events that can trigger planet-wide radio blackouts and long-lasting radiation storms. M-class flares are medium-sized; they can cause brief radio blackouts that affect Earth's polar regions. Minor radiation storms sometimes follow an M-class flare. Compared to X and M-class events, C-class flares are small and have few noticeable

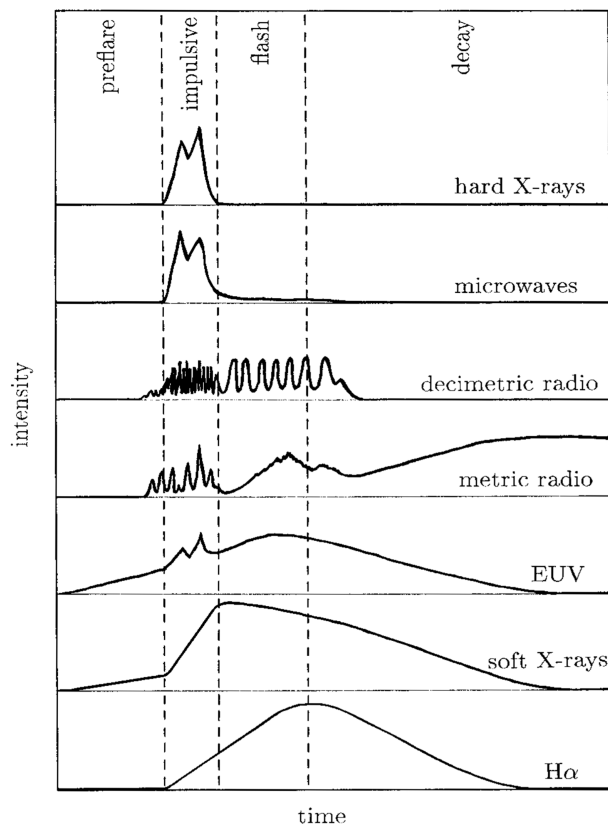


Figure 6.3: A schematic evolution of flare intensities at different wavelengths. The phases indicated at the top vary greatly in duration. In large events, the pre-flare phase lasts 10 min, the impulsive phase 1 min, the flash phase 5 min and the decay phase 1 hour [From encyclopaedia of astronomy and astrophysics, 2001].

consequences here on Earth (Table 6.1). In the encyclopedia of Astrophysics and Astronomy [2001], large flares are further subdivided into phases, i.e. the pre-flare phase, the impulsive phase, the flash phase and the decay phase (Figure 6.3). The

impulsive phase follows with rapid variations observed in radio, $H\alpha$ X-ray, ultraviolet and gamma wavelengths [Dennis and Schwartz, 1989]. The impulsive phase is characterised by intense spikes in hard X-ray and gamma ray emissions and a rapid increase in soft X-rays. The most substantial energy release takes place during the short impulsive phase lasting just minutes, with huge quantities of energy released into interplanetary environment [Hudson, 2011]. During the flash phase, soft X-ray flux exhibits a slow but steady decline while hard X-ray falls exponentially, energy is released steadily [Sturrock *et al.*, 1984]. The classification adopted in this study is based on the peak intensity of soft X-ray flux as recorded by the geostationary operational environmental satellite (GOES) network in the 1-8 E spectral bands. In GOES, flares are classified as A, B, C, M, and X (Table 6.1). Each class has a peak X-ray flux ten times greater than the preceding class.

Within each class there is further sub-division, this is attributed to a number between 1 and 9.9 representing a linear increase in peak X-ray flux. For example, an X_2 event has a peak X-ray flux twice as that of X_1 event.

Table 6.1: Classification of GOES soft X-ray flare

Classification	Peak Flux in 1-8 E Range (Wm^{-2})
A	$x < 10^{-7}$
B	$10^{-7} \leq x < 10^{-6}$
C	$10^{-6} \leq x < 10^{-5}$
M	$10^{-5} \leq x < 10^{-4}$
X	$10^{-4} \leq x$

6.2 Flare models

Due to complexities associated with flare events, there remains significant knowledge gap about the entire mechanism. The outstanding knowledge about flare is the rapid release of energy due to magnetic reconnection within the solar corona. The

huge quantities of energy released are stored in the active region magnetic field [Brown *et al.*, 1994]. The Sun's magnetic field is strongest at the active region; they can be identified by the appearance of dark sunspots where intense magnetic activity hinders convection.

The structure of flares varies considerably from complex to a simple loop of corona plasma confined by the magnetic field lines looping out of the convective zone. Various models have thus far been proposed. For example, Kopp and Pneuman [1976] proposed a model that requires a transient that opens up the magnetic field lines. As they close down and reconnect, energy is released that goes into accelerating electrons that travel down the magnetic field lines. These highly energetic particles will heat the dense chromosphere at the footpoints, and this plasma is heated and conducted into the loops. Besides the Kopp and Pneuman [1976], other proposed models are by Carmichael [1963], Sturrock [1968] and Hirayama [1974]. The current standard model for the development of flare combines the aforementioned works and is termed the 'CSHKP' model. However, there are shortcomings of the CSHKP model in that it fails to identify what causes instability in the initial magnetic system. Therefore, it is not appropriate for certain flare geometries [Aschwanden, 2006]. Nevertheless, it has successfully explained the majority of observable flare emissions.

The effect of solar flares on ionospheric absorption have been previously investigated [e.g. Hultqvist *et al.*, 1958; Alurka and Bhonsle, 1969; Contreira *et al.*, 2005, Richardson, 2012]. The general finding in these works is that at some threshold of flare events, there could be strong absorption a few hours after the solar flare leading to enhanced radio emission or SCNA. Krishnamurthi *et al.*, [1962] observed that initial conditions in the terrestrial atmosphere govern the production and maintenance of an SCNA during intense solar flare. Also, Contreira [2005] in their statistical summary of signal fading occurrence due to solar flares (at 6 MHz) showed the dependence of the stability of radio links in the HF range on solar activity. Small fluctuations in the ionospheric ionisation process may lead to amplitude fluctuations in the 6 MHz received signal. However, besides the general knowledge of absorp-

tion event following flare occurrence, it will be helpful to know the magnitude and time-scale of such absorption events in order to specify technical parameters of the communication system to be used when such events happen which is the motivation of this work. The methodology utilised is described in Section 6.3 below.

6.3 Data and methodology

6.3.1 Flare data

Solar flare event data used in this study is from the geostationary operational environmental satellite (GOES) system. GOES began operation in 1975 with the launch of GOES-1 and provides a source of continuous solar data. The system utilises numerous satellites stationed in the geosynchronous orbits. Four satellites are currently operational, GOES-12 to GOES-15. GOES-13 is designated operational East, stationed at 75° W and GOES-15 is designated operational West, stationed at 135° W. GOES-12 covers south America at 60° W and GOES-14 is in on-orbit storage at 105° W.

X-ray sensors are installed on the GOES satellites providing X-ray flux measurements with a one-minute time interval in the 0.5-4E and 1.0-8.0E spectra bands. GOES satellite can measure and record X-ray flux signature of all solar flares occurring on the Earth facing side of the Sun. This data is catalogued by the national oceanic and atmospheric administration (NOAA) of the space weather prediction centre (SWPC), USA.

6.3.2 Flare catalogue

All flare events reported between 1996-2009 were obtained from the GOES satellites X-ray sensors in the 1-8E spectra band. For each events, the data shows the start time, defined as the first minute in a sequence of four minutes, a steep monotonic increase in X-ray flux, the time of maximum X-ray flux and the end time defined as the time which the flux level decays to a point halfway between the maximum and pre-flare background. The data also includes the X-ray class (C_1 and above as

classes A and B are not recorded as a result of their high frequency and low intensity). In total the flare catalogue consists of 14,792 events, although within the analysis excluding the computation of annual flare count, only 14,772 were used, this is because some events containing missing or inaccurate data were ignored. 13,203 events were C-class, 1,443 were M-class and 126 events were X-class flares.

6.3.3 Cosmic noise absorption (CNA) data

This work studies the correlation of median maximum absorption with flare intensity (Figure 6.4); this approach was earlier adopted by Richardson [2012]. The result shows that there appears to be no effect on absorption before M4 class flares ($4 \times 10^{-5} \text{ Wm}^{-2}$), whereas, above class M4, there is a significant positive correlation between maximum absorption and peak flare intensity. The study also shows a relationship between mean duration of flares and flare intensity (Figure 6.5). The mean duration shows positive trend with the log of flare intensity. More variation is evident in the higher intensity flares due to the smaller sample size. To investigate the effect of solar flare on ionospheric absorption, CNA data corresponding to the time of flare events were compiled. However, flare events which occurred when the Sun was below the horizon at the riometer station would produce very little observable effects as the enhanced X-ray and UV flux produced by flares only reaches the Sun facing side of the ionosphere. The flare catalogue (discussed in 6.3.2) was filtered to include only events occurring when the Sun is above the horizon at the riometer station and corresponding CNA data were obtained. For this procedure, solar declination was calculated based on the time of flare events in universal time (UT). The right ascension and declination together with the coordinates for longitude and latitude of the riometer site were used to determine the solar elevation at the specific time. Flare events for which the Sun was below the horizon from one hour after the flare end time were filtered. For each of the remaining flare, IRIS data from beam the central beam (25) at a temporal resolution of 1-second was compiled, spanning from three hours before onset to three hours after the recorded end time. This procedure reduced the total number of events to 6,020 events. 5,393 were C-class, 504 were

M-class and 123 are X-class flares. The effects of flare on the absorption induced by the different classes of flares were then investigated.

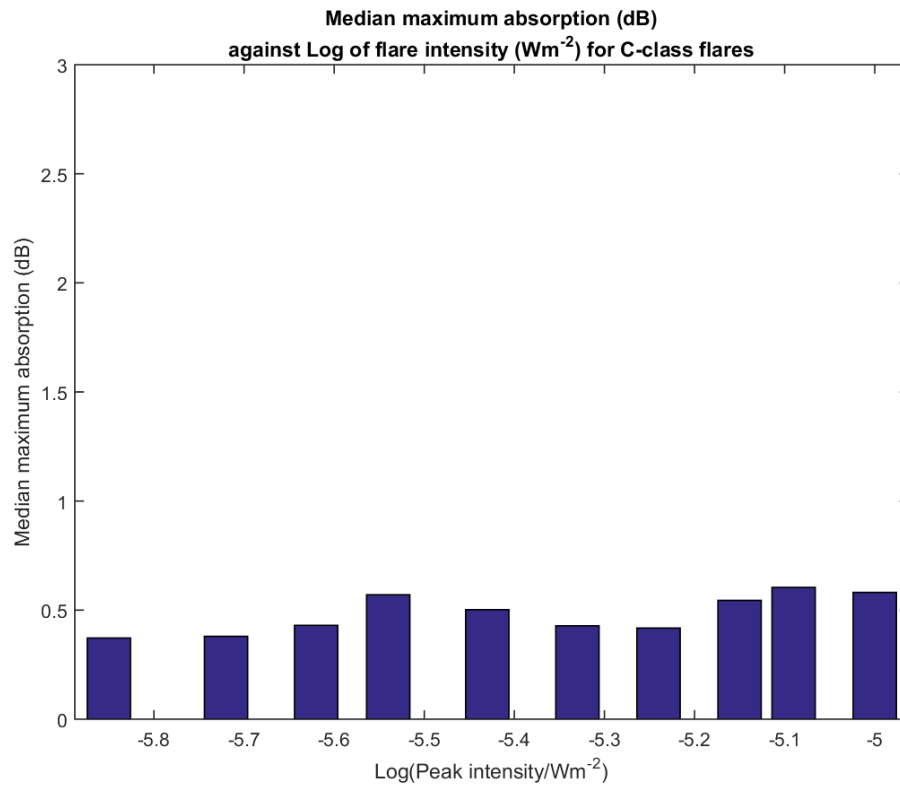


Figure 6.4a Plot of median maximum absorption (dB) against Log of peak flare intensity (Wm^{-2}) for C-class flares. The flares are binned by class (i.e. C1-C9.9) and the median peak absorption computed for each bin. Here there is no visible trend in median absorption within bin classes.

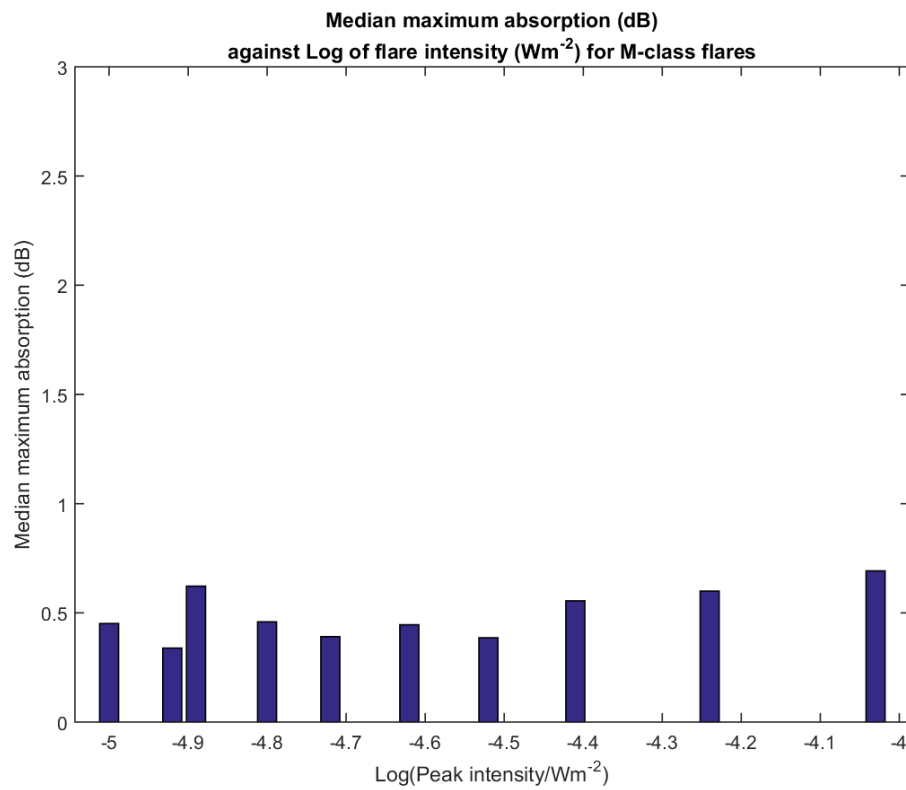


Figure 6.4b Plot of median maximum absorption (dB) against Log of peak flare intensity (Wm^{-2}) for M-class flares. The flares are binned by class (i.e. M1-M9.9) and the median peak absorption computed for each bin. Here there is visible trend in median absorption within bin classes from M4 class.

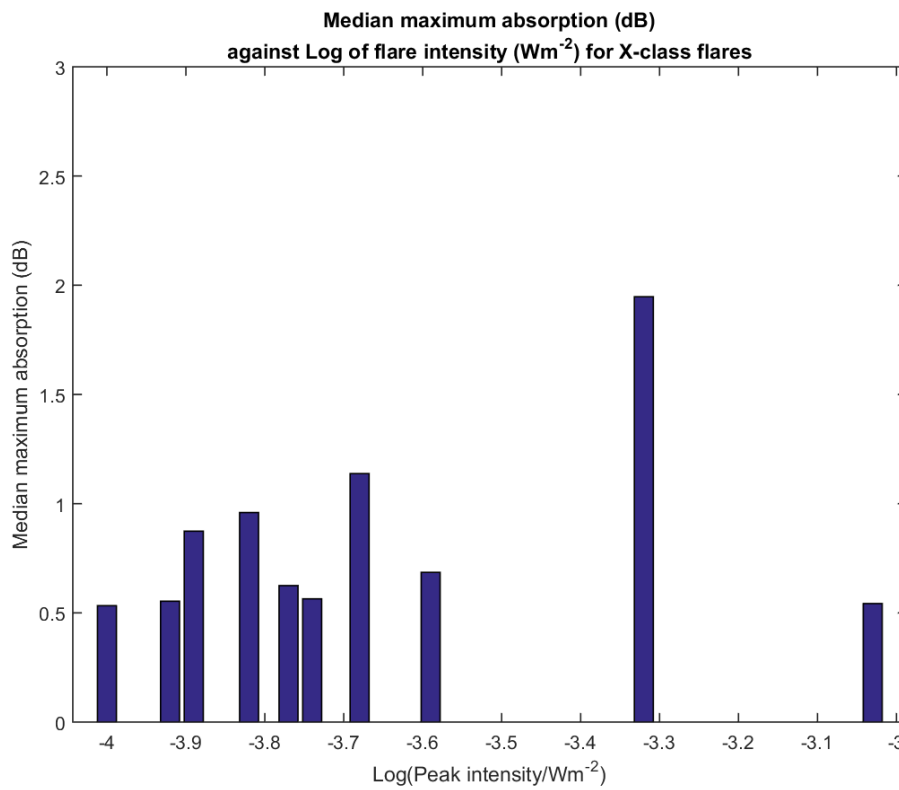


Figure 6.4c Plot of median maximum absorption (dB) against Log of peak flare intensity (Wm^{-2}) for X-class flares. The flares are binned by class (i.e. X1-X9.9) and the median peak absorption computed for each bin.

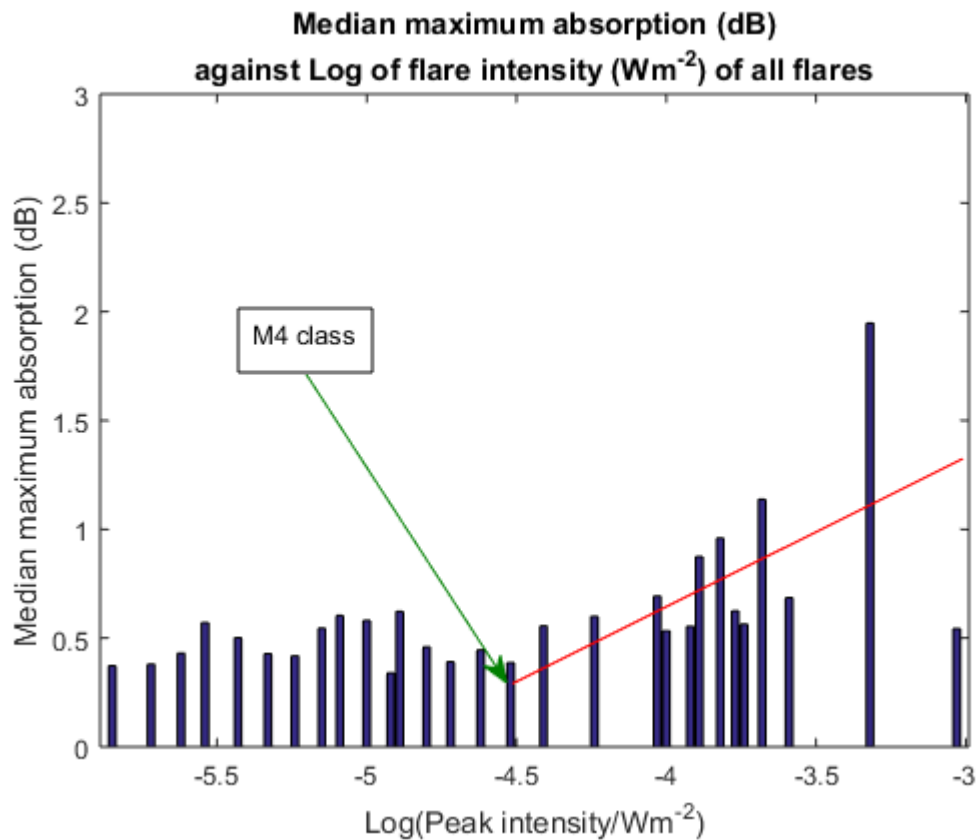


Figure 6.4d A combined plot of median maximum absorption (dB) against Log of flare intensity for classes C, M and X. The flares are binned by class and the median peak absorption computed for each bin. It can be seen that increasing intensity has very little effect on the corresponding peak absorption up to $4 \times 10^{-5} \text{ Wm}^{-2}$ (M4). Beyond this class, a significant positive trend is seen.

From Table 6.2, the statistics of the data utilised in shown.

Table 6.2: Showing statistics of IRIS Absorption and GOES Flare intensity dataset (1996-2009)

Class of event		Max absorption (dB)	Max intensity (Wm^{-2})	Flare duration (Mins)	Rise time (Mins)	Decay time (Mins)
C	Mean	0.43	3.10×10^{-6}	20	08	12
	Median	0.26	2.45×10^{-6}	13	09	16
	STD	0.79	1.98×10^{-6}			
M	Mean	0.54	2.36×10^{-5}	31	22	15
	Median	0.30	1.70×10^{-5}	21	20	15
	STD	1.19	1.66×10^{-5}			
X	Mean	0.74	2.34×10^{-4}	34	19	08
	Median	0.58	1.67×10^{-4}	24	15	05
	STD	0.64	1.33×10^{-4}			

The statistics from table 6.2 shows some properties of each class of flare such as the corresponding absorption that they generate, the time taken for flares to get to their peak value (rise time) and the decay time from point of maximum intensity. The more intense flare produce the highest magnitude of absorption, (i.e. the higher the intensity, the higher the absorption generated), whereas with regards to the relaxation time, the reverse seem to be the case, this is because the high intensity flare category (X-class) does decays faster compared with M and C-classes. The median relaxation time for X-class is 5 minutes while for C and M-classes median decay are 16 minutes and 15 minutes respectively. On the overall duration of events, X-class has a longer median duration than the C and M-classes. In the analysis the epoch analysis of absorption signature generated by each class will be shown to further observe the effect of each class of flare on absorption. Relationship between mean duration and intensity of flare is shown in Figure 6.5.

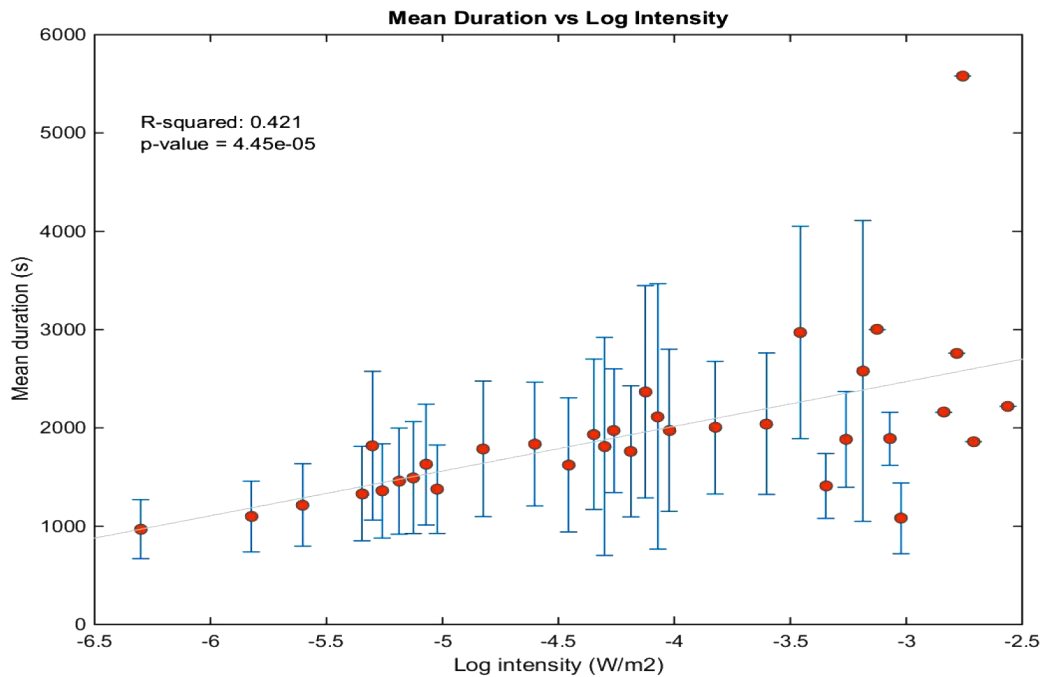


Figure 6.5: Plot of flare mean duration v log of flare intensity. The flares are binned by class and the mean duration is calculated for each. The error bar represents the standard error of the mean. The mean duration shows positive trend with the log of flare intensity. More variation is evident in the higher intensity flares due to the smaller sample size.

6.4 Procedure and methodology

Using the flare catalogue within solar cycle 23 (1996-2009), the characteristics of flare events were investigated. The annual flare counts were computed and the relation between peak flare intensity and flare duration was explored. The flare counts were binned into C, M and X-class flares and the mean duration computed for each class. The different classes were further binned into tenths of each class (peak intensity interval of 10^{-6} Wm^{-2} for C-class, 10^{-5} Wm^{-2} for M-class and 10^{-4} Wm^{-2} for X-class) and the mean duration computed.

The flare catalogue was then used to obtain the corresponding CNA data for each event. The one second resolution data was converted to one minute average to reduce scintillation in the data. The events were binned into C, M and X-class and the median absorption signature computed for each class. The median absorption signature was then used to produce flare induced models for each class. The

relationship between flare intensity and maximum corresponding absorption was investigated. Maximum value of absorption recorded in the hour following onset is taken as the maximum absorption for each event.

6.5 Results

6.5.1 Annual flare count

The first set of results within this study is based on the statistics of annual flare count. Figure 6.6 shows the annual flare count for C, M and X-class flares based on the total of 14,792 flare events from 1996-2009. Figure 6.6 agrees with previous works on the variation of solar flares with solar cycle [e.g. Warwick and Haurwitz, 1962; Weir and Brown, 1964]. More flares are observed during the solar maximum years (2000-2001) which corresponds with maximum presence of sunspots. It is observed that generally solar flares grow with the increasing phase of solar cycle and reduce towards solar minimum years. The correlation between annual flare count and the solar cycle informs on the magnetic origin of flares.

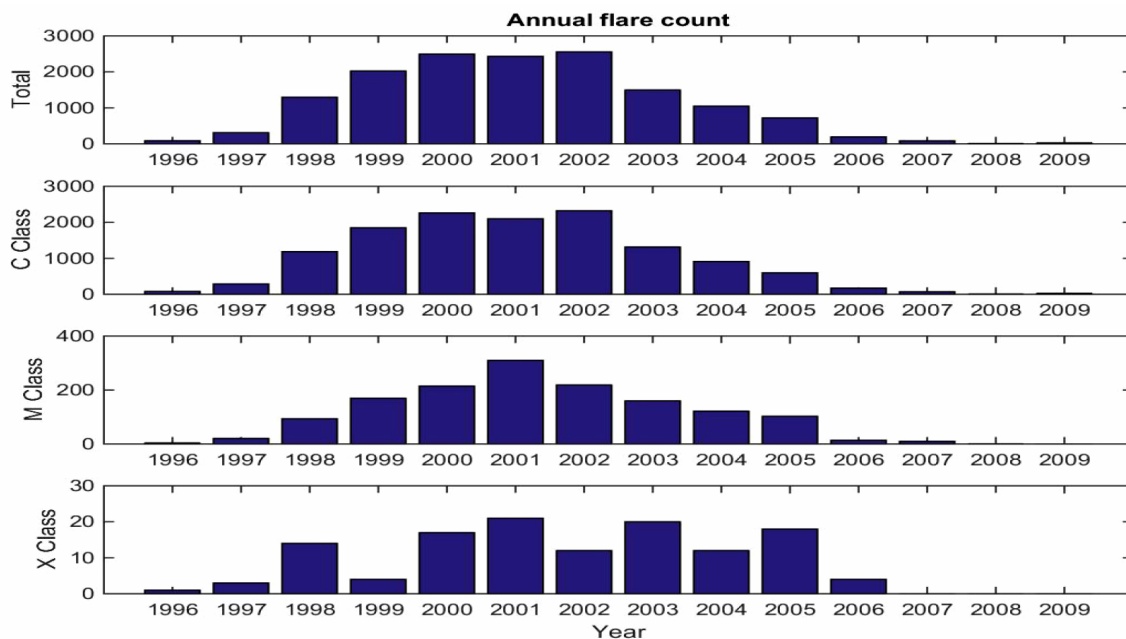


Figure 6.6: Annual flare count for C, M and X-class flare covering solar cycle 23 (1996-2009).

Counts for all classes show a clear variation with solar cycle.

Magnetic activity peaks at solar maximum with increasing number of flare eruption as a result of the complex magnetic structures within solar active regions causing reconnection.

On the investigation of monthly count of flares (Figure 6.7), there is no clear variation and as such it is difficult to draw any useful conclusion in this regard. Although in the three classes of flares, the least count is observed in February with the highest figures occurring in November. Also, the seasonal variation of flare (Figure 6.8) does not show any regular variation.

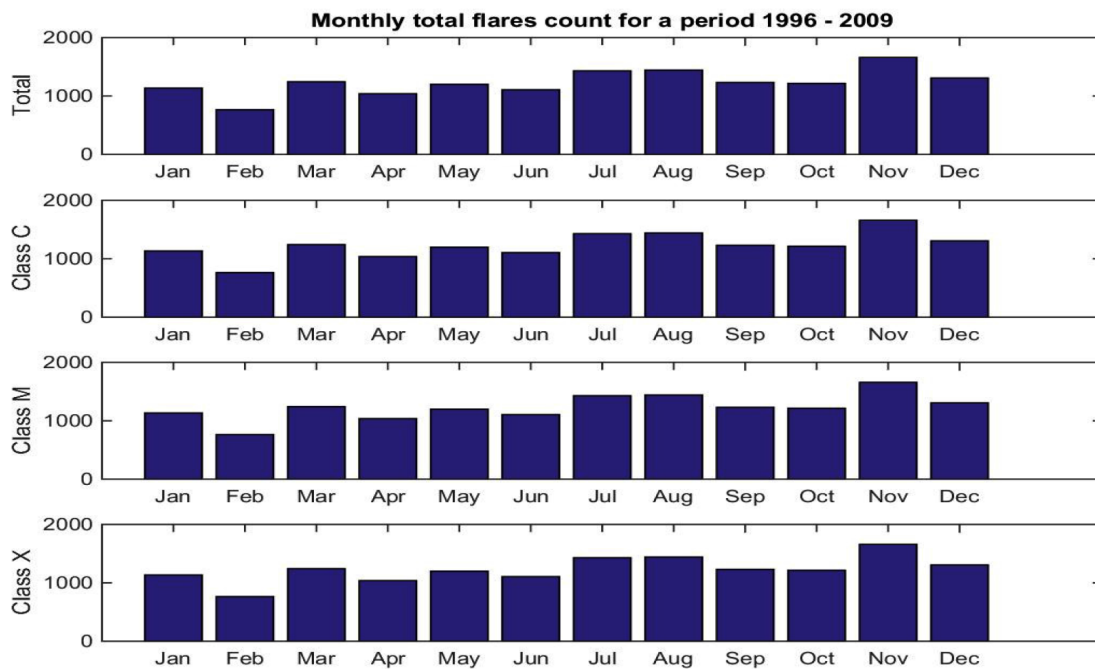


Figure 6.7: Variation of flare based on monthly occurrence during solar cycle 23 (1996-2009).

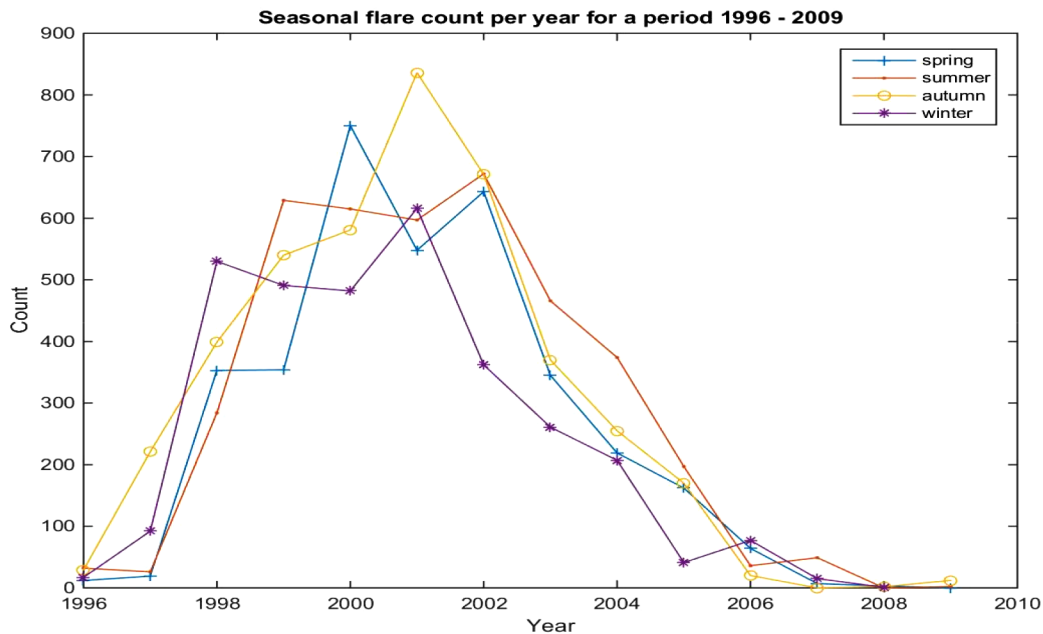


Figure 6.8: Variation of flare based on seasonal occurrence during solar cycle 23 (1996-2009).

Winter (December-February), Spring (March-May), Summer (June-August), Autumn (September-November).

6.5.2 Flare duration

The mean duration for C, M and X-class flare as shown in Figure 6.9. For C-class flare the mean duration is 20 minutes and 30 seconds, M-class has a mean duration of 30 minutes and X-class is 34 minutes and 30 seconds. The result suggests that flare class with higher intensity has longer duration. Figure 6.10 further illustrates the relationship between flare intensity and duration. In Figure 6.10, C-class events are binned into 10^{-6} Wm^{-2} intervals, M-class binned into 10^{-5} Wm^{-2} intervals and X-class binned into 10^{-4} Wm^{-2} intervals.

The mean duration for each interval is calculated and plotted against the logarithm of flare intensity. The Figure shows a proportionate increase of the mean duration as the log of intensity increases and a positive trend. The trend is very well defined for lower intensity flares but more variation is evident in the higher intensity flares as a result of smaller sample size. All flare class demonstrates a large standard deviation from the mean indicating that there is considerable variation in the dura-

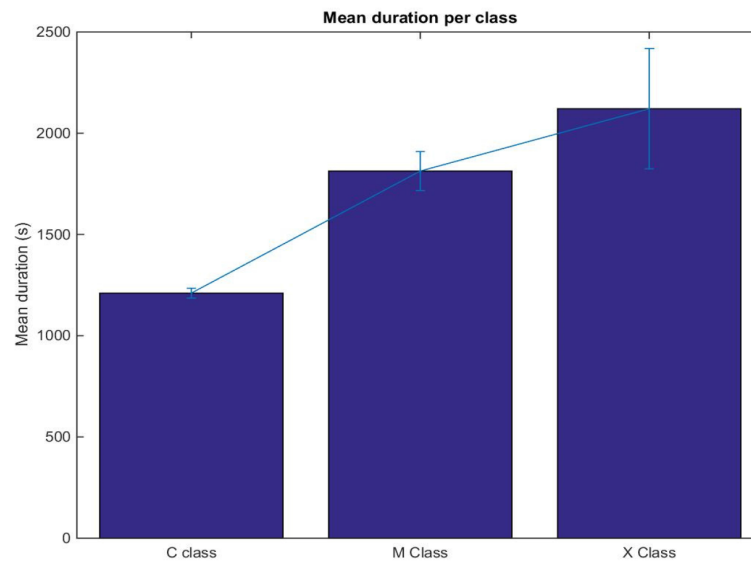


Figure 6.9: Showing mean duration for X, M and C-class flares between (1996-2009) as measured by the GOES satellites in 1.8E X-ray flux spectral band. The error bar represents the standard error of the mean. Increase in mean duration for higher peak intensity is apparent.

tion between individual flares of the same class. This indicates that although there is a relation between flare intensity and duration, there may be other factors that affects the duration of solar flares.

6.6 Relationships between flare parameters and absorption parameters

From Figure 6.11, it is seen that there is no observable effect on absorption with C-class flare however, there are some effects on M and X-class flares. To be able to see the effects clearly, Figure 6.12 shows median signature (without quartiles) for M and X-class flares.

To investigate the behaviour of absorption during flare events, plots of absorption and flare intensity at the same time are shown in figure 6.13 below.

The delay in the peak of flare intensity and peak absorption is as shown in Figure 6.14.

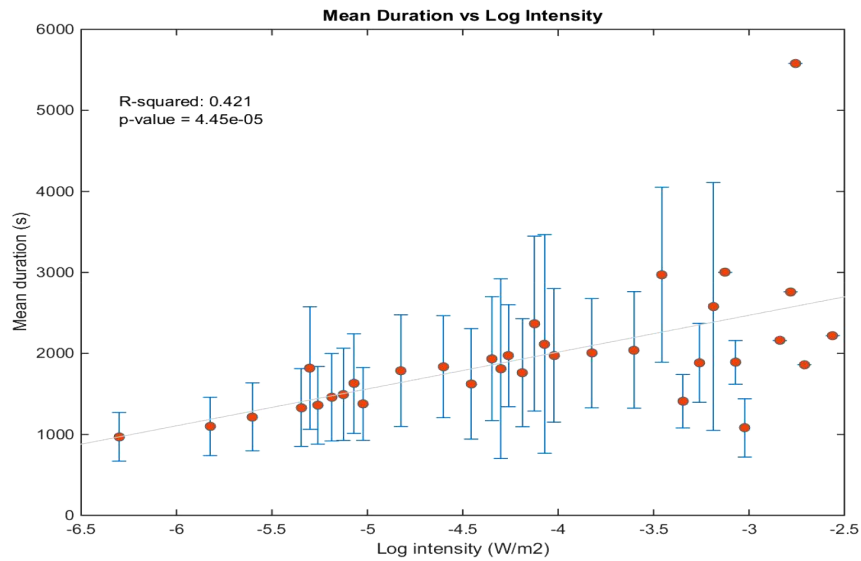


Figure 6.10: Plot of flare mean duration v log of flare intensity. The flares are binned by class and the mean duration is calculated for each. The error bar represents the standard error of the mean. The mean duration shows positive trend with the log of flare intensity. More variation is evident in the higher intensity flares due to the smaller sample size.

From figure 6.13, it is possible to relate the parameters of flare and absorption such as rise time, decay time and peaks values. Statistical relation of these parameters are shown in Figures 6.15-6.17.

6.7 Methodology for flare model

From Figures 6.15-6.17, the three main segments of flares and absorption have been considered. In each segment, (i.e. rise time, maximum point and decay time) a relation is established between flare and absorption. The relations are as stated in table 6.3 as below, flare events with zenith angles greater than 80 degrees (coinciding with night time period of riometer) were removed, and events with maximum absorption less than 0.5 dB were also not included.

From table 6.3, under the rise time and decay time columns, T_1 shows the rise time of absorption based on X which is the rise time of flare term. In the maximum absorption and peak intensity column, Y terms are absorption, X terms are flare intensity. Y term relates to absorption while X relates to flare intensity.

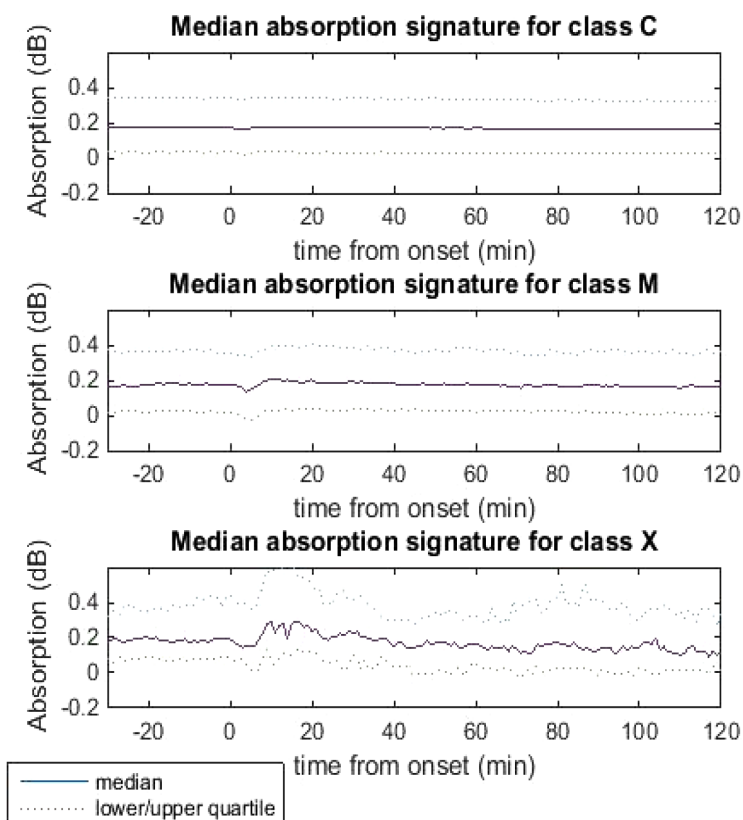


Figure 6.11: Superposed epoch analysis of median absorption signature for X, M and C-class flare between 1996-2009. The start times are as recorded by GOES. Absorption data is from beam 25 of IRIS Kilpisjärvi.

Based on equation (6.3), modelled absorption is generated and the result compared with riometer observation as shown in Figures 6.18-6.20. In order to generate an absorption profile the equations shown in Table 6.3 were used in equations (6.1), (6.2) and (6.3). Equation (6.1) shows exponential rise up to maximum flare intensity while equation (6.2) shows exponential decay from maximum flare intensity to the end time of flare while equation (6.3) contains both positive and negative exponentials from maximum intensity.

$$Y = Ae^{t/\tau_1} \quad (6.1)$$

$$Y = Ae^{-t/\tau_2} \quad (6.2)$$

$$Y = Ae^{t/\tau_1} + Ae^{-t/\tau_2} \quad (6.3)$$

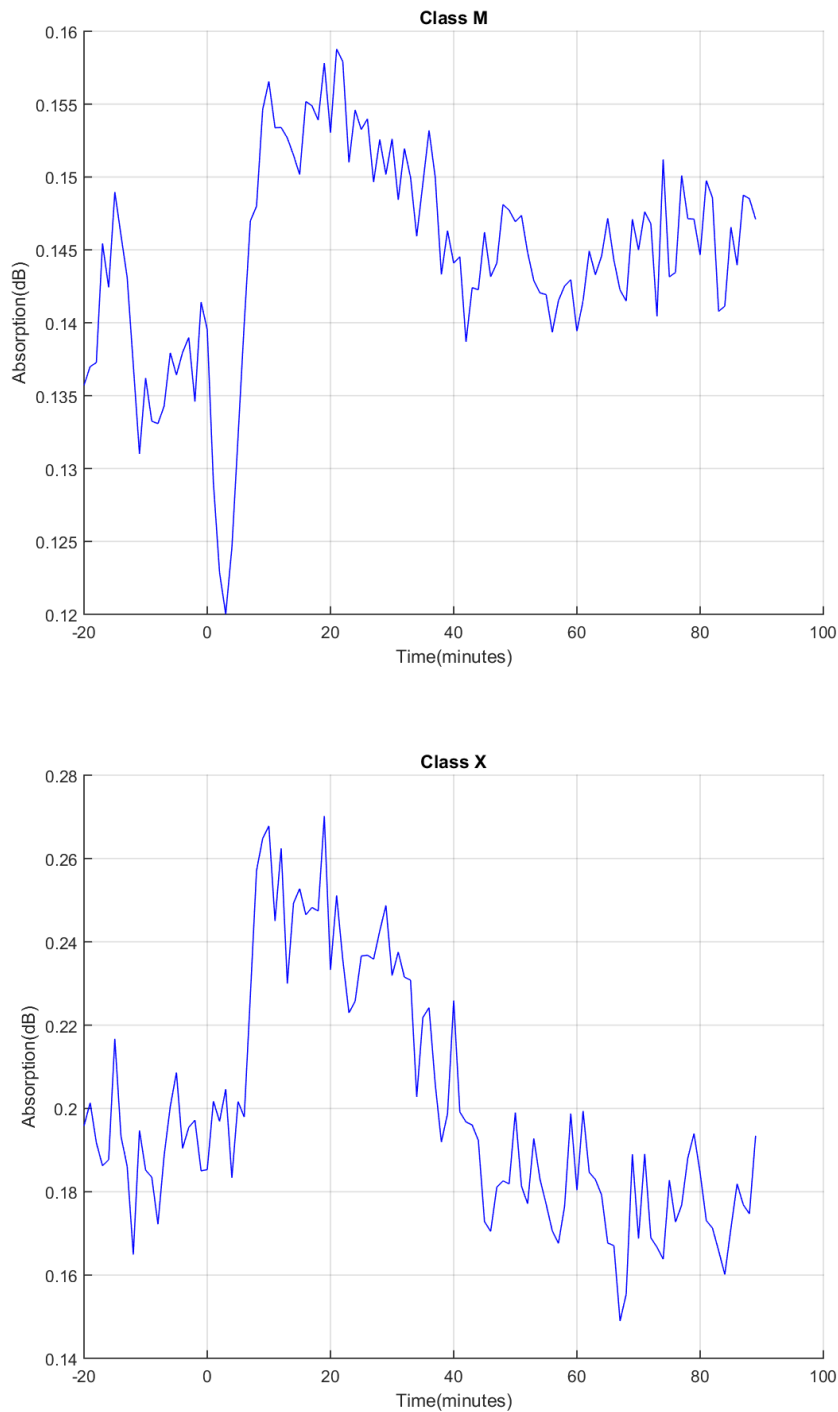
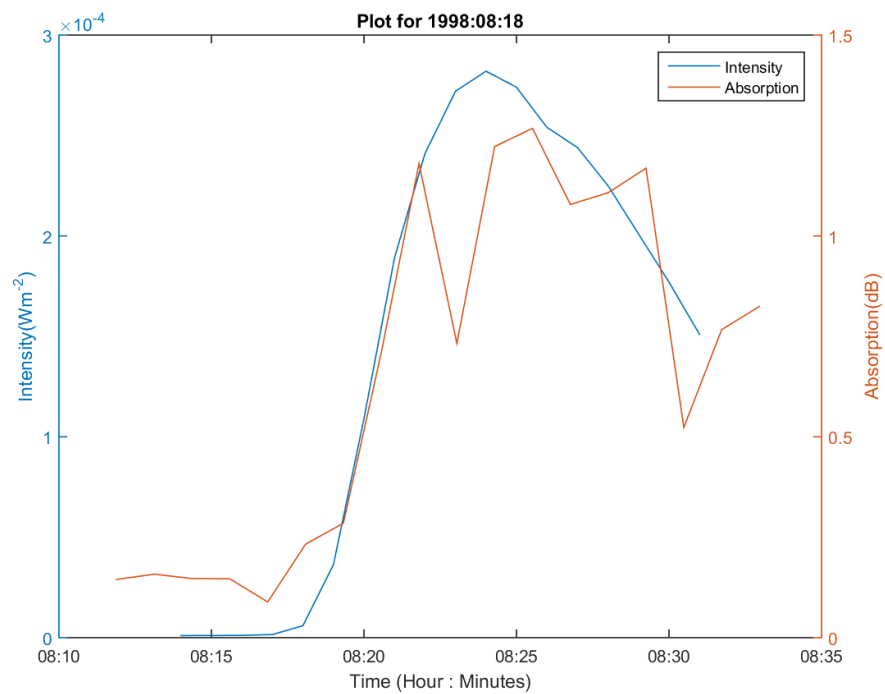
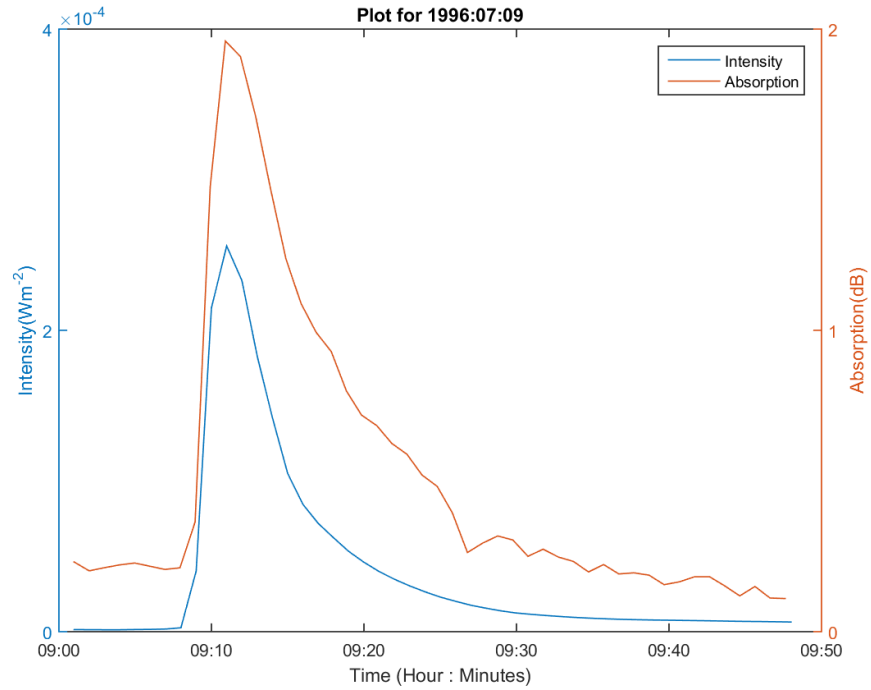


Figure 6.12: Median signature of absorption during solar flare events for M class flares (top panel) and X-class flares (bottom panel). Y-axis is absorption axis (dB); X-axis is time (minutes). Median absorption signature is seen from 20 minutes before start time to 90 minutes after start time. From the start time (0) there is a depression of 0.02 dB in median absorption signature in both M and X-class plots. Maximum is noticed about 18-19 minutes after start times in both plots.



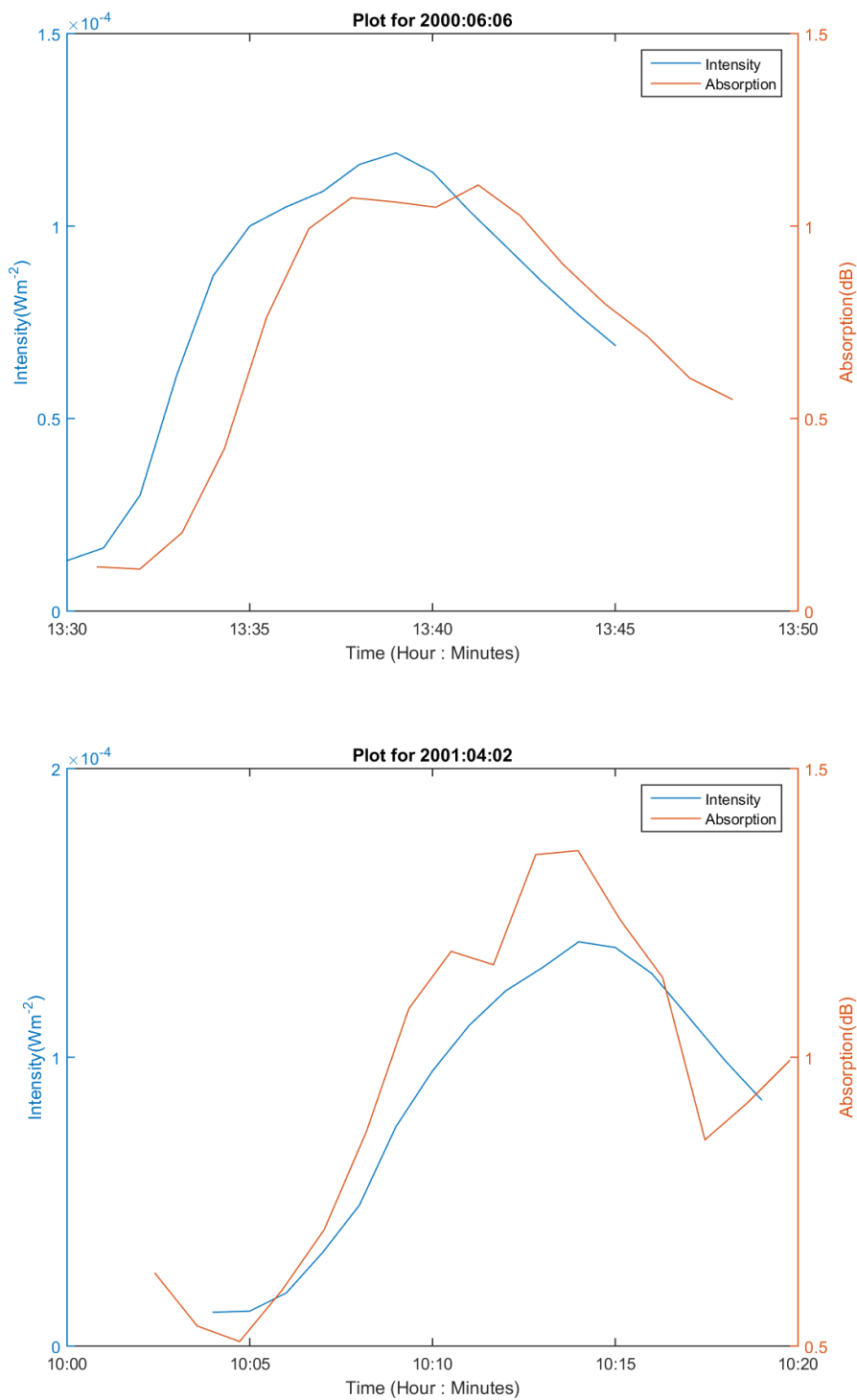


Figure 6.13: Plots of absorption (dB) and solar flare intensity for 4 different X-class flares. The rise time and decay time are somewhat symmetrical and delays are seen in the peak of intensity and peak of absorption.

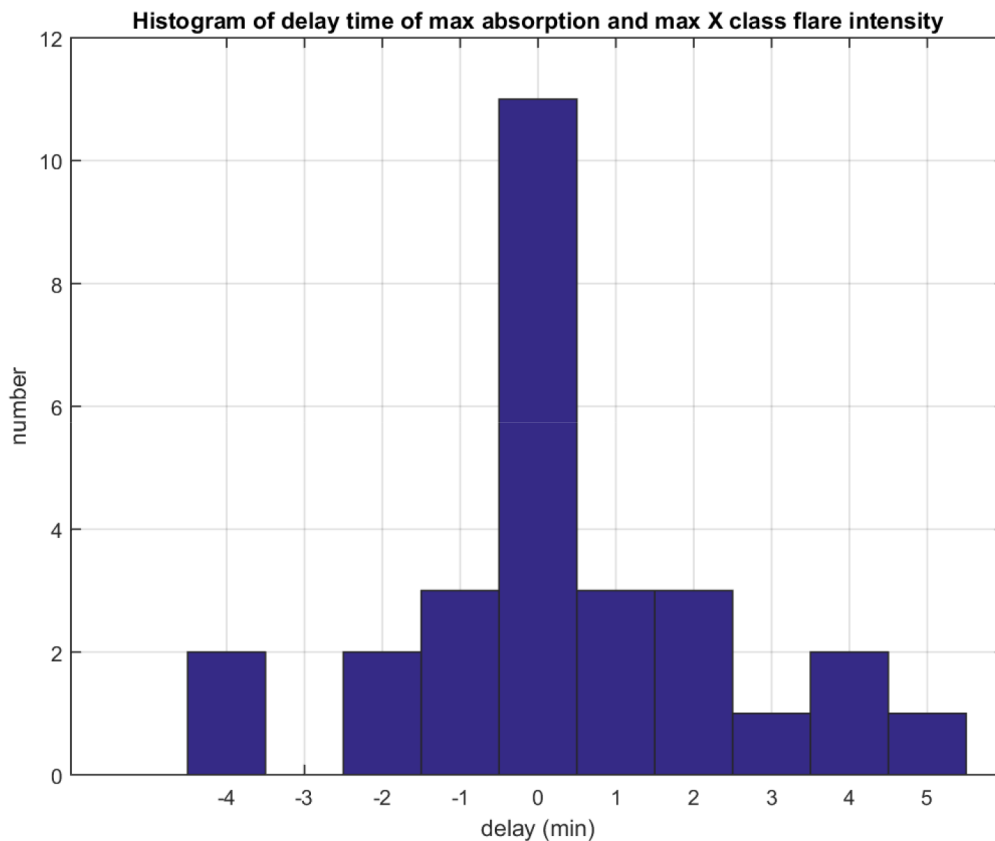


Figure 6.14: Showing delay between peak intensity of flare and peak absorption for X-class solar flare events of 1996-2009. Delay range from 4 minutes before to 5 minutes after flare intensity. Majority of the events do not show any delay (0) delay between peak intensity of flares and peak absorption.

Comparative plots of measured absorption and model result for M-class events are as in Figure 6.18.

6.8 Analysis and discussion

In some of the flare events, there are rapid negative spike within minutes of flare onset, followed by a longer duration but generally smaller magnitude positive peak in absorption. It is well established that the negative spike in absorption is not a result of changes within the ionosphere but due to the rapid increase in radiation being received during a flare event. The huge release of electromagnetic radiation increases the radio noise signal received by the riometer, giving the impression of reduced absorption in the ionosphere. This accounts for the rapid nature of the spike,

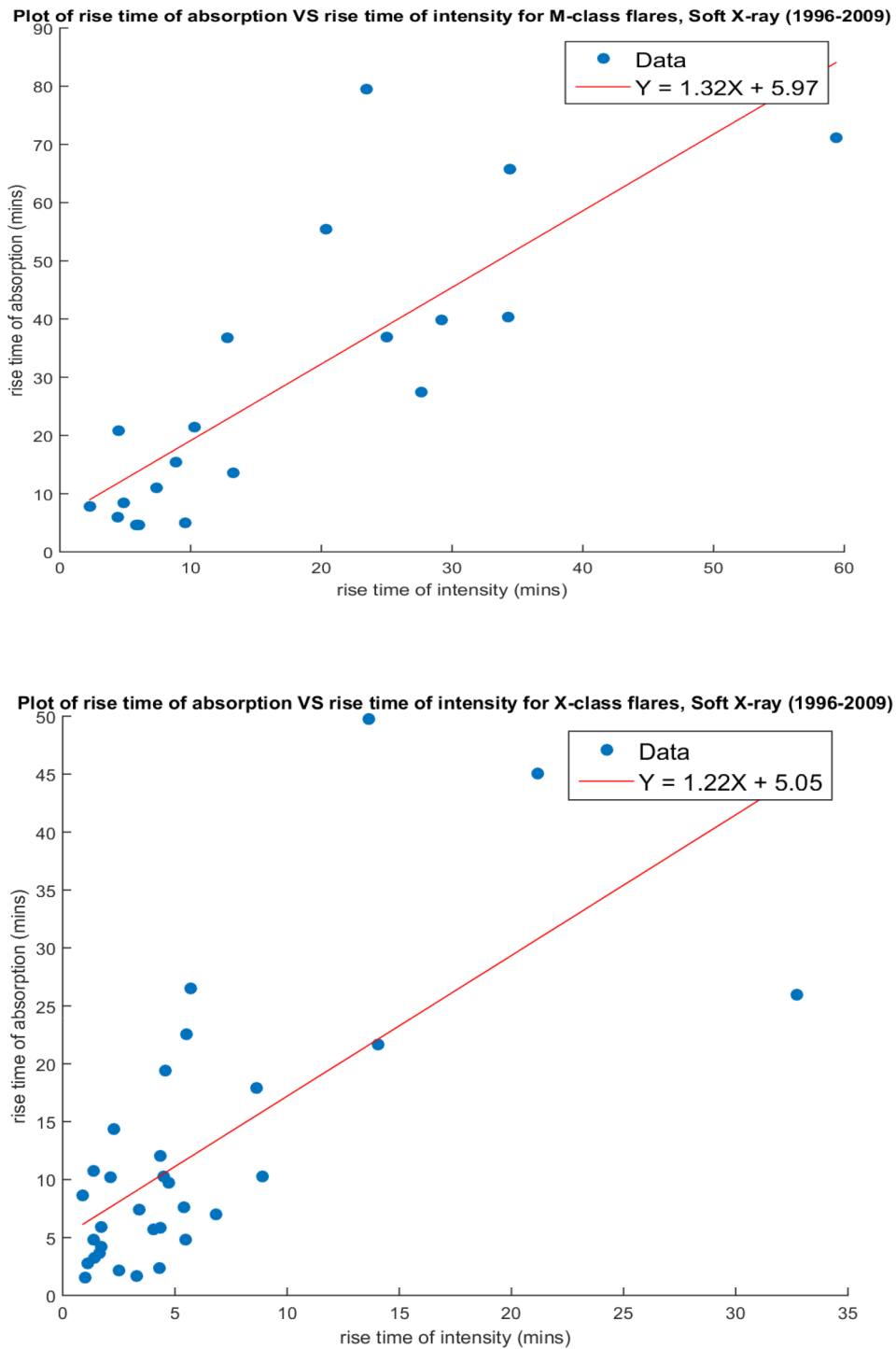


Figure 6.15: Plot of rise time of flare v rise time of absorption. Top panel show M-class relation, bottom panel shows X-class relation.

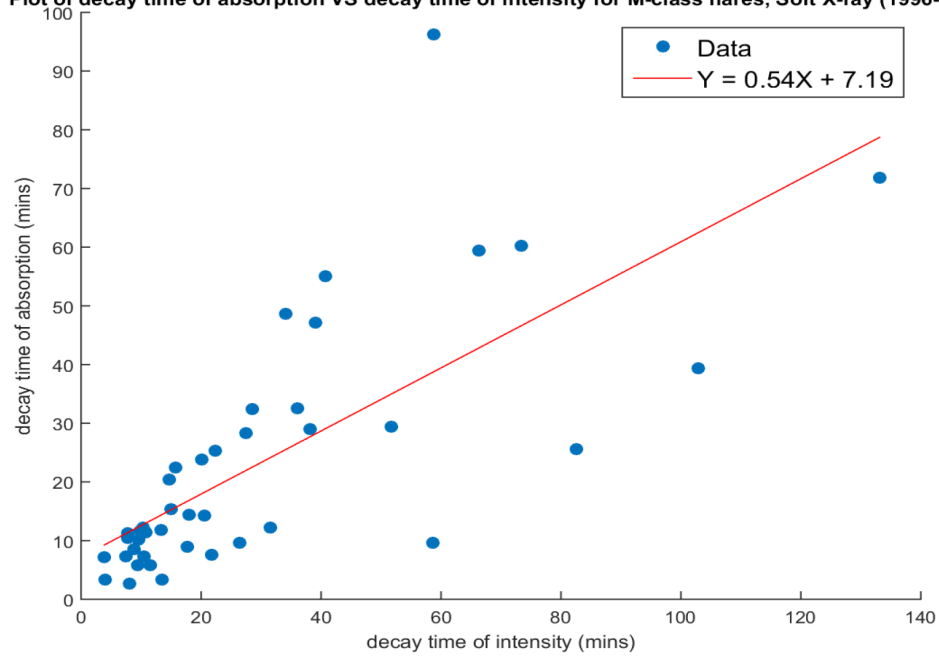
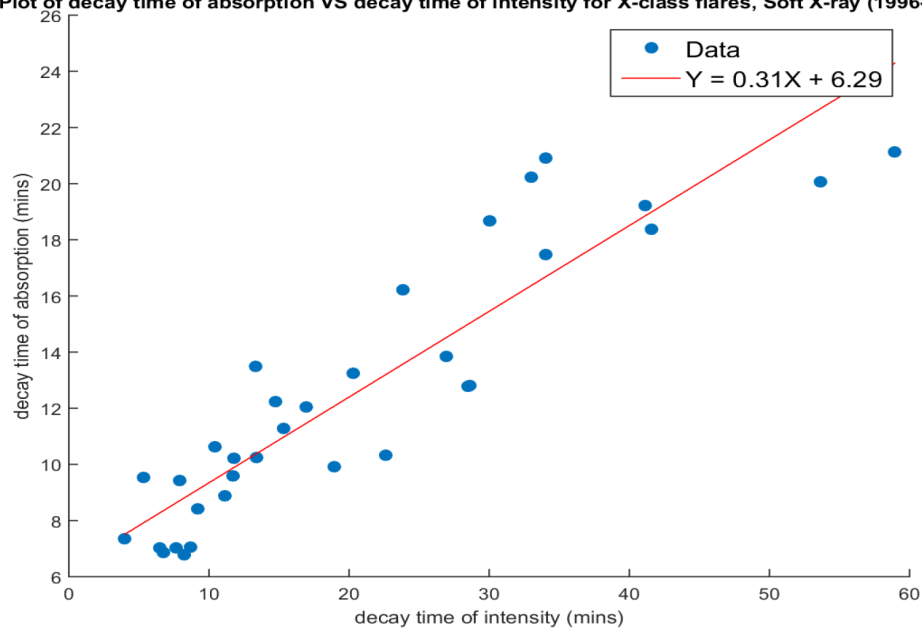
Plot of decay time of absorption VS decay time of intensity for M-class flares, Soft X-ray (1996-2009)**Plot of decay time of absorption VS decay time of intensity for X-class flares, Soft X-ray (1996-2009)**

Figure 6.16: Plot of decay time of flare v decay time of absorption. Top panel show M-class relation, bottom panel shows X-class relation.

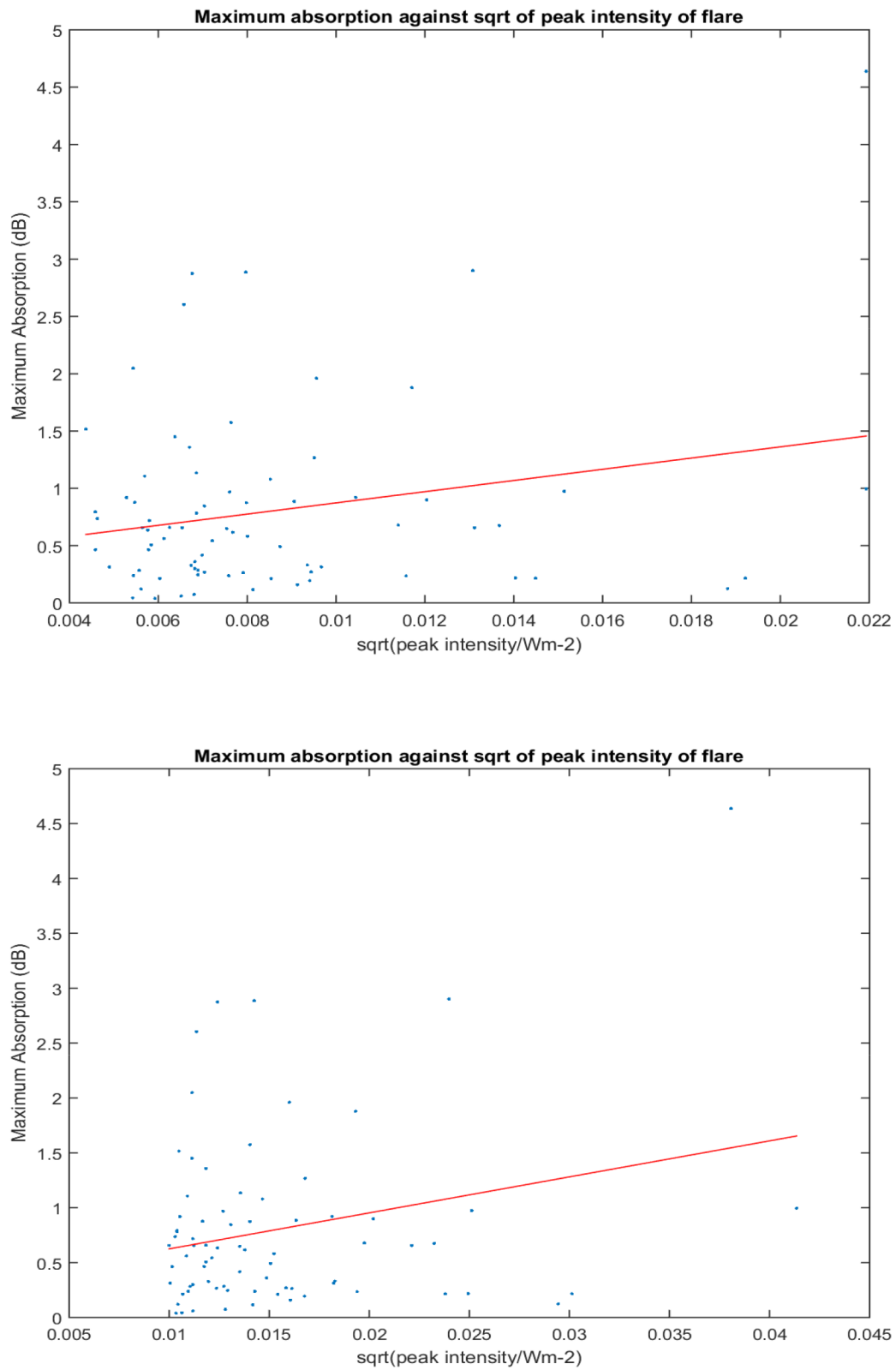
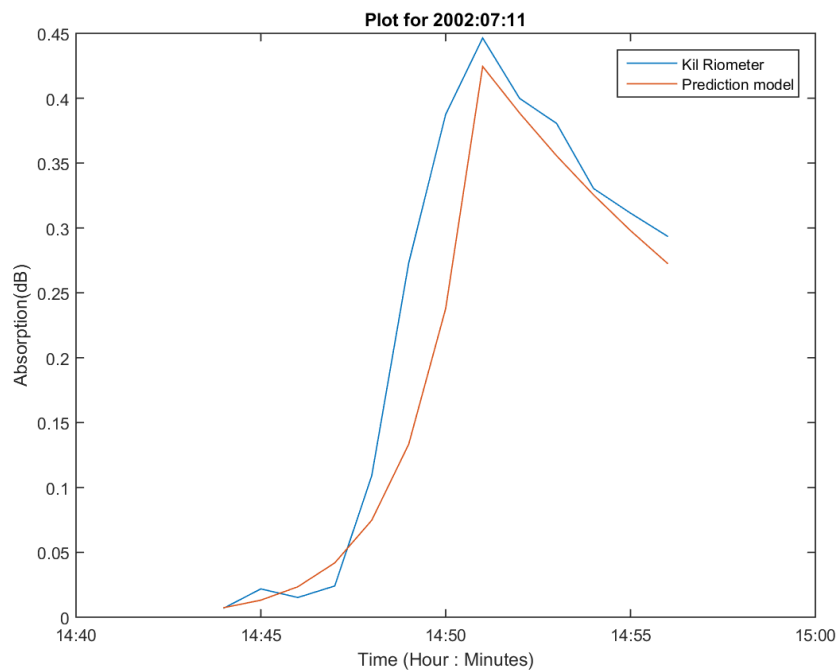
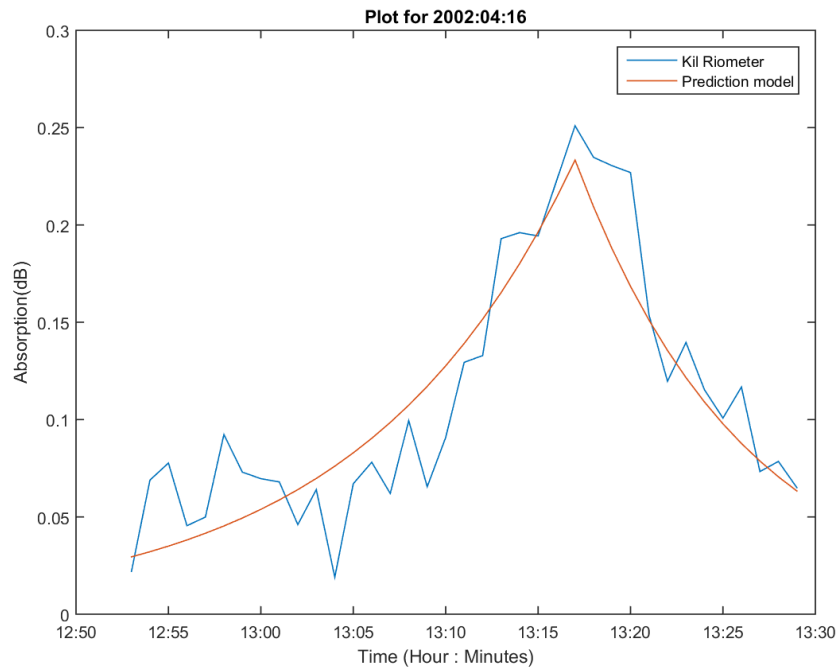


Figure 6.17: Plot of maximum absorption (dB) v square root of maximum flare intensity (Wm^{-2}). Top panel show M-class relation, bottom panel shows X-class relation.



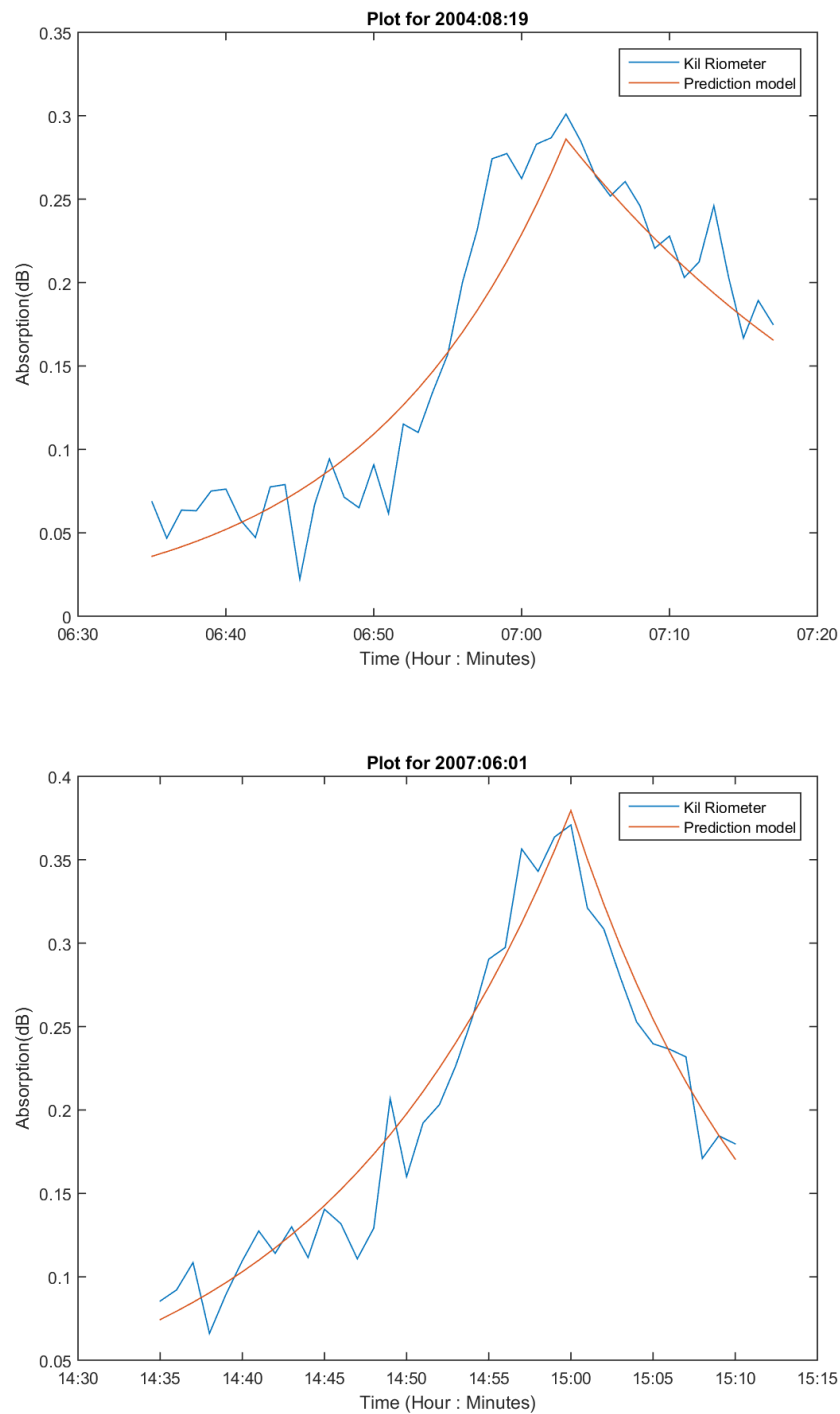


Figure 6.18: Plots of measured absorption (IRIS) in blue compared with model result in red for 4 M-class events. The events are within the dates utilised in obtaining the model (1996-2009). Measured absorption is shown as Kil (Kilpisjärvi riometer) riometer measurement, the model result is shown as prediction model in the legend of the plots.

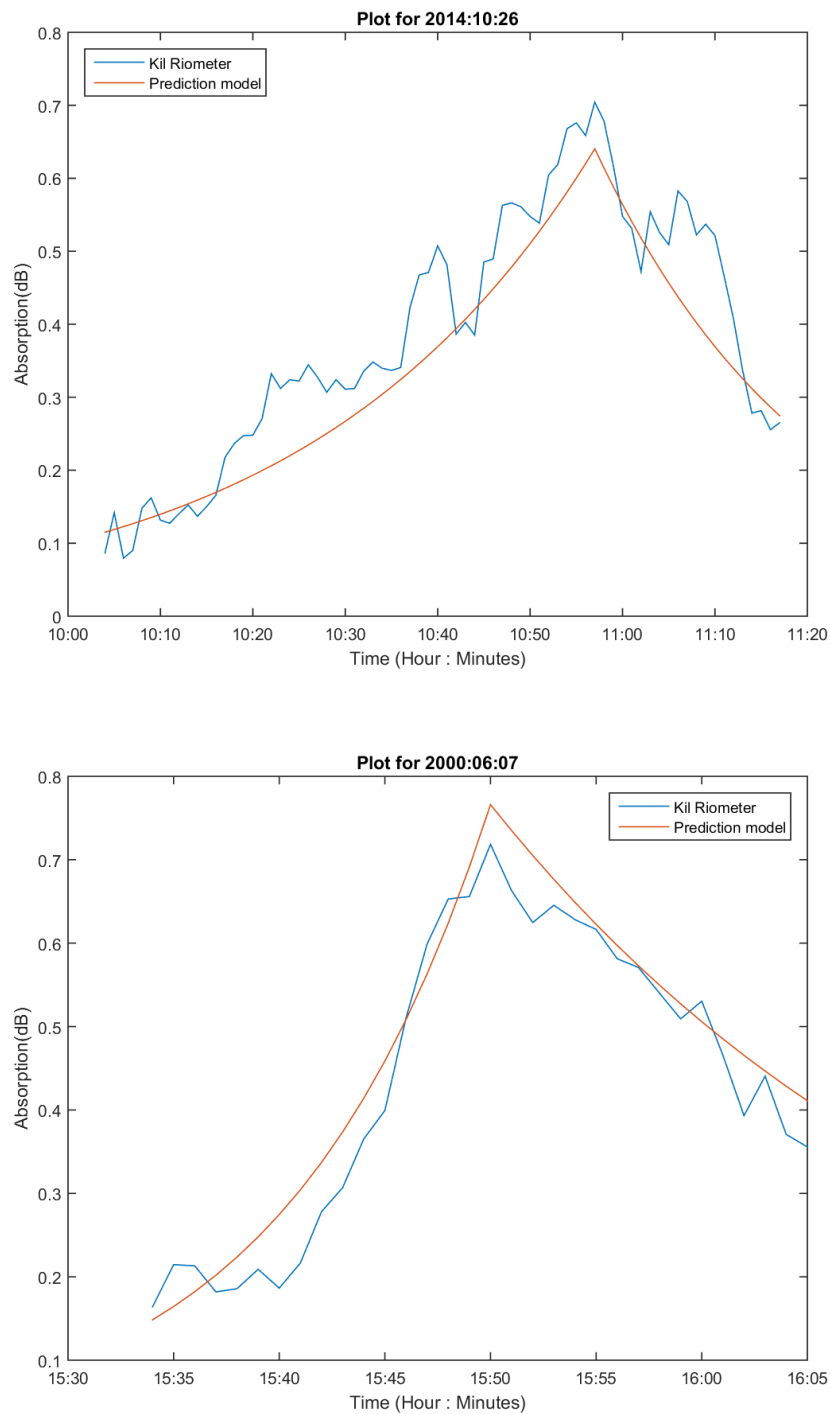


Figure 6.19: Plots of measured absorption (IRIS) in blue compared with model result in red for two X-class events. The events are within the dates utilised in obtaining the model (1996-2009).

Measured absorption is shown as Kil (Kilpisjärvi riometer) riometer measurement, the model result is shown as prediction model in the legend of the plots.

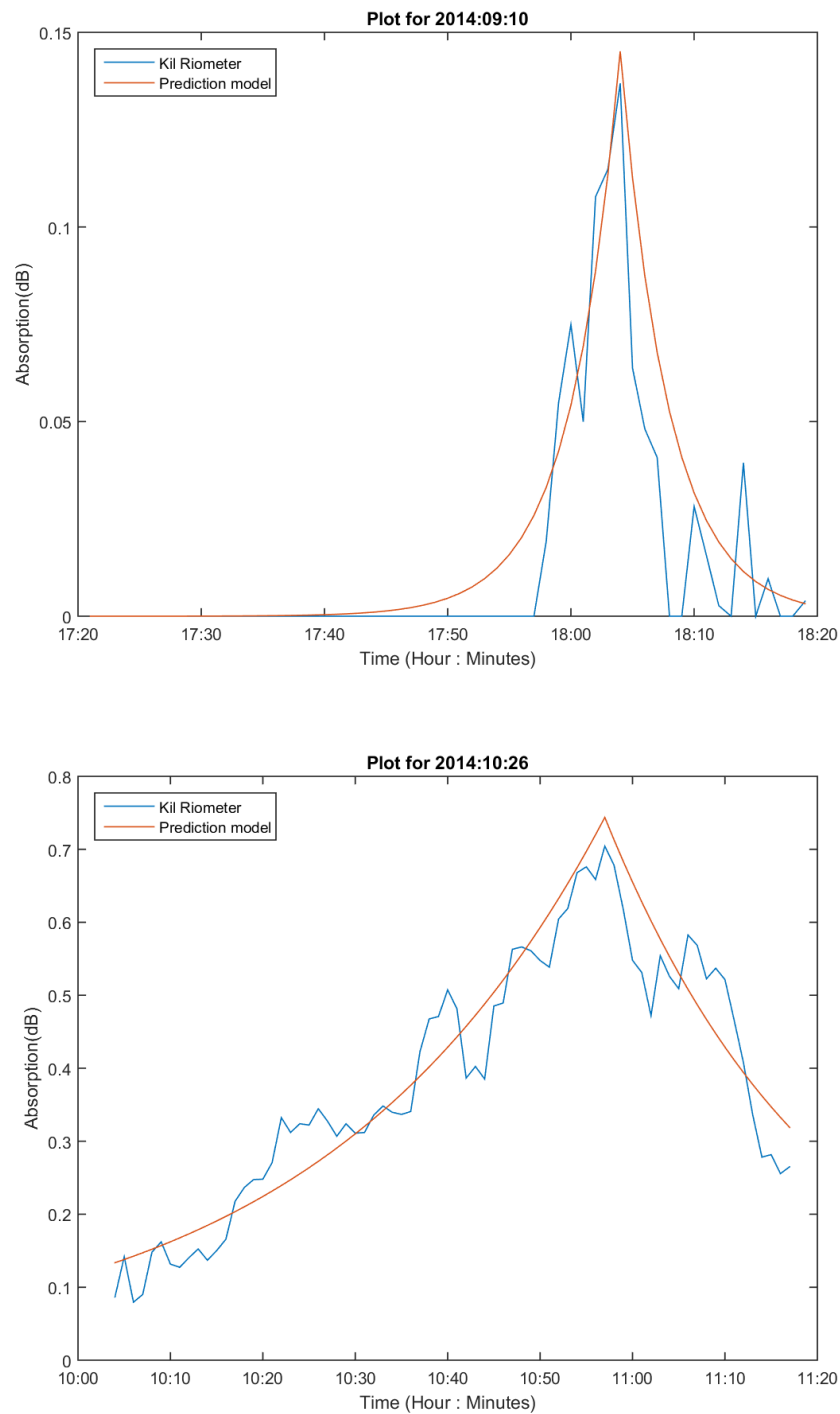


Figure 6.20: Plots of measured absorption (IRIS) in blue compared with model result in red for two X-class events. The events are X-class events that occurred outside the time frame utilised in the model. Measured absorption is shown as Kil (Kilpisjärvi riometer) riometer measurement, the model result is shown as prediction model in the legend of the plots.

Table 6.3: Table showing fit equations of parameters of absorption and flare.

Class of event	Relation for rise time of absorption and rise time of flare intensity	Relation for maximum absorption and peak flare intensity	Relation for decay time of absorption and decay time of flare intensity
M-class flares	$T_1 = 1.32X + 5.97$	$A = 48.90X + 0.38$	$T_2 = 0.54X + 7.19$
X-class flares	$T_1 = 1.22X + 5.05$	$A = 32.79X + 0.30$	$T_2 = 0.31X + 6.29$

and that it is less evident in lower intensity flares. The negative spike is not always observed if the Sun is not within a beam field of view or side lobes, the increased radio noise may not be received. As the negative spike is not a result of absorption in the ionosphere it is therefore of little importance in determining the impact of flares on ionospheric absorption.

Many flare events between 1996 and 2009 caused a measurable increase in absorption following the initial negative spike. This increase represents the sudden ionospheric disturbance produced by the increase in X-ray and UV flux during flare events. This increase in turn causes an increase in ionization leading to the peak in absorption by the D and lower E layer. The magnitude, duration and characteristic shape of the increase in absorption was found to vary considerably for different flare events. The results show that C-class flares have a negligible effect on absorption with no significant increase observed in the median absorption signature for all events between 1996 and 2009 (shown in Figure 6.8). This is further demonstrated by the relation between maximum absorption and flare intensity shown in Figure 6.17. It can be seen there is no significant increase in the maximum absorption recorded during events up to M4 class flares (intensity of $4 \times 10^{-5} \text{ Wm}^{-2}$). Beyond this, there is a noticeable increase in maximum absorption as flare intensity increases. This suggests there is a threshold for which flares below class M4 do not cause significant absorption effects in the ionosphere. This is likely because the increase in X-ray and UV flux does not cause sufficient ionisation to produce a measurable change in absorption.

For M-class flares the median absorption signature of events between 1996 and 2009 shows a significant effect on absorption (seen in Figure 6.8). It can be seen there is a distinct increase in absorption minutes after flare onset, reaching a maximum of 0.15 dB, 13 minutes from onset. The sudden ionospheric disturbance exhibits a fairly rapid period of rising absorption lasting under 10 minutes, followed by a more gradual steady decline to pre-flare levels lasting around 30 minutes. The rapid nature of the increase in absorption can likely be explained by a combination of factors. The absorption increases sharply partly because the enhancement of *XV*-ray and UV flux is very rapid due to the explosive nature of flare events. However the increase may also appear more rapid due to the preceding negative spike masking the beginning of the absorption event. For flares where the negative spike was not observed, the increase was seen to be more gradual. The slower decline back to pre-flare absorption levels corresponds to the typical slower decline in X-ray flux during flare events. Consequently the ionisation and recombination rates in the ionosphere take time to return to the pre-flare balance.

The X-class flares median absorption signature for 1996-2009 events also shows a significant effect on absorption (seen in Figure 6.10). The absorption signature exhibits a rapid increase in absorption reaching a maximum of 0.28 dB, nine minutes from onset, before a more gradual decline to pre-flare levels. The magnitude of the peak in absorption is almost double that seen in the M-class median absorption signature. This is a result of the larger increase in X-ray and UV flux from X-class flares causing notably more ionisation, resulting in the larger absorption effects. The duration of the ionospheric disturbance is seen to be very similar to the M-class events with absorption levels returning to normal around 45 minutes from onset. The upper quartile of the X-class flares (seen in Figure 6.11) exhibits a second peak in absorption around 80 minutes from onset not seen in the median. This peak is not seen in either the M or C-class flares. This indicates that very powerful flares produce a second ionospheric disturbance which could be a consequence of the extended flare phase observed in some very large events [Hudson, 2011]. During the extended flare phase, a second phase of X-ray emission is observed, which could lead to more ionisation and hence increased absorption.

The flare induced absorption model produced for M and X-class flares provides a basis for predicting the effect of M and X-class events. The model is based on the relational equations derived from (1) flare rise time and rise time in absorption (2) maximum absorption and the square root of peak intensity of flare and (3) decay time of flare and the decay time of absorption integrated into equations (6.1) and (6.2). Based on the median absorption signature of events between 1996 and 2009 and relations between parameters of flare and absorption were utilised to derive relations (Table 6.3) that were used in modelling absorption for flare events. However, there is a considerable variation between individual events, with a median absolute deviation in the absorption signature of 0.23 dB and 0.15 dB for X and M-class flares respectively. The considerable variation between the absorption recorded for individual events is likely a result of the highly variable nature of flares. The highly variable duration, emissions and associated solar activity such as CMEs make the prediction of associated absorption very complex. Hence at this stage the flare induced absorption models for X and M-class flares can only provide a crude estimate of absorption effects. However, they provide a valuable foundation from which the prediction of flare induced absorption may be refined with further study.

The model result compares better with measured absorption when the peak absorption and peak intensity occur at almost the same time (± 2 minutes). For events that have more than ± 2 minutes delay in the peaks of absorption and flare intensity, the result is not very good. Also an absorption profile that does not follow exponential rise and decay does not compare very well with observation.

Chapter 7

7.1 Conclusions

1. A number of methods have been proposed and utilised in predicting auroral absorption. Generally, most works have used geomagnetic indices such as K_p as coupling parameters in absorption prediction models, whereas the indices are not available real time. Solar wind parameters are now available in real time, this work used solar wind parameters as comprised in the Akasofu epsilon parameter as the coupling coefficient for absorption. Solar wind parameters are measured at the L1 Langragian point as recorded by advanced composite explorer (ACE) satellite. The idea of predicting absorption from solar wind parameters has been suggested by different authors especially those who have studied statistical relationships between solar wind parameters and absorption. It is also thought that a model based on solar wind parameters could provide an alternative as well as improvement to models that utilise geomagnetic indices. The technique utilised was to divide the dataset covering 1996-2009 to seasonal segments since it has been established that there is seasonal variation in absorption (e.g. Hargreaves, 2007, Krishnaswamy and Rosenberg, 1985). For each season, the dataset is further divided into hours of the day, following observed time variation of absorption (e.g. Kavanagh *et al.*, 2004). A linear relation is produced for every hour of the day within each season; these equations are then used to predict absorption based on seasons of occurrence.

From the result, it is seen that the model compares well with riometer observation (Kilpisjärvi, Finland) during solar quiet and moderate periods but shows significant

variation during active periods, periods of substorms and periods characterised by night time absorption spikes. Absorption spikes observed in the comparative plots of measured and modelled absorption (e.g. Figures 4.12-4.15) correspond with periods of substorm activity as measured by ground based magnetometer.

2. For a statistical model, absorption events occurring at all periods (1995-2006) were utilised. However, energetic precipitation during periods of specific solar activity (e.g. ICMEs and solar flares) is known to be associated with higher absorption. Hence, ICME and solar flare events have been identified and absorption during these periods is separately modelled.

3. ICMEs events analysed are as detailed in the Richardson and Cane [2010] catalogue. The various signatures used in identifying these events were shown in Table 5.2. The effect of ICMEs is known to last over days (typically a 2 day period). During ICMEs the response of the ionosphere to absorption is observed to be different owing to their time of occurrence identified as day or night based on the zenith angle of riometer station. Day time ICME events are classified as zenith less than 80 degrees ($\chi \leq 80$) and ($\chi \geq 100$) as night events (e.g. Seller 1977, Ranta, Ranta and Rosenberg, 1985).

An epoch analysis of day events commencing ICMEs shows peak absorption occurring few hours (1-2 hours) before start time during day events. This is due to splash precipitation of varying absorption occurring at the time; whereas for night commencing ICME events, absorption peak is observed between 2-3 hours after start time due to drizzle precipitation. To find a coupling parameter for day and night ICME absorption, epoch analysis of geophysical parameters such as the dynamic pressure, z -component of the IMF (B_z), solar wind velocity, and geophysical indices such as K_p and AE indices were performed. Dynamic pressure yields the best single parameter with day time absorption, while B_z yields the best single individual parameter for night time absorption. However, using pressure and B_z as coupling parameters for day and night time absorption did not yield a good measured v modelled result. To improve the result, more than one was utilised, a combination of pressure terms (viscous terms) and merging terms (IMF related terms) were ranked

based on their correlation with day and night time absorption. A combination of dynamic pressure and VB_z ranked best for day time absorption while nV^3 and B_z ranked best for night time absorption were utilised. To specify the model, linear regression in a quadratic form was utilised and equations 5.10 and 5.11 obtained for day and night time absorption respectively. Observation and model plots were shown.

4. On the response of the ionosphere to absorption during solar flares, different classes of flares bear different levels of effect on absorption. The variation is such that the intensity of flare determines its effect on radio absorption. Low intensity flares (C-class flares) do not show significant effect on absorption, whereas flares with higher intensity (M and X-class) do. X-class flares having the highest intensity bear the most significant effect on absorption.

5. On studying the relationship between parameters of flare and absorption, a significant positive correlation was observed between the mean flare duration for each class and the log of flare intensity. It was observed that low intensity flares could have a long duration equivalent to that of high intensity events; however, there was a decrease in short duration events as intensity increased. Thus, it is likely there is an underlying relation between peak flare intensity and flare duration, however, as a result of the complex mechanisms at work during flare, there may be other factors which have significant impact on flare duration.

6. There is a clear relation between the rise time of absorption and the intensity of the flare producing the absorption. Also, there is a significant correlation between the rise time of flares and median maximum absorption. Relationships between rise time of absorption and rise time of intensity were investigated and a formula relation was established, also relationship between maximum absorption and maximum intensity (square root) was investigated and an equation relating the two was established. Also, a relation was investigated for the relaxation time of flare from the point of maximum intensity and the decay in absorption from maximum absorption. The three relations (i.e. rise time of intensity v rise time of absorption, maximum absorption v square root of maximum intensity and the decay time of absorption

v the decay time in intensity) were used in specifying a flare induced absorption model.

7. Comparing absorption noticed during ICMEs with solar flare events, the absorption induced by ICMEs are of longer duration than those induced by solar flares. While solar flares induced absorption takes ($\sim 8-10$ minutes) to reach a peak value, ICMEs peaks after ($\sim 2-3$ hours). The magnitude of absorption during night time ICME events is higher than day time ICME events (for example, the peak absorption during day time ICME events is ~ 0.6 dB, whereas for night time events peak absorption is ~ 0.9 dB). Also, the magnitude of absorption during ICME events are generally higher than those observed during flare events as the peak median absorption signature during the most intense flare events (X-class) has a magnitude of 0.28 dB.

7.2 Further work

In other to test the reliability of the results of the models presented in Chapters 4, 5 and 6, it will be necessary to utilise the model on chains of riometer measurements in the global riometer array (GLORIA). The use of other riometer data will include factors such as longitudes and latitudes of those stations (for example, on the statistical analysis of Chapter 4) and zenith angle dependence for ICME and flare models. An improvement on the models for GLORIA will help to present a generalised statistical model, ICME and flare models. In the statistical model of Chapter 4, models of absorption during periods of substorms could be incorporated to account for absorption during substorms and night time spike events. To find a good coupling parameter for absorption, investigation with some other parameters that combines solar wind parameters may give an improved result. New coupling functions are been proposed based on new research findings such could be investigated to see if they yield any improvement on the Akasofu epsilon parameter utilised in this work. Since riometer is not available everywhere in the high latitude region, the possibility of finding a means of linking riometer data to inexpensive instru-

ment such as magnetometers could be explored. Statistical investigation could be extended to the South Pole to provide inter-hemispheric models.

With regards to the ICME model, a combination of parameters have been utilised as coupling parameter for absorption, however there is room for improvement on the combination of predictor and possibility of a simpler relation between absorption and predictor. For the flare model, parameters of flares have been related to parameters of absorption for predictive purposes. The zenith angle dependence of solar flare absorption could be investigated. The model presented for flare could not predict well when the absorption profile does not follow exponential profile; it is thus possible to improve on this to increase the conditions for the model to perform well. Finally, the models (statistics, ICME and flare) could be combined such that every segment of the combined model could be used for prediction in the form of a generalised model, in a way that the model identifies the segment of the model that would be useful under a specific solar condition. The statistical model could be used during periods of low and moderate solar activity while the ICME and flare could be applied during periods when such events occur.

References

- [1] Aggarwal, K. M., Nath, N., & Setty, C. S. G. K. (1979), *Collision frequency and the transport properties of electrons in the ionosphere*, Planetary and Space Science, volume 27, issue 6, pages 753–768, doi: 10.1016/0032-0633(79)90004-7.
- [2] Agy, V. (1970), *HF radar and auroral absorption*, Radio Science, volume 5, number 11, pages 1317–1324, doi: 10.1029/RS005i011p01317.
- [3] Agy, V. (1972), *A model for the study and prediction of auroral effects on HF radar*, Proc. AGARD conference on “Radars propagation in the Arctic”, AGARD-CP-97,32-1.
- [4] Agy, V. (1979), *Perspectives on the prediction of auroral absorption*, Special Topics in HF Propagation, Lisbon, Portugal, AGARD-CP-263.
- [5] Akasofu, S. I. (1979), *What is a magnetospheric substorm?*, In Dynamics of Magnetosphere, edited by S. I. Akasofu, pages 447–460, D. Reidel, Dordrecht, Netherlands, doi:10.1007/978-94-009-9519-2_23.
- [6] Alexeev, I. I., Kalegaev, V. V., Belenkaya, E. S., Bobrovnikov, S. Y., Feldstein, Y. I., & Gromova, L. I. (2001), *Dynamic Model of the Magnetosphere: Case study for January 9-12, 1997*, Journal of Geophysical Research, volume 106, no. A11, pages 683-693.
- [7] Alfvén, H., & Fälthammar, C. G. (1963), *Cosmical Electrodynamics*, Oxford University Press.
- [8] Alurkar, S. K., & Bhonsle, R. V. (1969), *Flare-time sudden enhancements of low frequency field strength and associated meter wave solar radio bursts*, Solar physics, volume 9, issue 1, pages 198-204, doi: 10.1007/BF00145741.
- [9] Aoki, T. (2005), *On the validity of Akasofu’s ϵ parameter and of the Vasyliunas et al. general formula for the rate of solar wind-magnetosphere energy input*, Earth, planets and space, volume 57, issue 2, pages 131-137, doi: 10.1186/BF03352557.

-
- [10] Appleton, E. V. (1925), *The Propagation of Radio Waves over the Earth*, Nature, volume 115, issue 2889, page 382, doi: 10.1038/115382d0.
- [11] Appleton, E. V., & Barnett, M. A. (1925), *Local reflection of wireless waves from the upper atmosphere*, Nature, 115, page 333, doi: 10.1038/115333a0.
- [12] Appleton, E. V., & Barnett, M. A. (1925), *On some direct evidence for downward atmospheric reflection of electric rays*, Proceedings of the Royal Society of London, 190, pages 621–641.
- [13] Appleton, E. V., Naismith, R., & Builder, G. (1933), *Ionospheric investigations in high latitudes*, Nature, vol. 132, pages 340–341, doi: 10.1038/132340a0
- [14] Appleton, E., & Piggott, W. R. (1954), *Ionospheric absorption measurements during a sunspot cycle*, Journal of Atmospheric and Terrestrial Physics, volume 5, issues 1–6, pages 141–172, doi:10.1016/0021-9169(54)90029-X.
- [15] Arnoldy, R. L. (1971), *Signature in the interplanetary medium for storms*, Journal of Geophysical Research, volume 76, page 5189, doi: 10.1029/JA076i022p05189.
- [16] Aschwanden, M. J. (2006), *Coronal magnetohydrodynamic waves and oscillations: observations and quests*, Philosophical Transactions of the Royal Society of London A: Mathematical, Physical and Engineering Sciences, volume 364, pages 417–432, doi: 10.1098/rsta.2005.1707.
- [17] Axford, W. I. (1962), *The Interaction between the solar wind and the earth's magnetosphere*, Journal of Geophysical Research, volume 67, no. A10, page 3791, doi/10.1029/JZ067i010p03791.
- [18] Axford, W. I. (1964), *Viscous interaction between the solar wind and the Earth's magnetosphere*, Planetary Space Science, volume 12, issue 1, page 45, doi:10.1016/0032-0633(64)90067-4.
- [19] Baker, D. N., Turner, N. E., & Pulkkinen, T. I. (2001), *Energy transport and dissipation in the magnetosphere during geomagnetic storms*, Journal of Atmospheric and Solar-Terrestrial Physics, volume 63, issue 5, page 421, doi:10.1016/S1364-6826(00)00169-3
- [20] Baker, D. N., Wiltberger, M. J., Weigel, R. S., Elkington, S. R. (2007), *Present status and future challenges of modelling the Sun–Earth end-to-end system*, Journal of Atmospheric and Solar-Terrestrial Physics, volume 69, issue 1-2, page 12, doi: 10.1016/j.jastp.2006.07.017.
- [21] Baker, D. N., Weigel, R. S., Rigler, E. J., McPherron R. L., Vassiliadis D., Arge C. N., Siscoe G. L., Spence H. E. (2004), *Sun-to-magnetosphere mod-*

-
- elling: CISM forecast model development using linked empirical models*, Journal of Atmospheric and Solar-Terrestrial Physics, vol 66, page 1491, doi: 10.1016/j.jastp.2004.04.011.
- [22] Balikhin, M. A., Boynton, R. J., Billings, S. A., Gedalin, M., Ganushkina, N., Coca, D., Weil, H. (2010), *Data based quest for solar wind-magnetosphere coupling function*, Geophysical Research Letters, volume 37, issue 24, doi: 10.1029/2010GL045733.
- [23] Barnden, L. R. (1973), *Forbush decrease 1966-1972: Their Solar and Interplanetary Associations and Their Anisotropies*, In International Cosmic Ray Conference, volume 2, page 1271.
- [24] Belcher, J. W., & Davis, L. (1971), *Large amplitude Alfvén waves in the interplanetary medium, 2*. Journal of Geophysical Research, volume 76, pages 3534-3536, doi: 10.1029/JA076i016p03534.
- [25] Berko, F. W., Hoffman, R. A., Burton, R.K., & Holzer, R. E. (1975), *Simultaneous particle and field observations of field-aligned currents*, Journal of Geophysical Research, volume 80, no. 1, pages 37–46, doi: 10.1029/JA080i001p00037.
- [26] Blum, E. J., Denisse, J. F., & Steinberg, J. L. (1954), *Influence de l'ionosphere sur la reception du rayonnement galactique de frequence 29.5 MC/S*, Comptes Rendus des Seances de L'Academie des Science, volume 238, page 1095.
- [27] Borovsky, J. E. (2008), *The Rudiment of a theory of solar wind/magnetosphere coupling derived from first principles*, Journal of Geophysical Research, volume 113, issue A8, doi: 10.1029/2007JA012646.
- [28] Borovsky, J. E., & Denton, M. H. (2006), *The differences between CME driven storms and CIR-driven storms*, Journal of Geophysical Research, volume 111, issue A7, doi: 10.1029/2005JA011447.
- [29] Bray, R. J., & Loughhead, R.E. (1957), *The Lifetime of Sunspot Penumbra Filaments*, Australian Journal of Physics, volume 11, no. 2, pages 185–190, CSIRO
- [30] Breit, G., & Tuve, M. A. (1925), *Note on a radio method of estimating the height of the conducting layer*, Journal of Geophysical Research, volume 30, issue 1, doi: 10.1029/TE030i001p00015.
- [31] Breit, G., & Tuve, M. A. (1926), *A test of the evidence of the existence of the conducting layer*, Physical Review, volume 28, page 554.

-
- [32] Browne, S., Hargreaves, J. K., & Honary, B. (1995), *An imaging riometer for ionospheric studies*, Electronics & communication engineering journal, volume 7, issue 5, pages 209–217, doi:10.1049/ecej:19950505.
- [33] Brown, R. R., & Driatsky, V. M. (1973), *Further Studies of Ionospheric and Geomagnetic effects of sudden impulses*, Planetary and Space Science, volume 21, issue 11, pages 1931–1935, doi:10.1016/0032-0633(73)90122-0.
- [34] Brueckner., G. E., Howard, R. A., Koomen, M. J., Korendyke, C. M., Michels, D. J., Moses, J. D., Socker, D. J., Dere, K. P., Lamy, P. L., Lebaria, A. L., Bout, M. V., Schwenn, R., Simnett, G. M., Bedford, D. K., & Eyles, C. J. (1995), *The Large Angle Spectroscopic Coronagraph (LASCO)*, Solar Physics, volume 162, issue 1, pages 357-402, doi: 10.1007/BF00733434.
- [35] Burlaga, L., Sittler, E., Mariani, F., & Schwenn, R. (1981), *Magnetic loop behind an interplanetary shock: Voyager, Helios, and IMP 8 observations*, Journal of Geophysical Research: Space Physics, volume 86, no. A8, page 6673, doi: 10.1029/JA086iA08p06673.
- [36] Burton, R. K., McPherron, R. L., & Russell, C. T. (1975), *An empirical relationship between interplanetary conditions and Dst*, Journal of Geophysical Research: Space Physics, volume 80, pages 4204–4214, doi: 10.1029/JA080i031p04204.
- [37] Carovillano, R. L., & Forbes, J. M. (1983), *Solar-Terrestrial Physics: Principles and Theoretical Foundations Based Upon the Proceedings of the Theory Institute Held at Boston College*, Springer Science & Business Media, ISBN 978-94-009-7194-3.
- [38] Cane, H. V. (2000), *Coronal mass ejections and Forbush decreases*, Space Science Reviews, volume 93, pages 55–77, doi:10.1023/A:1026532125747.
- [39] Cane, H. V., Richardson, I. G., & St Cyr, O. C. (2000), *Coronal mass ejections, interplanetary ejecta and geomagnetic storms*, Geophysical research letters, volume 27, issue 21, pages 3591–3594, doi: 10.1029/2000GL000111.
- [40] Cane, H.V, & Richardson I. G. (2003), *Interplanetary coronal mass ejections in the near-Earth solar wind during 1996-2002*, Journal of Geophysical Research: Space Physics, volume 108, issue A4, page 1156, doi: 10.1029/2002JA009817.
- [41] Cane, H. V., & Lario, D. (2006), *An introduction to CMEs and energetic particles*, Space science reviews, volume 123, pages 45–56, doi: 10.1007/s11214-006-9011-3.

-
- [42] Carmichael, H. U. G. H. (1964), *A process for flares*, NASA Special Publication, volume 50, page 451.
- [43] Cassen, P., & Szabo, J. (1970), *The viscous magnetopause*, Planetary and Space Science, volume 18, issue 3, pages 349–366, doi: 10.1016/0032-0633(70)90173-X.
- [44] Christensen-Dalsgaard, J., Dappen, W., Ajukov, S. V., & Anderson, E. R. (1996), *The current state of solar modelling*, Science, volume 272, issue 5266, pages 1286–1292, doi: 10.1126/science.272.5266.1286.
- [45] Contreira, D., Rodrigues, F. S., Makita, K., & Brum, C. G. (2004), *An experiment to study solar flare effects on radio-communication signals*, Advances in Space Research, volume 36, issue 12, pages 2455–2459.
- [46] Conway, W.S. (1959), *The upper boundary of the Van Allen radiation belts*, Nature, volume 184, pages 439–440, doi: 10.1038/184439a0.
- [47] Cowan, E. W. (1980), *An Earth dynamo with anisotropic resistivity*, Journal of Geophysical Research: Solid Earth, volume 85, pages 7242–7246, doi: 10.1029/JB085iB12p07242.
- [48] Coleman, Jr. (1971), *A model of the geomagnetic cavity*, Radio Science, volume 6, issue 2, page 321, doi: 10.1029/RS006i002p00321.
- [49] Delaboudinière, J. P., Artzner, G. E., Brunaud, J., Gabriel, A. H., Hochedez, J. F., Millier, F., & Kreplin, R. (1995), *EIT: Extreme-ultraviolet Imaging Telescope for the SOHO mission*, In The SOHO Mission, Springer Netherlands, volume 162, issue 1, pages 291–312, 10.1007/BF00733432.
- [50] Dennis, B. R., & Schwartz, R. A. (1989), *Solar flares: the impulsive phase*, Solar and Stellar Flares, volume 121, issue 1, pages 75–94, doi:10.1007/BF00161688.
- [51] Detrick, R. D., & Rosenberg, T. J. (1990), *A phased array radiowaves imager for studies of cosmic noise absorption*, Radio Science, volume 25, number 4, pages 325–338, doi: 10.1029/RS025i004p00325.
- [52] Denton, M. H., Borovsky, J. E., Skoug R. M., Thomsen M. F., Lavraud, B., Henderson M. G., McPherron R. L., Zhang J. C., & Liemohn, M. W. (2006), *Geomagnetic storms driven by ICME-and CIR-dominated solar wind*, Journal of Geophysical Research: Space Physics, volume 111, issue A7, doi:10.1029/2005JA011436.
- [53] Denton, M. H., & Borovsky, J. E. (2008), *Superposed epoch analysis of high-speed-stream effects at geosynchronous orbit: Hot plasma, cold plasma, and the*

-
- solar wind*, Journal of Geophysical Research: Space Physics, volume 113, issue A7, doi: 10.1029/2007JA012998.
- [54] Derek, M., Fallows, R., Norden, M., Aikio, A., Vierinen, J., Honary, F., Marple, S., & Ulich, T. (2015), *All-sky interferometric riometry*, Radio Science, volume 50, issue 10, pages 1050–1061, doi: 10.1002/2015RS005709.
- [55] Driatsky, V. M. (1966), *A study of the space and time distribution of auroral absorption according to observations of the riometer network in the Arctic*, Arctic and Antarctic Scientific Research Inst., Leningrad, volume 6, page 828.
- [56] D Region Absorption Prediction. Release2 [DRAP2], (2013), http://products.weather.gov/PDD/SWx_DRAP2_Op_PDD.pdf.
- [57] Du, A. M., Tsurutani, B. T., & Sun, W. (2011), *Solar wind energy input during prolonged, intense northward interplanetary magnetic fields: A new coupling function*, Journal of Geophysical Research: Space Physics, volume 116, doi.org/10.1029/2011JA016718.
- [58] Durham, I. T. (2006), *Rethinking the History of Solar Wind Studies: Eddington's analysis of comet morehouse*, Notes and Records, The Royal Society Journal of the History of science, volume 60, issue 3, pages 261–270 doi: 10.1098/rsnr.2006.0149.
- [59] Evans, R. M., Pulkkinen, A. A., Zheng, Y., Mays, M. L., Taktakishvili, A., Kuznetsova, M. M., & Hesse, M. (2013), *The SCORE scale: a coronal mass ejection typification system based on speed*, Space Weather, volume 11, issue 6, doi: 10.1002/swe.20058.
- [60] Echer, E., Gonzalez, W. D., & Tsurutani, B. T. (2008), *Interplanetary conditions leading to super-intense geomagnetic storms ($D_{st} \leq -250$ nT) during solar cycle 23*, Geophysical Research Letters, volume 35, no. 6, L06S03, doi:10.1029/2007GL031755.
- [61] Verniani, F. (Ed.) (1974), *Structure and dynamics of the upper atmosphere: proceedings of the 2d course of the International School of Atmospheric physics, Ettore Majorana Centre for Scientific Culture, held in Erice (Italy)*, volume 1, Elsevier Publishing Company, ISBN-10: 0444411054.
- [62] Foppiano, A. J., & Bradley, P. A. (1983), *Prediction of auroral absorption of high-frequency waves at oblique incidence*, Telecommunication Journal (Geneva), volume 50, no. 10, pages 547–560.

-
- [63] Foppiano, A. J., & Bradley, P. A. (1985), *Morphology of background auroral absorption*, Journal of atmospheric and terrestrial physics, volume 47, issue 7, pages 663–74, doi:10.1016/0021-9169(85)90102-3.
- [64] Foppiano, A. J. (1975), *A new method for predicting the auroral absorption of HF sky waves*, In CCIR Interim Working Party 64, Documents 3 and 10, International Telecommunication Union Geneva.
- [65] Foppiano, A. J., & Bradley, P. A. (1984), *Day to day variability of riometer absorption*, Journal of atmospheric and terrestrial physics, volume 46, issue 8, pages 689–696, doi: 10.1016/0021-9169(84)90130-2.
- [66] Forbush, S. E. (1937), *In the effects in cosmic-ray intensity observed during the recent magnetic storm*, Physical Review, volume 51, page 1108, doi:http://dx.doi.org/10.1103/PhysRev.51.1108.3
- [67] Forbush, S. E. (1938), *On cosmic-ray effects associated with magnetic storms*, Terrestrial Magnetism and Atmospheric Electricity, volume 43, issue 3, pages 203–218, doi: 10.1029/TE043i003p00203.
- [68] Greenberg, E. M., & LaBelle J. (2002), *Measurement and modeling of auroral absorption of HF radio waves using a single receiver*, Radio science, volume 37, issue 2, pages 6–12, doi: 10.1029/2000RS002550.
- [69] Gonzalez, W. D., Joselyn, J., Kamide, Y., Kroehl, H. W., Rostoker, G., Tsurutani, B. T., Vasyliunas, V.M. (1994), *What is a geomagnetic storm?*, Journal of Geophysical Research Letters, volume 99, issue A4, page 5771, doi: 10.1029/93JA02867.
- [70] Gosling, J.T. (2012), *Magnetic reconnection in the solar wind*, Space science review, volume 172, issue 1, pages 187–200, doi: 10.1007/s11214-011-9747-2.
- [71] Gosling, J. T., Pizzo, V., & Bame, S. J. (1973), *Anomalously low proton temperatures in the solar wind following interplanetary shock waves—Evidence for magnetic bottles?*, Journal of Geophysical Research, volume 78, pages 2001–2009, doi: 10.1029/JA078i013p02001.
- [72] Gosling, J. T. (1990), *Physics of Magnetic Flux Ropes*, American Geophysical Union, volume 58, pages 343–364, doi: 10.1029/GM058p0343.
- [73] Gosling, J. T., Baker, D. N., Bame, S. J., Feldman, W. C., Zwickl, R. D., Smith, E. J. (1987), *Accelerated plasma flows at the near-tail magnetopause*, Journal of Geophysical Research, volume 91, issue A3, pages 3029–3041, doi: 10.1029/JA091iA03p03029.

-
- [74] Hanson, W. B., & Moffett, R. J. (1966), *Ionization transport effects in the equatorial F-Region*, Journal of Geophysical Research, volume 71, issue 23, doi: 10.1029/JZ071i023p05559.
- [75] Hargreaves, J. K. (2007), *Seasonal variations in the incidence of auroral radio absorption events at very high latitude, and the influence of the magnetotail*, Annales Geophysicae, volume 25, pages 711–720.
- [76] Guarnieri, F. L., Tsurutani, B. T., Gonzalez, W. D., Echer, E., Gonzalez, A. L., Grande, M., & Soraas, F. (2006), *ICME and CIR storms with particular emphases on HILDCAA events*, ILWS Workshop, pages 19–20.
- [77] Hargreaves, J. K. (1995), *Solar terrestrial environment*, Cambridge university Press.
- [78] Hargreaves, J. K. (1969), *Auroral absorption of HF radio waves in the ionosphere: a review of results from the first decade of riometry*, Proceedings of the IEEE, volume 57, issue 8, pages 1348–1373, doi: 10.1109/PROC.1969.7275.
- [79] Hargreaves, J. K., & Sharp, R. D. (1965), *Electron precipitation and ionospheric radio absorption in the auroral zone*, Planetary and Space Science, volume 13, issue 12, pages doi: 1171–1183, 10.1016/0032-0633(65)90054-1.
- [80] Hargreaves, J. K., Feeney, M. T., Ranta, H., & Ranta, A. (1987), *On the prediction of auroral radio absorption on the equatorial side of the absorption zone*, Journal of atmospheric and terrestrial physics, volume 49, issue 3, pages 259–272, doi: 10.1016/0021-9169(87)90061-4.
- [81] Hargreaves, J. K., & Cowley, F. C. (1967), *Studies of auroral radio absorption events at three magnetic latitudes- 1. Occurrence and statistical properties of the events*, Planetary and Space Science, volume 15, issue 10, pages 1571–1583, doi: 10.1016/0032-0633(67)90090-6.
- [82] Hartz, T. R., Montbriand, L. E., Vogan, E. L. (1963), *A study of auroral absorption at 30 Mc/s*, Canadian Journal of Physics, volume 41, pages 581–595, doi: 10.1139/p63-061.
- [83] Herman, J. R., & Vargas-Vila, R. (1972), *Investigation of auroral ionospheric and propagation phenomena related to the Polar Fox II experiment*, Analytical Systems Corporation, report ASCR-7262.
- [84] Hills, T. W. (1979), *Rates of mass, momentum, and energy transfer at the magnetopause*, Magnetospheric boundary layers, volume 148, pages 325–332.
- [85] Hirayama, T. (1974), *Theoretical model of flares and prominences*, Solar Physics, volume 34, issue 2, pages 323–338, doi: 10.1007/BF00153671.

-
- [86] Hirshberg, J., & Colburn, D. S. (1969), *The interplanetary field and geomagnetic variations—a unified view*, Planetary and Space Science, volume 17, page 1183–1206, doi: 19690075250.
- [87] Honary, F., Marple, S. R., Barratt, K., Chapman, P., Grill, M., & Nielsen, E. (2011), *Invited Article: Digital beam-forming imaging riometer systems. Review of Scientific Instruments*, Review of Scientific Instruments, volume 82, 03131, doi:10.1063/1.3567309.
- [88] Hudson, H. S. (2011), *Global properties of solar flares*, Space Science Reviews, volume 158, issue 5, pages 5–41, 10.1007/s11214-010-9721-4.
- [89] Hultqvist, B., Aarons, J., & Ortner, J. (1958), *Effects of the solar flares of 7 July 1958 observed at Kiruna Geophysical Observatory, Sweden*, Tellus, volume 11, issue 3, pages 319–331, doi: 10.1111/j.2153-3490.1959.tb00037.x
- [90] Hultqvist, B. (1999), *Magnetospheric plasma sources and losses: Final report of the ISSI study project on source and loss processes of magnetospheric plasma*, volume 6, Springer Science & Business Media, ISBN: 978-94-011-4477-3.
- [91] Hundhausen, A. J. (1996), *Sizes and locations of coronal mass ejections: SMM observations from 1980 and 1984–1989*, Journal of Geophysical Research: Space Physics, pages 141–200, Wiley Online Library.
- [92] Hundhausen, A. J. (1997), *Coronal mass ejections*, Cosmic Winds and the Heliosphere, Tucson: Univ. Arizona Press, pages 259–296.
- [93] Hunsucker, R. D., & Hargreaves, J. K. (2007), *The high-latitude ionosphere and its effects on radio propagation*, Cambridge University Press.
- [94] Van Allen, J. A., & Frank, L. A. (1959), *Radiation measurement to 658,300 km with pioneer IV*, Nature, volume 184, doi: 10.1038/184219a0.
- [95] Jelly, D. H., & Brice, N. M. (1967), *Changes in Van Allen radiation associated with polar substorms*, Journal of Geophysical Research, volume 72, issue 23, pages 5919–5931, doi: 10.1029/JZ072i023p05919.
- [96] Jian, L. K., Russell, C. T., Luhmann, J. G., Anderson, B. J., Boardsen, S. A., Strangeway, R. J., Cowee, M. M., & Wennmacher, A. (2010), *Observations of ion cyclotron waves in the solar wind near 0.3 AU*, Journal of Geophysical Research, volume 115, issues 12, doi: 10.1029/2010JA015737.
- [97] Jian, L., Russell, C. T., Luhmann, J. G., & Skoug, R. (2006), *Properties of stream interactions at one AU during 1995–2004*, Solar Physics, volume 239, pages 337–392 doi: 10.1007/s11207-006-0132-3.

-
- [98] Jones, K. L. (1971), *Storm time variation of the F2-layer electron concentration*, Journal of Atmospheric and Terrestrial Physics, volume 33, issue 3, pages 379–389, doi: 10.1016/0021-9169(71)90143-7.
- [99] Jelly, D. (1970), *On the morphology of auroral absorption during substorms*, Canadian Journal of Physics, volume 48, issue 3, pages 335–345, doi: 10.1139/p70-045.
- [100] Guo, J., Feng, X., Emery, B. A., Zhang, J., Xiang, C., Shen, F., & Song, W. (2011), *Energy transfer during intense geomagnetic storms driven by interplanetary coronal mass ejections and their sheath regions*, Journal of Geophysical Research, Space Physics, volume 116, issue A5, pages 1–12. doi: 10.1029/2011JA016490.
- [101] Kan, J. R., & Lee, L. C. (1979), *Energy coupling function and solar wind-magnetosphere dynamo*, Geophysical Research Letters, volume 6, issue 7, pages 577–580, doi: 10.1029/GL006i007p00577.
- [102] Kamide, Y., Baumjohann, W., Daglis, I. A., Gonzalez, W. D., Grande, M., Joselyn, J. A., ... & Sharma, A. S. (1998), *Current understanding of magnetic storms: storm-substorm relationships*, Journal of Geophysical Research: Space Physics, volume 103, issue A8, pages 17705–17728, doi: 10.1029/98JA01426.
- [103] Kamide, Y., & Chian, A. C. L. (Eds.) (2007), *Handbook of the solar-terrestrial environment*, Springer Science & Business Media, ISBN 978-3-540-46315-3.
- [104] Kamide, Y., Yokoyama, N., Gonzalez, W., Tsurutani, B. T., Brekke, A., & Masuda, S. (1997), *Two step Development of Geomagnetic storms*, Citeseer, volume 103, issue A4, pages 6917–6921, doi: 10.1029/97JA03337.
- [105] Kavanagh, A. J., Honary, F., Donovan, E. F., Ulich, T., & Denton, M. H. (2012), *Key features of > 30 KeV electron precipitation during high speed solar wind streams: a supersonic epoch analysis*, Journal of Geophysical Research: Space Physics, volume 117, issue 6, pages 6917–6921, doi: 10.1029/2011JA017320.
- [106] Kavanagh, A. J. (2002), *Energy deposition in the lower auroral ionosphere through energetic particle precipitation*, a Ph.D thesis submitted to the department of Communication Systems, Lancaster University, Lancaster, United Kingdom.
- [107] Keith, T. S. (1991), *Observations from the Solar Maximum Mission*, Philosophical Transactions of the Royal Society of London A: Mathematical, Physical and Engineering Sciences, volume 336, pages 326–337.

-
- [108] Davies, K. (1990), *Ionospheric radio, IEE electromagnetic waves series 31*, Peter Peregrinus Ltd., London, United Kingdom.
- [109] Kivelson, M. G., & Russell, C. T. (1995), *Introduction to space physics*, Cambridge university press.
- [110] Klecker, B., Kunow, H., Cane, H. V., Dalla, S., Heber, B., Kecskemety, K., Klein, K-L, Kota, J., Kucharek, H., Lario, D., Lee, M. A., Popecki, M. A., Posner, A., Rodriguez-Pacheco, J., Sanderson, T., Simnett, G. M., & Roelof, E. C. (2006), *Energetic Particle Observations*, Space Sciences, volume 123, issue 1, pages 217–250, doi: 10.1007/s11214-006-9018-9
- [111] Klein, L. W., & Burlaga, L. F. (1982), *Interplanetary magnetic clouds at 1 AU*, Journal of Geophysical Research, vol. 87, pages 613-624, doi: 10.1029/JA087iA02p00613.
- [112] Kopp, R. A., & Pneuman, G. W. (1976), *Magnetic reconnection in the corona and the loop prominence phenomenon*, Solar Physics, volume 50, pages 85-98, doi:10.1007/BF00206193.
- [113] Krishnamurthi, M., Sastry, G. S., & Rao, T. S. (1962), *Sudden Cosmic Noise Absorption at 29 Mc/s*, Australian Journal of Physics, volume 15, page20, doi: 1962AuJPh..15...20K.
- [114] Krishnaswamy, S., & Rosenberg, T. J. (1985), *Riometer measurements of seasonal variations in auroral absorption at South Pole and Siple Stations*, Antarctic Journal, volume 20, page 131.
- [115] Lanzerotti, L. J. (2007), *Space Weather Effects on Communications*, NATO Science series, Series 30, eBook title: Space storm and space weather hazards, Published by Springer Praxis Books, pages 313–334, doi: 10.1007/978-94-010-0983-6_12.
- [116] Lester, M., Milan, S. E., Provan, G., Wild, J. A. (2006), *Review of ionospheric effects of solar wind magnetosphere coupling in the context of the expanding contracting polar cap boundary model*, Space science series of ISSI, eBook title: Solar dynamics and its effect on the heliosphere and Earth. volume 22, published by springer New York, USA, doi: 10.1007/978-0-387-69532-7_9.
- [117] Liu, Y. D., Luhmann, J. G., Lugaz, N., Möstl, C., Davies, J. A., Bale, S. D., & Lin, R. P. (2013), *On sun-to-earth propagation of coronal mass ejections*, The astrophysical journal, volume 769, issue 1, no. 45, doi:10.1088/0004-637X/769/1/45.

-
- [118] Little, C. G., & Leinbach, H. (1958), *Some measurement of high latitude ionospheric absorption using extraterrestrial radio waves*, Proceeding of the Institute of Radio Engineers (IRE), volume 46, issues 1, pages 334-348, doi: 10.1109/JRPROC.1958.286795.
- [119] Little, C. G., & Leinbach, H. (1959), *The riometer-a device for continuous measurement of ionospheric absorption*, Proceedings of the IRE, volume 47, issue 2, pages 315-320, doi: 10.1109/JRPROC.1959.287299.
- [120] Loewe, C. A., & Prölss, G. W. (1997), *Classification and mean behavior of magnetic storms*, Journal of Geophysical Research, Space Physics, volume 102, issue A7, pages 14209-14213, doi: 10.1029/96JA04020.
- [121] Longden, N. C. (2007), *Global precipitation effects following solar wind derive*, Ph.D thesis, submitted to the department of communication systems, Lancaster university, Lancaster, United Kingdom.
- [122] Longden, N., Denton, M. H., Honary, F. (2008), *Particle precipitation during ICME-driven and CIR-driven geomagnetic storms*, Journal of Geophysical Research: Space Physics, volume 113, issue A6, doi: 10.1029/2007JA012752.
- [123] Longden, N., Honary, F., Kavanagh, A. J., & Manninen, J. (2007), *The driving mechanisms of particle precipitation during moderate geomagnetic storm of 7 January 2005*, Annales Geophysicae, volume 25, pages 2053-2068, doi: 10.5194/angeo-25-2053-2007.
- [124] Meredith, N. P., Horne, R. B., Lam, M. M., Denton, M. H., Borovsky, J. E. & Green, J. C. (2011), *Energetic electron precipitation during high speed solar wind stream driven storms*, Journal of Geophysical Research, volume 116, issue A5, doi: 10.1029/2010JA016293.
- [125] McIlwain, C. E. (1961), *Co-ordinates for mapping the distribution of magnetically trapped particles*, Journal of Geophysical Research, volume 66, pages 3681-3691, doi: 10.1029/JZ066i011p03681.
- [126] McComas, J., Bame, S. J., Barker, P., Feldman, W. C., Phillips, J. L., Riley, P. & Griffee, J. W. (1998), *Solar Wind Electron Proton Alpha Monitor (SWEPAM) for the Advanced Composition Explorer*, Space Science Reviews, volume 86, issue 1-4, pages 563-612, doi: 10.1023/A:1005040232597.
- [127] Blanc, M. (1988), *Magnetosphere-ionosphere coupling*, Computer Physics Communications, volume 49, issue 1, pages 103-118, doi: 10.1016/0010-4655(88)90219-6.

-
- [128] Milan, S. E., Jones, T. B., Lester, M., Warrington, E. M., & Reeves, G. D. (1996), *Substorm correlated absorption on a 3200 km trans-auroral HF propagation path*, *Annales Geophysicae*, volume 14, issue 1, page 182–190, doi: 10.1016/0010-4655(88)90219-6.
- [129] Mitra, A. P., & Shain, C. A. (1953), *The measurement of ionospheric absorption using observations of 18.3 Mc/s cosmic radio noise*, *Journal of Atmospheric and Terrestrial Physics*, volume 4, pages 204–218.
- [130] Neugebauer, M., Goldstein, R. (1997), *Particle and field signatures of coronal mass ejections in the solar wind*, American Geophysical Union.
- [131] Newell, P. T., Sotirelis, T., Liou, K., Rich, F. J. (2008), *Pairs of solar wind-magnetosphere coupling functions: Combining a merging term with a viscous term works best*, *Journal of Geophysical Research: Space Physics*, volume 113, issue A4, doi: 10.1029/2007JA012825.
- [132] Nishino, M., Yamagishi, H., Stauning, P., Rosenberg, T. J., & Holtet, J. A. (1997), *Location, spatial scale and motion of radio wave absorption in the cusplatitude ionosphere observed by imaging riometers*, *Journal of Atmospheric and Terrestrial Physics*, volume 59, issue 8, pages 903–924
- [133] Nwankwo, V. U., Chakrabarti, S. K., & Ogunmodimu, O. (2016, July), *Probing geomagnetic storm driven magnetosphere-Ionosphere dynamics via propagation characteristics of very low frequency radio signals*, *Journal of Atmospheric and Terrestrial Physics*, doi: 10.1016/j.jastp.2016.04.014.
- [134] Ogunmodimu, O., Honary, F., & Marple, S. (2011), *Relationship between auroral absorption and the epsilon parameter*, 11th International Ionospheric Symposium, Alexandra, USA.
- [135] Ogunmodimu, O., & Honary, F. (2012), *Predicting auroral absorption from epsilon parameter*, 9th European Space Weather week, Brussels, Belgium.
- [136] Olsen, W. P. (1982), *The geomagnetic field and its extension into space*, *Advances in Space Research*, volume 2, issue 1, pages 13–17.
- [137] Ortner, J., Hultqvist, B., Brown, R. R., Hartz, T. R., Holt, O., Landmark, B., Hook, J. L., Leinbach, H. (1962), *Cosmic noise absorption accompanying storm commencements*, *JGR*, volume 67, issue 11, pages 4169–4186, doi: 10.1029/JZ067i011p04169
- [138] Osepian, A., & Kirkwood, S. (2004), *Cosmic radio-noise absorption bursts caused by solar wind shocks*, *Annales Geophysicae*, volume 22, issue 8, pages 2973–2987, doi: 10.5194/angeo-22-2973-2004.

-
- [139] Parker, E. N. (1958), *Dynamics of the interplanetary gas and magnetic fields*, The Astrophysical Journal, volume 128, page 664, doi: 10.1086/146579.
- [140] Parker, E. N. (1959), *Extension of the solar corona into interplanetary space*, Journal of Geophysical Research: Space Physics, volume 64, issue 11, page 1675–1681, doi: 10.1029/JZ064i011p01675.
- [141] Park, G. K. (2004), *Physics of space plasmas: an introduction*, Redwood City, CA; Addison-Wesley Publishing Co., ISBN: 0-8133-4130-2.
- [142] Stauning, P. (1996a), *High-latitude D-and E-region investigations using imaging riometer observations*, Journal of Atmospheric and Terrestrial Physics, volume 58, no. 6, pages 765–783, doi: 10.1016/0021-9169(95)00073-9
- [143] Stauning, P. (1996b), *Investigations of ionospheric radio wave absorption processes using imaging riometer techniques*, Journal of Atmospheric and Terrestrial Physics, volume 58, no. 6, pages 753–764, doi: 10.1016/0021-9169(95)00072-0.
- [144] Stauning, P. (1998), *Ionospheric radiowave absorption processes in the dayside polar cap boundary regions*, In Polar Cap Boundary Phenomena, NATO ASI series, series volume 509, Kluwer academic publishers, Springer Netherlands.
- [145] Piggott, W. R., & Rawer, K. (1961), *URSI handbook of ionogram interpretation and reduction*, published by Elsevier publishing company, Amsterdam.
- [146] Proelss, G. W. (1993), *On explaining the local time variation of ionospheric storm effects*, Annales Geophysicae, volume 11, no. 1, pages 1–9.
- [147] Pudovkin, M. I., Zaitseva, S. A., & Benevolenska, E. E. (1979), *The structure and parameters of flare streams*, Journal of Geophysical Research, volume 84, page 6649, doi: 10.1029/JA084iA11p06649.
- [148] Rakowski, C. E., Laming, J. M., & Lepri, S. T. (2007), *Ion charge states in halo coronal mass ejections: what can we learn about the explosion*, The Astrophysical Journal, volume 667, issue 1, pages 602–609, doi: 10.1086/520914.
- [149] Ranta, H., Ranta, A., Rosenberg, T. J. (1984), *The day to night absorption ratio in auroral and sub-auroral zone riometer measurements during auroral absorption*, Journal of atmospheric and terrestrial physics, volume 46, issue 5, pages 395–398, doi: 10.1016/0021-9169(84)90082-5.
- [150] Ratcliffe, J. A. (1959), *The magneto-ionic theory and its application to the ionosphere: a monograph*, Cambridge university press., Cambridge, United Kingdom, ISBN: 9780521060417.

-
- [151] Rawer, K. (1976), *Manual on ionospheric absorption measurements*, published by world data centre a for solar-terrestrial Physics, Boulder, Colorado, USA.
- [152] Rees, M. H. (1963), *Auroral ionization and excitation by incident energetic electrons*, Planetary and Space Science, volume 11, page 1209, doi: 10.1016/0032-0633(63)90252-6.
- [153] Reid, G. C. (1967), *Ionospheric disturbances*, In Physics of Geomagnetic Phenomena, volume 1, page 627.
- [154] Rigler, E. J., Baker, D. N., Weigel, R. S. (2004), *Adaptive linear prediction of radiation belt electron using kalman filter*, Space Weather, volume 2, issues 3, doi: 10.1029/2003SW000036.
- [155] Rishbeth, H., Fuller, R. T. J., & Rees, D. (1987), *Diffusive equilibrium and vertical motion in the thermosphere during a severe magnetic storm: a computational study*, Planetary and space science, volume 35, pages 1157–1165, doi: 10.1016/0032-0633(87)90022-5.
- [156] Richardson, I. G. (1997), *Using energetic particles to probe the magnetic topology of ejecta*, Coronal Mass Ejections, Wiley Online Library, volume 99, pages 189–198, doi: 10.1029/GM099p0189.
- [157] Richardson, I. G., & Cane, H. V. (2010), *Near-Earth Interplanetary coronal mass ejections during solar cycle 23 (1996-2009): Catalogue and summary of properties*, Solar Physics, volume 264, issue 1, pages 189–237, doi: 10.1007/s11207-010-9568-6.
- [158] Richardson, I. G. (2013), *Geomagnetic activity during the rising phase of solar cycle 24*, Journal of Space Weather and Space Climate, volume 3, issue A08, pages 1–11, doi: 10.1051/swsc/2013031.
- [159] Richardson, J. D., & Smith, C. W. (2003), *The radial temperature profile of the solar wind*, Geophysical research letters, volume 30, issue 5, doi: 10.1029/2002GL016551.
- [160] Ritchie, S. E., & Honary, F. (2009), *Advances in ionospheric propagation modelling at high latitudes*, Ionospheric radio Systems and Techniques (IRST 2009), 11th International conference of IET, Edinburgh, United Kingdom, doi: 10.1049/cp.2009.0029.
- [161] Ritchie, S. E., & Honary, F. (2009), *Storm Sudden Commencement and its effect on high latitude HF Communication Links*, Space Weather, volume 7, issue 6, pages 1–20, doi: 10.1029/2008SW000461.

-
- [162] Roberts, C. S. (1969), *Pitch-angle diffusion of electrons in the magnetosphere*, Reviews of Geophysics, volume 7, no. A1, page 305, doi: 10.1029/RG007i001p00305.
- [163] Rosenberg, T. J., Wang, Z., Rodger, A. S., Dudeney, J. R., & Baker, K. B. (1993), *Imaging riometer and HF radar measurements of drifting F region electron density structures in the polar cap*, Journal of Geophysical Research, volume 98, pages 7757–7764.
- [164] Russell, C. T., & Luhmann, J. G. (1997), *Earth magnetic field and magnetosphere, originally published in the encyclopedia of planetary sciences*, Chapman and Hall, New York, USA, pages 208–211.
- [165] Russell, C. T., & Shinde, A. A. (2003), *ICME identification from solar wind ion measurement*, Solar Physics, volume 216, issue 1, pages 285–294, doi: 10.1023/A:1026108101883.
- [166] Russell, C. T. (1974), *Correlated interplanetary magnetospheric observations*, Proceeding of the seventh ESLAB symposium held at Saulgau, W.Germany, 22–25 May, 1973.
- [167] Russell, C. T. (2010), *The solar wind interaction with the Earth’s magnetosphere: a tutorial*, IEEE transactions on plasma science.
- [168] Sauer, H. H., & Daniel, C. W. (2008), *Global mapping of ionospheric HF/VHF radio wave absorption due to solar energetic protons*, Space Weather, volume 6, issue 12, doi: 10.1029/2008SW000399.
- [169] Sheeley, N. R. Jr., Howard R. A., Koomen M. J., Michelis D. J., Schwenn R., Mühlhäuser K. H. (1985), *Coronal mass ejections and interplanetary shocks*, Journal of Geophysical Research: Space Physics, volume 90, pages 163–175, doi: 10.1029/JA090iA01p00163.
- [170] Schunk, R., & Nagy, A. (2009), *Ionospheres: physics, plasma physics and chemistry*, Cambridge university press, ISBN-13: 978-0521877060.
- [171] Schunk, H. G., & Demars, R. W. (1987), *Comparison of solutions to bi-maxwellian and maxwellian transport equations for subsonic flows*, Journal of Geophysical Research: Space Physics, volume 92, issue A6, pages 5969–5990, doi: 10.1029/JA092iA06p05969.
- [172] Sellers, B., Hanser, F.A., Strocio, M.A., Yates, K. (1977), *The night and day relationships between polar cap Riometer absorption and solar protons*, Radio Science, volume 12, issue 5, pages 779–789, doi: 10.1029/RS012i005p00779.

-
- [173] Shain, C. A., & Higgins, C. S. (1954), *Observation of the general background and discrete sources of 18.3 Mc/s cosmic noise*, Australian Journal of Physics, volume 7, page 130.
- [174] Shea, M. A., & Smart, D. F. (1996), *Solar proton fluxes as a function of the observation location with respect to the parent solar activity*, Advances in Space Research, volume 17, issue 4-5, pages 225–228, doi:10.1016/0273-1177(95)00574-X.
- [175] Shodhan, S., Crooker, N. U., Kahler, S. W., Fitzenreiter, R. J., Larson, D. E., Lepping, R. P., Siscoe, G. L., Gosling, J. T. (2000), *Counterstreaming electrons in magnetic clouds*, Journal of Geophysical Research: Space Physics, volume 105, issue A12, pages 27261–27268, doi: 10.1029/2000JA000060.
- [176] Shultz, M., & Lanzerotti, L. J. (1974), *Particle diffusion in the radiation belts*, Springer Science & Business Media.
- [177] Shirley, J. H., & Fainbridge, R. W. (1997), *Encyclopaedia of planetary sciences, in the series: encyclopaedia of Earth science series*, series edition 1, published by springers Netherlands, series ISBN: 1388-4360.
- [178] Sigernes, F., Dyrland, M., Brekke, P., Chernouss, S., Lorentzen, D. A., Ok-savik, K., & Deehr, C. S. (2011), *Two methods to forecast auroral displays*, Journal of Space Weather and Space Climate, volume 1, no. 1, doi: 10.1051/swsc/2011003.
- [179] Simpson, J. A. (1954), *Cosmic-radiation intensity-time variations and their origin. III. The origin of 27-day variations*, Physical Review, volume 94, issue 2, page 426, doi: <http://dx.doi.org/10.1103/PhysRev.94.426>
- [180] Sojka, J. J., & Schunk, R. W. (1983), *A theoretical study of the high latitude F region's response to magnetospheric storm inputs*, Journal of Geophysical Research: Space Physics, volume 88, issue A3, pages 2112-2122, doi: 10.1029/JA088iA03p02112.
- [181] Smith, C. W., L'Heureux, J., Ness, N. F., Acuña, M. H., Burlaga, L. F., & Scheifele, J. (1998), *The ACE magnetic fields experiment*, In The Advanced Composition Explorer Mission, volume 86, issue 1–4, pages 613–632, doi: 10.1023/A:1005092216668.
- [182] Spencer, E., Kasturi, P., Patra, S., Horton, W., Mays, M. L. (2011), *Influence of solar wind-Magnetosphere coupling functions on the Dst index*, Journal of Geophysical Research: Space Physics, volume 116, issue A12, doi: 10.1029/2011JA016780.

-
- [183] Størmer, C. (1955), *The polar aurora*, Clarendon Press.
- [184] Sturrock, P. A., Kaufman, P., Moore, R. L., Smith, D. F. (1984), *Energy release in solar flare*, Solar Physics, volume 94, issue 2, pages 341-357. doi:10.1007/BF00151322.
- [185] Sturrock, P. A. (1968), *A model of solar flares*, In Symposium-International Astronomical Union, Cambridge University Press, page 471, doi: 1968IAUS...35..471S.
- [186] Takahashi, K., Ohtani, S-I, & Anderson, B. J. (1995), *Statistical analysis of Pi 2 pulsation observed by the AMPTE CCE spacecraft in the inner magnetosphere*, Journal of Geophysical Research: Space Physics, volume 100, issue A11, pages 929–941, doi: 10.1029/95JA01849.
- [187] Taylor, H. E., & Hones, E. H. (1965), *Adiabatic motion of auroral particles on a model of the electric and magnetic fields surrounding the Earth*, Journal of Geophysical Research: Space Physics, volume 70, issue 15, 3605–3628, doi: 10.1029/JZ070i015p03605.
- [188] Tsyganenko, N. A. (1995), *Modelling the Earth's magnetospheric magnetic field confined within a realistic magnetopause*, Journal of Geophysical Research: Space Physics, volume 100, issue A4, pages 5599–5612, doi: 10.1029/94JA03193.
- [189] Tsunomura, S. (1998), *Characteristics of geomagnetic sudden commencement observed in middle and low latitudes*, Earth, planets and space, volume 50, issue 9, pages 755–772, doi: 10.1186/BF03352168.
- [190] Vodka, R. R., Smith, G., Hatfield, V. E., Tsunoda, R. T., Frank, V. R., & Perreault, P. D. (1978), *Chantika model of the high-latitude ionosphere for application to HF propagation prediction*, Rome air development center technical report, RADC-TR-78-7
- [191] Wang, C., & Du, D., Richardson, J. D. (2005), *Characteristics of the interplanetary coronal mass ejections in the heliosphere between 0.3 and 5.4 AU*, Journal of Geophysical Research: Space Physics, volume 110, issue A10, doi: 10.1029/2005JA011198.
- [192] Warwick, C.S., & Haurwitz, M. W. (1962), *A study of solar activity associated with polar-cap absorption*, Journal of Geophysical Research, volume 67, issue 4, pages 1317–1332, doi: 10.1029/JZ067i004p01317.
- [193] Webb, D. F., Cliver, E. W., Crooker, N. U., St. Cyr, O. C., & Thompson, B. J. (2000), *Relationship of halo coronal mass ejections, magnetic clouds,*

-
- and magnetic storms*, Journal of Geophysical Research, volume 105, issue A4, pages 7491–7508, doi: 10.1029/1999JA000275.
- [194] Weir, R. A., & Brown R.R. (1964), *On the contribution of solar-flare alpha particles to polar-cap absorption events*, Journal of Geophysical Research, volume 69, issue 11, page 2193–2198.
- [195] Wild, P. (2011), *Particle precipitation in the auroral ionosphere*, a thesis submitted for the award of doctor of philosophy, physics department, Lancaster university, United Kingdom.
- [196] Wu, C. C., & Lepping, R. P. (2007), *Comparison of the characteristics of magnetic cloud and magnetic cloud structures for the event of 1995-2003*, Solar Physics, volume 242, issue 159, doi:10.1007/s11207-007-0323-6
- [197] Yurchyshyn, V., Wang, H., Abrameko, V. (2004), *Correlation between speeds of coronal mass ejections and the intensity of geomagnetic storms*, Space Weather, volume 2, issue 2 doi: 10.1029/2003SW000020.
- [198] Yuting, N., Hoshino, M., Amano, T., Shirakawa, K., Higashimori, K. (2013), *Introduction to motion of charged particles in Earth's magnetosphere*, <http://www.s.u-tokyo.ac.jp/en/utrip/archive/2013/pdf/06NgYuting.pdf>
- [199] Zhang, M., & Low, B. C. (2005), *The hydromagnetic nature of solar coronal mass ejections*, Annual Review of Astronomy and Astrophysics, volume 43, pages 103–137, doi: 10.1146/annurev.astro.43.072103.150602.
- [200] Zhang, Y., & Paxton L. J. (2008), *An empirical Kp-dependent global auroral model based on TIMED/GUVI data*, Journal of Atmospheric and Terrestrial Physics, volume 70, issues 8–9, pages 1231–1242, doi: 10.1016/j.jastp.2008.03.008.
- [201] Zhang, G., & Burlaga, L. F. (1988), *Magnetic clouds geomagnetic disturbances and cosmic ray decreases*, Journal of Geophysical Research: Space Physics, volume 93, issue A4, pages 2511–2518, doi: 10.1029/JA093iA04p02511.
- [202] Zolesi, B., & Cander, L. R. (2014), *Ionospheric prediction and forecasting*, published by springer Verlag Berlin, Heidelberg, ISBN 978-3-642-34829-5.
- [203] Zurbuchen, T. H., Hefti, S., Fisk, L. A., Gloeckler, G., Schwadron, N. A. (2000), *Magnetic structure of the slow solar wind: Constraints from composition data*, Journal of Geophysical Research: Space Physics, volume 105, 18327–18336, doi: 10.1029/1999JA000427.

-
- [204] Zurbuchen, T. H., & Richardson, I. G. (2006), *In-Situ solar wind and magnetic field signatures of interplanetary coronal mass ejections*, Space Sciences Reviews, volume 123, issues 1–3, pages 31–43, doi: 10.1007/s11214-006-9010-4.
- [205] Zwickl, R. D., Asbridge, J. R., Bame, S. J., Feldman, W. C., Gosling, J. T., & Smith, E. J. (1983), *Plasma properties of driver gas following interplanetary shocks observed by ISEE-3*, In JPL solar wind five, NASA conference publication CP-2280, pages 711–717, (SEE N84-13067 03-92).